

PhD thesis

A geodynamic model of the northern North Atlantic

Birte-Marie Ehlers



Reviewer

Prof. Dr. Vikram Unnithan, Dr. Wilfried Jokat,
Prof. Dr. Joachim Vogt and Dr. Carmen Gaina

Date of Defence: 27th March 2009
School of Engineering and Science

Alfred Wegener Institute for Polar
and Marine Research, Bremerhaven
Jacobs University Bremen, Bremen



Abstract

The Arctic region plays an important role in the configuration of the present day global climate. In particular the Fram Strait area, which is presently the only deep-water gateway between the Arctic Ocean and the world ocean, namely the Atlantic Ocean, accounts for the Arctic region climate. Until now it is still speculative how and when the deep-water connection through the Fram Strait opened due to its tectonic and geologic evolution, and how strong this opening influenced northern ocean circulations. It is assumed that the change of the northern ocean circulations correlate with long-term climate changes.

This study provides a compilation of a geodynamic model of the northern North Atlantic, which is continued to the Arctic Ocean. The tectonic and bathymetric development of the northern North Atlantic and the Arctic Ocean is investigated, especially the complicated bathymetry of the connection between these two oceans. The development of young ocean basins, sills and fracture zones resulted in the 200 km wide and up to 3000 m deep Fram Strait. Due to the movements of the Eurasia, the Greenland, and the North American plates, as well as sediment accumulation changes, the width and seafloor depth of the Fram Strait was significantly modified since its initial break-up.

New geophysical data in the northern North Atlantic and in the Arctic Ocean, gathered by the Alfred Wegener Institute during the last years, make this study possible. The results present an advanced age model of the oceanic crust in the Norwegian-Greenland Sea, in the Fram Strait area, and in the Eurasia Basin. This age model describes the timing of the initial seafloor spreading of 54 Ma for the Eurasia Basin and the Norwegian-Greenland Sea, 38 Ma for the southern Boreas Basin, 28 Ma for the southwestern Gakkel Ridge, 21 Ma for the connection of the Mohns and Knipovich Ridges, 21 Ma for the Molloy Basin, and 12 Ma for the Lena Trough. The study indicates that initial seafloor spreading continued along all ridges north of the Greenland Fracture Zone with ultra-slow spreading rates. Furthermore, the age model provides refined rotation parameters for the involved plates.

New seismic reflection data in the Boreas, the Molloy and the Eurasia basins are used to compare the observed basement depth with a theoretically calculated subsidence, which is corrected for the observed sediment loads. The subsidence study shows how the development of oceanic crust in the northern North Atlantic and in the Arctic Ocean is mainly influenced by thermal cooling, sediment accumulation and isostatic balance. Additionally, the crustal roughness is analysed. The large and unique ridge system with ultra-slow spreading rates allows to complement the global roughness data base. This study indicates the relationship between crustal roughness, ridge morphology and spreading rates and shows that the basins north of the Greenland-Fracture Zone were formed at ultra-slow spreading axial rift valleys during its entire evolution.

The age model, the kinematic parameters, the crustal evolution analyses and a compilation of additional geophysical data (seismic reflection and refraction, bathymetry and gravity data) provide a basis for a palaeobathymetric reconstruction. This reconstruction

is accomplished with a modified version of the “BalPal v.0.9” software. The palaeobathymetric reconstruction shows a model of seafloor depth, basement depth and sediments thickness for every 5 Myr since 55 Ma until today. This model results in a timing of the Fram Strait opening of 25 Ma for a shallow-water exchange. From 17 Ma on, a deep-water exchange below 1500 m water depth between the northern North Atlantic and the Arctic Ocean was possible. The results are compared to previous available studies.

The palaeobathymetric reconstruction provides an insight into the tectonic and sedimentary processes during the development of the investigated oceanic basins. Furthermore, it shows that deep basement structures existed before initial seafloor spreading started. It is assumed that seafloor spreading followed a phase of stretching of continental crust.

To link the results of the palaeobathymetric reconstruction to the global climate history, palaeoceanographic model scenarios are calculated for the present day bathymetric configuration and the palaeobathymetry of the Middle Miocene (15 Ma), the Early Miocene (20 Ma) and the Middle Eocene (45 Ma). The results of the model runs show the conditions of ocean circulation of a land-locked Arctic Ocean for 45 Ma. At 20 Ma, a deep-water inflow of warm and saline Atlantic water through the Fram Strait is established. For the 15 Ma model scenario this study gives evidence for the onset of a deep-water outflow from the Arctic Ocean to the northern North Atlantic. This onset of a two-way deep-water exchange through the Fram Strait may be an important factor for the onset of the Middle Miocene climate optimum. Cold and low saline deep-water is transported south to the Atlantic Ocean.

This study shows the complex relationship between plate tectonics, the crustal development, sediment accumulations, bathymetric changes and changes in ocean circulation in the northern North Atlantic and in the Arctic Ocean and speculates on their link to global past long-term climate changes. The results are a basis for future tectonic, sedimentary, oceanographic and climate research.

Contents

1	Introduction	1
1.1	Basin evolution	4
1.1.1	Continental rifting	4
1.1.2	Evolution of oceanic basins: Seafloor spreading and ocean ridge axis	6
1.2	Ocean gateways	7
1.3	The Fram Strait - Arctic Ocean gateway	9
1.3.1	Arctic tectonic history	9
1.3.2	Arctic geological history	12
1.3.3	Plate tectonic and palaeobathymetric reconstructions	12
1.3.4	Arctic climate history	14
1.4	Arctic ocean circulations	16
1.4.1	Deep-water circulation	16
1.4.2	Ocean circulations in the northern North Atlantic and the Arctic Ocean	17
2	Data	21
2.1	Bathymetry	21
2.2	Magnetics	22
2.3	Gravity	24
2.4	Sea level changes	25
2.5	Seismic reflection and refraction profiles	26
2.6	Palaeobathymetric reconstructions	27
3	Methods	29
3.1	Analysis of magnetic data	30
3.1.1	Tectonic reconstruction parameters	30
3.2	Subsidence analysis of oceanic crust	31
3.2.1	Thermal subsidence	31
3.2.2	Sediment corrected subsidence	32
3.3	RMS roughness calculations	33
3.4	Palaeobathymetric reconstruction	34
3.5	Oceanographic model experiment	37
3.5.1	Preparation of palaeobathymetric data	38

3.5.2	Ocean circulation model experiment	38
4	Scientific Manuscripts	41
5	Paper 1: Subsidence and crustal roughness	45
5.1	Summary	45
5.2	Introduction	46
5.3	Data	49
5.3.1	Seismic reflection profiles	49
5.3.2	Magnetic Data	52
5.4	Analysis	55
5.4.1	Spreading Rates	55
5.4.2	Subsidence	57
5.4.3	Roughness	58
5.5	Discussion	60
5.6	Conclusions	64
6	Paper 2: A palaeobathymetric study	69
6.1	Summary	69
6.2	Introduction	70
6.3	Data base	73
6.3.1	Bathymetry	73
6.3.2	Magnetics and age model	73
6.3.3	Seismic data	76
6.4	Data and Methods	76
6.4.1	Magnetic data and the age of oceanic crust	76
6.4.2	Seismic data	76
6.4.3	Subsidence analysis	79
6.4.4	Continent ocean transition zone	79
6.4.5	Palaeobathymetric reconstructions	80
6.5	Results	84
6.5.1	Magnetics and age model	84
6.5.2	Palaeobathymetric reconstruction	84
6.6	Discussion	95
6.6.1	Lomonosov Ridge, Eurasia Basin, Yermak Plateau and Lena Trough	98
6.6.2	Molloy Basin and Hovgård Ridge	100
6.6.3	Boreas Basin and Norwegian-Greenland Sea	102
6.6.4	Jan Mayen Fracture Zone, Kolbeinsey Ridge and Aegir Ridge . . .	103
6.6.5	Greenland-Faeroe Ridge	103
6.6.6	Comparison of the basins north of the Jan Mayen Fracture Zone . .	103
6.7	Conclusions	104

7	Paper 3: A palaeoceanographic modelling study	111
7.1	Summary	111
7.2	Introduction	112
7.3	Palaeobathymetry data	115
7.4	Model	117
7.5	Results	118
7.6	Discussion	135
7.7	Conclusions	138
8	Tectonic models	143
8.1	Tectonic model of bathymetric data	143
8.2	Tectonic model of magnetic data	147
8.3	Tectonic model of gravity data	151
8.4	Future tectonic model of bathymetry data	155
9	Discussion and conclusions	157
10	Outlook	161
A	Additional figures	173
A.0.1	Reconstruction of palaeobathymetry	174
A.0.2	Reconstruction of palaeo-basement depth	190
A.0.3	Reconstruction of palaeo-sediment thickness	202
A.0.4	World wide palaeobathymetry for oceanographic modelling	214
A.0.5	Modelled crustal thickness	218
B	Additional tables	219
B.0.6	Sampled angles of rotation	220
B.0.7	Input data “BalPal v. 0.9”	221

List of Figures

1.1	Bathymetric map (ETOPO2) of the norther North Atlantic and the Arctic Ocean	2
1.2	Evolution of plate margins	5
1.3	The most prominent ocean gateways in the northern and southern hemisphere	8
1.4	Modelled subsidence of the Lomonosov Ridge	11
1.5	Reconstruction of the Late Conozoic	13
1.6	Global deep-sea oxygen and carbon isotope records	15
1.7	Bathymetric map (ETOPO2) with paths of surface and deep-wataer ocean currents in the northern North Atlantic and the Arctic Ocean	18
2.1	Present day water depth from the ETOPO2v2 grid including the IBCAO grid for the northern North Atlantic and the Arctic Ocean	22
2.2	The Gammaa5-grid	23
2.3	Comparison of the Gammaa5-grid and the new aeromagnetic grid	24
2.4	Gravity data of the Arctic Gravity Project north of 64°N	25
2.5	Sea level changes	26
2.6	Published seismic reflection and refraction data	27
2.7	Global palaeobathymetry for 20 Ma	28
3.1	Overview on the available data, the applied methods and the continued processing of the results	29
3.2	Theoretical thermal and sediment corrected subsidence	32
3.3	Sediment corrected subsidence	32
3.4	Example of profile for roughness calculation	34
3.5	Schematic diagram of the methods applied for a palaeobathymetric reconstruction	36
3.6	Land-sea masks for a modelling with the MPIOM 1.3	39
5.1	Bathymetry map of the international bathymetric chart of the Arctic Ocean (IBCAO) and seismic reflection profiles	47
5.2	Measured and modelled magnetic data along profile AWI-20020500	50
5.3	Measured and modelled magnetic data along profile AWI-20020500	51
5.4	Line drawing of the profile 20010100 in the Nansen Basin	52
5.5	Line drawing of the profile 20010460 in the Nansen Basin	53

5.6	Line drawing of the profile 20010300 in the Amundsen Basin	53
5.7	Age model for the Molloy and Knipovich ridges region	54
5.8	Magnetic modelling of a profile crossing the Molloy Ridge	55
5.9	Magnetic modelling of a profile crossing the Knipovich Ridge	56
5.10	Roughness versus half spreading rate	61
5.11	Roughness versus half spreading rate for this study	63
6.1	Bathymetry map of the international bathymetric chart of the Arctic Ocean (IBCAO)	71
6.2	Age model of the northern North Atlantic and the Arctic Ocean	74
6.3	Merging of gridded magnetic data	75
6.4	Available seismic reflection and refraction data	77
6.5	Distribution of grid cells for the palaeobathymetric reconstruction	82
6.6	Age of oceanic crust	85
6.7	Time slices of 5 Myr steps of the palaeobathymetric modelling for the seafloor depth	87
6.8	Time slices of 5 Myr steps of the palaeobathymetric modelling for the basement depth	88
6.9	Time slices of 5 Myr steps of the palaeobathymetric modelling for the sediment thickness	89
6.10	Time slices of 5 Myr steps from 15 Ma to 30 Ma	91
6.11	Time slices of 1 Myr steps from 16 Ma to 19 Ma	93
6.12	Cross sections through the Fram Strait	97
6.13	Development of the seafloor depth by time	98
6.14	Sediment mass accumulation for the basins in the northern North Atlantic and the Arctic Ocean	101
7.1	Bathymetry map of the international bathymetric chart of the Arctic Ocean (IBCAO) and ocean currents	113
7.2	Palaeobathymetric reconstruction for 0 Ma, 15 Ma, 20 Ma and 45 Ma	116
7.3	Land-sea masks and chosen poles for the modelled time slices	117
7.4	Present bathymetric map with modelled ocean current directions	119
7.5	Palaeobathymetric map for Middle Miocene (15 Ma) with modelled ocean current directions	120
7.6	Palaeobathymetric map for Early Miocene (20 Ma) with modelled ocean current directions	121
7.7	Modelled salinities and currents in 10 m depth for the present day condition	122
7.8	Modelled salinities and currents in 10 m depth for Middle Miocene (15 Ma)	123
7.9	Modelled salinities and currents in 10 m depth for Middle Miocene (20 Ma)	124
7.10	Modelled salinities and temperature along the West Spitsbergen Current for the present day conditions	125
7.11	Modelled salinities and temperature along the West Spitsbergen Current for Middle Miocene (15 Ma)	126

7.12	Modelled salinities and temperature along the West Spitsbergen Current for Early Miocene (20 Ma)	127
7.13	Modelled salinities and temperature along the East Greenland Current for the present day conditions	129
7.14	Modelled salinities and temperature along the East Greenland Current for Middle Miocene (15 Ma)	130
7.15	Modelled salinities and temperature along the East Greenland Current for Early Miocene (20 Ma)	131
7.16	Vertical profiles of salinities and temperatures averaged along the West Spitsbergen Current	132
7.17	Vertical profiles of salinities and temperatures averaged along the East Greenland Current	133
7.18	Vertical profiles of salinities and temperatures averaged in the Eurasia Basin	134
7.19	Atlantic meridional overturning circulation	136
8.1	Rotated bathymetric data, 0Ma–15Ma	144
8.2	Rotated bathymetric data, 20Ma–35Ma	145
8.3	Rotated bathymetric data, 40Ma–50Ma	146
8.4	Rotated magnetic data, 0Ma–15Ma	148
8.5	Rotated magnetic data, 20Ma–35Ma	149
8.6	Rotated magnetic data, 40Ma–50Ma	150
8.7	Rotated gravity data, 0Ma–15Ma	152
8.8	Rotated gravity data, 20Ma–35Ma	153
8.9	Rotated gravity data, 40Ma–50Ma	154
8.10	Present day bathymetry data and rotated bathymetry data for the future .	156
10.1	Arctic regions of interest for future palaeobathymetric reconstructions . . .	162
10.2	Ocean currents in the Atlantic Ocean	164
A.1	Palaeobathymetric reconstruction for 0 Ma	174
A.2	Palaeobathymetric reconstruction for 5 Ma	175
A.3	Palaeobathymetric reconstruction for 10 Ma	176
A.4	Palaeobathymetric reconstruction for 15 Ma	177
A.5	Palaeobathymetric reconstruction for 16 Ma	178
A.6	Palaeobathymetric reconstruction for 17 Ma	179
A.7	Palaeobathymetric reconstruction for 18 Ma	180
A.8	Palaeobathymetric reconstruction for 19 Ma	181
A.9	Palaeobathymetric reconstruction for 20 Ma	182
A.10	Palaeobathymetric reconstruction for 25 Ma	183
A.11	Palaeobathymetric reconstruction for 30 Ma	184
A.12	Palaeobathymetric reconstruction for 35 Ma	185
A.13	Palaeobathymetric reconstruction for 40 Ma	186
A.14	Palaeobathymetric reconstruction for 45 Ma	187

A.15 Palaeobathymetric reconstruction for 50 Ma	188
A.16 Palaeobathymetric reconstruction for 55 Ma	189
A.17 Palaeo-basement reconstruction for 0 Ma	190
A.18 Palaeo-basement reconstruction for 5 Ma	191
A.19 Palaeo-basement reconstruction for 10 Ma	192
A.20 Palaeo-basement reconstruction for 15 Ma	193
A.21 Palaeo-basement reconstruction for 20 Ma	194
A.22 Palaeo-basement reconstruction for 25 Ma	195
A.23 Palaeo-basement reconstruction for 30 Ma	196
A.24 Palaeo-basement reconstruction for 35 Ma	197
A.25 Palaeo-basement reconstruction for 40 Ma	198
A.26 Palaeo-basement reconstruction for 45 Ma	199
A.27 Palaeo-basement reconstruction for 50 Ma	200
A.28 Palaeo-basement reconstruction for 55 Ma	201
A.29 Palaeo-sediment thickness reconstruction for 0 Ma	202
A.30 Palaeo-sediment thickness reconstruction for 5 Ma	203
A.31 Palaeo-sediment thickness reconstruction for 10 Ma	204
A.32 Palaeo-sediment thickness reconstruction for 15 Ma	205
A.33 Palaeo-sediment thickness reconstruction for 20 Ma	206
A.34 Palaeo-sediment thickness reconstruction for 25 Ma	207
A.35 Palaeo-sediment thickness reconstruction for 30 Ma	208
A.36 Palaeo-sediment thickness reconstruction for 35 Ma	209
A.37 Palaeo-sediment thickness reconstruction for 40 Ma	210
A.38 Palaeo-sediment thickness reconstruction for 45 Ma	211
A.39 Palaeo-sediment thickness reconstruction for 50 Ma	212
A.40 Palaeo-sediment thickness reconstruction for 55 Ma	213
A.41 Palaeobathymetry data of the North Atlantic and the Arctic ocean combined with the world wide palaeobathymetry data for 0Ma	214
A.42 Palaeobathymetry data of the North Atlantic and the Arctic ocean combined with the world wide palaeobathymetry data for 15Ma	215
A.43 Palaeobathymetry data of the North Atlantic and the Arctic ocean combined with the world wide palaeobathymetry data for 20Ma	216
A.44 Palaeobathymetry data of the North Atlantic and the Arctic ocean combined with the world wide palaeobathymetry data for 45Ma	217
A.45 Calculations of modelled crustal thickness for a present day northern North Atlantic and Arctic Ocean	218

List of Tables

5.1	Profile section, half spreading rates, age range, length of profile section, roughness, R_i , and predicted roughness, R_C	59
6.1	Available seismic reflection and refraction data	78
6.2	Re-identified magnetic anomalies and their corresponding rotation parameters	81
6.3	Past sea level changes	86
6.4	Total sediment mass, total grid cell area, total sediment volume and total sediment mass/grid cell	98
8.1	Extrapolated rotation parameters	155
9.1	Timing of the initial seafloor spreading	158
B.1	sampled parameters of rotation	220
B.2	Example grid cell for “BalPal v. 0.9”	221
B.3	Parameters for “BalPal v. 0.9”	222

Chapter 1

Introduction

Investigations about the geodynamic evolution of the northern North Atlantic are essential with respect to its tectonic and geological history, to understand the history of ocean circulations and more importantly, the history of long-term regional and global climate changes. Various studies exist about the timing of the Fram Strait deep-water gateway opening, but they remain speculative due to a lack of high resolution data. The present day climatic conditions in high latitudes make the investigation of the northern North Atlantic and the Arctic Ocean difficult. Between the Charlie Gibbs and the Jan Mayen fracture zones (Figure 1.1) a palaeobathymetric reconstruction exists (Wold, 1995). New geophysical data, gathered by the Alfred Wegener Institute, provide for the first time a basis for a northward continuation of a detailed palaeobathymetric study in the northern North Atlantic and in the Arctic Ocean for the last 55 Myr. This study combines the available geophysical knowledge of the investigated area. To date, the results of geophysical experiments in the northern North Atlantic and in the Arctic Ocean were treated separately. The palaeobathymetric reconstructions yield the possibility to gather a palaeoceanographic model experiment in order to analyse past changes in the ocean circulation as a consequence of the tectonic movements. The influence of palaeobathymetric and ocean circulation variabilities on climate changes is investigated.

Various problems in the understanding of the development of the northern North Atlantic and the Arctic Ocean still exist:

- When did initial seafloor spreading start in the northern North Atlantic and in the Arctic Ocean?
- Did the spreading rate change during the basin evolution?
- Which conclusions drawn from the present day conditions can be applied to the basin evolution?
- Did the ocean basin basement and seafloor develop as the theory about subsidence predicts?

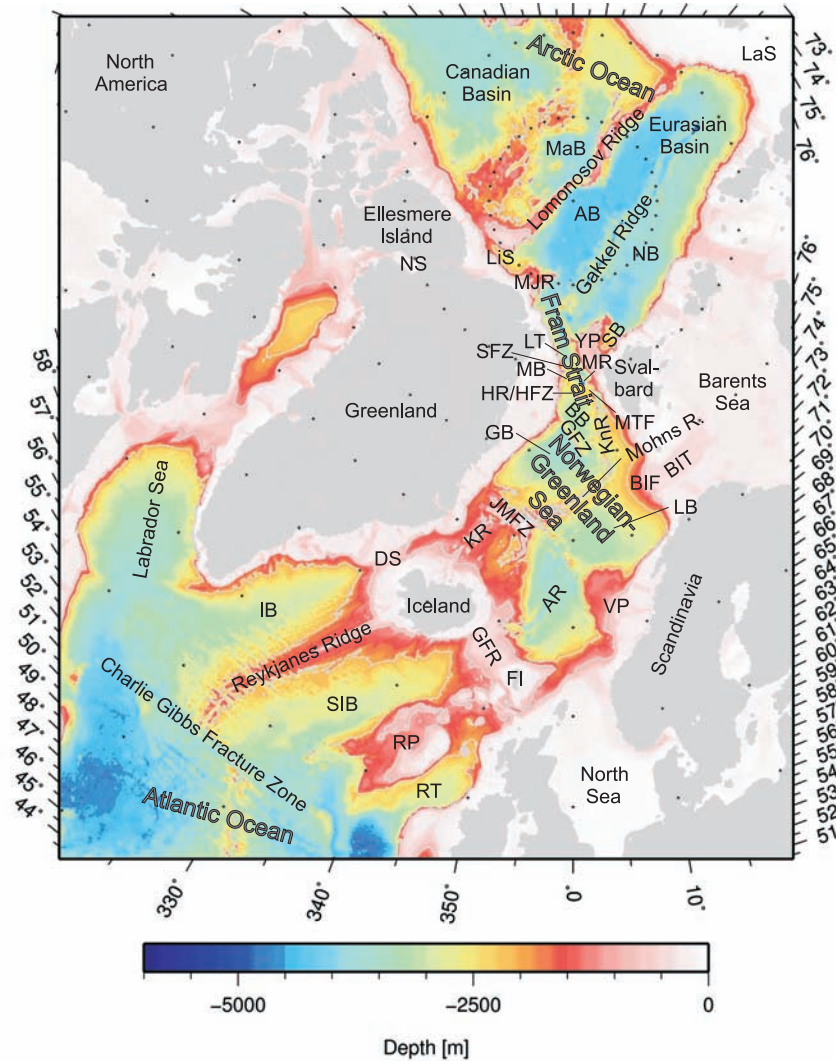


Figure 1.1: Bathymetric map (ETOPO2 (Jakobsson et al., 2001)) of the northern North Atlantic and the Arctic Ocean, AB: Amundsen Basin, AR: Aegir Ridge, BB: Boreas Basin, BIF: Bear Island Fan, BIT: Bear Island Trough, DS: Denmark Strait, FI: Faeroe Islands, GB: Greenland Basin, GFR: Greenland-Faeroe Ridge, GFZ: Greenland Fracture Zone, HR: Hovgård Ridge, IB: Irminger Basin, JMFZ: Jan Mayen Fracture Zone, KnR: Knipovich Ridge, KR: Kolbeinsey Ridge, LB: Lofoten Basin, LaS: Laptev Sea, LiS: Lincoln Sea, LT: Lena Trough, MB: Molloy Basin, MaB: Makarov Basin, MJR: Morris Jesup Rise, MR: Molloy Ridge, MTF: Molloy transform Fault, NB: Nansen Basin, NS: Nares Strait, RP: Rockall Plateau, Rockall Trough, SB: Sophia Basin, SFZ: Spitsbergen Fracture Zone, SIB: South Iceland Basin, VP: Vøring Plateau, YP: Yermak Plateau.

-
- How did the northern North Atlantic and the Arctic Ocean evolve after the onset of seafloor spreading?
 - What was the seafloor depth during initial seafloor spreading?
 - How does the sediment accumulation influence the seafloor and basement depth?
 - When did the Fram Strait open?
 - When was the deep-water connection through the Fram Strait established?
 - How was the water circulation affected by the change in bathymetry?
 - Did the opening of the Fram Strait influence the regional and global long-term climate?

This study is aimed to find answers to these pertinent questions and investigates the present day configuration of the ocean basins in the northern North Atlantic and the Arctic Ocean. A crustal age model is developed by a re-identification of magnetic anomalies. Additionally, subsidence calculations and roughness analyses are compiled and a palaeobathymetric reconstruction is calculated. The software package “BalPal v.0.9” (Wold, 1995) is modified and a data base of 1515 grid cells is compiled. The palaeobathymetric reconstruction provides a basis for a palaeoceanographic study, which tests the influence of the changing bathymetry to ocean circulations. New and published data are combined in various geophysical methods to present evidence on the geodynamical evolution of the northern North Atlantic and the Arctic Ocean. The results of the different analyses and models are interpreted and discussed.

This thesis starts with an introduction chapter about the general development of ocean basins, ocean gateways and the tectonic and geological history of the northern North Atlantic and the Arctic Ocean. Attention is also given to tectonic and palaeobathymetric reconstructions, the Arctic climate history and northern ocean circulations. The second chapter presents primarily new and published bathymetry, magnetic, gravity and seismic data. In the following chapter the methods applied are described. Chapter 4 introduces the three scientific journal publications, which present the results and interpretations of this study. The first article presents a detailed crustal age model for the Boreas Basin and the Fram Strait and includes subsidence calculations and roughness analyses (Chapter 5). The second article (Chapter 6) presents and interprets the results of the palaeobathymetric reconstruction, which are the basis for the palaeoceanographic model experiment described in the third article (Chapter 7). Chapter 8 discusses tectonic models of bathymetry, magnetic and gravity data. The thesis closes with a chapter of discussion and conclusions (Chapter 9) and a final outlook chapter (Chapter 10). The Appendix contains additional figures and tables.

1.1 Basin evolution

For the analysis presented in chapter 5 and 6, an understanding of the development of the ocean basins in the northern North Atlantic and in the Arctic Ocean is essential. This section describes the common development of ocean basins from the rifting process of continental margins to seafloor spreading along ocean ridge axis, to get an insight into the evolution of the northern North Atlantic and the Arctic Ocean.

1.1.1 Continental rifting

A continental rift is defined as elongate depression, where the entire thickness of the lithosphere has deformed under the influence of extensional forces (Neumann and Ramberg, 1978; Burchfiel, 1980). An example of a presently active rift is the East African Rift.

The lithosphere underlying rifts is generally abnormally thin and invaded by high temperature, low density and low velocity material (Figure 1.2(a)). In this respect, they are similar to ocean ridges, which mark accretive or constructive plate margins where new oceanic lithosphere originates.

Continental rifting follows a phase of crustal doming, which is preceded by volcanism with magma derived from the mantle (Davidson and Rex, 1980). The primary cause of the initiation of rifting is the presence of some sort of thermal anomaly in the upper mantle (Kusznir and Park, 1984). This is observed along many rifts (Morgan, 1983; Ben-Avraham and von Herzen, 1987; Hooper, 1990). The lithosphere-asthenosphere boundary is temperature controlled. Any increase in temperature causes a rise of the boundary and consequently thins the lithosphere. Thermal anomalies can probably originate from hotspot activities. Evidence on the rifting process is available from passive continental margins. These margins are distinguished into volcanic and non-volcanic margins. They differ in the temperature of the underlying asthenosphere (Keary and Vine, 1996).

Courtillot (1982) and Courtillot and Vink (1983) describe a simple model of rift propagation. A rift is probably formed along existing lines of weakness in a continent, such as old sutures. Extensional forces deform and thin the lithosphere. Initial rifting begins along the future plate boundaries and thinning reduces the strength of large areas of the lithosphere. The uniformity of lithosphere causes the plates to remain attached at a number of so called locked zones, whereas seafloor spreading already started along weak zones (Figure 1.2(b)). Oceanic crust is produced along the rift, which leads to a stretching of the locked zones on one or both sides. The rift penetrates the locked zone so that its outer part is carried away by each plate. The part which is still locked, continues to stretch until it becomes invaded by the rift. The magnetic character of these deformed zones is different from that of typical oceanic crust and produce a magnetic quiet zone at the new continental margin (Keary and Vine, 1996).

Further information about the crustal development is provided by the basement depth of rifted continental crust. Crustal extension and crustal thinning (Myhre and Eldholm, 1988) can result in local pull-apart basins. Large crustal thinning implies that continental crust was deeply subsided before seafloor spreading started (Engen et al., 2008). For

example, assuming Airy isostasy and a 31.2 km thick unstretched continental crust without a sediment load, a 4.3 km deep continental basin would have formed.

This study concentrates on the crustal development in the northern North Atlantic and in the Arctic Ocean. Between Svalbard, Norway and Greenland (Figure 1.1) continental rifting culminated in seafloor spreading that led to the opening of the northern North Atlantic (Talwani and Eldholm, 1977) and propagated in the Eurasia Basin. The next section briefly describes the onset of seafloor spreading and the formation of ocean ridge axis.

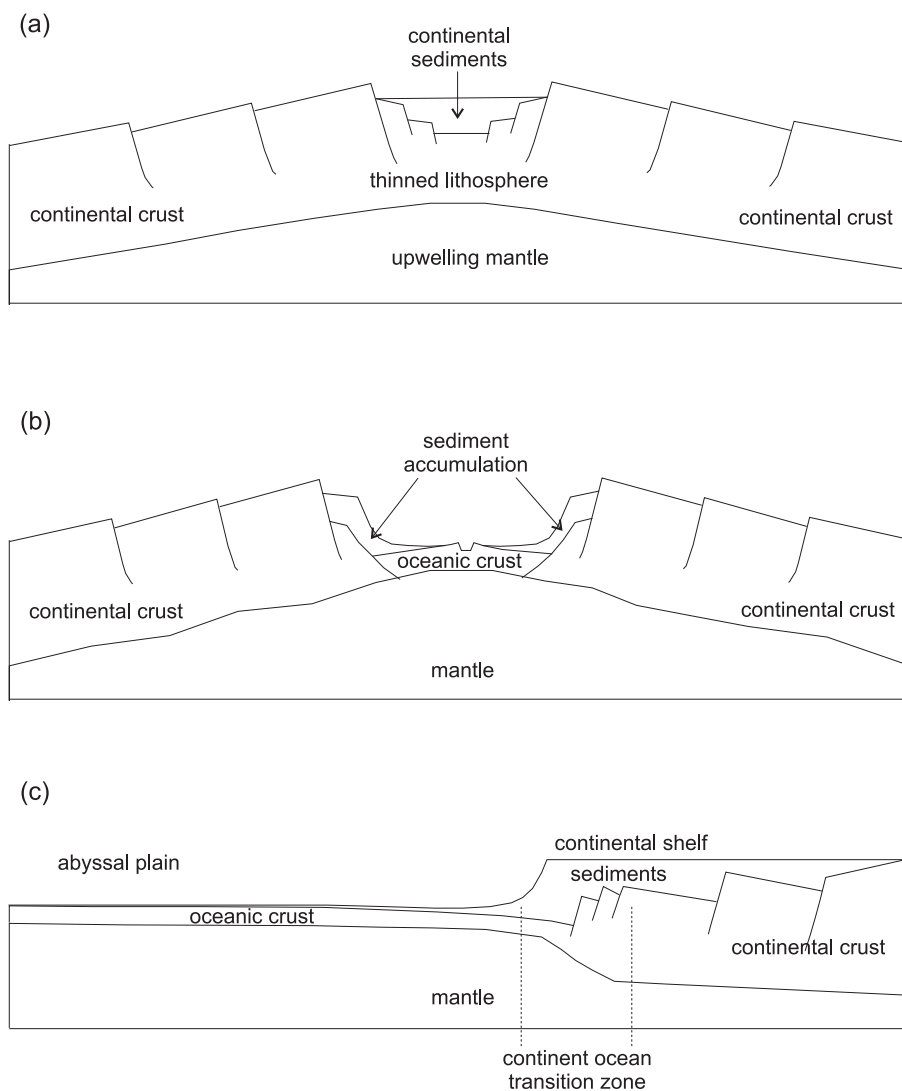


Figure 1.2: Evolution of plate margins (modified after Hoffman et al. (1974)): (a) thinned continental crust, (b) initial seafloor spreading, (c) transition from oceanic basin to the continental shelf.

1.1.2 Evolution of oceanic basins: Seafloor spreading and ocean ridge axis

Continental rifting is followed by seafloor spreading, which is an important investigation parameter in this study (Chapter 5 and 6). New oceanic crust is created along the oceanic ridges. The ocean gradually grows with a progressive creation of lithosphere. The continents marginal to the ocean move apart. The crest of oceanic ridges are in average 2 km–3 km higher than adjacent ocean basins. The topography of the ocean basins runs parallel to the crest and can locally be rugged.

Oceanic basins show typical characteristics in geophysical measurements. Much information about oceanic areas has been provided by geophysical surveys undertaken from ships or aircrafts. A pattern of stripes is characteristic for magnetic measurements of oceanic crust. It is defined by steep gradients separating linear regions of high amplitude positive and negative anomalies. These magnetic measurements visualize the seafloor spreading process. The continuity of these magnetic lineations is interrupted by oceanic fracture zones. Magnetic lineations are generally 10 km–20 km wide and characterised by a peak-to-peak amplitude of 500 nT–1000 nT (Keary and Vine, 1996). They run parallel to the axis of the mid-ocean ridge system and are commonly symmetric about the ridge axis.

Mid ocean ridges are classified based on their structural, morphological and volcanological characteristics. They have been divided into fast spreading ridges with full spreading rates of 80 mm/y–180 mm/y, intermediate spreading ridges with 55 mm/y–70 mm/y and slow spreading ridges with less than 55 mm/y. Spreading ridges with a full spreading rate of less than 20 mm/y are characterised as ultra-slow spreading ridges (Dick et al., 2003). Globally only a few ultra-slow spreading ridges exist, for example the Southwest Indian Ridge between Africa and Antarctica and the Gakkel Ridge in the Arctic Ocean (Snow and Edmonds, 2007). Spreading rates are not constant through the evolution of oceanic basins.

A comparison between fast and slow spreading ridges shows that they have roughly the same crustal thickness of 6 km–7 km, whereas at ultra-slow spreading ridges crust is thinner (1 km–4 km) (Reid and Jackson, 1981; Bowen and White, 1994; Jokat et al., 2003).

It is assumed that fast spreading ridges tend to be dominated by volcanism whereas the morphology of ultra-slow spreading ridges is dominated by tectonics. However, the Gakkel Ridge shows more volcanism than expected (Snow and Edmonds, 2007).

The different types of spreading rates coincide with different types of ridge morphology. Fast spreading ridges show a central high, intermediate spreading ridges have a smooth axial ridge topography and slow spreading ridge axes obtain a central valley. The morphology and spreading rate of an axial ridge also correlate to the magma supply (Morgan and Chen, 1993). These characteristics of axial ridges are linked to the basement topography of the adjacent oceanic basins (Malinverno, 1991), which can be described by crustal roughness. This study is engaged in the calculation of crustal roughness at profiles crossing the northern North Atlantic and Arctic Ocean ultra-slow spreading mid ocean ridges. Until now, global roughness studies lack results from ultra-slow spreading ridge axis and hence, the previous curve fit, which was interpolated from existing global roughness values, is

modified in this study (Chapter 5).

1.2 Ocean gateways

Numerous ocean basins and ocean ridges build the world's oceans, which are connected by ocean gateways. These ocean gateways are responsible for a water exchange between the oceans. During earth history, various ocean gateways opened and closed due to plate tectonic movements. The development of ocean gateways has a profound effect on global circulation and global climate. For example, various studies prove the influence of the Panama gateway closing and the opening of marine gateways around Antarctica on global circulations and climate changes (Haug and Tiedemann, 1998; Stickley et al., 2004; Livermore et al., 2005). The ocean gateway width and depth influence the exchange of mass, heat and salt. Most prominent ocean gateways during the last 50 Myr are the Panama Gateway, the Drake Passage, the Tasman Strait and the Fram Strait (Figure 1.3).

Panama gateway

The gradual closing of the Panama gateway lasted from 13 Ma to 1.9 Ma (Haug and Tiedemann, 1998). The Late Cenozoic closure of the seaway between the North and South American continents probably caused extensive changes in ocean circulations and Northern Hemisphere climate. Due to this closure, a reorganisation of ocean circulation took place at 4.6 Ma. The shallowing of seawater intensified the Gulf Stream and introduced warm and saline water masses to high northern latitudes, which strengthened the deep-water formation in the Labrador Sea and favoured Early Pliocene warming in the Northern Hemisphere.

Drake Passage

Today, the Drake Passage connects the Pacific and Atlantic oceans. Due to a major change in the motion of the South American and Antarctic plates at about 50 Ma, crustal extension and thinning led to the opening of small oceanic basins (Livermore et al., 2005). Finally a deep-water connection developed between 34 Ma and 30 Ma. The timing of the deep-water opening in the Drake Passage correlates with climatic events and supports the view that it was a trigger for abrupt Eocene-Oligocene climate deterioration and the growth of extensive Antarctic ice sheets (Livermore et al., 2005).

Tasman Strait

The Tasman Strait shows an increased deepening from 35.5 Ma on (Stickley et al., 2004). Between 33.5 Ma and 30.2 Ma, the first energetic bottom currents increased and finally after 30.2 Ma the gateway was completely opened. The Tasman Strait opening also correlates to the onset of Antarctic glaciations at the end of the Eocene (about 33.5 Ma).

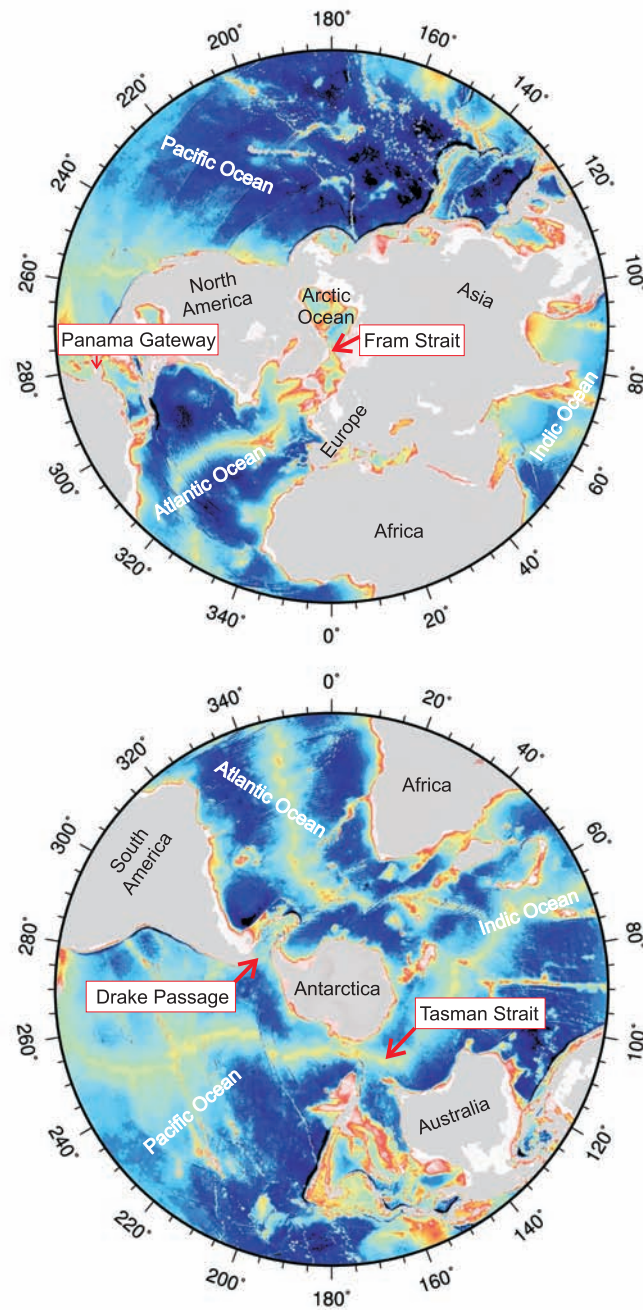


Figure 1.3: Bathymetric map (ETOPO2 (NGDC, 2006)) illustrating the most prominent ocean gateways. Top: northern hemisphere with Panama Gateway and Fram Strait, bottom: southern hemisphere with Drake Passage and Tasman Strait.

Fram Strait

This study concentrates on the Arctic Ocean and the northern North Atlantic, especially in the Fram Strait region. The Fram Strait connects the Arctic Ocean and the Atlantic Ocean. Today it is the only deep-water connection between the Arctic Ocean and a world ocean and hence, an important ocean gateway. Until now it is still speculative when the opening of the Fram Strait had an essential influence on ocean currents, the regional and the world climate (Jakobsson et al., 2007). Information about the depth and width of the gateway during its evolution as well as about palaeoceanographic water exchange are significant for an insight into a correlation of the Fram Strait opening and climate changes. This study deals with the present day crustal subsidence and roughness (Chapter 5), with the reconstruction of palaeobathymetry data (Chapter 6) and with a palaeo-circulation model (Chapter 7) in the Fram Strait and adjacent areas. The following section describes this Arctic Ocean gateway in greater depth.

1.3 The Fram Strait - Arctic Ocean gateway

To resolve the various problems in the understanding of the development of the northern North Atlantic and the Arctic Ocean, a closer look into the Arctic Ocean gateway is necessary. This section introduces the published results the Arctic tectonic and the Arctic geological history and introduces available tectonic and palaeobathymetric reconstructions. Changes in the Fram Strait configuration probably implicated long-term climate changes. To correlate the geodynamic evolution of the Fram Strait and climate variabilities, this section presents an overview about the Arctic climate history.

The most important impact on the climate seems to be the exchange of deep-water between the Arctic Ocean and the northern North Atlantic through the Fram Strait. The timing of the onset of such an exchange still remains speculative and justifies further investigations at the Arctic sea development.

The Arctic Sea belongs to a class of ocean basins known as mediterranean seas (Dietrich et al., 1990). A mediterranean sea is defined as a part of the world ocean, which has limited communication with the major ocean basins. The only deep-water gateway between the Arctic Ocean and the northern North Atlantic is the Fram Strait between Greenland and Svalbard (Figure 1.1). Presently the Fram Strait is about 200 km wide and up to 3000 m deep, and connects the Eurasia Basin and the Norwegian-Greenland Sea (Figure 1.1). It is important to define the onset of the deep-water exchange through the Fram Strait in order to verify a relationship between the tectonic and bathymetric changes, the changes in ocean circulation and the climate evolution.

1.3.1 Arctic tectonic history

The description of the Arctic tectonic history is in a chronological order from the Early Cretaceous to the present.

Cretaceous (145 Ma–66 Ma)

The first tectonic movements in the Arctic Ocean resulted in the opening of the Canada Basin between 140 Ma and 120 Ma (Lawver et al., 1990). Seafloor spreading preceded crustal extension and crustal thinning (Myhre and Eldholm, 1988) resulting in local pull-apart basins. After seafloor spreading started in the Canada Basin, initial stretching of continental crust between the Rockall Plateau and Eurasia started between 118 Ma and 84 Ma (Srivastava and Roest, 1989). In Late Cretaceous, seafloor spreading started between the Rockall Plateau and Ireland (Lawver et al., 1990), and propagated north of the Charlie Gibbs Fracture Zone. At about 84 Ma, seafloor spreading began in the Labrador Sea and separated Greenland from the Arctic Canada. This process ceased at 37 Ma (Roest and Srivastava, 1989), and from then on, Greenland moved as a part of the North American plate. The opening of the Labrador Sea did not produce any deep-water pathway to the Arctic Ocean, but a dextral strike-slip movement started between Eurasia and Greenland along the Trolle-Land Fault Zone at 80 Ma (Håkansson and Pedersen, 1982).

Palaeocene (66 Ma–56 Ma)

The dextral strike-slip movement between Eurasia and Greenland at 60 Ma resulted in initial stretching between the Lomonosov Ridge and Eurasia (Lawver et al., 1990) and formed the Eurasia Basin. At 57 Ma, the tectonic regime between Norway, Svalbard and Greenland changed (Lawver et al., 1990). Transtensional movements shifted to extensional movements between Greenland and Norway and, between Greenland and Svalbard, strike-slip movements shifted to a transpressional regime.

Eocene (56 Ma–34 Ma)

Since 56 Ma, tectonic changes in the Palaeocene resulted in seafloor spreading in the Norwegian-Greenland Sea along the Mohns Ridge, and in the Eurasia Basin along the Gakkel Ridge (Vogt et al., 1979). Seafloor spreading in this area lasts until present day.

The Lomonosov Ridge moves as a part of the North American plate. It runs from the Lincoln Sea to the eastern Laptev Sea and divides the Arctic Ocean into the Canada and the Eurasia basins. During the tectonic evolution of the Arctic Ocean the Lomonosov Ridge subsided below sea level on its entire length (Moore et al., 2006) (Figure 1.4).

Vogt et al. (1979) assume that during the time of plate reorganisation (57 Ma) the Morris Jesup Rise and the Yermak Plateau respectively were formed as volcanic rises. In contrast, Jackson et al. (1984) and Feden et al. (1979) assume that the southern Yermak Plateau is a continental fragment that originated from the triple junction between Eurasia, Greenland and North America, whereas the northern part is interpreted to be of volcanic origin. Geissler and Jokat (2004) and Jokat et al. (2008) suspect that the southern part of the Yermak Plateau consists of continental crust whereas the northernmost part is interpreted to have a volcanic overprint. The structures in the north east have partly formed during Early Cenozoic rifting of the Lomonosov Ridge. Strong volcanism forming parts of the Morris Jesup Rise and the Yermak Plateau coincides with the beginning of the separation of North Greenland and Svalbard. The separation is enforced by the Gakkel Ridge, which begins to propagate to the south into the Lena Trough.

Since the tectonic movements between Greenland and North America ceased (37 Ma), the tectonic motion between Greenland and Eurasia changed to oblique spreading (Talwani and Eldholm, 1977). Seafloor spreading started along the southern Knipovich Ridge and propagates to the north.

Miocene (23 Ma–5 Ma)

To balance the movements in the Eurasia Basin in the north and in the Boreas Basin in the south, finally seafloor spreading also initiated along the Molloy Ridge.

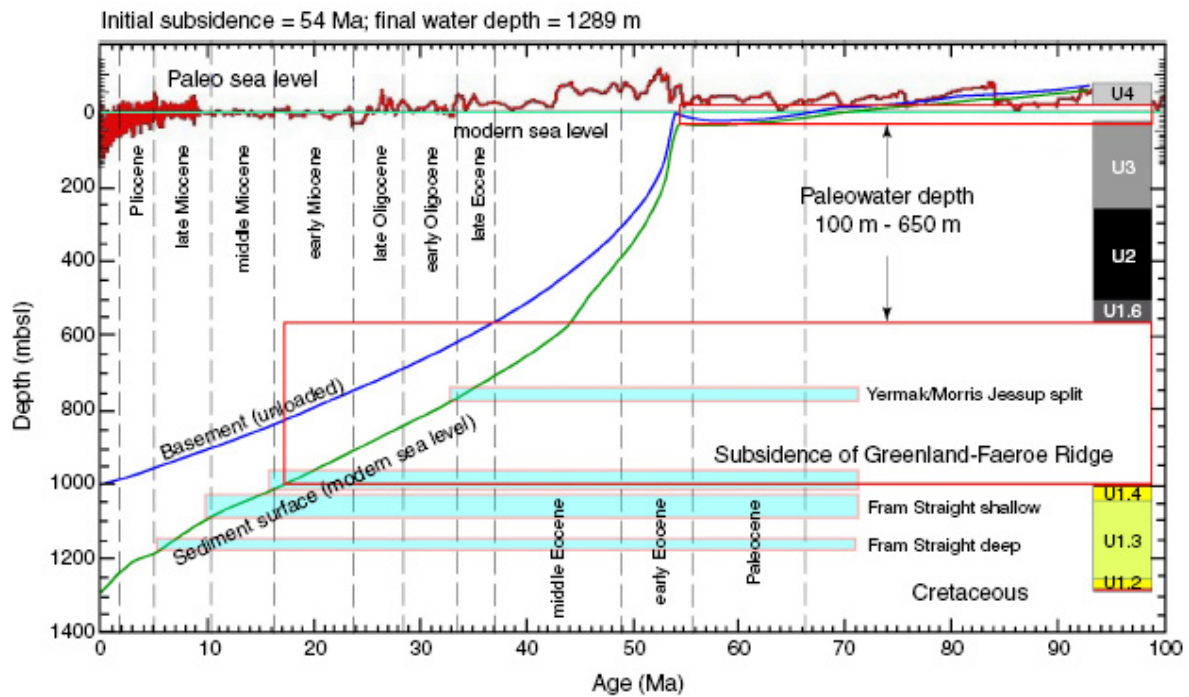


Figure 1.4: After Moore et al. (2006): Modelled subsidence of the Lomonosov Ridge assuming simple postrifting (post 54 Ma) thermal subsidence to modern water depths. The upper subsidence curve (red) shows the subsidence of the ridge without a sediment loading correction. The lower curve (green) shows the subsidence of the sediment surface through time using an Airy correction for sediment loading. Subsidence is calculated relative to present-day sea level. However, an estimate of paleosea-level from Miller et al. (2005) is shown at the top of the plot. No correction has been applied to account for variation in loading resulting from variation in sea level. The column on the right of the figure depicts the lithostratigraphic units recovered from the Lomonosov Ridge, plotted relative to their age-depth position on the lower subsidence curve.

1.3.2 Arctic geological history

From its formation in Early Cretaceous to the Oligocene, the Arctic Ocean is a land-locked basin, completely surrounded by Eurasia, Asia, North America and Greenland (Kristoffersen, 1990). There was no deep-water connection to a world ocean. By analysing a sediment core from the crest of the Lomonosov Ridge, Jakobsson et al. (2007) found evidence for a ventilated Arctic Ocean from 17.5 Ma on. This change of ventilation regime seems to be attributed to the tectonic opening of the Fram Strait and coincides with the onset of the Middle Miocene climate optimum. The cause of this relationship is still unclear.

Oscillations in sea level created an “on-off switch” of Arctic Ocean circulations, which is represented by alternating layers in the sediment core between 18.2 Ma and 17.5 Ma. With a further Fram Strait deepening, sea level changes were no longer significant to the conditions of the Arctic Ocean and it stayed ventilated by oxygen-rich deep-water since 17.5 Ma. The initial corridor for a deep-water exchange developed before seafloor spreading and extended into the Fram Strait.

Parallel to the oceanic basin development, sediments accumulated in the basins and along the East Greenland, Svalbard and Norwegian margins. The age and distribution of sediments is primarily governed by the tectonic evolution. The mass and origin of sediments give insights into climate conditions during the basin development. Especially glacial deposits give evidence of phases of glaciations. They can be found since the Middle Miocene along the East Greenland margin (Berger and Jokat, 2008) and since 2.5 Ma along the Svalbard-Barents sea margin (Solheim et al., 1998). The glacial deposits are two to three times higher on the eastern side of the Fram Strait than on the East Greenland margin. The opening of the Fram Strait also influenced the sediment accumulation in the Arctic Ocean and the northern North Atlantic by changes of ocean currents. The opening of the Fram Strait allows a transport of glacially eroded material from the uplift of the northern Barents Shelf by icebergs to the northern North Atlantic (Knies and Gaina, 2008).

1.3.3 Plate tectonic and palaeobathymetric reconstructions

Plate tectonic and palaeobathymetric reconstructions are a key information to demonstrate a causal link between the opening of gateways and long-term climate events. One of the aims of this study is to model the development of the seafloor and basement depth, in connection with a tectonic reconstruction (Chapter 6). Detailed interpretation of the age of oceanic crust can constrain a plate tectonic reconstruction. Until now a detailed age model for the Fram Strait region was not available due to a lack of high resolution magnetic data. Furthermore, an improved palaeobathymetric reconstruction needs information about the seafloor depth, the sediment thickness and the basement depth for the investigation area derived from seismic stratigraphy data.

The analysis of the palaeobathymetry data provides information on the timing of the initial opening of the ocean basins and the deep-water gateway. Previous plate tectonic reconstructions suggest a Middle Miocene (Kristoffersen, 1990) or Late Miocene (Lawver et

al., 1990) formation of the Fram Strait as Arctic Ocean gateway. The first reconstructions were based on bathymetric contours which reflect contourite deposits. The reconstruction of Kristoffersen (1990) is shown in figure 1.5. North America and Eurasia depart from each other. The bathymetry contour lines present an approximately 500 m deep Fram Strait at 26 Ma, which deepens to a narrow channel of 2000 m until 15 Ma. The reconstruction of Kristoffersen (1990) is based on the poles of rotation for magnetic anomaly 5 and 13 from Talwani and Eldholm (1977), with interpolation for intermediate times and the present day bathymetry. The seafloor depth is not changed by time due to subsidence and sediment accumulation.

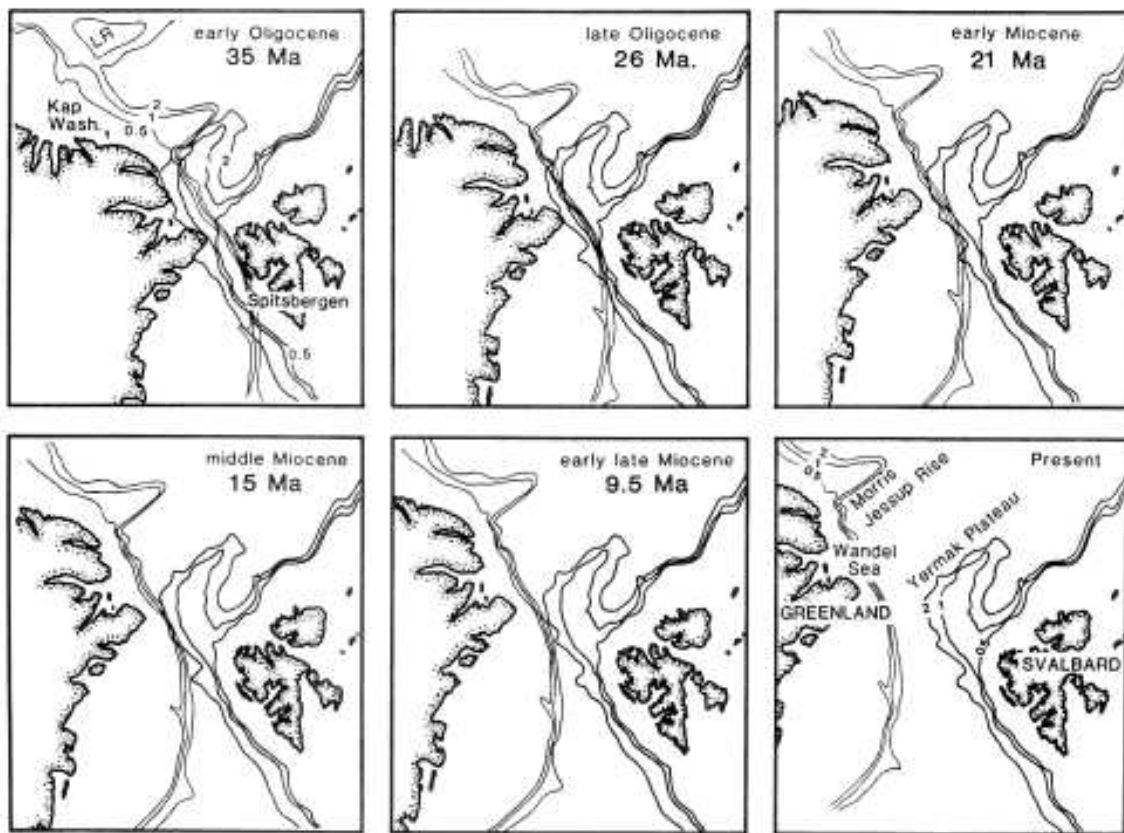


Figure 1.5: Reconstruction of the Late Cenozoic relative position of the North American Plate with respect to Europe (fixed), using poles of rotation for magnetic anomaly 5 and 13 from Talwani and Eldholm (1977), with interpolation for intermediate times. Water depth in km. After Kristoffersen (1990).

In addition to bathymetric data, Engen et al. (2008) used gravity data for a palaeobathymetric reconstruction. Regional Bouguer maps were applied to interpret crustal structure. They found a continuous oceanic corridor in the Lena Trough during Early Miocene times (20 Ma–15 Ma), when the continental crust of Svalbard and Greenland was no longer in

contact across the Molloy and Spitsbergen fracture zones (Figure 1.1). For the region south of the Jan Mayen Fracture Zone, a palaeobathymetric model is provided by Wold (1995).

1.3.4 Arctic climate history

The Earth's climate system has experienced continuous changes during the last 65 Myr, with extremes of expansive warmth with ice-free poles and extremes of cold with massive continental ice-sheets and polar ice caps (Zachos et al., 2001). The primary forces that drive long-term climate are:

- Earth's orbital geometry
- plate tectonics

The orbitally related climate rhythms oscillate about a climate mean that is consequently drifting in response to gradual changes in Earth's major boundary conditions. These boundary conditions include:

- continental geography and topography
- oceanic gateway locations and bathymetry
- concentration of atmospheric greenhouse gasses

These boundary conditions are amongst others controlled by plate tectonics.

Zachos et al. (2001) investigated sediment cores recovered by the **Deep Sea Drilling Project** (DSDP) and the **Ocean Drilling Program** (ODP). They analysed the $\delta^{18}\text{O}$ concentration which correlates with temperature changes. With increasing temperature the $\delta^{18}\text{O}$ concentration increases as well. The $\delta^{18}\text{O}$ record exhibits a number of steps and peaks that reflects episodes of global warming and cooling, as well as ice-sheet growth and decay. Figure 1.6 shows the results of the $\delta^{18}\text{O}$ analysis and connects it with global tectonic events. For example, a warm phase peak in Middle Miocene (17 Ma to 15 Ma) represents the onset of a climate optimum. Since then, temperature increased until today. In the Early Pliocene, after a warming trend until about 3.2 Ma, the $\delta^{18}\text{O}$ increases again. This increase reflects the onset of the northern hemisphere glaciations (Zachos et al., 2001).

Large-scale glaciations are a good indicator of climate conditions. Intensive glaciations at the Earth's poles during the Cenozoic are linked to the opening of the polar gateways, namely the Fram Strait in the north, and the Drake and Tasmanian passages in the south (Zachos et al., 2001). Most information about climate changes in the history of the Arctic region is derived from analysis of the deposited sediments. The existence of Northern Hemisphere ice sheets can be demonstrated on the basis of proxy data and ice-rafted debris from the Nordic seas. Eldrett et al. (2007) suggest the existence of (at least) isolated glaciers on Greenland between Late Eocene and Oligocene (30 Ma and 38 Ma). Helland and Holms (1997) found a minimum age for the beginning of ice formation in southern Greenland and in the North Atlantic with Middle Miocene. Berger and Jokat (2008) propose that

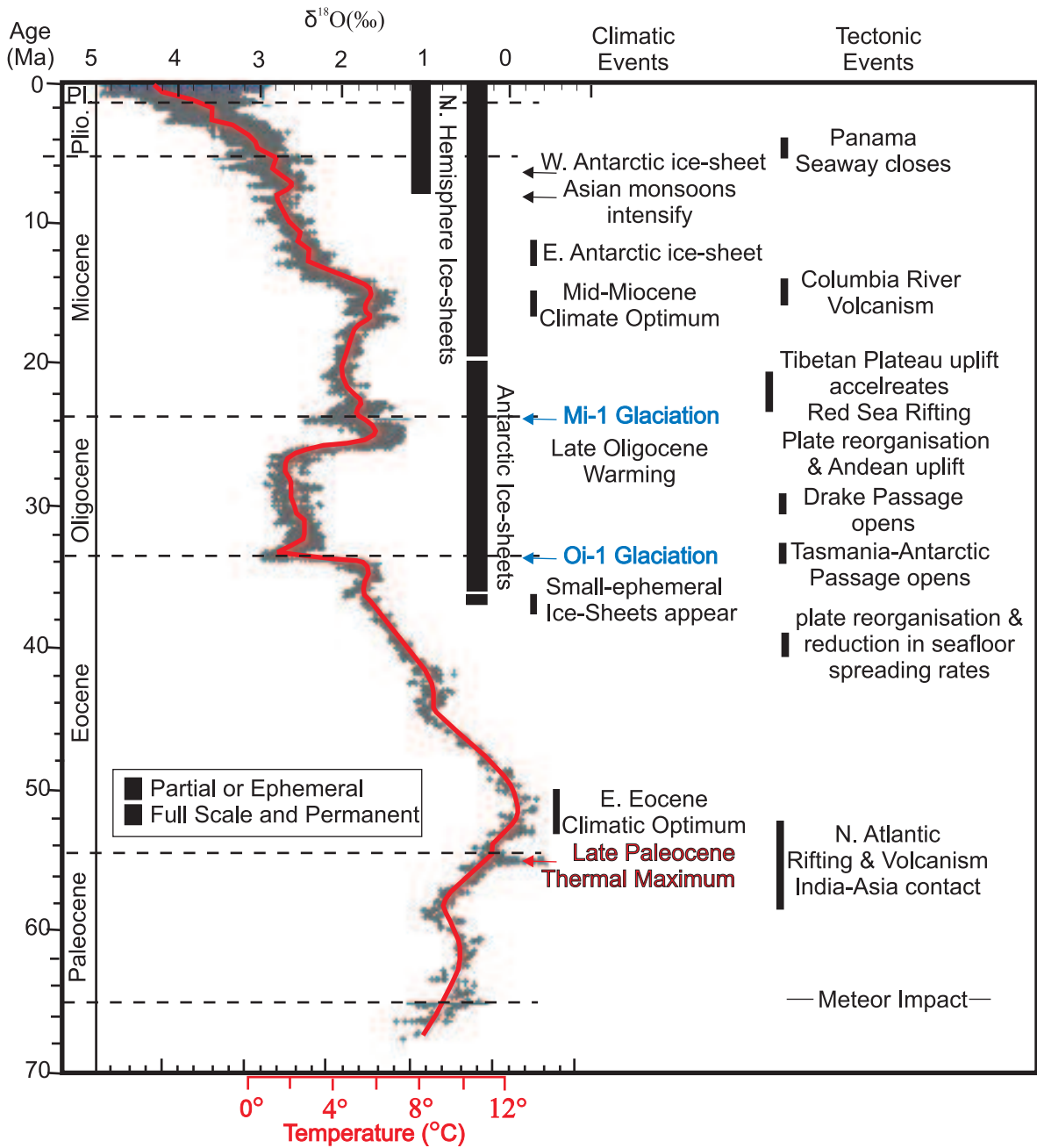


Figure 1.6: After Zachos et al. (2001): Global deep-sea oxygen and carbon isotope records based on data compiled from more than 40 DSDP and ODP sites.

the glaciations of East Greenland might have already started in Middle Miocene (some 15 Ma). Ice-rafted sediments were deposited in Middle Miocene from 14 Ma in the Fram Strait (Wolf-Welling et al, 1996) and on the mid-Norwegian margin from 12.6 Ma onwards

(Fronval and Jansen, 1996). A regional cooling event is dated to 9.8 Ma in Iceland (Mudie and Helgason, 1983). The Scandinavian glaciers reached sea level at 5.5 Ma and northern Europe was extensively glaciated in Late Pliocene (2.57 Ma) (Jansen and Sjøholm, 1991).

This study should provide a link between the geodynamic evolution of the northern North Atlantic and the Arctic Ocean (Chapter 5 and 6) and these long-term climate changes. In particular, the onset of the Middle Miocene climate optimum and the changes in ocean circulations are investigated in greater depth (Chapter 7). To get a closer insight into the Arctic oceanography, the following section introduces an overview of the northern North Atlantic and the Arctic Ocean ocean circulations

1.4 Arctic ocean circulations

The palaeobathymetric reconstruction calculated in this thesis (Chapter 6) provides a basis for a palaeoceanographic modelling (Chapter 7), which gives evidence on the variation of ocean circulations and mass, heat and salt transport due to bathymetric changes. The modelling aims to verify the relationship between the opening of the deep-water Fram Strait gateway, the changes of ocean circulations and changes of the regional and global long-term climate. This section discusses the deep-water circulation in order to compare the modelled palaeobathymetric circulations and the present day ocean circulations, and to understand the influence of the ocean circulation variation. Furthermore, it introduces the present and past ocean circulations between the northern North Atlantic and the Arctic Ocean.

1.4.1 Deep-water circulation

The changes in Arctic heat budget are of major interest since one is aware of Arctic Ocean's possible link to global climate (Schauer and Fahrback, 2004). The understanding of climate changes in the Arctic Ocean region requires knowledge of the mean oceanographic circulations. Throughout the world deep-water circulation carries heat, salinity, oxygen, CO₂ and other properties from high latitudes in winter to low latitudes (Stewart, 2007). Dominant oceanic heat source for the Arctic Ocean is the inflow of Atlantic water combined with an export of polar water and ice through the Fram Strait.

Deep-water circulations have very important consequences:

- The contrast between cold deep-water and warm surface-waters determines the stratification of the ocean. Stratification strongly influences ocean dynamics.
- The volume of deep-water is higher than the volume of surface-water. Currents in the deep ocean are relatively weak and can have volume transports comparable to the surface volume transport.
- The fluxes of heat and other parameters carried by the deep circulation influence heat budget and climate of the earth. The fluxes vary from decades, to centuries, to

millennia, and this variability modulates climate over such time intervals. The ocean may be the primary cause of variability in climate over times ranging from years to decades.

Thermohaline circulation of the world's ocean is maintained by the sinking of dense water masses in high latitudes. In most cases these water masses form in marginal seas or on shelves and slide down the continental slopes.

Deep-water circulations are dependent on the bathymetric configuration of the ocean basins. Especially the exchange of deep-water between adjacent ocean basins is restricted by the gateway bathymetry. One particular phenomenon is the "overflow", where dense near-bottom waters cross sills between ocean basins (Price and Baringer, 1994).

1.4.2 Ocean circulations in the northern North Atlantic and the Arctic Ocean

The present day ocean circulation in the Arctic Ocean is dominated by thermohaline forcing because the Arctic Ocean belongs to the mediterranean seas (Dietrich et al., 1990). In contrast to the dynamics of the major ocean basins, where most currents are driven by the wind and modified by thermohaline effects, currents in mediterranean seas are driven by temperature and salinity differences and are modified by wind action. The reason for the dominance of thermohaline forcing is the topography. Mediterranean seas are separated from the major ocean basins by sills, which limit the exchange of deeper waters. Today such a deep-water exchange is observed in the Fram Strait between the northern North Atlantic and the Arctic Ocean.

The timing of the opening of a deep-water connection through the Fram Strait is still speculative, although the deep-water formation in the Fram Strait is a key driver of global thermohaline circulation and hence, for global climate (Jakobsson et al., 2007). Deep-water in the Arctic region circulates on average below 1500 m water depth (Kristoffersen, 1990). Schauer and Fahrback (2004) characterise deep-water as water below 700 m which approximately coincides with the depth of the 0 °C isotherm.

Besides the gateway depth, the gateway width is an essential factor for an exchange of deep Arctic water. The Arctic Ocean has been relatively isolated from the global ocean circulation during most of the geological history (Moran et al., 2006). Lawver et al. (1990) suggest that a shallow water connection between the Arctic Ocean and the North Atlantic formed between 15 Ma and 10 Ma. They assume that the corridor of oceanic crust between Greenland and Svalbard was not wide enough until 7.5 Ma to 5 Ma to start the deep-water circulation. In contrast, Kristoffersen (1990) suggests a shallow water connection already existed in the Late Oligocene from 34 Ma to 23 Ma. The passageway deepened to approximately 2 km until Middle Miocene.

After the opening of the deep-water connection through the Fram Strait, an exchange of warm Atlantic and cold Arctic water (Jakobsson et al., 2007) was possible. The results of ODP site 909 at the northern Hovgård Ridge (Figure 1.1) show restricted ocean circulation between 20 Ma and 17 Ma. Ice-rafted sediments are observed since probably 15 Ma (Winkler

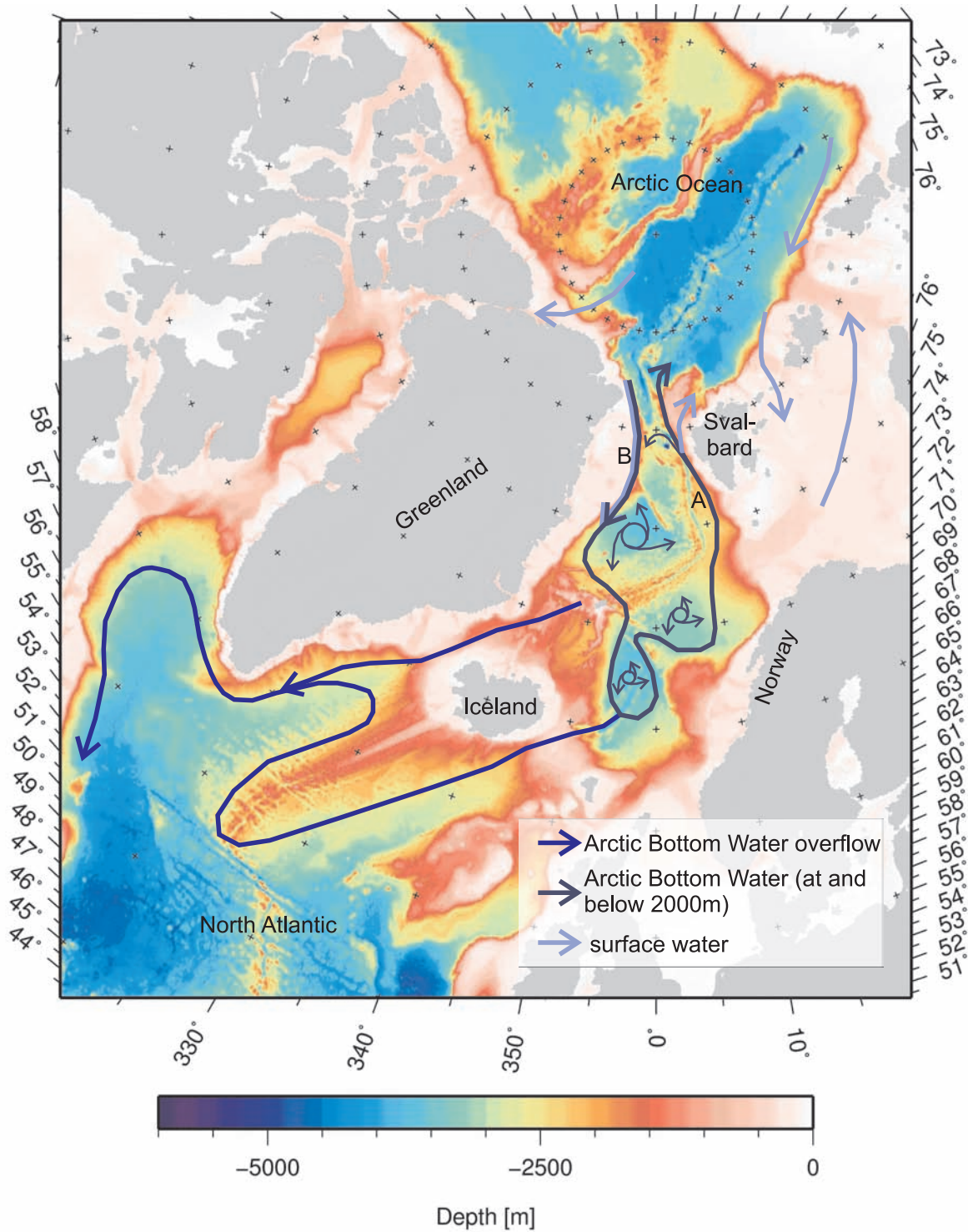


Figure 1.7: Bathymetric map (ETOPO2) with paths of surface and deep-water ocean currents in the northern North Atlantic and the Arctic Ocean (after Aagaard et al. (1985); Rudels et al. (2002)), A: West Spitsbergen Current, B: East Greenland Current.

et al., 2002). Furthermore, studies about a core from the crest of the Lomonosov Ridge (Figure 1.1) in the central Arctic Ocean (IODP Expedition 302 (ACEX) in 2004) result in a change of ventilation history in the Arctic Ocean that was completed at about 17.5 Ma (Jakobsson et al., 2007).

Today, the deep-water of the Arctic Seas circulates internally with moderate rates of deep-water exchange between the Eurasia Basin and the Norwegian-Greenland Sea (Figure 1.1). The Greenland-Iceland-Faeroe-Scotland Ridge always represented a shallow barrier. There, the source of an overflow is not water from the bottom of the Norwegian-Greenland Sea, but from a depth close to 1000 m at present day (Peterson and Rooth, 1976). A 0.5 km–0.9 km deep gateway repeatedly opened and closed in response to the pulsating Iceland Hotspot (Wright and Miller, 1996). Today, a total of 4 Sv crosses the Greenland-Iceland-Faeroe-Scotland Ridge. The timing of an initial overflow of the Greenland-Iceland-Faeroe-Scotland Ridge coincides with the timing of the Fram Strait opening (Eldholm et al., 1994).

Present understanding of the circulation of the Arctic Ocean is largely built on a combination of hydrographic measurements and observations of ice motion. The ice drift appears to be largely decoupled from the circulation below a few tens of meters (Aagaard, 1989).

Today the circulation between the northern North Atlantic and the Arctic Ocean (Figure 1.7) consists of the northward flowing West Spitsbergen Current and the southward flowing Norwegian- and East Greenland currents (Fahrback et al., 2001). These currents have a maximum in spring and a minimum in summer. The average monthly mean adds up to 9.5 ± 1.4 Sv towards the north, and 1.1 ± 1.7 Sv towards the south. The West Spitsbergen Current has a strong barotropic and a weaker baroclinic component, whereas the East Greenland Current has barotropic and baroclinic components of similar magnitude.

Warm and saline Atlantic water flows into the Arctic Ocean. There it is cooled by heat loss to the atmosphere and freshened mainly by river inflow and by mixing with Pacific waters. This mixing forms a relatively fresh shallow outflow of polar waters. The formation of sea ice increases the salinity of water columns. Saline deep-water leaves the Arctic Ocean through the Fram Strait to the south. This overflow affects the water mass modification in the Norwegian-Greenland and the Iceland seas and feeds to some extent the overflow into the North Atlantic.

The complicated topography of the Fram Strait leads to a splitting of the northward flowing West Spitsbergen Current in at least three branches (Quadfasel et al., 1987) (Figure 1.7). One of these branches follows the shelf edge, enters the Arctic Ocean north of Svalbard and crosses the Yermak Plateau. Here, the flow is limited to the Yermak Plateau depth of approximately 600 m (Schauer and Fahrback, 2004). The second branch flows northward along the north western slope of the Yermak Plateau and the third branch recirculates immediately in the Fram Strait between 78°N and 80°N (Perkin and Lewis, 1984; Bourke et al, 1988; Gascard et al., 1995). The size and strength of these three branches largely determine the input of the oceanic heat to the Arctic Ocean (Schauer and Fahrback, 2004). The branch crossing the Yermak Plateau transports the warmest water (Aagaard et al., 1987).

The ocean circulation in the northern North Atlantic and the Arctic Ocean presents the

present day ocean circulation configuration. This configuration is used for a comparison of recent and modelled past circulations in this study. The past tectonic and bathymetric variations influenced palaeoceanographic circulations, especially the deep-water exchange through the Fram Strait. The calculation of a new palaeobathymetric reconstruction and a palaeoceanographic model in this study form the basis to further investigate the onset of the deep-water exchange and its correlation to past climate changes.

Chapter 2

Data

To reconstruct the geodynamic evolution of the northern North Atlantic and the Arctic Ocean, a data set of various geographical, geological and geophysical data is necessary. This chapter introduces the available data for the tectonic (Chapter 5 and 6), the palaeobathymetric (Chapter 6) and the palaeoceanographic (Chapter 7) studies.

2.1 Bathymetry

The present day water depth is used for the preparation of the crustal age model, for the subsidence calculations (Chapter 5) and especially for the palaeobathymetric reconstruction (Chapter 6). The water depth is derived from the ETOPO2v2 grid (NGDC, 2006) (Figure 2.1) in which the **I**nternational **B**athymetric **C**hart of the **A**rctic **O**cean (IBCAO) (Jakobsson et al., 2001) is included.

The bathymetric data (NGDC, 2006) show a distinct difference between the oceanic basins and the shelf regions. Due to high sediment loads along the shelf break, the bathymetry data do not indicate the continent-ocean transition zone very well. The mid ocean ridges as well as various fracture zones can be identified. The Fram Strait area shows a complicated topography. The Mohns Ridge, which runs southwest to the northeast, continues up to the northsouth running Knipovich Ridge (Figure 1.1 and 2.1). The Knipovich Ridge and the Mohns Ridge are connected by the Molloy Transform Fault. Between the Molloy Ridge and the Lena Trough, the Spitsbergen Fracture Zone evolved and balanced seafloor spreading at the two adjacent ridges. North of the Spitsbergen Fracture Zone, the Gakkel Ridge runs northward through the Arctic Ocean. It crosses the Eurasia Basin to the Laptev Sea. The Eurasia Basin and the Canada Basin are separated by the Lomonosov Ridge.

The southwestern Eurasia Basin is restricted by the Morris Yesup Rise and the Yermak Plateau. The present bathymetric structures in the northern North Atlantic and in the Arctic Ocean can be explained by tectonic and volcanic activities, by the evolution of oceanic basins, and by sediment accumulation.

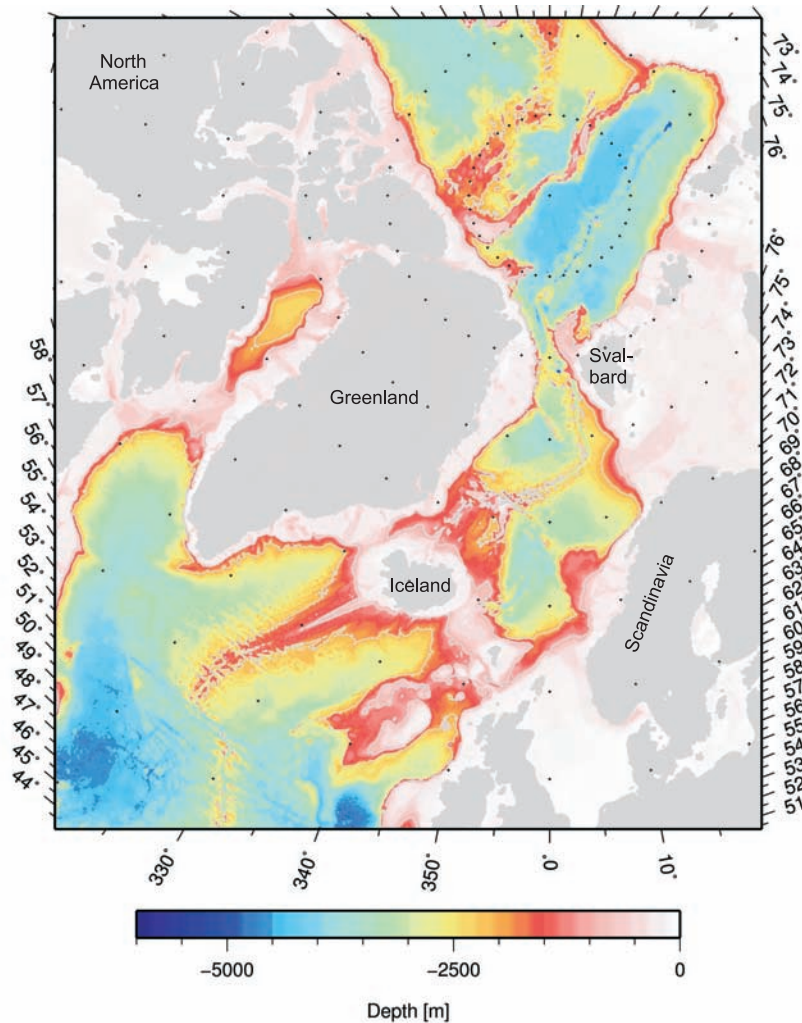


Figure 2.1: Present day water depth from the ETOPO2v2 (NGDC, 2006) grid including the IBCAO grid (Jakobsson et al., 2001) for the northern North Atlantic and the Arctic Ocean.

2.2 Magnetics

A detailed age model of the oceanic crust in the northern North Atlantic and in the Arctic Ocean (Chapter 5 and 6) is derived from the interpretation of magnetic data. The northern North Atlantic and the Arctic Ocean magnetic data were compiled by Verhoef et al. (1996). His “**G**ridded **A**eromagnetic and **M**arine **M**agnetics of the **N**orth **A**tlantic and **A**rctic” with a resolution of 5 km (Gammaa5) data are presented in figure 2.2. Especially in the Fram Strait region the anomaly pattern is mostly diffuse. A new aeromagnetic data grid was generated from data gathered by the Alfred Wegener Institute between 76.5°N and 85°N (Leinweber, 2006). A comparison of the Gammaa5-grid and the new aeromagnetic grid is shown in figure 2.3.

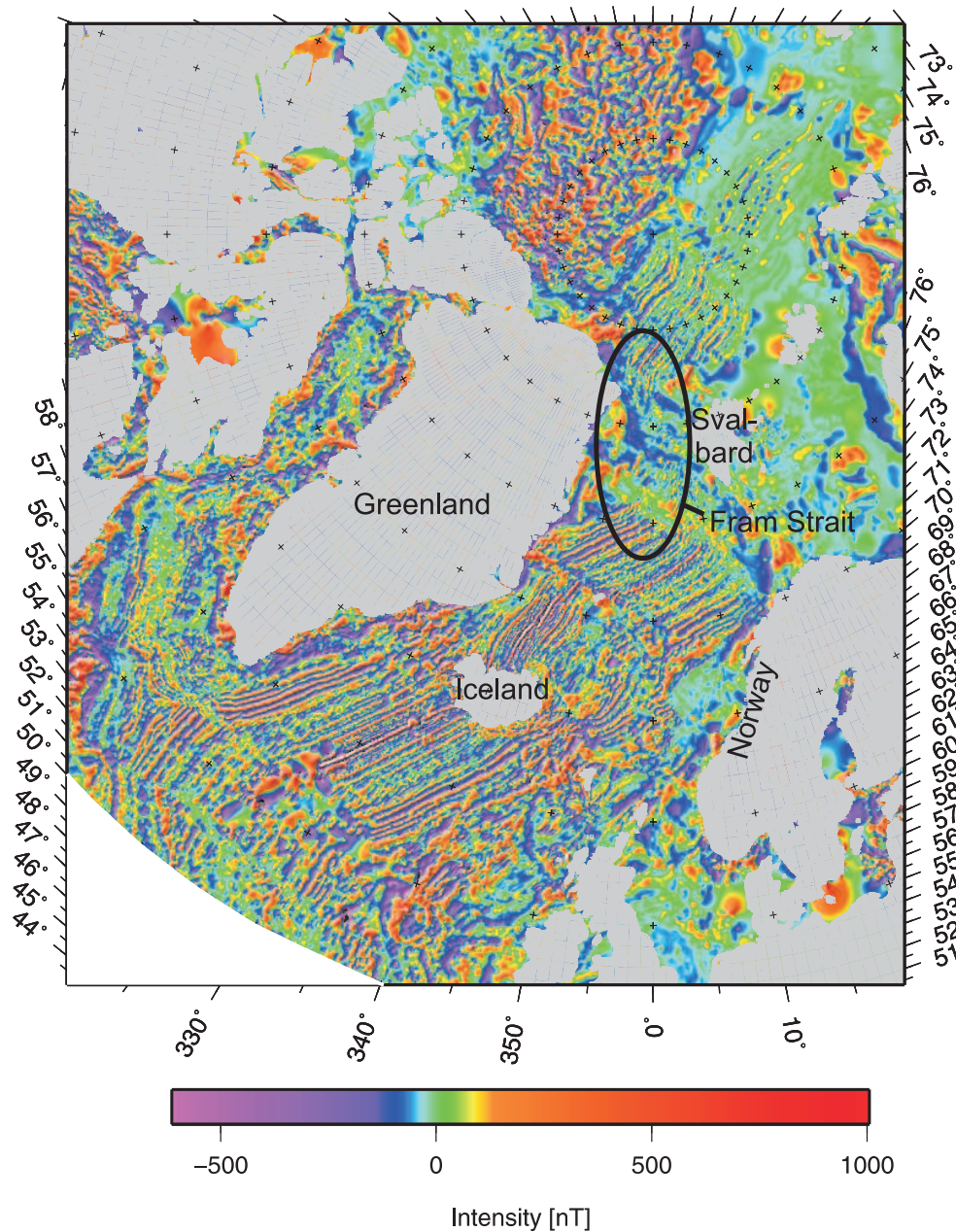


Figure 2.2: The Gammaa5-grid from Verhoef et al. (1996). Note the low resolution of magnetic data in the Fram Strait (black oval).

The new aeromagnetic grid provides a more detailed anomaly pattern for the Boreas Basin, the Molloy Basin and the Lena Trough. For this study, the new aeromagnetic grid complements the Gammaa5-grid. The magnetic anomalies often characterise the magnetic properties of the underlying rocks.

The new magnetic data in the Fram Strait region presents the first detailed re-identification

of magnetic spreading anomalies. Although various age models exist between the Charlie Gibbs Fracture Zone and the Arctic Ocean, the Gammaa5-grid does not allow detailed identifications of the magnetic spreading anomalies. The most detailed age model until now exist for the Eurasia Basin (Brozena et al., 2003). The rift model from Wold (1995) is used as an age model between the Charlie Gibbs Fracture Zone and the Jan Mayen Fracture Zone.

2.3 Gravity

Gravity data provide information on the evolution of the northern North Atlantic and the Arctic Ocean and more specially distinguish oceanic and continental crust. The gravity field of the Arctic Ocean and the northern North Atlantic was compiled from ship, airborne and submarine data in the Arctic Gravity Project (AGP, 2006). The gravity data from the Arctic Gravity Project (AGP, 2006) show the free-air gravity anomalies of the Arctic

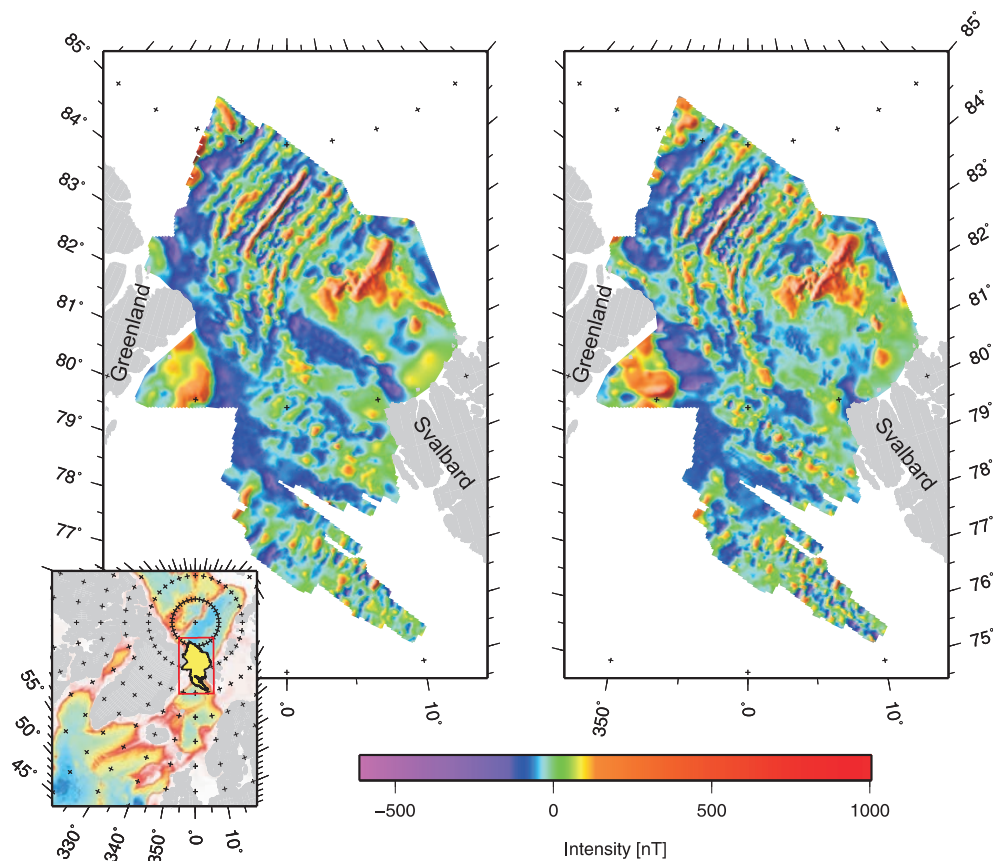


Figure 2.3: Comparison of the Gammaa5-grid (Verhoef et al., 1996) and the new aeromagnetic grid (Leinweber, 2006). Left: the clipping from the Gammaa5-grid (Verhoef et al., 1996) in the context of the new aeromagnetic grid, right: new aeromagnetic grid (Leinweber, 2006).

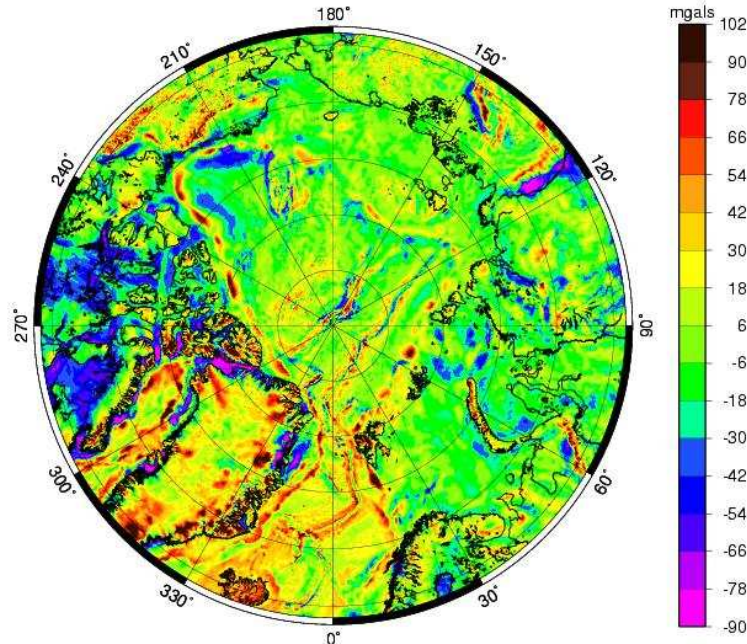


Figure 2.4: Gravity data of the Arctic Gravity Project (AGP, 2006) north of 64°N.

Ocean and adjacent areas in a resolution of 5' x 5' with an applied atmospheric correction (Figure 2.4).

Along the continental margins of East Greenland and southwest Svalbard Vogt et al. (1998) identified the “Arctic Margin Gravity High”. These gravity anomalies result from glacial trough mouth fans. Therefore, gravity data give evidence for the course of the shelf break and helps to define the continent-ocean transition zone where no seismic refraction data are available. Gravity data are also used for the analysis of crustal models and to model the tectonic opening history (Boebel, 2000; Engen et al., 2008). Engen et al. (2008) used a regional Bouguer map for the interpretation of crustal structure. They observed high Bouguer gradients across sheared margin segments and lower gradients across rifted segments.

2.4 Sea level changes

The sea-level changes play an important role in the palaeobathymetric reconstruction (Chapter 6). The changes are analysed for example by Haq et al. (1987) (Figure 2.5). The sea-level cycle charts derived from seismo-stratigraphic data is complemented by depositional models. Therefore, sea-level fluctuation during the past 250 Myr is recorded in

greater detail. The time of the sea-level cycle chart is modified using the Geological Time Scale 2004 of Gradstein et al. (2004).

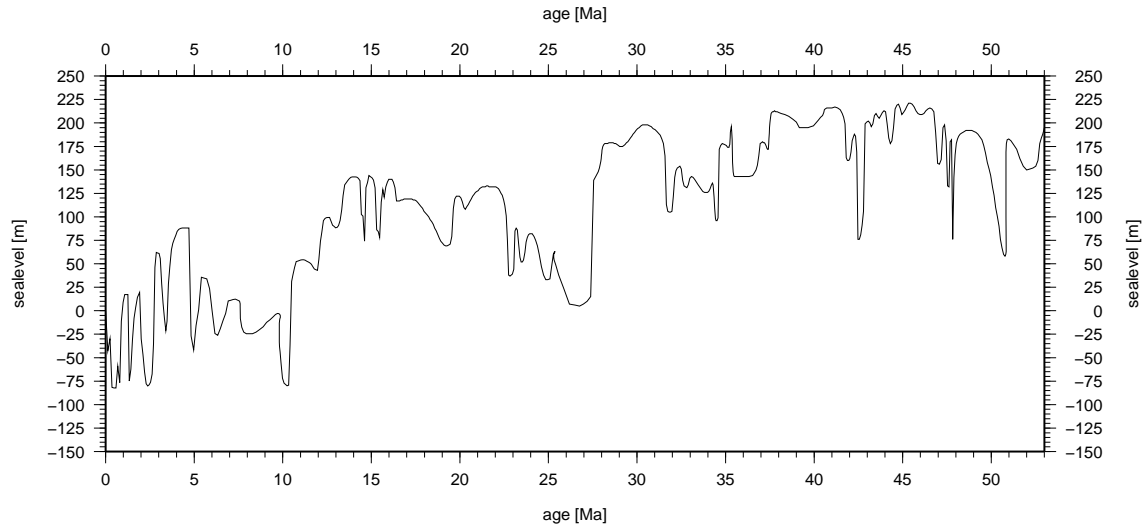


Figure 2.5: Sea level changes after Haq et al. (1987).

2.5 Seismic reflection and refraction profiles

Seismic reflection and refraction seismic data provide essential information about the structure and depth of the crust and therefore for subsidence calculation and roughness analysis (Chapter 5) and for a palaeobathymetric reconstruction (Chapter 6). The data provide information about the seafloor depth, the basement depth and topography, and the sediment thickness. The data sets can also confirm the location of the ridges, fracture zones and continent-ocean transition zones.

Between the Charlie Gibbs and the Jan Mayen Fracture zones, various single channel seismic reflection profiles exist (Wold, 1995). North of the Jan Mayen Fracture Zone, especially along the Norwegian, Barents Sea and Svalbard margins, seismic reflection and refraction profiles were collected since many years (Table 6.1). The density of seismic lines along the East Greenland margins was sparse. New seismic reflection and refraction profiles were gathered by the Alfred Wegener Institute between 2001 and 2004 (Thiede, 2002; Jokat, 2003, 2004; Stein, 2005). For the first time these data offer detailed information of the Greenland, Boreas and Molloy basins, the Lena Trough, the Yermak Plateau and the Nansen and Amundsen basins, as well as of their adjacent shelf areas. The new seismic lines supplement the available seismic lines along the Norwegian margins and enable the first palaeobathymetric study of the northern North Atlantic and the Arctic Ocean. A lack of data still exists particularly in the Eurasia Basin, in the northern Lena Trough and in the younger parts of the Norwegian-Greenland Sea close to the Mohns Ridge.

location and size of the grid cell, the present seafloor depth, the present sediment thickness, the present basement depth, the change of sea level for the time of reconstruction, the present thermal age of crust, ages and lithology of sedimentary layers, and whether the crust is of oceanic or continental origin. This palaeobathymetric reconstruction supplements the calculated palaeobathymetric reconstruction of this study in the south. For the palaeoceanographic modelling (Chapter 7), global palaeobathymetric data are needed. For oceanic basins this data are provided by Müller et al. (2008) (Figure 2.7).

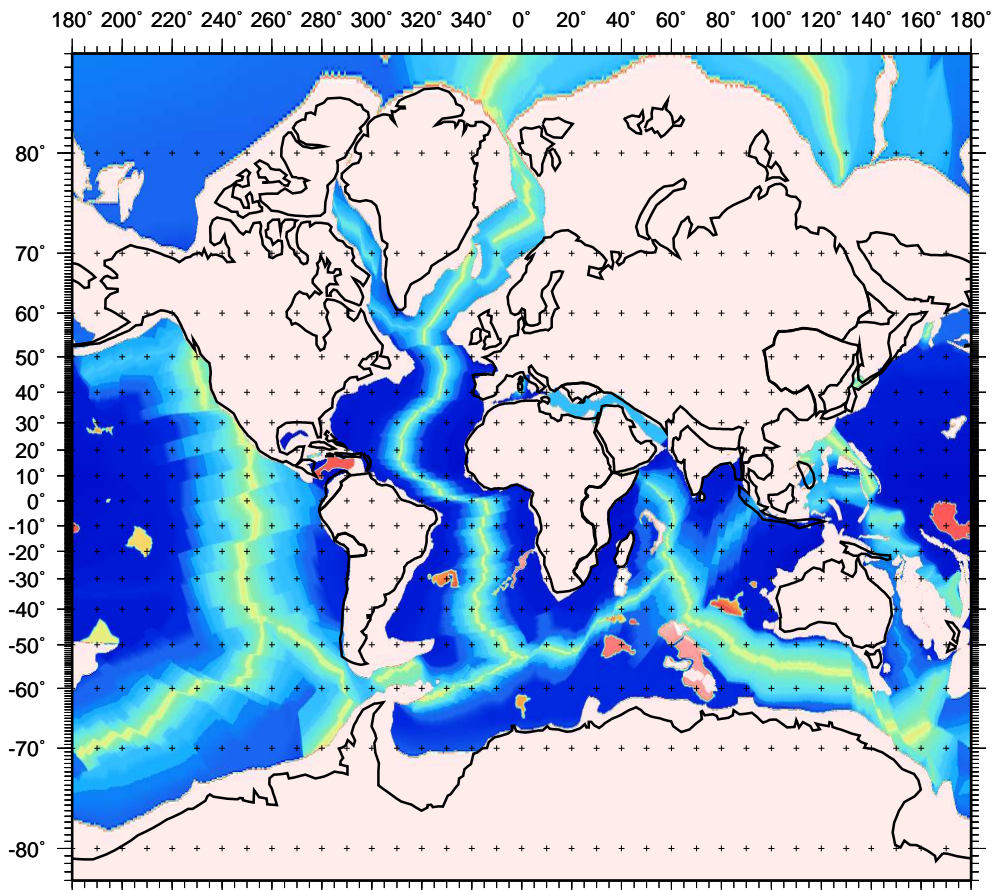


Figure 2.7: Global palaeobathymetric data of ocean basins for 20 Ma from Müller et al. (2008), used for the palaeoceanographic modelling.

Chapter 3

Methods

The aim of this study is to use a geodynamic model for a palaeobathymetric reconstruction of the northern North Atlantic and the Arctic Ocean. This reconstruction provides a basis for a palaeoceanographic model experiment. The results of this study (Chapter 5, 6 and 7) are achieved by using several geophysical and oceanographic methods. These methods are presented in the following chapter. Figure 3.1 gives an overview on the relation of the introduced data, the methods used and their results.

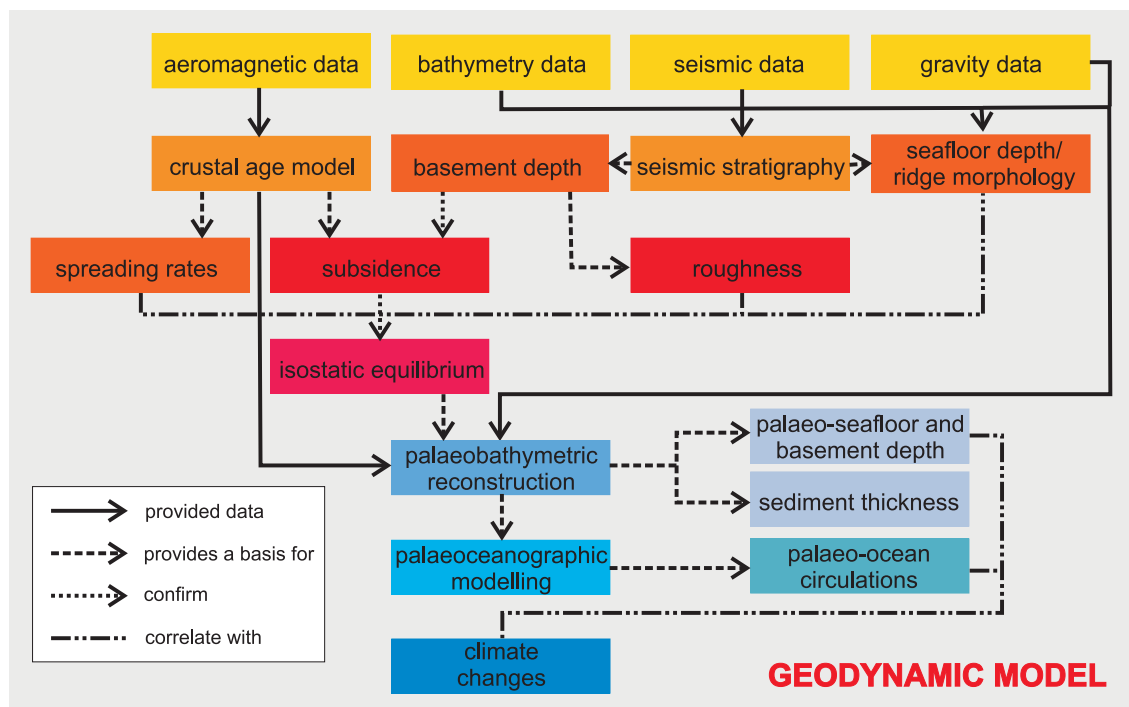


Figure 3.1: Overview on the available data, the applied methods and the continued processing of the results. Yellow: available data (Chapter 2), orange-red: methods and results used in chapter 5, light blue: method and results of chapter 6, green: method and result of chapter 7.

3.1 Analysis of magnetic data

The geomagnetic data of the GAMMAA5-grid (Verhoef et al., 1996) (Figure 2.2, 2.3) and the new aeromagnetic data grid (Leinweber, 2006) are analysed to determine the age of oceanic crust and the resulting spreading velocities. The identification of magnetic anomalies provides detailed rotation angles for a tectonic reconstruction.

Re-identification of magnetic spreading anomalies

To determine the age of the oceanic crust for the northern North Atlantic and the Eurasia Basin in more detail, magnetic anomalies are re-identified. The identifications of Brozena et al. (2003) were used as reference in the Eurasia Basin (Figure 1.1). To improve the resolution of the identification the zero crossing of the magnetic anomalies were picked parallel to the oceanic ridge axis (Figure ??). Topographic effects were excluded to avoid an impact on the analysis. Therefore, the magnetic identifications were compared to the bathymetric data.

Age of oceanic crust

The age of oceanic crust is determined with the help of re-identified magnetic spreading anomalies. To estimate the age of the spreading anomalies, magnetic modelling by the 2D magnetic modelling program MAGBATH (Hey et al., 1986) was used (Figure 5.2, 5.3, 5.8 and 5.9). The magnetic modelling consists of fitting measured and calculated data by varying estimated spreading rates to obtain the best fit. The measured data were chosen along profiles in spreading direction which show pronounced spreading anomalies. The age of the magnetic anomalies is determined (Table 6.2) after the Geological Time Scale 2004 of Gradstein et al. (2004).

Spreading rates

The spreading rates result from the magnetic modelling along profiles across the investigated basins (Figure 5.2, 5.3, 5.8 and 5.9). The resulting age of the re-identified spreading anomalies allows a calculation of spreading rates for the entire ocean basins (Table 5.1). The spreading rates give evidence for the ridge and basin evolution as an initial condition for a palaeobathymetric reconstruction. Spreading rates during the evolution of the ocean basins allow further interpretation of the ridge morphology and basement topography.

3.1.1 Tectonic reconstruction parameters

For the investigated area, the re-identified magnetic anomalies (Figure 5.7 and ??) are the same age on both directions of the ridge, even if spreading is not symmetric. The

magnetic modelling estimates the age of the oceanic crust and therefore a rotation of the detailed re-identified anomalies will result in new detailed rotation angles (Table 6.2). The poles of rotation are used from Gaina et al (2002), without any modification. Both picked anomalies, which were produced at the same time along the mid ocean ridge, should be congruent after a rotation.

3.2 Subsidence analysis of oceanic crust

Oceanic crust is accreted along active oceanic ridge systems. Thermal cooling and isostatic balance causes subsidence of oceanic crust. The depth and heat flow of oceanic crust varies with increasing age. Subsidence analysis allows to calculate the theoretical depth of oceanic crust for different time periods.

3.2.1 Thermal subsidence

Parsons and Sclater (1977) proposed a simple cooling model which describes the introduced depth age relationship of oceanic crust:

$$d_w = d_r + \frac{2\rho_a\alpha T_a}{\rho_a - \rho_w} \sqrt{\frac{\chi t}{\pi}} \quad (3.1)$$

with the following parameters

d_w : thickness of water column

d_r : standard depth at ridge axis (2500 m)

ρ_a : density of asthenosphere ($3.3 \cdot 10^3 \frac{kg}{m^3}$)

α : thermal expansion coefficient ($3 \cdot 10^{-5} \frac{1}{^\circ C}$)

T_a : temperature along spreading axis (1300 °C)

ρ_w : water density ($1.03 \cdot 10^3 \frac{kg}{m^3}$)

χ : thermal diffusivity ($10^{-6} \frac{m^2}{s}$)

These parameters are mean values and it is assumed that they are constant through time. Hence, subsidence is just depended on the age of oceanic crust ($t < 70$ Myr):

$$d_w = 2.5 + 0.35 \cdot \sqrt{(t)} \quad (3.2)$$

The age-depth relationship allows the theoretical calculation of the basement depth for different times of the ocean basin evolution (Figure 3.2). The model is valid for isostatic compensated oceanic crust without a sediment load. In case of absent sediments, the theoretical calculated basement and seafloor depth are equal.

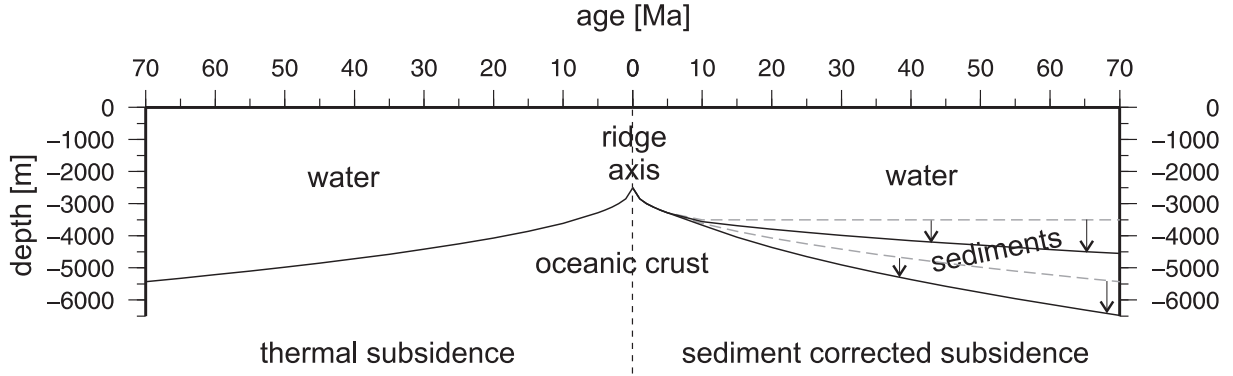


Figure 3.2: Theoretical thermal and sediment corrected subsidence. The dashed gray lines show the uncorrected seafloor depth and the uncorrected basement depth.

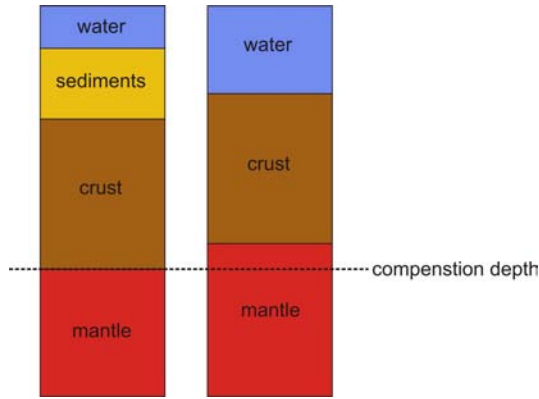


Figure 3.3: Initial condition of the mantle and crust covered with sediments and water (left). Conditions of mantle with a water column that replaces the sediment cover (right).

3.2.2 Sediment corrected subsidence

Sediment accumulation intensifies the subsidence of oceanic crust. Allen and Allen (1990) extend the thermal subsidence for a correction S_s of the sediment load d_s . The sediment cover is replaced by a corresponding water column $d_{w_{aa}}$ (Figure 3.3) and is subtracted from the sediment thickness resulting in a crustal depth without sediment cover:

$$S_s = d_s - d_{w_{aa}} \quad (3.3)$$

$$d_{w_{aa}} = d_s \frac{\rho_a - \rho_s}{\rho_a - \rho_w} \quad (3.4)$$

with ρ_a : density of asthenosphere, ρ_s : density of sediments and ρ_w : density of water.

The sediment density is described by:

$$\rho_s = \rho_g - \frac{\rho_w - \rho_g}{z_2 - z_1} \frac{\phi_0}{c} (e^{-cz_2} - e^{-cz_1}) \quad (3.5)$$

with ρ_g : grain size, ϕ_0 : porosity, c : compaction coefficient, z_1 : basement depth, z_2 : seafloor depth.

To compare the thermal subsidence to the sediment corrected subsidence, a sediment correction was calculated for a normal thermal basement depth and a 3500 m deep seafloor. Figure 3.2 shows the difference between the thermal subsidence and the sediment corrected subsidence. On the right side the thermal subsidence with sediment load (grey dashed line) is compared to the sediment corrected subsidence.

For this study subsidence were calculated for the profiles AWI-20020700 in the Boreas Basin, AWI-20020500 in the Molloy Basin, AWI-20010100, AWI-20010460 in the Nansen Basin and AWI-20010300 in the Amundsen Basin. Parameters concerning the sediment characteristics were derived from ODP boreholes sites 909 and 913 (Myhre et al., 1995). The sediment correction S_s is applied to the thermal subsidence d_w and yields the theoretical basement depth d_t of oceanic crust:

$$d_t = d_w + S_s \quad (3.6)$$

The subsidence calculation tests if the observed basin can be described by the presented theory. If the calculated subsidence fits to the general trend of the basement depth, it would be possible to re-calculate the palaeo-seafloor and -basement depth with subsidence calculations.

3.3 RMS roughness calculations

Crustal root mean square roughness describes the basement topography of oceanic crust. The calculation of root mean square roughness provides a possibility to classify oceanic spreading rates and centres. Roughness implies an indirect record of axial morphology and can provide observational constraints on the nature of changes in axial morphology, crustal thickness and tectonics (Ma and Cochran, 1997).

Data at ultra-slow spreading ridges is sparse, especially in the northern North Atlantic and in the Arctic Ocean. Hence, this study can amend the global roughness data set for the ultra-slow end, and provides a basis to calculate an advanced global relationship of crustal roughness, spreading rates and ridge morphology.

To calculate RMS roughness, a data set of basement topography is needed (Figure 3.4). The topographic roughness (R) of the basement is defined as the root mean square (RMS) deviation of the residual basement relief (h), along a given length of the profile, measured at equidistant positions (Malinverno, 1991). The following equation is used for the calculation of R :

$$R_i = \sqrt{\frac{\sum_{i=1}^n h_i^2}{n}}, \text{ for } i = 1, 2, \dots, n \quad (3.7)$$

with h : difference between a reference surface and the basement (Figure 3.4). The reference surface can be the calculated subsidence (Hayes and Kane, 1991) as well as an empirical trend of the basement (Malinverno and Cowie, 1993). The chosen length of a profile section for calculated RMS roughness should exceed tens of kilometres, preferably about 100 km (Malinverno, 1991). Malinverno (1991) also proposed a power law to describe the relationship of roughness R and full spreading rate v :

$$R_c = 1296 \cdot v^{-0.539} \quad (3.8)$$

This power law does not consider the axial morphology. Goff et al. (1997) studied the statistical properties of abyssal hill morphology and showed that for identical spreading rates both the axial morphology and the RMS roughness change. Considering this conclusion, a discussion of separate power law curves for axial valley-adjacent and axial high-adjacent values is necessary.

3.4 Palaeobathymetric reconstruction

The palaeobathymetric modelling is based on the method of backstripping introduced by Steckler and Watts (1978). The palaeobathymetric reconstruction combines palaeobathy-

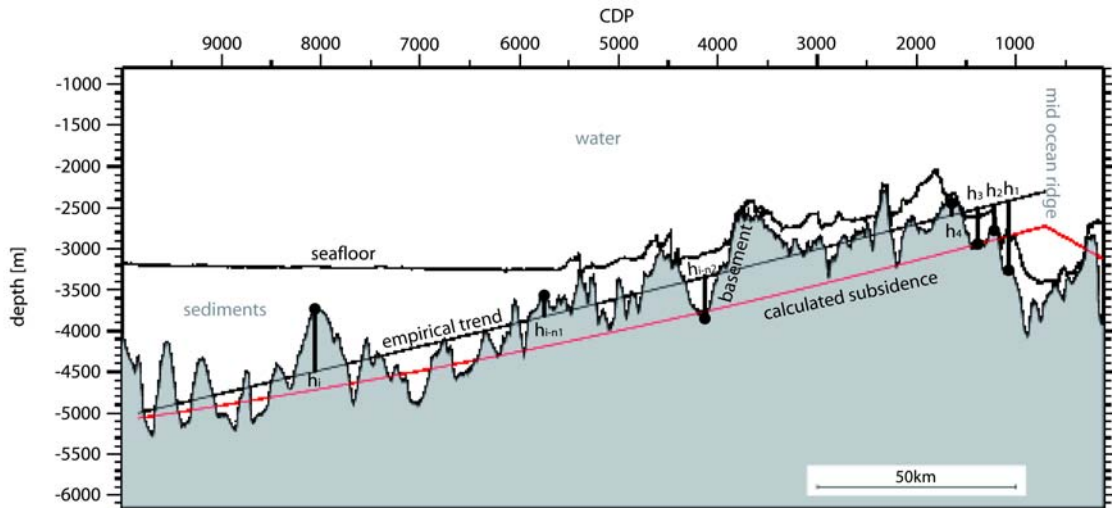


Figure 3.4: Example of profile for roughness calculation. Red line: calculated subsidence, black line: empirical trend, which is used as reference surface in this study. The difference between the reference surface and the basement is marked by h_1-h_4

metric modelling and plate tectonic modelling. The intention of such a reconstruction is to calculate the seafloor and basement depth, the sediment load, and to rotate the plates for a chosen age of reconstruction.

The palaeobathymetric reconstructions are executed by the program packet “BalPal v.0.9” (Wold, 1995). “BalPal v.0.9” is written in the C-programming language and works with gridded data with a resolution of $1^\circ \times 1^\circ$ in latitude and longitude. For this study the software was modified to use a variable grid size for the palaeobathymetric modelling. The resolution is adapted to the density of seismic lines and to the dimensions of the investigated area.

The presented data yield information for the palaeobathymetric modelling and the plate tectonic modelling. For this study, 1515 new grid cells with an cell size of 0.5° in latitude and longitude are compiled, north of the Jan Mayen Fracture Zone. Collectively, 1820 km of seismic lines in the Arctic Ocean, 968 km seismic reflection profiles on the Yermak Plateau, 5265 km of seismic reflection and refraction seismic data along the Svalbard, Barents Sea and Norwegian margins, and 10218 km of new seismic reflection data and related seismostratigraphy, are used for this study (Figure 2.6). The data along the East Greenland Margin, on the Yermak Plateau and in the Arctic Ocean are available in a digital format, whereas the data along the Svalbard, Barents Sea and Norwegian margins are digitised from various publications (Table 6.1). The seafloor and basement depth and the depth of the sediment layers are projected to the midpoints of the grid cells. An example of a grid cell is shown in appendix B, table B.2. Each of the 1515 grid cells of this study contain information about:

- the location and size of the grid cell
- present day depth of the seafloor
- present day sediment thickness
- present day basement depth
- change of sea level for the time of reconstruction
- thermal age of the crust
- age of sedimentary layer
- crustal density and compensation depth
- porosity-density relationship for sediments
- continent-ocean-boundary

The poles of rotation and rotation angles provide additional parameters for the plate tectonic reconstruction of the modelled palaeobathymetric data (Appendix B, Table B.1).

The palaeobathymetric calculations in “BalPal v.0.9” (Wold, 1995) are based on the present day modelled crustal thickness. This crustal thickness for the seismic profiles in the

region north of the Jan Mayen Fracture Zone is presented in appendix B, figure A.45. The calculation for the palaeobathymetric modelling is executed for columns with the height equal to the compensation depth and a basis of 1 m^2 in each grid cell. The steps of the calculation are displayed in figure 3.5 and listed below:

- Sediments younger than the age of reconstruction are removed from the column within the grid cell.
- The remaining sediment column is restored to its prior unloaded condition due to compaction of accumulated sediments. This process is called decompaction.
- The effect of thermal subsidence is removed.
- The change of the sea level is corrected to its position during the age of reconstruction relative to the present sea level.
- The grid cell column is brought to isostatic equilibrium.

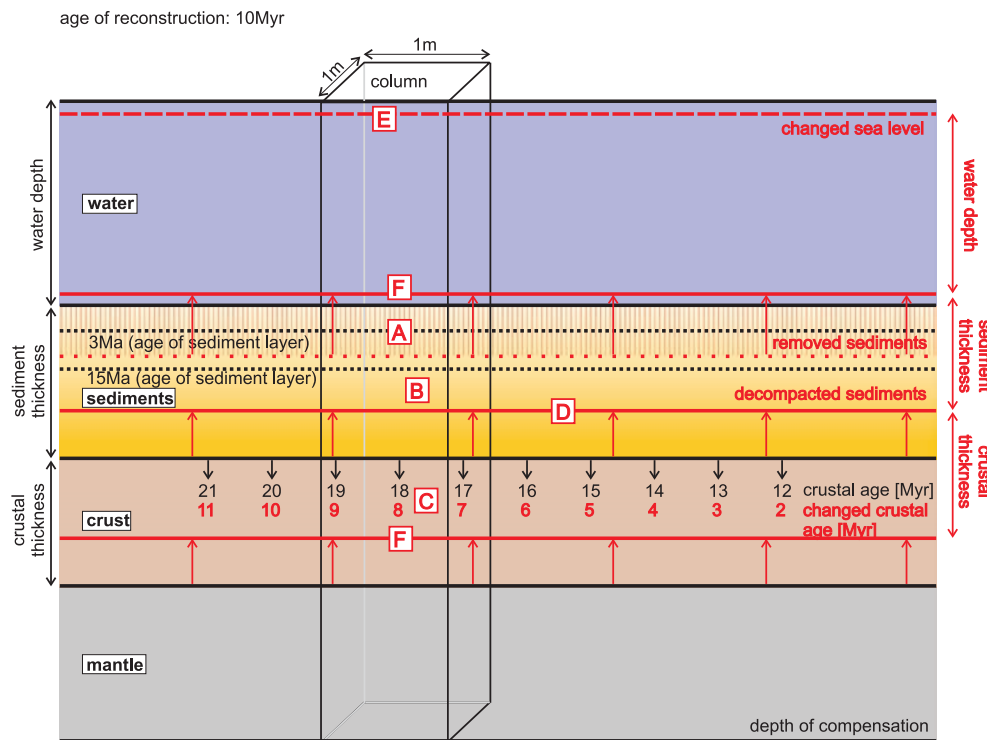


Figure 3.5: Schematic diagram of the methods applied for a palaeobathymetric reconstruction. Black labels: before the reconstruction, red labels: changes after the reconstruction, A: sediments younger than the age of reconstruction are removed from the column within the grid cell, B: decompaction of remaining sediments, C: change to age of reconstruction, D: removal of effect of thermal subsidence, E: change of sea level, F: isostatic equilibrium.

First, the water depth (z) is calculated for oceanic lithosphere without sediment accumulation. The depth compensation constant is subtracted from the crust thickness and the water depth, to yield the mantle thickness above the compensation depth. The column is divided into a water layer, a crustal layer and a mantle layer and the total mass for the column above the compensation depth is calculated. The layers of the water, sediments and crust are given by the grid cell data base and the program parameters (Appendix B, Table B.3). By calculating the mantle thickness and mass, the layers are supplemented by a mantle layer.

The present sediment layers are included into the column. The total thickness, mass and density is calculated for the whole stratigraphic column. The solidity is estimated for various depths. This previous analyses lead to the calculation of the crustal thickness.

To consider the different water masses due to different sea levels through time, the data of sea level change (Haq et al., 1987) is included. The palaeobathymetric modelling program changes the age of the crust to the chosen age of reconstruction. The program removes the younger stratigraphic layers. The removal of younger sediments results in a modification of solidity S , which is the converse of porosity. The reconstructed solidity S_{new} is lower than the present solidity $S_{present}$. The decompacted thickness of the sediment layers is then calculated by:

$$T_{decompacted_sediments} = \frac{S_{present}}{S_{new}} \cdot T_{present_thickness} \quad (3.9)$$

With decreasing age the density of the mantle is also decreasing. The new mantle density results in an uplift of the column. The calculation of the new thickness of the column also considers the sea level changes. Finally, the column is isostatically balanced. The isostatic equilibrium is calculated after Airy hypothesis of isostatic compensation (Keary and Vine, 1996).

The results of the palaeobathymetric reconstruction are presented in chapter 6 and additionally in the appendix A (Figures A.1–A.40).

3.5 Oceanographic model experiment

This study provides a detailed palaeobathymetric model of the northern North Atlantic and the Arctic Ocean, which is included into a global palaeobathymetric data set (Müller et al., 2008). The palaeobathymetric data set is an essential basis for the interpretation of oceanographic model scenarios, which deals with large geological time scales (>1 Myr). The new detailed reconstruction in the Fram Strait area delivers boundary conditions on the onset of the deep-water exchange between the northern North Atlantic and the Arctic Ocean. The question, how the ocean circulation was effected by palaeobathymetric changes, and if the circulation variability correlates to climate changes can be analysed by a oceanographic model experiment. Due to the time limitation of this study, it was not possible to perform a full palaeoceanographic modelling, since the ocean model software packages are quite large and complex. Hence, the technical part of the oceanographic

model runs was accomplished by the Climate Sciences/Paleo-climate Dynamics Division at the Alfred Wegener Institute. To get an insight on the limitation of the calculation of an oceanographic model experiment, the used model is described in the following section 3.5.2. The interpretation of the model runs is done within this thesis (Chapter 7).

3.5.1 Preparation of palaeobathymetric data

Palaeobathymetric data are a basis for the palaeoceanographic modelling. To model ocean circulations, a world wide bathymetric data set is required. To obtain preferably precise results for the northern North Atlantic and the Arctic Ocean, the calculated palaeobathymetric reconstruction of this study is implemented into the world wide palaeobathymetric data of Müller et al. (2008). The merged palaeobathymetric data of this study and Müller et al. (2008) contain mainly data for the oceanic crust. The shelf areas are defined as 200 m deep, and the continents are set to a constant height of 1000 m above sea-level (Appendix A, Figures A.41–A.44).

3.5.2 Ocean circulation model experiment

A modelling of ocean circulations illustrates the correlation between ocean currents and bathymetric changes. **Ocean General Circulation Models** (OGCMs) are used as numerical laboratory for oceanic investigation (Marsland et al., 2003). For this study the oceanographic modelling the **Max Planck Institute Ocean Model** (MPIOM) version 1.3 was used (Marsland et al., 2003) and was completed by the Climate Sciences/Paleo-climate Dynamics Division at the Alfred Wegener Institute. The MPIOM 1.3 is the ocean-sea ice component of the Max Planck Institute climate model and is a primitive equation model with hydrostatic and Boussinesq assumptions (Marsland et al., 2003). It includes an embedded dynamic/thermodynamic sea ice model, with a viscous-plastic rheology, following Hibler (1979), and a bottom boundary layer scheme for the flow across steep topography. In this study, the model grid of MPIOM 1.3 is used as uncoupled model with the present day climatological forcing data set, which is taken from the German OMIP climatology (Röske, 2006). It is important to consider that even for palaeobathymetric configurations, the present climate forcing is used because atmospheric forcing for the presented time slices does not exist. Hence, the palaeoceanographic model experiment is regarded as being a sensitivity study to the influence of the changes in palaeobathymetry.

The palaeoceanographic model experiment is run in the following steps:

- The world wide palaeobathymetric results are converted to a staggered Arakawa C-grid (Arakawa and Lamb, 1977) in horizontal discretisation. The vertical discretisation is on a so-called “z-coordinate” system and includes partial vertical grid cells.
- The surface layer thickness is adjusted to account for the sea surface elevation and sea ice/snow draft where appropriated.

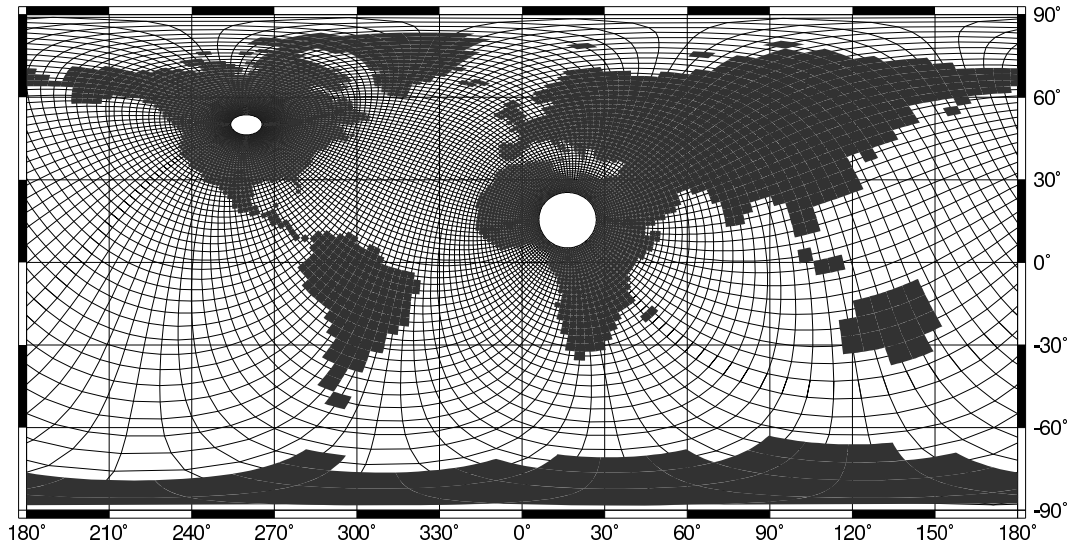


Figure 3.6: Land-sea masks for a modelling with the MPIOM 1.3 in this study. To obtain a high resolution in the northern North Atlantic and the Arctic Ocean, the positions of the poles are chosen to lay in North America and North Africa.

- The MPI-OM model uses a bipolar orthogonal spherical coordinate system (Marsland et al., 2003). If the poles are antipodes (diametrically opposed), the coordinate system is reduced to a rotated spherical grid. In this study the position of the poles is not diametrically opposed. Their positions are chosen according to the zonal and meridional resolution and are used to define the spatial mesh. The arrangement of the poles affects the resolution in the region of interest (Figure 3.6).
- The model uses the surface salinity and temperature from Steele et al. (2001) as starting value for the initialisation of MPIOM.
- The monthly mean river discharge and surface fields of heat, freshwater and momentum fluxes at the air/sea interface are also taken into account.
- In addition, MPIOM 1.3 includes an improved version of the **bottom boundary layer** (BBL).

In this study the formal horizontal resolution of the model is 3° (longitude) and 1.8° (latitude) and the vertical resolution is 20 levels in water depth of 10 m, 30 m, 50 m, 75 m, 110 m, 155 m, 215 m, 295 m, 400 m, 535 m, 700 m, 895 m, 1125 m, 1400 m, 1750 m, 2200 m, 2750 m, 3400 m, 4200 m and 5350 m, respectively. The model run is integrated for 1000 years. The calculated models are analysed for the zonal and meridional velocities, the salinity and temperature, and salinity-depth and temperature-depth distributions in the northern North Atlantic, as well as in the Arctic Ocean. The Atlantic meridional overturning circulation (MOC) is calculated. The results of the modelled ocean circulation scenarios are presented and discussed in chapter 7.

Chapter 4

Scientific Manuscripts

This chapter gives an overview about the scientific manuscripts, which were prepared within this PhD thesis “A geodynamic model of the northern North Atlantic” and are presented in the chapters 5, 6 and 7.

Subsidence and crustal roughness of ultra-slow spreading ridges in the northern North Atlantic and the Arctic Ocean

Birte-Marie Ehlers and Wilfried Jokat

Alfred Wegener Institute for Polar and Marine Research, Am Alten Hafen 26,
27568 Bremerhaven, Germany

Geophysical Journal International, 177, May 2009, p 451–462

Accepted 2008 November 26; Received 2008 November 3; in original form 2007 June 14

This article presents results from a detailed re-identification of new aeromagnetic data in the Fram Strait area. An age model of the oceanic crust is developed for the northern North Atlantic and parts of the Arctic Ocean by magnetic modellings and indicates the ultra-slow spreading rate history of the entire investigation area. The age model and new seismic reflection data are a basis for a subsidence analysis in the Boreas, Molloy and Eurasia basins. The subsidence analysis gives evidence on the evolution of the oceanic basins and tests, if the development can be reconstructed by a theoretical subsidence calculation.

Furthermore, the new aeromagnetic and seismic reflection data provide the depth and topography of the acoustic basement in the ocean basins and the axial morphology of the mid ocean ridges. Previous studies presume a relationship of the axial morphology, the spreading rate and the crustal roughness. For the first time, this study can present results of a roughness analysis of ultra-slow spreading basins, which amend the global roughness data set and allow a calculation of new curve fits to specify the assumed relationship.

Palaeobathymetric study of the North Atlantic and the Eurasia Basin

Birte-Marie Ehlers and Wilfried Jokat

Alfred Wegener Institute for Polar and Marine Research, Am Alten Hafen 26,
27568 Bremerhaven, Germany

Geophysical Journal International

Received 2009 May 22; in original form 2008 October 15

The second manuscript presents a northward continuation of a palaeobathymetric reconstruction of Wold (1995) between the Charlie Gibbs and the Jan Mayen fracture zones. A compilation of new and available geophysical data and the modification of the software package “BalPal v. 0.9” Wold (1995) allow a new and detailed palaeobathymetric reconstruction between the Jan Mayen Fracture Zone and the Lomonosov Ridge.

This paper describes the enlargement of the detailed Fram Strait age model (Chapter 5) to the Norwegian-Greenland Sea and to the Eurasia Basin, which results in detailed angles of rotation for the tectonic reconstruction and hence, completes the available rotation parameters. The geophysical data sources, the compilation of 1515 new grid cells as well as the method of the calculation of a palaeobathymetric reconstruction are described. Hence, chapter 5 provides the validity of subsidence calculations in the investigation area.

The palaeobathymetric reconstruction results in past seafloor and basement depths and in sediment thicknesses, which are discussed due to the onset of the Fram Strait opening. Especially, the onset of a deep-water connection between the northern North Atlantic and the Arctic Ocean is investigated to correlate the timing of the Fram Strait opening to long-term climate changes.

A palaeoceanographic modelling study of the Cenozoic northern North Atlantic and the Arctic Ocean

Birte-Marie Ehlers¹, Martin Butzin^{1,2}, Klaus Grosfeld¹ and Wilfried Jokat¹

¹Alfred Wegener Institute for Polar and Marine Research, Am Alten Hafen 26,
27568 Bremerhaven, Germany

²University of Bremen, MARUM-Center for Marine Environmental Sciences,
P.O. Box 33 04 40, 28334 Bremen, Germany

Global and Planetary Change
submitted 2008 December 17

The third scientific article deals with a palaeoceanographic model experiment. It uses the results of the previous two articles. To evaluate the influence of the changes

in palaeobathymetry to ocean circulations and to long-term climate changes, respectively, four oceanographic model scenarios are calculated for a present day control run and for Middle Miocene, Early Miocene and Middle Eocene time slices. The model input data is the palaeobathymetric reconstruction, which is presented in chapter 6 and which is for this study included into a global palaeobathymetry data set.

To perform a sensitivity test on the consequences of the tectonic movements in the northern North Atlantic and the Arctic Ocean, it was desirable to use the new palaeobathymetric grid in programs, which model oceanographic circulations. The opening situation in the Fram Strait area with present boundary conditions would at least give a rough insight on the consequences of these tectonic movements.

This work could not be done completely within this PhD study, because of the complex software and the time needed for the model runs. A model run for one time slice took about 10 days. To complete this analysis, I asked for support to conduct the model runs within the Climate Sciences/Paleo-climate Dynamics Division at the Alfred Wegener Institute. The used MPIOM 1.3 model was operated by the co-authors Martin Butzin and Klaus Grosfeld, who have worked with this software in recent years. The analysis and interpretation of the resulting ocean circulations is done as part of this study to test the influence of the Arctic gateway on the climate variability of the past. In absence of detailed information on the atmospheric forcing and the oceanographic conditions at that time, the present day oceanographic and atmospheric knowledge is applied.

To test the model experiment, the present day control run is compared to observed ocean circulation data from literature. The results of the palaeoceanographic model scenarios are investigated due to the changes of ocean circulations in the northern North Atlantic and in the Arctic Ocean, which are caused by changes in the palaeobathymetry. The main focus of this paper is on the onset of the deep-water exchange through the Fram Strait. The ocean model experiment gives evidence for a correlation of palaeobathymetric changes, the onset of deep-water circulations between the northern North Atlantic and the Arctic Ocean and global climate changes.

Chapter 5

Subsidence and crustal roughness of ultra-slow spreading ridges in the northern North Atlantic and the Arctic Ocean

Birte-Marie Ehlers and Wilfried Jokat

Alfred Wegener Institute for Polar and Marine Research, Am Alten Hafen 26,
27568 Bremerhaven, Germany

Geophysical Journal International, 177, May 2009, p 451–462

Accepted 2008 November 26; Received 2008 November 3; in original form 2007 June 14

5.1 Summary

Five basin-wide seismic reflection profiles of up to 550 km each were acquired in the Arctic Ocean and the northern North Atlantic in 2001 and 2002. The main objective was to investigate the depth to the basement and to analyse the crustal structure, morphology and roughness of ultra-slow spreading ridges of the Gakkel, Molloy and Knipovich ridges. To date, little is known of the ultra-slow spectrum of such spreading ridges. The seismic profiles of all investigated ridges show similar morphological characteristics with deep axial valleys and rough basement topography. Magnetic data compilation and interpretation suggests that the ultra-slow spreading systems are fairly stable and existed during the entire evolution of the basins to the north of the Greenland Fracture Zone. The thermal subsidence curve was calculated and corrected for sediment loads, and crustal roughness values are estimated for all five profiles. The resulting roughness values append the global roughness data set for ultra-slow spreading systems. The results are higher than those

predicted by interpolating existing global roughness. This study confirms the presence of a global relationship between crustal roughness, ridge morphology and spreading rates. New curve fits, supporting the global relationship, are discussed. Data on present spreading rates, ridge morphology, subsidence and roughness provide a better insight into the development of the axial ridge morphology in the study area. The results show that the basins to the north of the Greenland Fracture Zone were formed at ultra-slow spreading axial rift valleys and continued spreading at ultra-slow rates to the present day configuration.

Key words: Arctic region, Atlantic Ocean, Sedimentary basin processes, Marine magnetism and palaeomagnetism

5.2 Introduction

Several methods have been used in the past to classify oceanic spreading rates and centres. One approach is to categorise mid-ocean ridge processes based on calculation of root mean square (RMS) crustal roughness. In this context, roughness implies an indirect record of axial morphology and can provide observational constraints on the nature of changes in axial morphology, crustal thickness and tectonics (Ma and Cochran, 1997).

The relationship between subsidence and age has been known for many years (Parsons and Sclater, 1977). In recent years, several studies have compared crustal roughness values with ridge parameters such as spreading velocity, crustal thickness, faulting, segmentation or ridge morphology (Malinverno and Cowie, 1993; Small, 1994; Goff et al., 1997; Minshull, 1999). The existence of a relationship between spreading rate and roughness was first published by Menard (1967) and Sclater and Francheteau (1970).

Dick et al. (2003) point out that on the basis of various studies at faster spreading centres, mid ocean ridges have been divided into fast spreading rates (80–180 mm/y full rate), intermediate spreading rates (55–70 mm/y) and slow spreading rates (less than 55 mm/y). Spreading ridges with full spreading rates of less than 20 mm/y are characterised as ultra-slow spreading ridges. Several ultra-slow spreading ridges are present in the Arctic, but these ridges remain poorly characterised.

Abyssal hill morphology results from a complex combination of tectonics (surface faulting) and constructional (volcanic) processes, which occur at or near the ridge axis (Goff et al., 1993). In particular, spreading ridges with a full rate of less than 20 mm/y change between volcanic activity and normal faulting of crustal blocks due to tectonic strain during drifting. This change causes the roughness of the basement surface (Louden et al., 1996).

MacDonald (1982) assumes that crustal morphology reflects the spreading velocity with slow spreading ridges characterised by a deep axial valley and fast spreading ridges, such as the East Pacific Rise, characterised by a central high. But ridge tectonics is not just a function of spreading rates. It also depends on the ridge geometry, the mantle composition and the thermal structure of the crust (Dick et al., 2003).

Based on observations and extrapolations of faster spreading ridges, on theoretical modelling of the melting processes, and on the thermal structure of the crust, the Gakkal

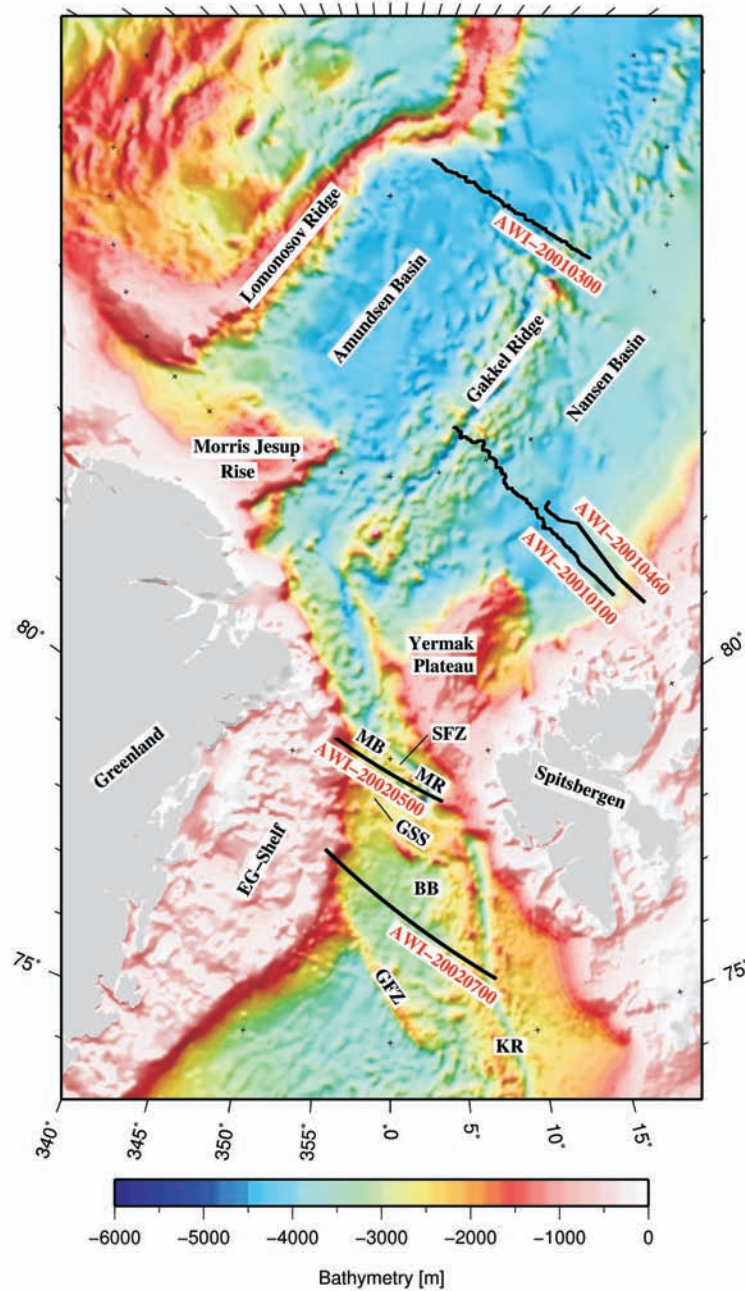


Figure 5.1: Bathymetry map of the international bathymetric chart of the Arctic Ocean (IBCAO) (Jakobsson et al., 2001). The black lines show the seismic reflection profiles AWI-2001000, AWI-20010300 and AWI-20010460 in the Arctic Ocean and AWI-20020500 and AWI-20020700 in the northern North Atlantic, close to the Molloy Ridge (MR) and in the Boreas Basin (BB). KR: Knipovich Ridge, MB: Molloy Basin, SFZ: Spitsbergen Fracture Zone, GSS: Greenland Spitsbergen Sill, GFZ: Greenland Fracture Zone.

Ridge should have sparse volcanism, as well as very limited hydrothermal activity, and low melting of the underlying mantle. However, Michael et al. (2003), divided the Gakkel Ridge into a 300 km-long central amagmatic zone, which lies between abundant, continuous volcanism to the west and large, widely spaced volcanism centres to the east. Furthermore, spreading velocity decreases towards the east while crustal thickness does not vary, and is controlled by the magmatic activity along the ridge (Jokat and Schmidt-Aursch, 2007).

As existing global roughness models lack data from ultra-slow spreading systems, analyses from the ultra-slow spreading systems at the Gakkel Ridge in the northern North Atlantic and Fram Strait, as well as the adjacent basins, are of special interest. The calculation of crustal roughness along the Knipovich and Molloy ridges in the northern North Atlantic and along the Gakkel Ridge in the Arctic Ocean can provide an insight into their morphological evolution. In present configuration, these ridges have ultra-slow spreading rates and a deep axial morphology.

According to the classification of mid ocean ridges (Dick et al., 2003), the Gakkel Ridge has been an ultra-slow spreading system since the formation of the first oceanic crust at magnetic chron 24 (54 Ma). The half spreading rates at the Gakkel Ridge varied between 3 and 10 mm/y during initial opening (Karasik, 1968; Vogt et al., 1979). Half spreading rates decrease from 7.3 mm/y in the Fram Strait to 3.2 mm/y in the Laptev Sea (DeMets et al., 1994).

Age models of oceanic crust based on identifications of magnetic anomalies are used to predict tectonic models for the northern North Atlantic and the Arctic Ocean (Lawver et al., 1990; Kristoffersen, 1990). They indicate that active seafloor spreading in the Arctic Ocean and the northern North Atlantic probably started during chron 24 (53 Ma) at the Gakkel Ridge (Vogt et al., 1979) and at the Mohns Ridge in the Norwegian-Greenland Sea (Talwani and Eldholm, 1977; Eldholm et al., 1987). In between these two systems, seafloor spreading at the Knipovich Ridge started to propagate northward from chron 13 (33 Ma) (Eldholm et al., 1990), whereas the onset of seafloor spreading at the Molloy Ridge took place in the Early Miocene (21 Ma). For the Norwegian-Greenland Sea and the Eurasian Basin, Brozena et al. (2003) identified magnetic isochrones for the Gammaa-5 grid (Verhoef et al., 1996). This identification is restricted to 11 isochrons between chrons 5 and 25. These models are rather speculative, especially due to the lack of data in the Arctic region.

This study presents new seismic data from the Arctic Ocean and northern North Atlantic (Boreas and Molloy basins) (Figure 5.1), refines age models derived from magnetic data, and calculates crustal roughness values for ultra-slow spreading ridges. Based on the above parameters, it is possible to constrain ultra-slow spreading ridges in the Arctic Ocean and the northern North Atlantic for the first time, and thereby provide a clearer picture of the geodynamic evolution of these oceanic basins.

5.3 Data

5.3.1 Seismic reflection profiles

Five reflection profiles of the northern North Atlantic and Arctic Ocean were studied. The profiles 20020500 and 20020700 from the northern North Atlantic (Figure 5.1) were acquired by RV Polarstern with a 24 litre VLF airgun cluster and an 800 m streamer during the expedition ARKXVIII/2 cruise in 2002 (Jokat, 2003). In this contribution, we will not discuss the seismic data in the Boreas and Molloy basins in detail but limit the discussion only to the shape of the oceanic basement. Both seismic profiles were depth-migrated (FD-migration) using velocity information from sonobuoy wide-angle recordings. Two sonobuoys were deployed on profile 20020500 (CDP 5750 and 7300) and three sonobuoys on profile 20020700 (CDP 5100, 10700 and 15450). The acoustic velocity of p-waves in the water is revealed as 1.48 km/s, in sediments as 1.8 km/s up to 3.2 km/s, and for the top of the acoustic basement as 3.3 km/s, with an error of 0.2 km/s. Therefore, the depth-migration has an error of about 160 m for the position of the acoustic basement with a sediment thickness up to 2000 m. Because of the small number of deployed sonobuoys, the velocity model is interpolated along the profiles.

Profile 20020500 (Figure 5.1, 5.2) runs SE–NW, parallel to the Spitsbergen Fracture Zone and the Greenland Spitsbergen Sill, from the axial rift valley of the Molloy Ridge to the East-Greenland Shelf. The line crosses the ridge at $79^{\circ}20'N$, $003^{\circ}44'E$ (Figure 5.2, CDP 1180). The water depth close to the ridge averages 2750 m, and a rough basement surface is observed over the entire profile length. The average relief is about 1000 m, with a maximum basement jump of 2000 m at about $79^{\circ}38'N$, $000^{\circ}59'E$ (Figure 5.2, CDP 3800). Northwest of this position, the basement deepens to an average depth of 4700 m. Here, 2000 m thick sediments cover the basement, whereas the southeastern part is bare or only sparsely sedimented. On the northwestern part of the profile, the basement rises to 2500 m. Here, it is not clear if oceanic crust is still present, or if this part of the profile belongs to the continent-ocean transition zone. The axial rift valley of the Molloy Ridge lies at a depth of nearly 4000 m, and is completely free of sediments.

Profile 20020700 (Figures 5.1, 5.3) crosses the entire Boreas Basin as well as the axial valley of the Knipovich Ridge at $76^{\circ}05'N$, $007^{\circ}13'E$ (CDP 705). The average water depth is 2600 m, and the basement surface is as rough as observed on profile 20020500. Near the axial rift valley, almost no sediments exist. In contrast to profile 20020500, there is no basement jump where the sediment cover starts. The sediments thicken more or less constantly towards the NE-Greenland shelf. The sediment thickness varies up to a maximum of 2000 m. The basement deepens continuously from southeast to northwest, except for a 1500 m high and 15 km wide basement ridge/seamount at $77^{\circ}24'N$, $000^{\circ}02'E$ (Figure 5.3, CDP 10100). Northwest of this feature, the sediment thickness averages 2500 m over a basement at 5500 m to 6000 m depth ($77^{\circ}46'N$, $002^{\circ}09'W$; Figure 5.3, CDP 12800). Towards the NE-Greenland margin, basement shoals to 4500 m over a distance of 5000 m: a gradient of 30%. On the westernmost part of the profile, the basement rises from 5000 m to 2000 m. This area (Figure 5.3, CDP 12000–15000) is supposed to be the seaward

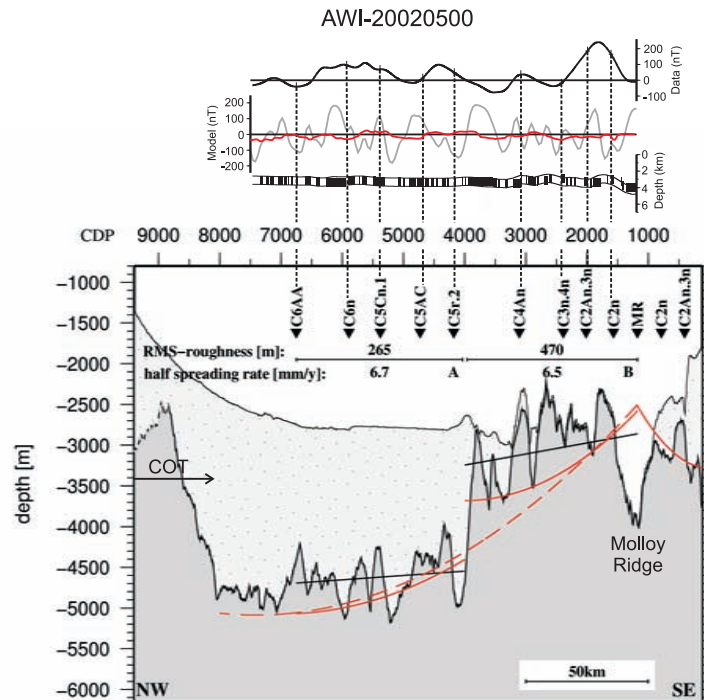


Figure 5.2: top: measured (black line), modelled (grey line) and filtered modelled magnetic data (red line) along profile AWI-20020500, parameters for modelling: magnetic layer thickness 1 km, susceptibility $k=0.0045$, inclination $I=82.6^\circ$, declination $D=-5.9^\circ$, present day total intensity $F=54453.8$ nT (after IGRF) and on-axis magnetisation $J=20$ A/m. bottom: Line drawing of profile AWI-20020500 in the Molloy Basin crossing the Molloy Ridge (MR). Dark grey: basement, light and dotted grey: sediment cover. Red lines: thermal subsidence curve (south-eastern part) and sediment-corrected subsidence curve (north-western part). Dashed red line: subsidence curve for the whole oceanic crust northwest of the Molloy Ridge. Black line: empirical trend of basement depth used for RMS roughness calculation. All seismic reflection profiles of Fig. 2 and 3 are plotted in the same scale, COT: continent-ocean-transition.

termination of the continent-ocean transition zone.

The three seismic reflection profiles 20010100, 20010300 and 20010460 (Figures 5.1, 5.4–5.6) are located in the Arctic Ocean (Jokat and Micksch, 2004), and are used for a roughness study in the western Eurasia Basin. These profiles are aligned almost perpendicular to the Gakkel Ridge, and were acquired with a 241 airgun array and a short streamer (48 channels, 6.25 m group spacing, 300 m active section) together with the USCGC Healy, due to the dense sea ice cover in this region (Thiede et al., 2002). The acoustic p-wave velocities for the profiles are described in Jokat and Micksch (2004).

Profiles 20010100 (Figure 5.4) and 20010460 (Figure 5.5) (Jokat and Micksch, 2004) were shot in the Nansen Basin, and start north of the Svalbard continental margin. Profile 20010100 (Figure 5.4) reaches the axial valley of the Gakkel Ridge at approximately $85^\circ 36' \text{N}$, $016^\circ 41' \text{E}$ (CDP 21100). The axial valley has a water depth of 4800 m. East of

the ridge, the flank of the Gakkel Ridge shows some pronounced basement highs around $85^{\circ}13'N$, $020^{\circ}14'E$ (CDP 18000). In this area, the sediment cover is sparse or even absent. Southeast of a 1500 m high seamount at $84^{\circ}43'N$, $022^{\circ}05'E$ (CDP 15000), the sediments continuously start to thicken towards the south. The water depth in the abyssal plain is about 4000 m. A seamount disrupts the sediment cover at $84^{\circ}18'N$, $022^{\circ}39'E$ (CDP 12420), where the water depth shoals to 3710 m. The basement deepens down to 7500 m in the eastern part of the line.

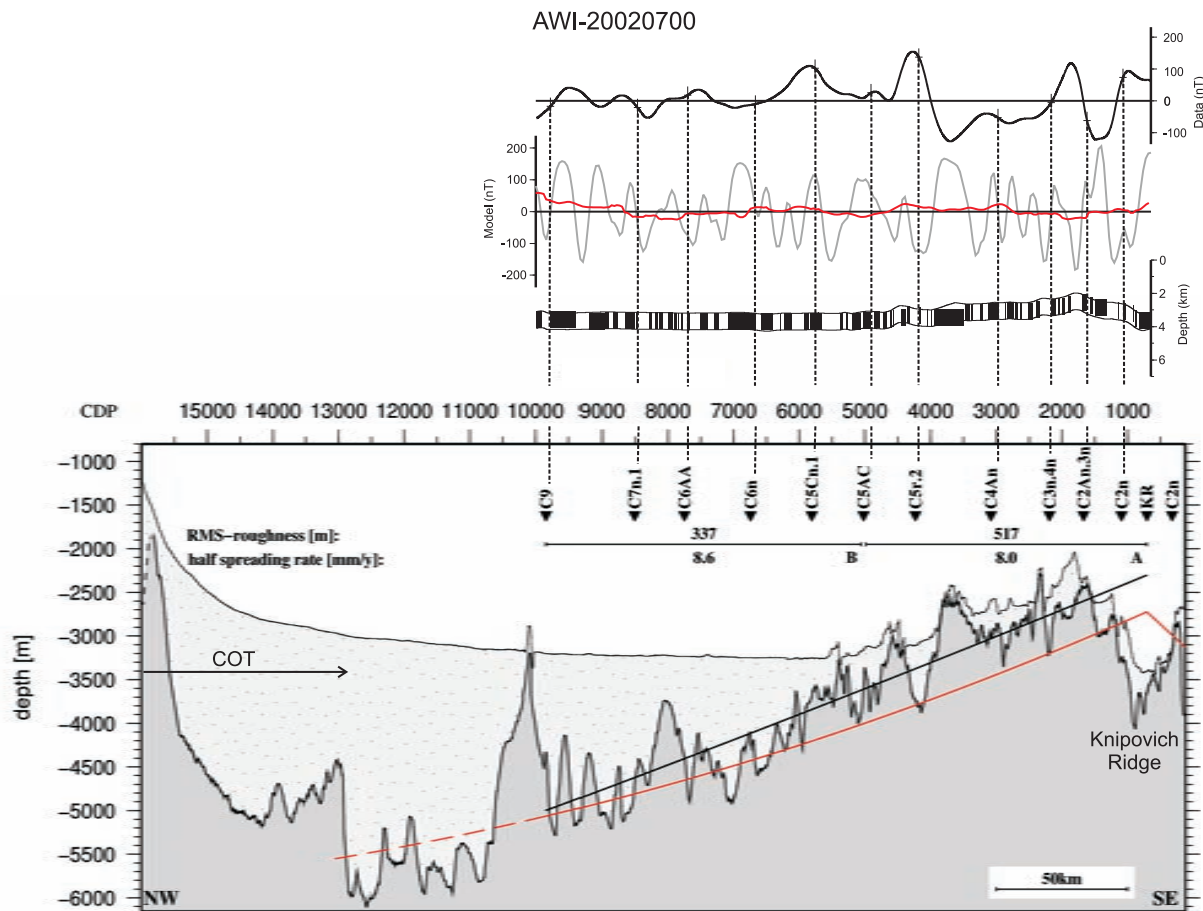


Figure 5.3: top: measured (black line), modelled (grey line) and filtered modelled magnetic data (red line) along profile AWI-20020700, parameters for modelling: magnetic layer thickness 1 km, susceptibility $k=0.0045$, inclination $I=81.0^{\circ}$, declination $D=-2.5^{\circ}$, present day total intensity $F=53771.51$ nT (after IGRF) and on-axis magnetisation $J=20$ A/m. bottom: Line drawing of profile AWI-20020700 in the Boreas Basin crossing the Knipovich Ridge (KR). Dark grey: basement, light and dotted grey: sediment cover. Red line: thermal subsidence (close to the Knipovich Ridge) and sediment-corrected subsidence (basement with sediment covered) merged and fitted to one subsidence curve. Dashed red line: extrapolated subsidence curve. Black line: empirical trend of basement depth used for RMS roughness calculation, COT: continent-ocean-transition.

The second profile in the Nansen Basin is line 20010460 (Figure 5.5) (Micksch, 2004). It is offset by 120 km to the east relative to line 20010100. Up to 3000 m of sediments overlie a basement surface with a relief of about 1000 m. The basement becomes shallower in the north (towards the Gakkel Ridge) and in the south (towards the Svalbard continental margin).

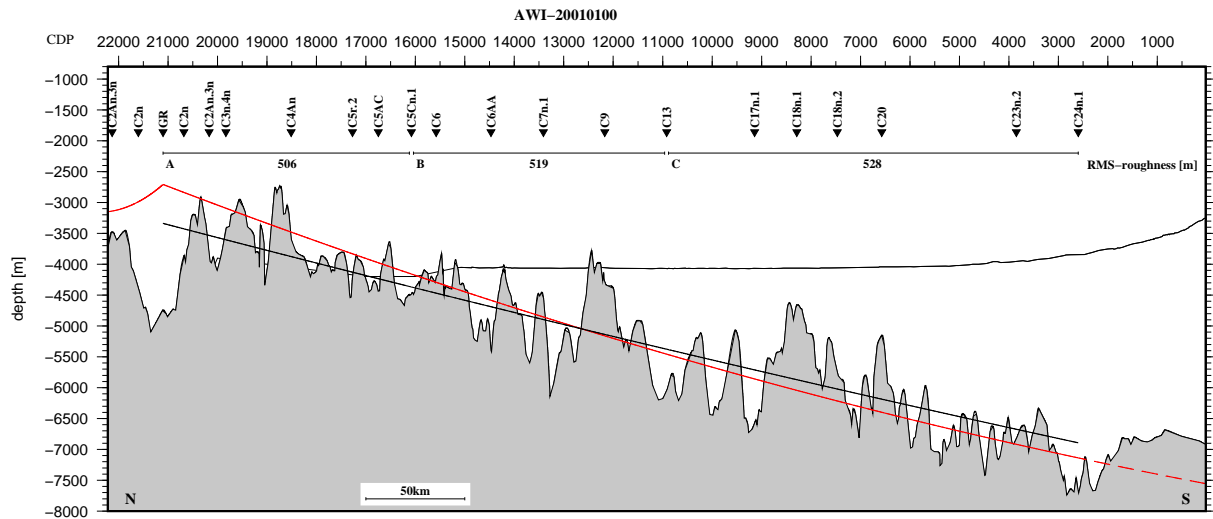


Figure 5.4: Line drawing of the profile 20010100 in the Nansen Basin crossing the Gakkel Ridge (GR). Red line: sediment-corrected subsidence curve, dashed red line: extrapolated subsidence curve, black line: empirical trend of basement depth used for RMS roughness calculation, top: age model modified after Brozena et al. (2003).

The seismic line 20010300 (Figure 5.6) (Jokat and Micksch, 2004) in the Amundsen Basin starts near 86°N at the Gakkel Ridge. From about $86^{\circ}34'\text{N}$, $073^{\circ}53'\text{E}$ (CDP 1500) to $87^{\circ}12'\text{N}$, $077^{\circ}50'\text{E}$ (CDP 5000), the rough basement deepens from 3000 m to 4500 m, and has no sediment cover. North of this position, the basement drops by 2000 m over a distance of 15 km. From here on, the seismic reflection data show a sediment cover with a mean thickness of 1700 m, which continues to the foot of the Lomonosov Ridge. This sediment cover is disturbed by a seamount at $87^{\circ}21'\text{N}$ $080^{\circ}33'\text{E}$ (CDP 6900). A 7000 m deep basement low at $82^{\circ}31'\text{N}$, $099^{\circ}40'\text{E}$ (CDP 13250) indicates the largest sediment thickness of the profile, before the basement depth shallows in the direction of the Lomonosov Ridge.

5.3.2 Magnetic Data

Aeromagnetic data freely available for the region of the northern North Atlantic between the Greenland Fracture Zone and the Spitsbergen Fracture Zone was used for this study (GAMMA5-Grid; Verhoef et al. (1996)). The anomaly pattern in the Molloy and Boreas basins in this data set is mostly diffuse. Hence, new aeromagnetic data gathered by the

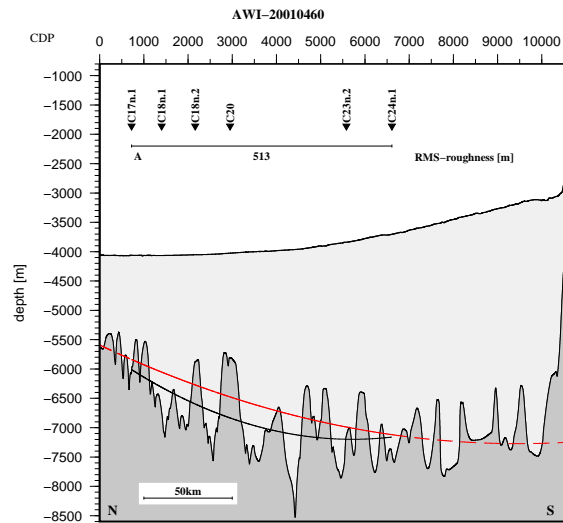


Figure 5.5: Line drawing of the profile 20010460 in the Nansen Basin. Red line: sediment-corrected subsidence curve, dashed red line: extrapolated subsidence curve, black line: empirical trend of basement depth used for RMS roughness calculation, top: age model modified after Brozena et al. (2003).

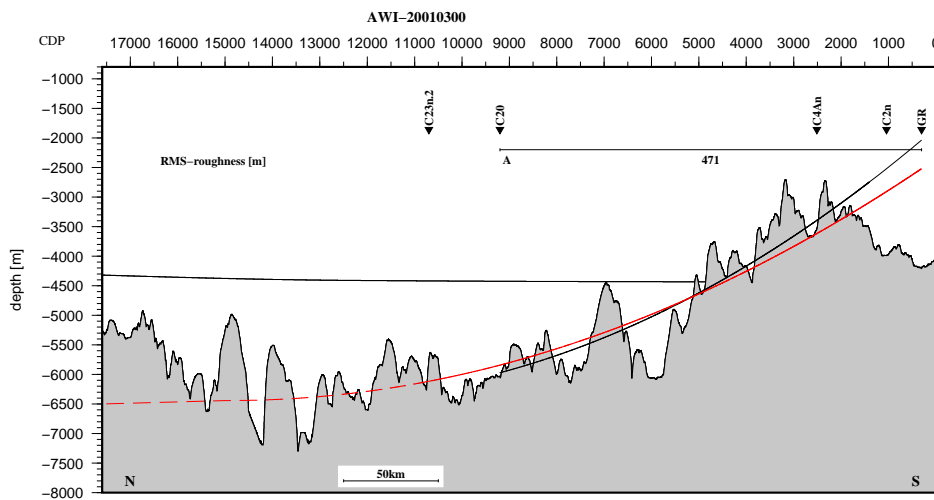


Figure 5.6: Line drawing of the profile 20010300 in the Amundsen Basin crossing the Gakkel Ridge (GR). Red line: sediment-corrected subsidence curve, dashed red line: extrapolated subsidence curve, black line: empirical trend of basement depth used for RMS roughness calculation, top: age model modified after Brozena et al. (2003).

Alfred Wegener Institute were used to supplement the existing surveys (Figure 5.7) (Leinweber, 2006). The helicopter survey was designed to follow the assumed spreading direction. Though, the overall magnetic anomaly field remained diffuse, a better resolution and hence identification of the anomalies was achieved in the Boreas and Molloy basins. The

aeromagnetic anomalies in both data sets are more pronounced in the Boreas Basin than in the Molloy Basin.

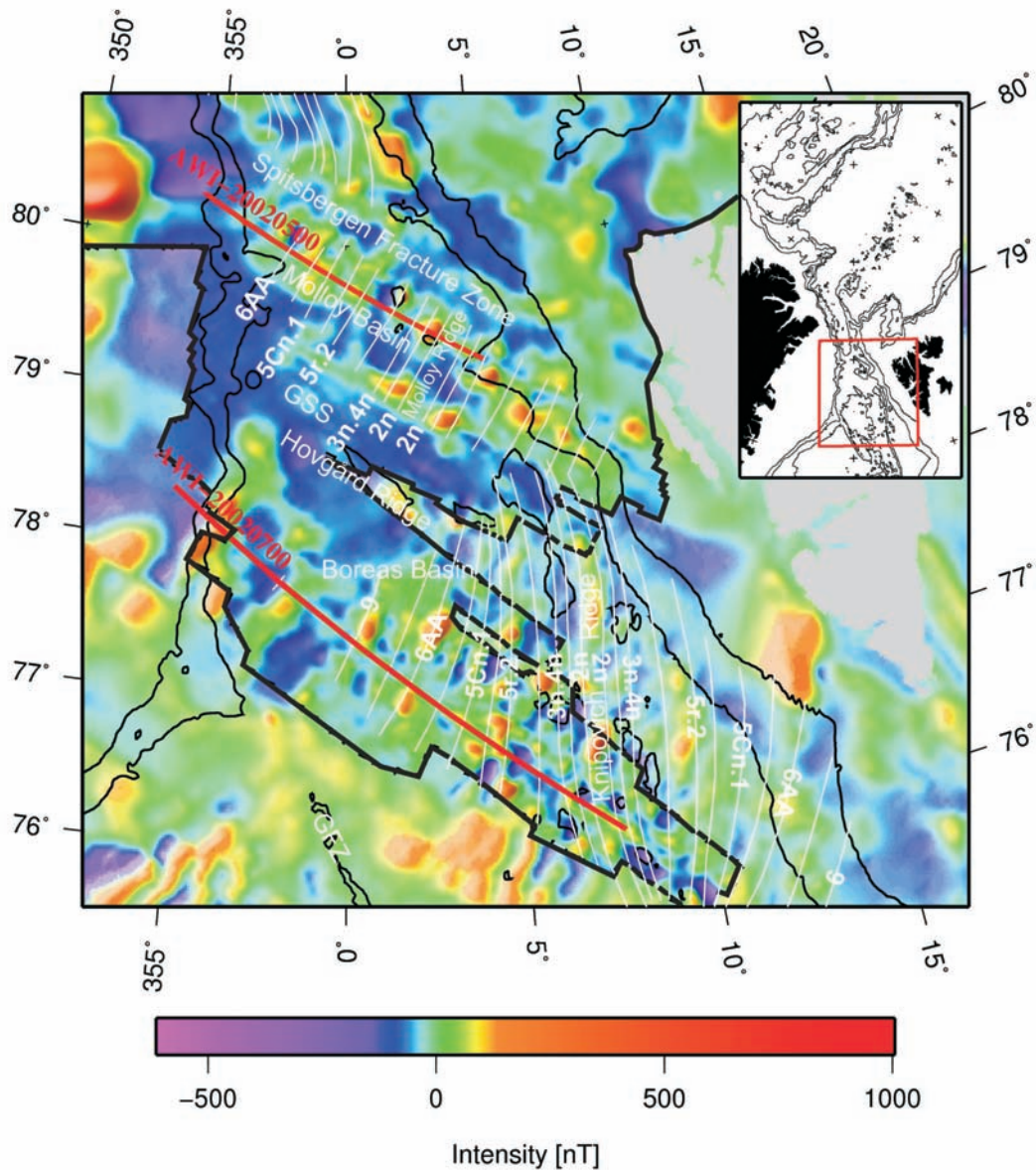


Figure 5.7: Age model for the Molloy and Knipovich ridges region. The white lines illustrate the re-identified magnetic chrons labelled after Gradstein et al. (2004). The seismic reflection profiles 20020500 and 20020700 are marked in red. The black line shows the limits of the new magnetic grid for the Fram Strait (Leinweber, 2006). Additional magnetic data illustrated with lower intensity comes from the GAMMAA5 grid (Verhoef et al., 1996). GSS: Greenland Spitsbergen Sill, GFZ: Greenland Fracture Zone.

5.4 Analysis

The analysis consists of a calculation of the spreading rates based on a magnetic modelling, and applies an age depth relationship for subsidence calculations. Additionally roughness calculations are made.

5.4.1 Spreading Rates

Method

Along the seismic reflection profiles, seafloor spreading magnetic anomalies were re-identified based on identifications by Brozena et al. (2003) of magnetic anomalies at the Gakkel and Mohns ridges. Therefore, the 2D magnetic modelling program MAGBATH (Hey et al., 1986) was used, and ages for the anomalies were determined according to the Geological Time Scale 2004 (Gradstein et al., 2004). The magnetic modelling consisted of varying estimated spreading rates to obtain the best fits between measured and calculated anomalies. The assumed magnetic layer thickness, magnetic susceptibility, declination, inclination and the present day total intensity are listed in figures 5.2 and 5.3. For the identification of anomalies, an effort was made to avoid topographic elements impacting the analysis.

Since the aeromagnetic data do not show the most pronounced anomalies along the seismic lines (Figures 5.2, 5.3), transects 23 km south of line 20020500 (Figure 5.8) and 27 km south of line 20020700 (Figure 5.9) were used.

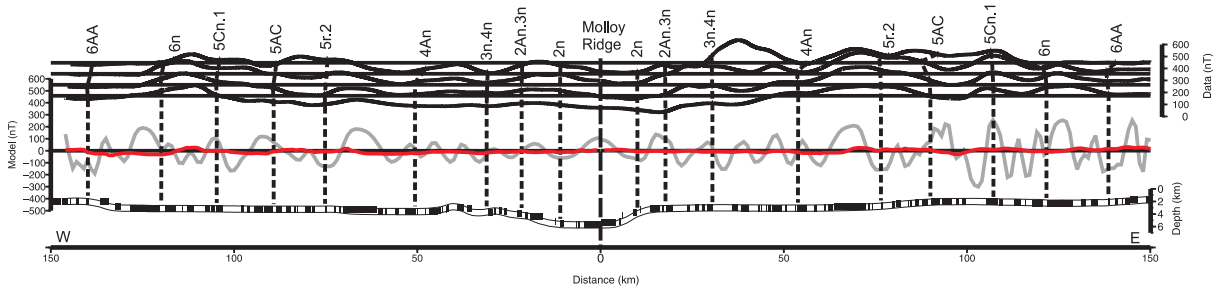


Figure 5.8: Magnetic modelling of a helicopter survey 23 km south of profile 20020500 crossing the Molloy Ridge. The black line shows four measured profiles with a line spacing of 5 km, the grey line the modelled data and the red line the filtered modelled data. At the bottom, the geomagnetic time scale after Gradstein et al. (2004) is presented. The re-identified isochrones are marked for a comparison of the measured and modelled data.

Four profiles in the vicinity of the above modelled lines were used to check the spatial continuity of the anomalies and their correct identification. The profiles have a line spacing of 5 km for the transect crossing the Molloy Ridge (Figure 5.8) and 10 km for the transect crossing the Knipovich Ridge (Figure 5.9).

Even though the resolution of the new aeromagnetic grid is substantially better, the magnetic anomalies presented in this dataset are not as detailed as the calculated anomalies

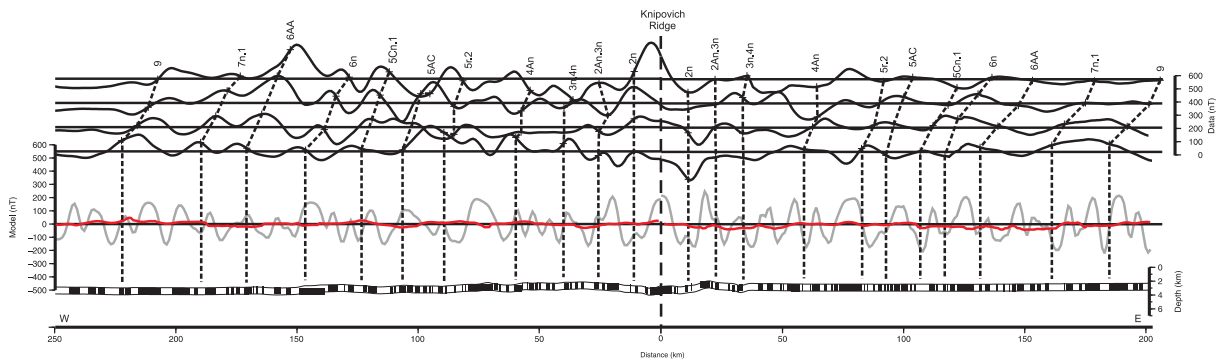


Figure 5.9: Magnetic modelling of a helicopter survey 27 km south of profile 20020700 crossing the Knipovich Ridge in the Boreas Basin. The black line shows four measured profiles with a line spacing of 10 km, the grey line the modelled data and the red line the filtered modelled data. At the bottom, the geomagnetic time scale after Gradstein et al. (2004) is presented. The re-identified isochrones are marked for a comparison of the measured and modelled data.

in the magnetic modelling. Comparing the modelled and measured anomalies, positive polarisations of the measured data include anomaly groups of the modelled data. Thus, we applied an appropriate filter to the computed anomalies from the model. Furthermore, some anomalies in the measured data are generated by topographic effects.

Results

The re-identified anomalies are presented in figure 5.7 (white lines). Whereas seafloor spreading at the Gakkel Ridge and in the Norwegian-Greenland Sea began during chron C24, at about 54 Ma (Brozena et al., 2003), seafloor spreading in the Molloy Basin started at about 21 Ma (during chron C6AA (this study); Figure 5.7). The northern part of the Knipovich Ridge (east of the Hovgård Ridge) contains magnetic anomalies up to the beginning of chron C5 (10 Ma), whereas anomalies in the Boreas Basin can be clearly identified in the sequence up to chron C9 (28 Ma; Figure 5.7).

The magnetic data grid (Figure 5.7) shows that anomaly C9 east of the Knipovich Ridge is located just a few kilometres from the supposed continent-ocean transition zone off the Barents Sea, which corresponds to the 1000m and 2000m bathymetry contour line. Anomaly C9 can probably be found in the Boreas Basin at $77^{\circ} 22' \text{N}$, $000^{\circ} 15' \text{E}$ (Figure 5.3; CDP 9840) west of the Knipovich Ridge.

The basement lies at a depth of 5700 m northwest of the basement ridge/seamount at $77^{\circ} 24' \text{N}$, $000^{\circ} 02' \text{E}$ (Figure 5.3, CDP 10100). If this great depth indicates the presence of oceanic crust, seafloor spreading might have started earlier than chron C9 (28 Ma).

Along profile 20020500, the half spreading rate was about 6.6 mm/y from the opening during chron 6AA (21 Ma) until today. Half spreading rates along line 20020700 started with 8.9 mm/y at chron 9 (28 Ma). Since 10 Ma, the oceanic crust accreted at an average half spreading rate of 6.2 mm/y. In the Arctic Ocean (line 20010100), half spreading rates

for the Nansen Basin range from 7.5 mm/y at 54 Ma to 33 Ma to 6.7 mm/y from 33 Ma to 16 Ma, and 6.0 mm/y from 16 Ma until the present. For the Amundsen Basin, the average half spreading rates of profile 20030300 is 4.7 mm/y. A spreading asymmetry between the Nansen and Amundsen basins first was reported by Vogt et al. (1979), who presented two curves for the northern and southern rift flank of the Gakkel Ridge with a difference in half spreading rates of 10–20 %.

In this study, half spreading rates east of the Molloy Ridge (0–12 Ma: 6.5 mm/y, 12–21 Ma: 6.3 mm/y) are similar to the values west of the ridge, whereas the rates at the Knipovich Ridge (0–14 Ma: 6.2 mm/y, 14–28 Ma: 6.4 mm/y) show an asymmetry of about 20–25 %, with higher rates on the western side.

5.4.2 Subsidence

Method

We applied the Parsons and Sclater (1977) age-depth relationship in combination with a sediment correction (Allen and Allen, 1990) for the seismic reflection profiles 20010100, 20010300 and 20010460. The loading effect of the sediment is treated as a problem of local isostatic balance (Allen and Allen, 1990). We applied the same formulas for profiles 20020500 and 20020700. For the area close to the ridge, where oceanic crust is quite young and only sparsely covered by sediments, thermal subsidence calculations Parsons and Sclater (1977) were used to calculate the average basement depth. In areas with a large sediment cover, we corrected the subsidence curve for the sediment load (Allen and Allen, 1990). The resulting values were fitted using quadratic regression (red solid lines, Figures 5.2, 5.3, 5.4–5.6).

In case of profile 20020500, we observed a significant basement jump (CDP 3800) and hence the profile was divided into two parts which were treated separately.

The subsidence calculations for profiles 20010100, 20010300 and 20010460 use crustal ages based on the age model of Brozena et al. (2003) and on the GAMMAA5-Grid (Verhoef et al., 1996). For the subsidence analysis of profile 20020500 and 20020700, the age model based on the new geomagnetic data grid (Figure 5.7; Leinweber (2006)) is used which was described in the previous chapter.

Results

The seismic reflection profiles in the Nansen, Amundsen, Molloy and Boreas basins show that the basement deepens as the oceanic crust ages and the sediment load increases (Figures 5.2, 5.3, 5.4–5.6). To correlate the observed as well as the theoretical basement depth, the calculated subsidence curves are shown in figures 5.2, 5.3 and 5.4–5.6. The dashed red lines show the extrapolated subsidence for the regions where age cannot be identified by magnetic anomalies, but where the depth of basement indicates oceanic crust.

All subsidence curves (Figures 5.2, 5.3, 5.4–5.6) based on the described age model fit the general trend of the basement as observed in the seismic reflection data. The mean

deviation between the calculated subsidence and the empirical trend of the basement relief for all five profiles averages 244 m. The best fit achieves profile 20010300 with 119 m.

Especially close to the axial rift valley of the Molloy and the Knipovich ridges, the oceanic crust is shallower than the theory predicts. This phenomenon is also observed on profile 20010300 close to the Gakkel Ridge. The basement surface in the northwestern part of profile 20020700 shows a good correlation to the extrapolated subsidence curve (dashed red line; Figure 5.3).

Assuming an error of 0.5 Myr for the age of the re-identified isochrones, the calculated subsidence values have an uncertainty of about 40 m.

5.4.3 Roughness

Method

Topographic roughness (R), is defined as the root mean square (RMS) deviation of residual basement relief (h), along a given length of the profile (Malinverno, 1991). The following equation is used for the calculation of R:

$$R_i = \sqrt{\sum_{i=1}^n \frac{h_i^2}{n}}, \text{ for } i = 1, 2, \dots, n \quad (5.1)$$

in which h is the difference between a reference surface and the basement. The reference curve can be a straight line fit to the basement (Malinverno and Cowie, 1993) or the theoretical subsidence curve (Hayes and Kane, 1991). In this study, we used an empirical trend of the basement instead of the theoretical subsidence curves. Although the results of the theoretical subsidence reproduce the general trend of the basement, using the theoretical subsidence for roughness calculation biases the results, even after subtracting the square of mean value of the segment h from the variance. Another advantage of using an empirical trend of the basement as reference surface is that the roughness calculations are independent from the crustal age model. The chosen length of the profile section should exceed some tens of kilometres, preferably about 100 km (Malinverno, 1991), in order to overcome self-affinity problems and influences of window borders. A power law derived from many measurements on oceanic ridge systems describing the relationship of roughness R and full spreading rate, v, is given by Malinverno (1991) as

$$R_c = 1296 \cdot v^{-0.539} \quad (5.2)$$

This power law only describes the relationship between RMS roughness and spreading rate and does not consider the axial morphology. Goff et al. (1997) studied the statistical properties of abyssal hill morphology and showed that for identical spreading rates both the axial morphology and the RMS roughness change. Regarding this conclusion, separate power law curves for axial valley-adjacent and axial high-adjacent values are calculated for this study as well.

For a roughness analysis, the empirical trends of the basement were calculated with an equal spacing of one CDP (25m). Afterwards, we subtracted the basement depth values from the calculated empirical trend of basement depth to obtain the residual basement relief (h). R_i was calculated using equation 5.1.

Profile sections were selected to calculate crustal roughness according to the knowledge of the crustal age or spreading rates, respectively, because spreading rates were not constant through time at all three ridges (this study). Therefore, the roughness calculation was done for separate intervals bounded by magnetic anomalies or the ridge axis. For profile 20020500, it was not possible to obtain interval borders further apart than 70 km because of a change in spreading rates at the basement jump at CDP 3800 (Table 5.1).

Results

	section	half spreading rate [mm/y]	age range [Ma]	length of profile section [km]	roughness R_I [m]	roughness R_C [m] [Malinverno (1991)]	roughness R_C [m] [this study]
<i>Nansen Basin</i>							
20010100	A	6.0	0–16	125	506	340	432
	B	6.7	16–33	127	519	320	405
	C	7.5	33–53	207	528	301	380
20010460	A	7.5	37–53	147	513	301	380
<i>Amundsen Basin</i>							
20010300	A	4.7	0–42	223	471	387	497
<i>Boreas and Molloy basins</i>							
20020500	A	6.5	0–11	70	470	325	413
	B	6.7	11–21	68	265	320	405
20020700	A	8.0	0–14	107	517	291	366
	B	8.6	14–28	120	337	280	351

Table 5.1: Profile section, half spreading rates, age range, length of profile section, roughness, R_i , and predicted roughness, R_C , after the power law of Malinverno (1991) and after the power laws of this study, for the five profiles in the Arctic Ocean and northern North Atlantic

The results of the roughness analysis are presented in table 5.1. All new roughness values (this study) are calculated at ultra-slow spreading rates in ocean basins with axial rift valleys.

The RMS roughness of all five axial valley-adjacent profiles (Table 5.1) located in the Arctic Ocean and the northern North Atlantic results in high roughness values from 265 m up to 528 m. The standard variation amounts to 93 m. Figure 5.10 shows the relationship of the half spreading rate and the results of the roughness analysis with the standard variation

as error bars. The grey area marks the range of the ultra-slow spreading velocities for the Gakkel Ridge.

Figure 5.11 presents data from axial valley-adjacent and axial high-adjacent roughness values. Especially for half spreading rates between 17 mm/y and 36 mm/y, both roughness values from axial rift valleys and axial rift highs exist. Therefore, based on the new roughness data, two separate power law curve fits are calculated

- for axial valley-adjacent values:

$$R_c = 1811 \cdot (2v)^{-0.5767} \quad (5.3)$$

- for axial high-adjacent values:

$$R_c = 1290 \cdot (2v)^{-0.5898} \quad (5.4)$$

The correlation coefficient is 0.86 for equation (5.3) and 0.71 for equation (5.4). The results of the various curve fits are shown in figure 5.11.

5.5 Discussion

Seismic reflection data shows deep axial valleys and rough basement topography for all five profiles (Figures 5.2, 5.3, 5.4–5.6). Combining the results of the seismic reflection profiles and of the new aeromagnetic data grid (Figure 5.7), an enhanced age model was developed. This age model, which is confirmed by magnetic modelling (Figures 5.2, 5.3, 5.8 and 5.9), suggests half spreading rates for all investigated basins to be located in the ultra-slow range based on classification of mid ocean ridges (Dick et al., 2003). Half spreading rates range from 6.0 mm/y to 8.6 mm/y.

For the Gakkel, Molloy and Knipovich ridges, the main reason for such ultra-slow spreading seems to be the slow absolute rates of motion of the bounding Eurasian and North American plates (Vogt et al., 1979). These plates are not undergoing significant subduction. Furthermore, the proximity of the ridges to the Euler pole of rotation (Gaina et al., 2002) also results in low angular velocities and therefore, ultra-slow spreading. Ultra-slow spreading causes fast cooling of the asthenosphere, increasing the viscosity and lowering crustal production rates (Sleep and Rosendahl, 1979).

The age-depth relationship of Parsons and Sclater (1977) in combination with a sediment correction (Allen and Allen, 1990) was applied to the re-identified age model. The observed depth to basement can be explained by the thermal subsidence and the sediment loads. The theoretical subsidence curves (red lines, Figures 5.2, 5.3, 5.4–5.6) differ from the empirical trends of the basement (black lines, Figures 5.2, 5.3, 5.4–5.6) by up to 400 m. The uncertainty of the calculated subsidence curves can be attributed to errors in the age model of oceanic crust and in the sediment thickness derived from the seismic reflection data.

In figure 5.10, published roughness values (Goff, 1991; Goff et al., 1997; Bird and Pockalny, 1994; Henstock and White, 1996; Ranero et al., 1970; Minshull, 1999; Weigelt and Jokat, 2001) are shown in a global context, highlighting the relationship between crustal roughness and half spreading rates. The new roughness values supplement the global data for the ultra-slow end of the spectrum. The calculated roughness values for ultra-slow spreading rates range from 265m to 528m. These are only dependent on the basement depth derived from seismic reflection data. The values are higher than roughness values derived from ridge-adjacent areas with higher spreading rates. The results support

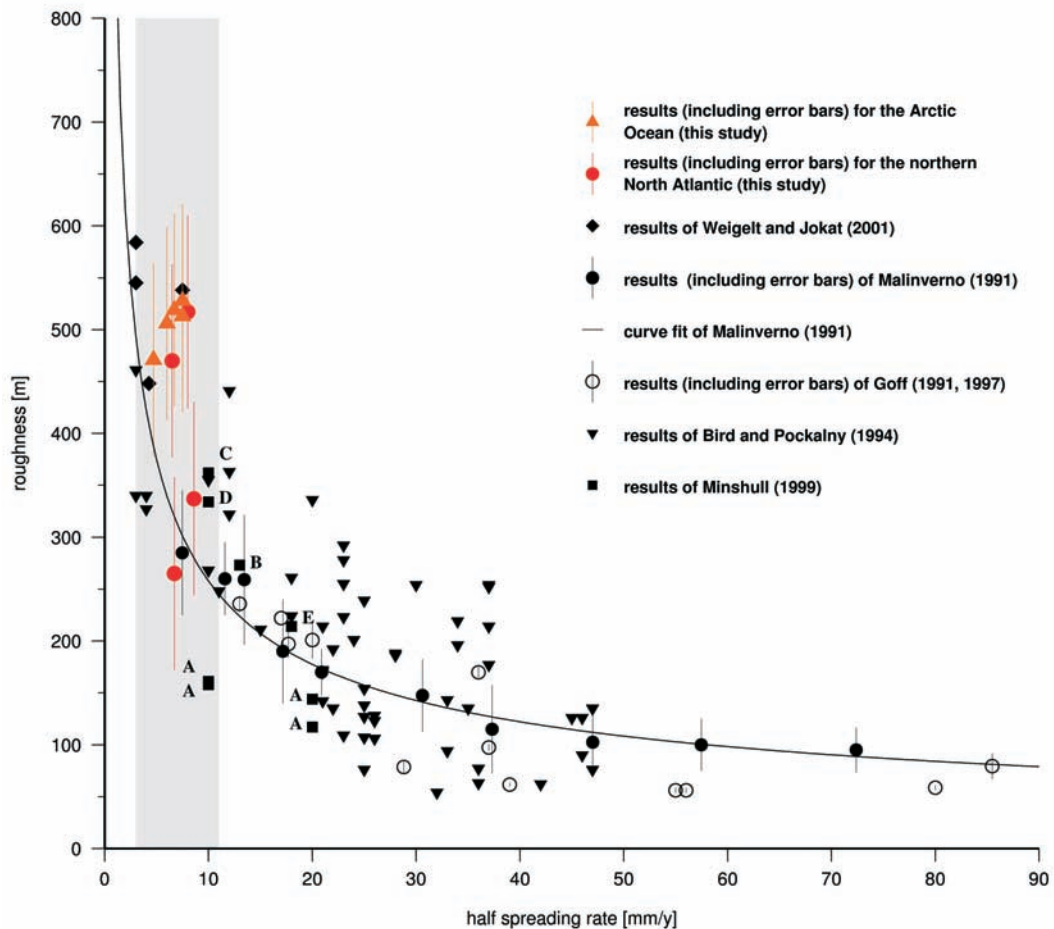


Figure 5.10: Roughness [m] versus half spreading rate [mm/y]. The results of Goff (1991); Goff et al. (1997) come from the southern Mid Atlantic Ridge and the Pacific Ocean, the results of Bird and Pockalny (1994) are from the South Australia Basin and the Argentine Basin. The roughness values of Minshull (1999) are from A: Blake Spur Fracture Zone (Morris et al., 1993), B: west flank of the Mid-Atlantic Ridge at 28°N, C: Canary Basin (Ranero et al., 1970), D: OCEANS area at the Cape Verde abyssal plain (Henstock and White, 1996) and E: east flank of the Atlantic Ridge at the equator. The black line represents the curve fit of Malinverno (1991). The grey area marks the range of the half spreading rates for the Gakkel Ridge

the global correlation of spreading rates and crustal roughness. The roughness values do not correlate with the magmatic and amagmatic segmentation (Michael et al., 2003) or the crustal thickness (Jokat and Schmidt-Aursch, 2007), respectively.

With exception of the roughness value for the north western part of profile 20020500, all new roughness values worked on for the Fram Strait and the Arctic Ocean, including the ones by Weigelt and Jokat (2001), lie above the Malinverno (1991) curve fit. The roughness values of Bird and Pockalny (1994) are generally higher than the RMS roughness data of Malinverno (1991) at ultra-slow spreading rates (<20 mm/y), but similar at intermediate rates (21–40 mm/y). The results of Goff (1991) and Goff et al. (1997) for intermediate and fast spreading rates lie under the Malinverno curve for most data points. The values for slow spreading rates lie above the curve. In general, the difference between roughness predictions from Malinverno (1991) and other authors increases as spreading rates decrease (Figure 5.10). Most crustal roughness values result in higher values for slow spreading rates and in lower values for fast spreading rates. For spreading rates of 20 mm/y to 40 mm/y, the roughness values range about 100 m around the curve fit. Hence, a discussion regarding a new curve fit including the new roughness data is justified.

The error bars for the roughness calculations, which are displayed in figure 5.10, cannot account for the difference between the power law curve fit (Malinverno, 1991) and the roughness values. To specify the difference between crustal roughness values and the power law fit, besides spreading rates and roughness values, the axial morphology is taken into account. Goff et al. (1997) divided the roughness analysis in values derived from axial rift valleys, intermediate rift axes and axial rift highs. If the ridge morphology is taken into account, the values calculated close to axial rift valleys are on average about 50 m higher than axial high-adjacent values (Figure 5.11). We conclude that a single power law is not sufficient to predict the relationship between spreading rates and crustal roughness. A step-function relationship of half spreading rates and roughness may be a possible solution. The sharp increase of crustal roughness values for slow spreading rates and small changes in roughness for fast spreading rates determine the calculation of a polynomial relationship.

For axial valley-adjacent roughness values, the results of the power law (5.3) are higher than Malinverno (1991) predicts. The mean deviation adds up to 40 m. In contrast, the results of the curve fit of axial high-adjacent roughness values (5.4) are on average 23 m less than the calculated values of Malinverno's power law.

Identical morphology along ultra-slow spreading ridges thus provides roughness values of a wider range than along faster ridges. As an example, roughness values at 6.5 mm/y–6.7 mm/y half spreading rate range over 254 m, from 265 m to 519 m (Figure 5.10, Table 5.1), whereas roughness values at 28.8 mm/y–30.6 mm/y half spreading rate range over 69 m, from 79 m to 148 m.

Equation 5.3 was used to calculate roughness values RC based on the estimated spreading rates (Table 5.1) from the re-identified isochrones in the Boreas Basin, Molloy Basin and in the Arctic Ocean. The RMS roughness Ri (equation 5.1) is an average of 55 m higher than RC calculated after equation 5.3 (this study) and 140 m higher than RC calculated after Malinverno (1991) (equation 5.2). Since the results of this study are derived from axial valley-adjacent roughness values, equation 5.4 is only based on data from Goff (1991);

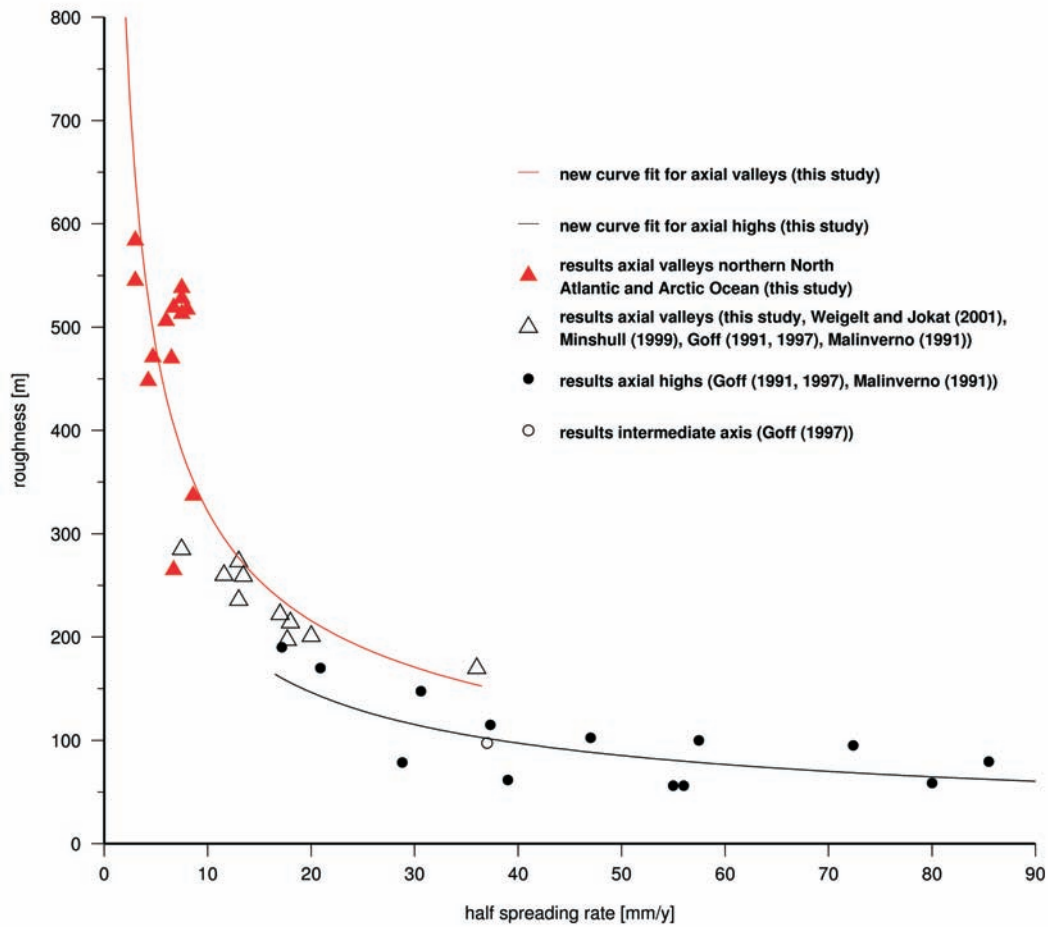


Figure 5.11: Roughness [m] versus half spreading rate [mm/y]. The results of Goff (1991); Goff et al. (1997), Malinverno (1991) and this study are separated in axial valley-adjacent, intermediate and axial high-adjacent roughness values. The red line represents the curve fit for axial valley-adjacent roughness values (this study), the black line shows the curve fit for axial high-adjacent roughness values (this study)

Goff et al. (1997) and Malinverno (1991). Using the existing database, just one roughness value with an intermediate axial morphology is available. Therefore, it is not possible to infer a relationship between intermediate axial morphology, roughness and spreading rate.

In this study, the high roughness values obtained from all five analysed seismic reflection profiles (Table 5.1) with ultra-slow seafloor spreading rates in the investigated basins with axial rift valleys indicate a correlation between spreading rate, axial morphology and roughness values. In the Arctic Ocean, Boreas Basin and at the Molloy Ridge seafloor spreading was initiated at ultra-slow spreading rates, and based on the age model continued at slightly decreasing spreading velocities until today (Figures 5.2, 5.3, 5.4–5.6, 5.7). The analysis of roughness shows higher roughness values during the entire evolution of the

basins and hence we conclude that the Gakkel, Molloy and Knipovich ridges have always been axial rift valleys.

5.6 Conclusions

The sediment corrected thermal subsidence predicts the general trend of the observed basement depths in the Nansen, Amundsen, Boreas and Molloy basins. An exception occurs at the flanks close to the spreading centres, where the theoretical subsidence is larger than the measured basement depth.

The global data set of RMS roughness has been updated with new values for ultra-slow spreading systems based on roughness calculations of seismic reflection profiles in the Arctic Ocean, the northern North Atlantic and Fram Strait.

The roughness values from basins with ultra-slow spreading rates and axial rift valleys derived in this study are higher than those predicted by the power law of Malinverno (1991). Furthermore, the axial valley-adjacent and axial high-adjacent roughness values were separated. Two curve fits describe the relationship of the seafloor spreading rate, the RMS roughness and the ridge morphology.

All five seismic reflection profiles show the ridge as deep axial valleys and basins with rough basement topography. The new spreading rate model shows that all basins were formed at ultra-slow spreading rates and continued spreading at the same rate. For the investigated basins, a good correlation between spreading rate, morphology and roughness exists.

The results also indicate that the entire ocean floor north of the Greenland Fracture Zone was formed at ridges with axial rift valley morphology with ultra-slow spreading rates and continued to spread at these rates, creating a rough basement topography. This constant ultra-slow spreading rate during the formation and basin evolution is of special interest for future research in geodynamic and plate tectonics.

Acknowledgements

We thank the captain and crew of RV Polarstern for their support and Tim Minshall, John Goff and Donna Shillington for their helpful reviews, which improved this manuscript very much. Furthermore, thanks is given to Vikram Unnithan and Aysel Sorensen for improving the English of the manuscript.

Bibliography

- Allen, P. A. and Allen, J. R. (1990). Basin analysis principles & applications, Blackwell Science Publications, 272 pp.
- Bird, R. T. and Pockalny, R. A. (1994). Late Cretaceous and Cenozoic seafloor and oceanic basement roughness: Spreading rate, crustal age and sediment thickness correlations, *Planetary Science Letter*, 123, 239–254
- Brozena, J.M., Childers, V.A., Lawver, L.A., Gahagan, L.M., Forsberg, R., Faleide, J.I. and Eldholm, O. (2003). New aerogeophysical study of the Eurasia Basin and Lomonosov Ridge: Implications for basin development, *Geology*, 31, 825–828
- DeMets, C., Gordon, R.G., Argus, D.F. and Stein, S. (1994). Effect of recent revisions to geomagnetic reversal time scale on estimates of current plate motions, *Geophys. Res. Lett.*, 21, 2191–2194
- Dick, H. J. B., Lin, J. and Schouten, H. (2003). An ultraslow-spreading class of ocean ridge, *Nature*, 405–412
- Eldholm, O., Faleide, J. I. and Myhre, A. M. (1987). Continent-ocean transition at the western Barents Sea/Svalbard continental margin, *Geology*, 15, 1118–1122
- Eldholm, O., Karasik, A. M. and Reksnes, P. A. (1990). The North American plate boundary, in *The Arctic Ocean region*, Band L of *The Geology of North America*, 171–184, eds Grantz, A., Johnson, L. and Sweeney, J. F., Geological Society of America, Boulder, Colorado
- Gaina, C., Roest, W. R. and Müller, R. D. (2002). Late Cretaceous - Cenozoic deformation of northeast Asia, *Earth and Planetary Science Letter*, 197, 273–286
- Goff, J. A. (1991). A global and regional stochastic analysis of near-ridge abyssal hill morphology, *Journal of Geophysical Research*, 96(B13), 21713–21737
- Goff, J. A., Malinvero, A., Fornari, D. J. and Cochran, J. R. (1993). Abyssal Hill Segmentation: Quantitative Analysis of the East Pacific Rise Flanks 7°S–9°S, *Journal of Geophysical Research*, vol. 98, no. B8, 13851–13862

BIBLIOGRAPHY

- Goff, J. A., Ma, Y., Shah, A., Cochran, J. R. and Sempéré (1997), Stochastic analysis of seafloor morphology on the flank of the Southeast Indian Ridge: The Influence of ridge morphology on the formation of abyssal hills, *Journal of Geophysical Research*, vol. 102, no. B7, 15521–15534
- Gradstein, F., Ogg, J. and Smith, A. (eds.) (2004). *A Geological Time Scale 2004*, Cambridge University Press
- Hayes, D. E. and Kane, K. A. (1991). The dependence of seafloor roughness on spreading rate, *Geophysical Research Letters*, 18(8), 1425–1428
- Henstock, T. J., White, R. S. (1996). Along-axis variability in crustal accretion at the Mid-Atlantic ridge: Results from the OCEAN study, *Journal of Geophysical Research*, B6(101), 13673–13688
- Hey, R. N., Kleinrock, M. C., Miller, S. P., Atawater, T. M. and Searle, R. C. (1986). Sea Beam/Deep-Tow investigation of an oceanic propagating rift system, *Journal Geophysical Research*, 91, 3369–3393
- Jakobsson, M. and IBCAO Editorial Board Members (2001). Improvement to the International Bathymetric Chart of the Arctic Ocean (IBCAO): Updating the Data Base and the Grid Model, *EOS, Trans. Am. Un.*, 82 (47), Fall Meet. Suppl., Abstract OS11B-0371
- Jokat, W. (ed.) (2003), *The Expedition ARKTIS XVIII/2 of RV “Polarstern” in 2002, Contributions of the Participants*, *Berichte zur Polar- und Meeresforschung*, 449.
- Jokat, W. and Micksch, U. (2004). Sedimentary structure of the Nansen and Amundsen basins, Arctic Ocean, *Geophysical Research Letters*, 31, no.2, 4pp.
- Jokat, W. and Schmidt-Aursch, M. C. (2007). Geophysical characteristics of the ultraslow spreading Gakkel Ridge, Arctic Ocean, *Geophysical Journal International*, 168, 983–998
- Karasik, A. M. (1968). Magnetic anomalies of the Gakkel Ridge and origin of Eurasian subbasin of the Arctic Ocean, *Geophysical Methods Prospect. Arctic*, 5, 8–19
- Kristoffersen, Y. (1990). On the tectonic evolution and palaeoceanographic significance of the Fram Strait gateway, *Geological History of the Polar Oceans: Arctic Versus Antarctic*, Bleil, U. and Thiede, J. (eds.), Kluwer Academic Publishers, 63–76
- Lawver, L. A., Müller, R. D., Srivastava, S. P. and Roest, W. (1990). The opening of the Arctic Ocean, *Geological History of the Polar Oceans: Arctic Versus Antarctic*, Bleil, U. and Thiede, J. (eds.), Kluwer Academic Publishers, 29–62
- Leinweber, V.T. (2006). Abschätzung von Sedimentmächtigkeiten in der Framstraße anhand magnetischer Daten, *Diploma thesis Karl-Franzens-University Graz*, 96pp

- Louden, K. E., Osler, J. C., Srivastava, S. P. And Keen, C. E. (1996). Formation of oceanic crust at slow spreading rates: New constraint from an extinct spreading center in the Labrador Sea, *Geology*, vol. 24, no. 9, 771–774
- Ma, L. Y. and Cochran, J. R. (1997). Bathymetric roughness of the Southeast Indian Ridge: Implications for crustal accretion at intermediate spreading rate mid-ocean ridges, *Journal of Geophysical Research*, vol. 102, no. B8, 17697–17711
- MacDonald, K.C. (1982), Mid-ocean ridges: fine scale tectonic, volcanic and hydrothermal processes within the plate boundary zone, *Annual Review of Earth and Planetary Sciences*, vol. 10, 155–190
- Malinverno, A. (1991). Inverse square-root dependence of mid-ocean ridge flank roughness on spreading rate, *Nature*, 352, 58–60
- Malinverno, A. and Cowie, P. A. (1993). Normal faulting and the topographic roughness of mid-ocean ridge flanks, *Journal of Geophysical Research*, 98(B10), 17921–17939
- Menard, H. W. (1967), Sea-floor spreading, topography, and the second layer, *Science*, vol. 157, no. 3791, 923–924
- Michael, P. J., Langmuir, C. H., Dick, H. J. B., Snow, J. E., Goldstein, S. L., Graham, D. W., Lehnert, K., Kurras, G., Jokat, W., Mühe, R. and Edmonds, H. N. (2003). Magmatic and amagmatic seafloor generation at the ultraslow-spreading Gakkel ridge, Arctic Ocean, *Nature*, vol. 423, 956–961
- Micksch, U. (2004). Sedimentary structure, subsidence history roughness analysis of Nansen and Amundsen Basin, Arctic Ocean, Diploma thesis University of Karlsruhe
- Minshull, T. A. (1999). On the roughness of Mesozoic oceanic crust in the western North Atlantic, *Geophysical Journal International*, 136, 286–290
- Morris, E., Detrick, R. S., Minshull. T. A., Mutter, J. C., White, R. S., Su, W. and Buhl, P. (1993). Seismic structure of oceanic crust in the western North Atlantic, *Journal of Geophysical Research*, 98, 13879–13903
- Parsons, B. and Sclater, J. G. (1977). An analyses of the variation of ocean floor bathymetry and the heat flow with age, *Journal of Geophysical Research*, 82(5), 803–827
- Ranero, C.R., Banda, E., Buhl, P. (1970). The crustal structure of the Canary Basin: Accretion process at slow spreading centres, *Journal of Geophysical Research*, 102 (B5), 10185–10201
- Sclater, J. G. and Francheteau, J. (1970). The implications of terrestrial heat flow observations on current tectonic and geochemical models of the crust and upper mantle of the earth, *Geophysical Journal of the Royal astronomical Society*, 20, 509–542

BIBLIOGRAPHY

- Sleep, N. H. and Rosendahl, B. R. (1979). Topography and tectonics of mid-ocean ridge axis, *Journal of Geophysical Research*, 84(B12), 6831–6839
- Small, C. (1994). A global analysis of mid-ocean ridge axial topography, *Geophysical Journal International*, 116, 64–84
- Talwani, M. and Eldholm, O (1977). Evolution of the Norwegian-Greenland Sea, *Geol. Soc. Am. Bul.*, 88, 969–999
- Thiede, J. and the Shipboard Scientific Party (2002), POLARSTERN ARKTIS XVII/2, Cruise Report: AMORE 2001 (Arctic Mid-Ocean Ridge Expedition), *Berichte zur Polar- und Meeresforschung*, 421
- Verhoef, J., Macnab, R., Roest, W., Arjani-Hamed, J. and the project team (1996). Magnetic anomalies of the Arctic and North Atlantic and adjacent land areas. GAMMAA5 (Gridded Aeromagnetic and Marine Magnetism of the North Atlantic and Arctic, 5 km), Geological Survey of Canada, Open File 3125a (CD-Rom)
- Vogt, P. R., Taylor, P. T., Kovacs, L. C. and Johnson, G. L. (1979). Detailed aeromagnetic investigations of the Arctic Basin, *Journal of Geophysical Research*, 84, 1071–1089
- Weigelt, E. and Jokat, W. (2001). Peculiarities of roughness and thickness of oceanic crust in the Eurasian Basin, Arctic Ocean, *Geophysical Journal International*, (145), 505–51

Chapter 6

Palaeobathymetric study of the North Atlantic and the Eurasia Basin

Birte-Marie Ehlers and Wilfried Jokat

Alfred Wegener Institute for Polar and Marine Research, Am Alten Hafen 26,
27568 Bremerhaven, Germany

Geophysical Journal International

Received 2009 May 22; in original form 2008 October 15

6.1 Summary

The Fram Strait is an important gateway for deep-water masses which are exchanged between the northern North Atlantic and the Arctic Ocean. Until now the timing of the first deep-water exchange is still speculative. New aeromagnetic and seismic data north of the Jan Mayen Fracture Zone in combination with existing compiled geological and geophysical data provide control on the age of the seafloor, basement depth and sediment thickness. This study focuses to constrain the period when the first exchange of deep-water took place.

A derived palaeobathymetric model contributes to our understanding of the tectonic processes during the evolution of the oceanic basins. The model is based on subsidence calculations corrected for sediment loads and isostatic equilibrium, and yields palaeo-seafloor depth, palaeo-basement depth and palaeo-sediment thicknesses.

This palaeobathymetric model provides evidence for an initial deep-water exchange through the Fram Strait starting at 17 Ma. The model further suggests that crustal rifting prior to initial seafloor spreading was responsible for the deep-water connection. The reconstruction model indicates that the first possibility for a deep-water overflow from the Norwegian-Greenland Sea to the North Atlantic could have been between 15 Ma and 20 Ma. This confirms that the Yermak Plateau played an important role in the exchange of

shallow water between the northern North Atlantic and the Arctic Ocean before opening of the deep-water Fram Strait gateway.

Based on new data, this study provides a detailed insight into the subsidence and uplift of the investigated basins which is interesting for future palaeoceanographic modelling, and has implications for the timing of the formation of the North Atlantic Depth Water (NADW) and for climate research.

Key words: Arctic region, Plate motions, Sedimentary basin processes, Tectonic and climate interactions

6.2 Introduction

The Fram Strait lies between Greenland and Svalbard, and connects the North Atlantic with the Arctic Ocean. Today it is circa 200 km wide and up to 3000 m deep. This strait is the only deep-water connection between the Arctic Ocean and adjacent seas and, therefore, an important gateway. The reconstruction of the opening history between the Atlantic Ocean and the Arctic Ocean is critical for understanding long term climate changes. Intensive glaciations at the Earth's poles during the Cenozoic, are linked to the opening of the polar gateways (Knies and Gaina, 2008). The opening of the Fram Strait correlates with a general cooling of the northern hemisphere. In this context, the gateway width and depth is an essential parameter for an exchange of deep Arctic water, which circulates on average below 1500m water depth (Kristoffersen, 1990).

In the late Cretaceous, seafloor spreading in the central Atlantic propagated northward between the Rockall Plateau (Figure 6.1) and Ireland (Srivastava and Tapscott, 1986). From 92 Ma, seafloor spreading started in the southern Labrador Sea and separated North America from Greenland. In this region, seafloor spreading continued until chron 13 (37 Ma) (Roest and Srivastava, 1989).

The opening of the Labrador Sea did not produce any deep-water pathways to the Arctic Ocean and as such, the Arctic Ocean has been relatively isolated from global circulation during most of its geological history (Moran et al., 2006). It was a land-locked basin from its formation in the early Cretaceous to the Oligocene (Kristoffersen, 1990). Initial stretching between the Lomonosov Ridge, which moves as a part of the North American plate, and Eurasia, began at 60 Ma (Srivastava and Tapscott, 1986) and formed the Eurasia Basin. Vogt et al. (1979) assume that during the time of plate reorganisation the volcanic Morris Jesup Rise and Yermak Plateau were formed at the triple junction between Eurasia, Greenland and North America. About 4 Myr later (chron 25, 56 Ma), initial seafloor spreading in the Eurasia Basin started between the Lomonosov Ridge and the Barents Shelf. During this time, the tectonic regime between North America and Eurasia changed from trans-tensional to extensional, and the regime between Greenland and Svalbard, from strike-slip to transpressional (Srivastava and Tapscott, 1986). Since seafloor spreading ceased in the Labrador Sea, the motion between Greenland and Svalbard changed to oblique spreading (Talwani and Eldholm, 1977). This change initiated seafloor spreading between Greenland

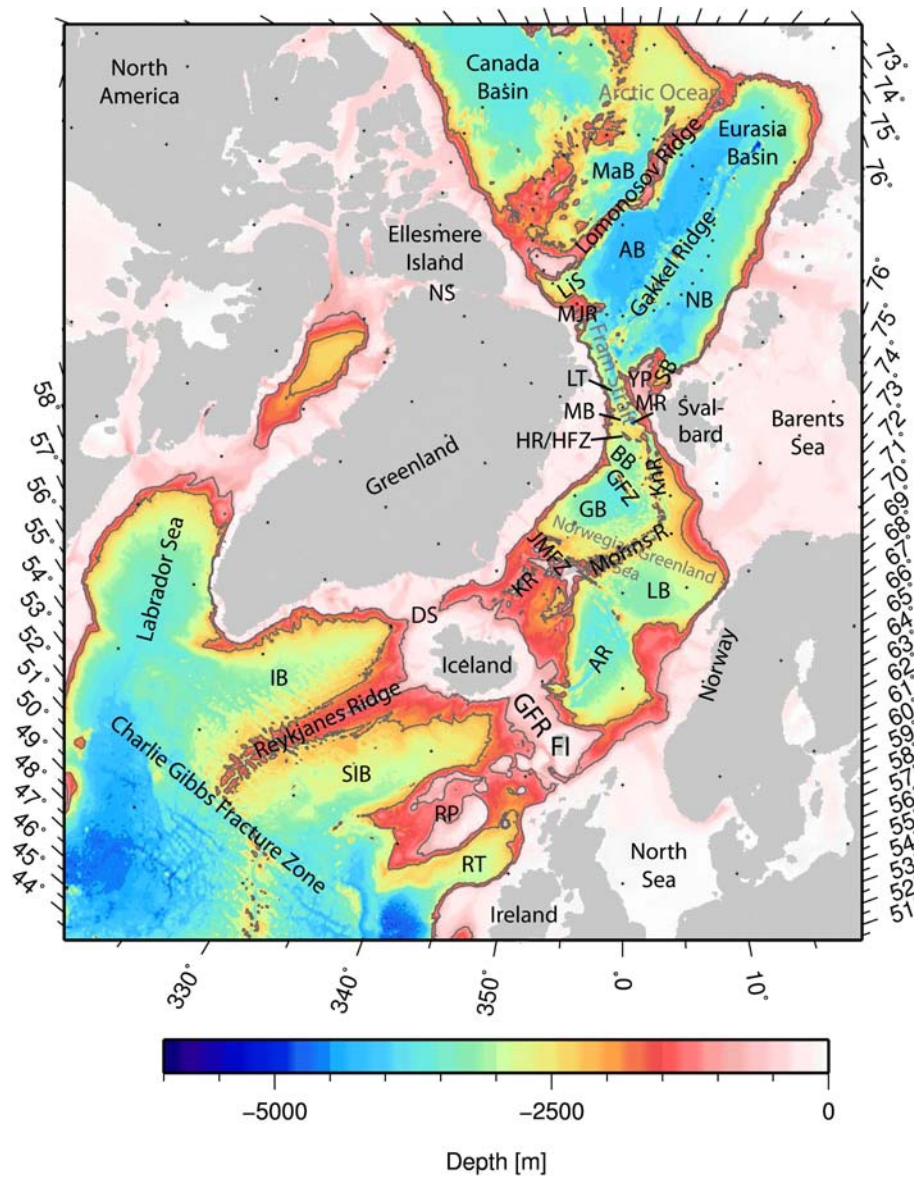


Figure 6.1: Bathymetry map of the international bathymetric chart of the Arctic Ocean (IBCAO) (Jakobsson et al., 2001). The grey lines show the 1000 m and 2000 m bathymetric contour lines. AB: Amundsen Basin, AR: Aegir Ridge, BB: Boreas Basin, DS: Denmark Strait, FI: Faeroe Islands, GB: Greenland Basin, GFR: Greenland-Faeroe Ridge, GFZ: Greenland Fracture Zone, HR/HFZ: Hovgård Ridge/Hovgård Fracture Zone, IB: Irminger Basin, JMFZ: Jan Mayen Fracture Zone, KnR: Knipovich Ridge, KR: Kolbeinsey Ridge, LB: Lofoten Basin, LiS: Lincoln Sea, LT: Lena Trough, MB: Molloy Basin, MaB: Makarov Basin, MJR: Morris Jesup Rise, MR: Molloy Ridge, NB: Nansen Basin, NS: Nares Strait, RP: Rockall Plateau, RT: Rockall Trough, SB: Sophia Basin, SIB: South Iceland Basin, YP: Yermak Plateau

and Svalbard along the Knipovich Ridge (Srivastava and Tapscott, 1986).

The Morris Jesup Rise and the Yermak Plateau began to separate by seafloor spreading around chron 13 (33 Ma) (Feden et al., 1979). The Yermak Plateau may have a composite origin. The northernmost basement block is of volcanic origin formed during the final separation (Jokat et al., 2008; Jackson et al., 1984). The structures in the north east have partly formed during Early Cenozoic rifting of the Lomonosov Ridge. The oldest sediments in the grabens of the Yermak Plateau might be about 35 Myr old. Jokat et al. (2008) assume, that the deep basins in-between the basement highs of the northwestern Yermak Plateau may have allowed a first limited water exchange between the Arctic Ocean and the North Atlantic before the opening of the Fram Strait.

The timing for the opening of a deep-water connection through the Fram Strait is speculative. Srivastava and Tapscott (1986) suggest that a shallow water connection between the Arctic Ocean and the North Atlantic formed between 15 Ma and 10 Ma, but they note that the corridor of oceanic crust between Greenland and Svalbard was not wide enough until 7.5 Ma to 5 Ma to allow deep-water circulation. Kristofferson (1990) assumed a shallow water connection by late Oligocene. This passage way deepened to about 2 km until middle Miocene. Jakobsson et al. (2007) found evidence for a ventilated Arctic Ocean from 17.5 Ma by analysing a sediment core from the crest of the Lomonosov Ridge and relates this result to the opening of the Fram Strait. The transition from a land-locked and poorly ventilated sea, to a ventilated sea, started at 18.2 Ma and lasted 0.7 Myr. Jakobsson et al. (2007) argue that the deep-water circulation probably changed due to changes in sea level. However, from 17.5 Ma the Fram Strait deepened and sea level changes were no longer significant.

Extension in the Eurasia Basin propagated southward and northward in the Norwegian-Greenland Sea. Two additional basins between Greenland and Eurasia formed: (i) the Molloy Basin at 21 Ma and (ii) the Boreas Basin at 33 Ma (Eldholm et al., 1994). The Hovgård Ridge (Myhre et al., 1982) was rifted from the Svalbard margin around 36 Ma (Figure 6.1) and remains as a continental fragment located between the Molloy and Boreas basins along the Hovgård Fracture Zone.

The Greenland-Faeroe Ridge (Figure 6.1) formed as a result of excessive volcanism from the Iceland Hotspot. Simultaneously seafloor spreading started between Greenland and the Faeroe Islands, which are assumed to be underlain by continental crust (Bott et al., 1976). The Greenland-Faeroe Ridge is a shallower barrier than the Fram Strait and therefore the circulation between the Arctic Ocean and the northern North Atlantic is limited to the Norwegian-Greenland Sea. Wright and Miller (1996) propose that a 0.5–0.9 km deep gateway across the Greenland-Faeroe Ridge controlled the deep-water exchange between the North Atlantic and the Arctic Ocean. This gateway may have repeatedly opened and closed in response to the pulsating Iceland hotspot, with initiation of the strong overflow of deep-water between 19 Ma and 15 Ma.

Various existing tectonic reconstructions for the northern North Atlantic and the Arctic Ocean are based on magnetic, bathymetric, gravity and core data (Sclater et al., 1977; Srivastava and Tapscott, 1986; Kristoffersen, 1990; Wold, 1995). Depth to the oceanic basement can be calculated from these tectonic reconstructions, but the detailed evolution

of the seafloor depth (including sedimentation) requires more information. For example, a model of palaeo-water depth is required to determine the timing of an initial deep-water exchange. Therefore, the sediment loads, sediment stratigraphy, -lithology and basement depth should be known in order to create a palaeobathymetric model and reconstruction. Such a palaeobathymetric reconstruction was compiled by Wold (1995), for the area south of the Jan Mayen Fracture Zone to the Charlie Gibbs Fracture (Figure 6.1) Zone.

This study contributes to this previous work and presents a palaeobathymetric reconstruction for the Norwegian-Greenland Sea and the adjacent basins up to the Arctic Ocean. The reconstruction incorporates the sediment load, the sediment stratigraphy and lithology. Basement depth is calculated from a new tectonic model, derived from newly acquired magnetic and seismic data (Figures 6.2, 6.4).

6.3 Data base

6.3.1 Bathymetry

The present-day water depth is taken from the International Bathymetric Chart of the Arctic Ocean (IBCAO) (Jakobsson et al., 2001) and the ETOPO2v2 grid (NGDC, 2006) (Figure 6.1).

The bathymetric data show the present-day position of the spreading axes of the Reykjanes Ridge, Aegir Ridge, Kolbeinsey Ridge, Mohns Ridge, Knipovich Ridge, Molloy Ridge and the Gakkel Ridge (Figure 6.1). The northern North Atlantic is characterized by numerous fracture zones, such as the Greenland-Faeroe Ridge, Jan Mayen Fracture Zone, Greenland Fracture Zone and the Hovgård Ridge. The general water depth of less than 2000 m is significantly shallower than the oceanic basins.

6.3.2 Magnetism and age model

Verhoef et al. (1996) compiled Gammaa-5 magnetic data for the northern North Atlantic and the Arctic Ocean, shown in figure 6.2 and 6.3. We improved this magnetic grid by including newly acquired aeromagnetic data between 76.5°N and 85°N, gathered by the Alfred Wegener Institute (Leinweber, 2006; Ehlers and Jokat, 2009) (Figure 6.2 and 6.3, dashed red line) As a result a more detailed anomaly pattern for the Boreas and Molloy basins and the Lena Trough can be identified.

The seafloor spreading model for the region south of the Jan Mayen Fracture Zone is based on the rifting model of Wold (1995). In the southern part of the Eurasia Basin, magnetic isochrones from Brozena et al. (2003) are used. Their identification is restricted to 11 isochrons between chron 5 and 25.

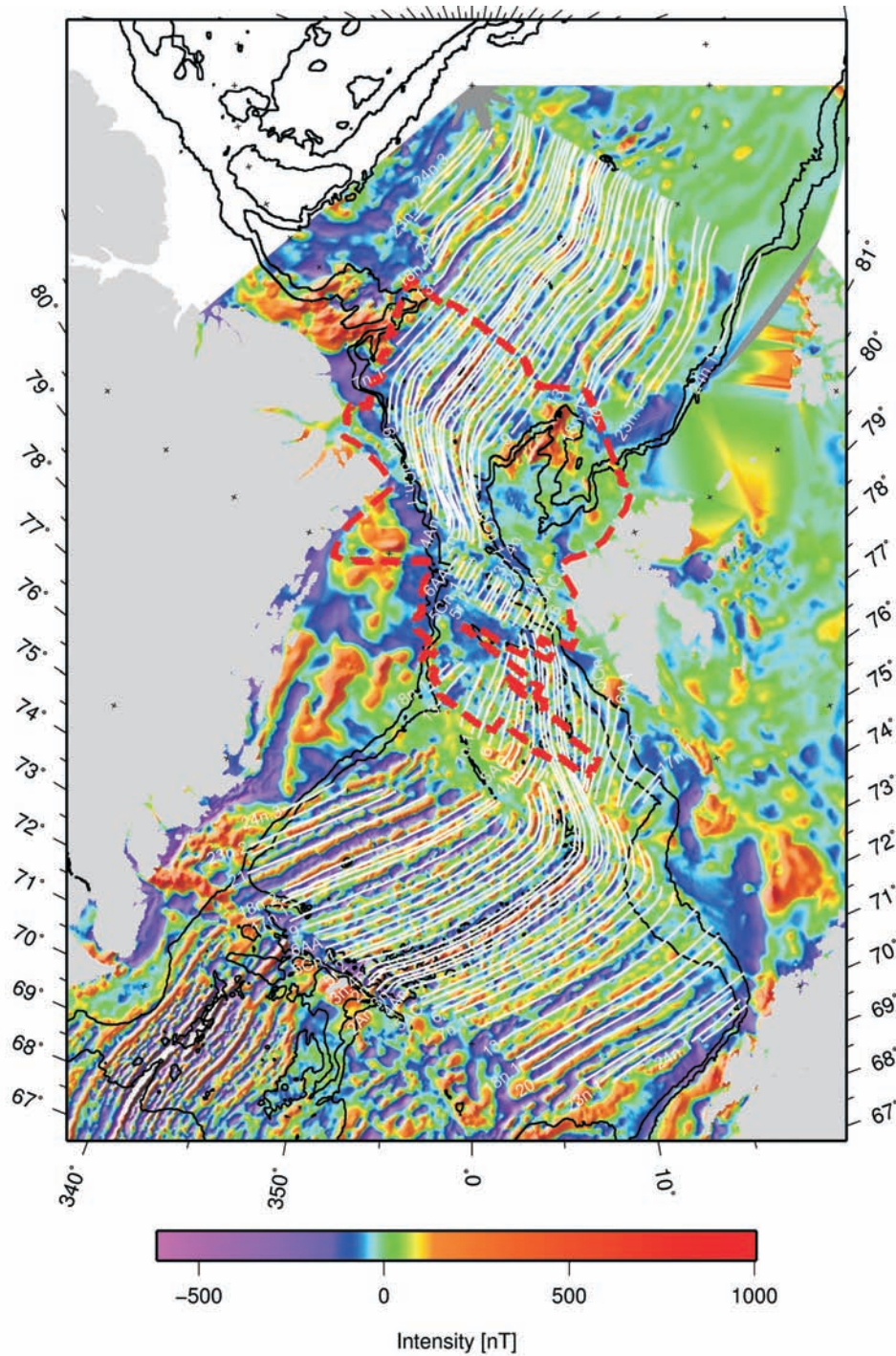


Figure 6.2: Age model of the northern North Atlantic and the Arctic Ocean. The white lines illustrate the re-identified magnetic anomalies labelled after Gradstein et al. (2004) (Table 6.2). The dashed red shows the limits of the new magnetic data grid for the Fram Strait and adjacent areas (Leinweber, 2006). Additional magnetic data is derived from the GAMMAA5 grid (Verhoef et al., 1996)

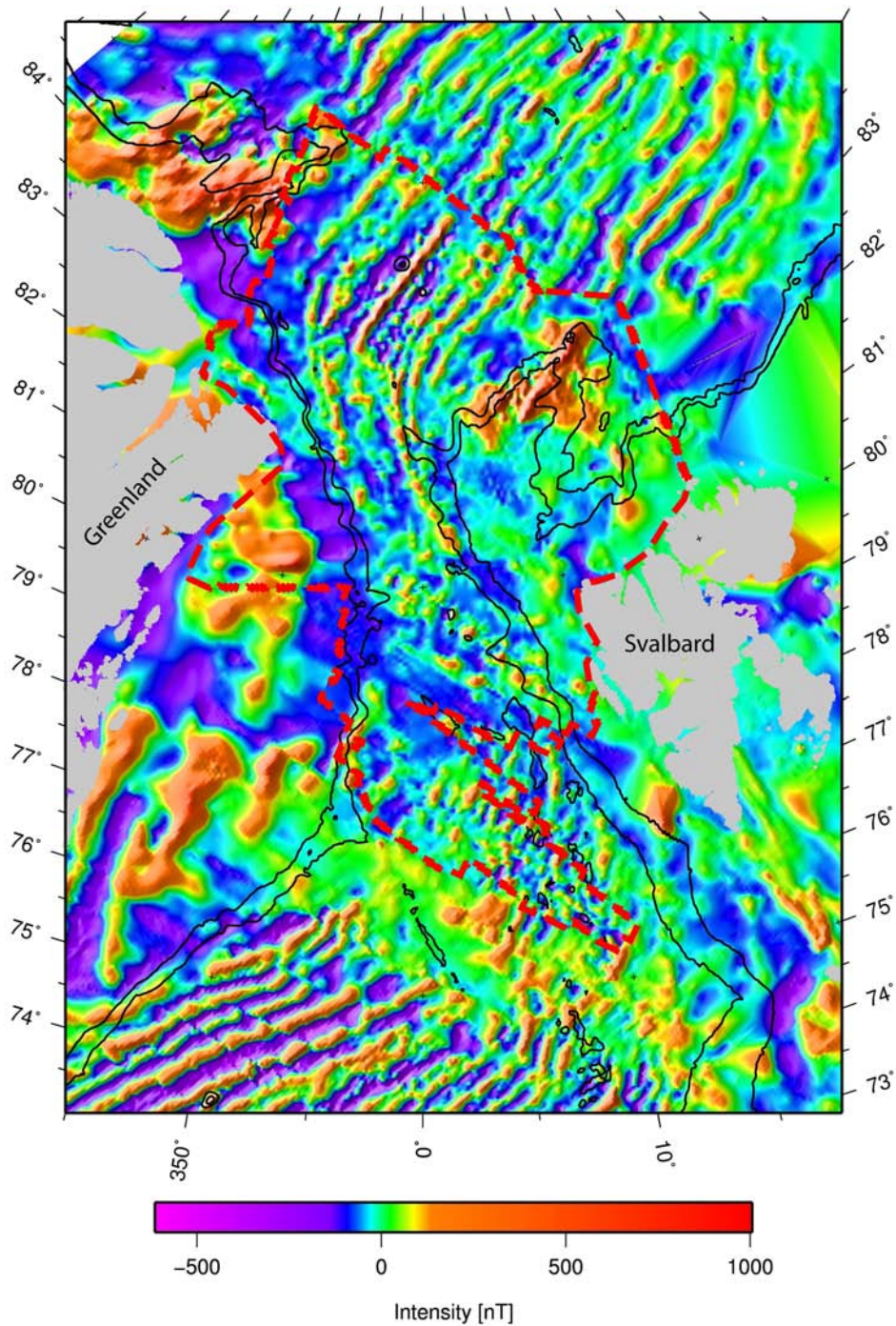


Figure 6.3: Merging of the Verhoef et al. (1996) gridded magnetic data and the AWI magnetic database (dashed red line, Leinweber (2006)) for the Fram Strait and adjacent areas.

6.3.3 Seismic data

Seismic reflection data provide detailed information about sediment thickness, depth to basement, crustal thickness and -structure, and can be a useful tool to define the continent-oceanic crust transition zone. Wold (1995) used various single channel seismic reflection profiles for his model between the Charlie Gibbs and the Jan Mayen Fracture zones. The stratigraphic-lithologic compilation of Wold (1995) is based on DSDP/ODP boreholes.

In this study, we compile seismic reflection and refraction data in the north of the Jan Mayen Fracture Zone, the Norwegian-Greenland Sea, the Fram Strait and in the Arctic Ocean (Figure 6.4). These datasets are shown in figure 6.4 and are listed in table 6.1. The new seismic reflection profiles, gathered by the Alfred Wegener Institute between 2001 and 2004, offer the first detailed sediment information for the Greenland, Boreas and Molloy basins, as well as the Lena Trough, Yermak Plateau, Nansen- and Amundsen basins and their adjacent shelf areas. These datasets are supplemented by existing seismic reflection and refraction data on the Spitsbergen shelf, Barents Sea shelf and the Norwegian shelf. A lack of data still exists in the Arctic Ocean, particularly in the northern Lena Trough and in the younger parts of the Norwegian-Greenland Sea, close to the Mohns Ridge.

6.4 Data and Methods

6.4.1 Magnetic data and the age of oceanic crust

We combined the Verhoef et al. (1996) gridded magnetic data with the AWI magnetic database (Leinweber, 2006; Ehlers and Jokat, 2009) and re-interpreted the magnetic anomalies (Figure 6.3). The zero crossings of the anomalies were picked parallel to the oceanic ridge axis (Figure 6.2). The identification of Brozena et al. (2003) in the southern Eurasia Basin was used as reference and topographic effects were excluded by a comparison to the bathymetric data to avoid an impact on the analysis. Magnetic modelling was used to estimate the ages of the anomalies (Ehlers and Jokat, 2009), based on the Geological Time Scale 2004 (Gradstein et al., 2004). The existing poles of rotation (Gaina et al, 2002; Srivastava, 1985) and the age of the oceanic crust (this study) provide detailed rotation angles (table 6.2) for the newly interpreted magnetic anomalies. Special attention was paid to keep the picked anomalies congruent with the rotation of the coeval oceanic crust which evolved at a mid ocean ridge at the same time. These rotation angles form the basis for the reconstruction of the plate tectonic evolution within the palaeobathymetric model. The interpolation of the rotation angles provides additional angles to specific corresponding ages.

6.4.2 Seismic data

The seismic reflection data in the Greenland Basin (Berger and Jokat, 2008), Boreas Basin and Molloy Basin (Berger and Jokat, 2009) are correlated to ODP boreholes 909 and 913 (Myhre et al., 1995) in Berger and Jokat (2008) and Berger and Jokat (2009). The

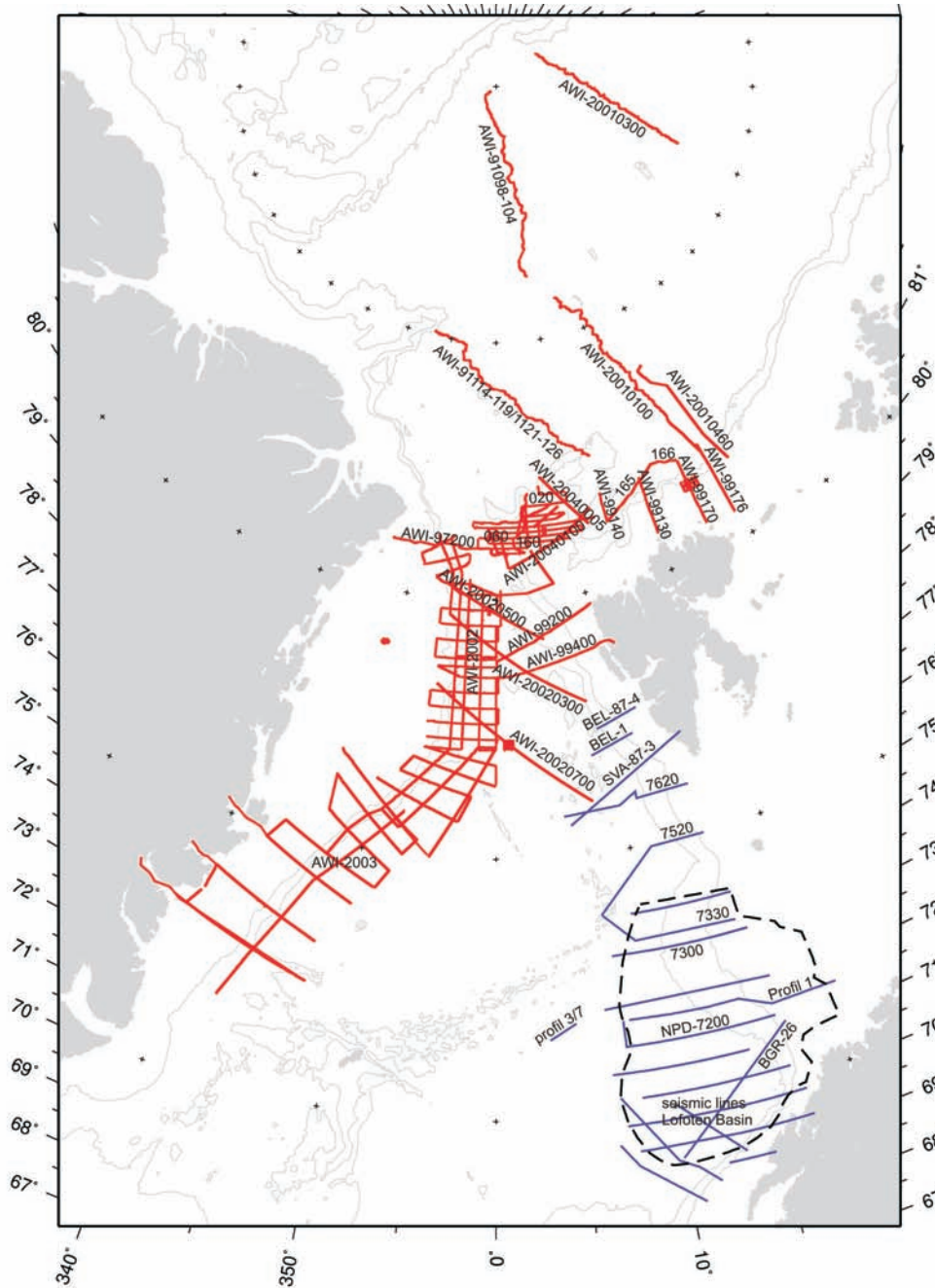


Figure 6.4: Available seismic reflection and refraction data for the Norwegian-Greenland Sea, the Molloy and Boreas basins, the Lena Trough, the Yermak Plateau and the Eurasian Basin. Information about the profiles is listed in table 6.1

profile	information					references
	rfl/ rfr	crustal thick- ness	base- ment depth	sediment thick- ness	sediment ages [Ma]	
profile 3	rfr	x	x	x		Klingelhöfer et al. (2000)
profile 7	rfr	x	x	x		Klingelhöfer et al. (2000)
AWI-99200	rfr	x	x	x		Czuba et al. (2000)
AWI-99400	rfr	x	x	x		Ritzmann et al. (2004)
BEL-87-4	rfl					Solheim et al. (1998)
SVA-87-3	rfl		x	x	0.44, 1, 2.3	Ljones et al. (2004)
	rfr	x				Ljones et al. (2004)
AWI-91098– 91104	rfl		x	x		Weigelt and Jokat (2001)
AWI-91114– 91126	rfl		x	x		Weigelt and Jokat (2001)
AWI-20010100/ 300/460	rfl		x	x		Jokat and Micksch (2004)
AWI-2004005/ 020/060/100/160	rfl		x	x	2.6	personal communi- cation Geissler
AWI-99130/140/ 165/166/170/176	rfl		x	x	2.6, 35	personal communi- cation Geissler
NPD- POLARN17	rfl		x	x	2.6, 35	personal communi- cation Geissler
AWI-2002 (grid)	rfl		x	x	3, 5, 15	Berger and Jokat (2009)
AWI-2003 (grid)	rfl		x	x	15	Berger and Jokat (2008)
AWI-97260	rfr	x	x	x		Ritzmann (2004)
BEL-1	rfl		x	x	0.44, 1, 2.3	Faleide et al. (1996)
7620	rfl		x	x	0.44, 1, 2.3	Faleide et al. (1996)
seismic lines Lofoten Basin (grid)	rfl		x	x	0.44, 1, 2.3	Fiedler and Faleide (1996)
7520	rfl		x	x	0.44, 1, 2.3	Faleide et al. (1996)
7330	rfl		x	x	0.44, 1, 2.3	Faleide et al. (1996)
NPD-7300	rfl		x	x	0.44, 1, 2.3	Fiedler and Faleide (1996)
NPD-7200	rfl		x	x	0.44, 1, 2.3	Fiedler and Faleide (1996)
Profil 1	rfl		x	x	0.44, 1, 2.3	Faleide et al. (1996)
BGR-26	rfl		x	x	0.44, 1, 2.3	Fiedler and Faleide (1996)
Crustal transact 1–2	rfr	x	x	x	2.3	Tsikalas et al. (2005)

Table 6.1: Available seismic reflection (rfl) and refraction (rfr) data, information content about crustal thickness, basement depth, sediment thickness and sediment age correlations of profiles and references

stratigraphy of seismic data in the Lena Trough and Yermak Plateau were acquired by Geissler and Jokat (2004), Jokat et al. (2008) and Geissler (personal communication). The vertical axes of the profiles along the Yermak Plateau are only available in two way travel time, and were first converted into depth in meters by applying a general velocity-depth function after Geissler (2008, personal communication) listed below:

$$velocity(time) = -2.5353(time/2)^3 + 6.0939(time/2)^2 - 1.9622(time/2) + 1.8983 \quad (6.1)$$

An average velocity for the sediment load was assumed. The time-depth conversion for the profiles along the Norwegian Shelf was calculated according to the sediment velocity distribution of Ljones et al. (2004).

The stratigraphic ages of the sediments are shown in table 6.1. However, for seismic reflection profiles without sediment ages definition we assume that the youngest sediments are present-day accumulations and the bottom sediments of similar age as the underlying oceanic crust. The sediment ages are interpolated linearly between the top and bottom layers or between two correlated horizons. It was also assumed that the sedimentation rate between two correlated sediment layers is constant.

6.4.3 Subsidence analysis

In this study, we assume oceanic crust subsidence according to the depth-age relationship for the thermal subsidence $d_w = 2.5 + 0.35\sqrt{age}$ (2) of Parsons and Sclater (1977) and according to the sediment load S_s . The thermal subsidence d_w was therefore adjusted for the sediment load (Allen and Allen, 1990) in order to yield the theoretical basement depth d_t : $d_t = d_w + S_s$ (3).

We farther assume that thermal subsidence of the continental crust and the crust beneath the Morris Jesup Rise as well as the Yermak Plateau has a low influence on the palaeo-basement depths and therefore, only sediment accumulation was considered. The described development of the Yermak Plateau is taken into account. The age of the oldest deposited sediments is set to 450 Myr for the stretched continental segment and to 35 Myr for the northernmost volcanic segment.

6.4.4 Continent ocean transition zone

For the palaeobathymetric reconstruction, a distinction between continental and oceanic crust is important because different crustal types vary in crustal density and subsidence characteristics. This is especially evident along passive margins with differential stretching during formation, where the definition of the transition zone is difficult (Wold, 1995). The seismic refraction profiles show crustal thickness for the continental- and oceanic crust. Table 6.1 lists the seismic refraction profiles used to estimate the position of the continent ocean transition zone. Talwani and Eldholm (1973) proposed that a gravity gradient might be diagnostic for the location of the continent-ocean boundary at rifted passive margins.

Engen et al. (2008) propose that high Bouguer gradients are observed across sheared margin segments whereas lower gradients are shown across rifted margins. Therefore, gradients in gravity data (Arctic Gravity Project, 2006) were used to locate the continent-ocean boundary in regions that are not covered by refraction seismic data.

In addition, the gravity data of the Arctic Gravity Project (2006) and the IBCAO bathymetry data (Jakobsson et al., 2001) were also used to identify the continent ocean transition zone, since gravity highs are coincident with the shelf break. These results correlate well with the 1000 m and 2000 m bathymetry contour lines (Figure 6.1).

6.4.5 Palaeobathymetric reconstructions

The palaeobathymetric reconstruction is based on the method of backstripping introduced by Steckler and Watts (1978). The purpose of such a reconstruction is to calculate the seafloor- and basement depth, and the sediment load for a chosen age of reconstruction.

The kinematic model of this palaeobathymetric reconstruction is based on the rotation parameters listed in table 6.2. Note that the position of North America is fixed. The model describes the movement of the continents and the timing of the evolution of oceanic crust.

The present day basement-depths and sediment thicknesses are derived from the seismic reflection and refraction data (table 6.1). The seismic data north of the Jan Mayen Fracture Zone are attached to grid cells with a size of $0.5^\circ \times 0.5^\circ$ in latitude and longitude. In addition to seafloor and basement depth, seismic stratigraphic data are provided for each grid cell. Up to three sediment layers with corresponding ages from borehole data are also included. Linear sedimentation is assumed for grid cells with no stratigraphic information, and for sediment layers with no detailed age correlation. The type of crust is noted for each grid cell in order to calculate the past sediment loads. The past depth of oceanic crust depends on thermal subsidence and the sediment load.

The palaeobathymetric reconstructions are calculated in the program packet “BalPal v. 0.9” (Wold, 1995). “BalPal v. 0.9” is written in the C-programming language and works with gridded data. For this study, the software was modified to use a variable grid size for the palaeobathymetric reconstruction. The resolution was adapted to the density of seismic lines and to the dimensions of the investigation area (Figure 6.5).

Sediments younger than the age of reconstruction are removed from each grid cell. The remaining sediments are then decompacted in order to derive the overall thickness of all the sediment layers for the age of reconstruction. The effect of thermal subsidence was removed and the sea level changed to its position as at the age of reconstruction (Haq et al., 1987). We chose the sea level curve of Haq et al. (1987) because it is based on world wide data. Finally the backstripping program brings the entire grid cell into isostatic equilibrium. Knowing the depth of compensation, the mass for a 1 m^2 wide column of mantle, crust, sediments and water is estimated. The Airy-type isostasy mass has to be constant after decompacting the sediments, removing the effect of thermal subsidence and changing the sea level.

The data presented in this study consist of 668 cells compiled by Wold (1995), between the Charlie Gibbs and the Jan Mayen fracture zones in a $1^\circ \times 1^\circ$ latitude-longitude grid

poles of rotation: Eurasia–North America					
anomaly	longitude[°]	latitude[°]	reference	angle[°] (this study)	age[Ma] (GTS2004)
2n	132.98	66.44	Gaina (2002)	-0.31	1.945
2An.3n	132.98	66.44	Gaina (2002)	-0.69	3.33
3n.4n	132.98	66.44	Gaina (2002)	-1.05	5.235
4An	132.98	66.44	Gaina (2002)	-1.79	8.769
5r.2	132.98	66.44	Gaina (2002)	-2.6	11.614
5AC	132.98	66.44	Gaina (2002)	-3.03	13.734
5Cn.1	132.98	66.44	Gaina (2002)	-3.61	16.26
6	132.59	68.91	Gaina (2002)	-4.43	18.748
6AA	132.59	68.91	Gaina (2002)	-5.15	21.159
7n.1	132.59	68.91	Gaina (2002)	-5.92	24.044
9	132.59	68.91	Gaina (2002)	-6.95	27.826
13	131.53	68.22	Gaina (2002)	-8.14	33.266
17n.1	131.53	68.22	Gaina (2002)	-9.1	37.235
18n.1	131.53	68.22	Gaina (2002)	-9.59	38.032
18n.2	131.53	68.22	Gaina (2002)	-10.01	39.464
20	131.53	68.22	Gaina (2002)	-10.45	41.59
21	138.44	65.38	Gaina (2002)	-12.72	47.235
23n.1	138.44	65.38	Gaina (2002)	-13.57	50.73
23n.2	138.44	65.38	Gaina (2002)	-14.18	51.901
24n.1	144.26	63.07	Gaina (2002)	-14.62	52.648
24n.3	144.26	63.07	Gaina (2002)	-15.26	53.808

poles of rotation: Greenland–North America					
anomaly	longitude[°]	latitude[°]	reference	angle[°] (this study)	age[Ma] (GTS2004)
13	-84	62.8	Srivastava (1984)	-0.01	33.266
17n.1	-84	62.8	Srivastava (1984)	-0.89	37.235
18n.1	-84	62.8	Srivastava (1984)	-1.09	38.032
18n.2	-84	62.8	Srivastava (1984)	-1.43	39.464
20	-84	62.8	Srivastava (1984)	-1.91	41.59
21	-134.35	39.29	Srivastava (1984)	-1.0	47.235
23n.1	-134.35	39.29	Srivastava (1984)	-1.2	50.73
23n.2	-134.35	39.29	Srivastava (1984)	-1.26	51.901
24n.1	-134.35	39.29	Srivastava (1984)	-1.3	52.648
24n.3	-134.35	39.29	Srivastava (1984)	-1.37	53.808

Table 6.2: Re-identified magnetic anomalies and their corresponding poles of rotation, reference, rotation angle and age after the Geological Time Scale (GTS) 2004 (Gradstein et al., 2004)

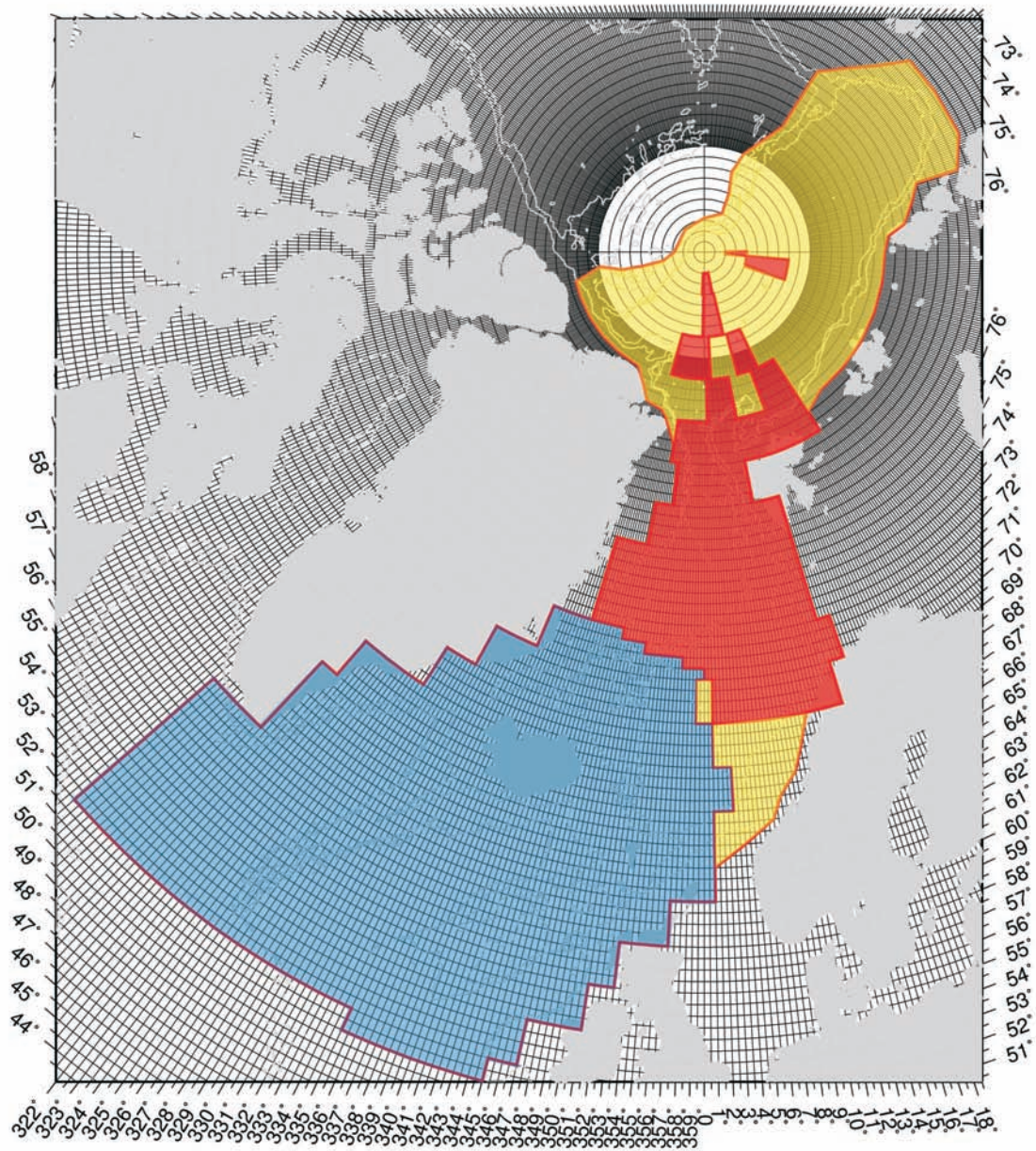


Figure 6.5: Distribution of grid cells for the palaeobathymetric reconstruction. Blue area: data from Wold (1995); red area: data compilation of this study, yellow area: areas without sufficient information, is interpolated due bathymetric data and information of adjacent areas

(Figure 6.5, blue area) and of 1515 grid cells compiled for this study with a grid cell size of $0.5^\circ \times 0.5^\circ$ north of the Jan Mayen Fracture Zone (this study, Figure 6.5, red area).

In our study, the grid cells contain information from the existing data (Lofoten Basin, West Svalbard Shelf) and new data (NE Greenland Shelf, Greenland Basin, Boreas Basin, Molloy Basin, Lena Trough and Yermak Plateau) (table 6.1). This information includes:

- the location and size of the grid cell
- present depth of the seafloor (Jakobsson et al., 2001)
- present sediment thickness (seismic reflection and refraction data (Table 6.1))
- present basement depth (seismic reflection and refraction data (Table 6.1))
- change of sea level for the time of reconstruction (Haq et al. (1987) modified after Gradstein et al. (2004))
- thermal age of the crust (oceanic crust: Brozena et al. (2003); Ehlers and Jokat (2009) this paper; continental crust: 450 Ma)
- age of sedimentary layer (Table 6.1)
- density, mean thickness and compensation depth (compensation depth: 100 km, reference thickness of oceanic crust: 6500 m, density of seawater 1027 kg/m^3 , density of oceanic crust 2900 kg/m^3 , density of continental crust 2850 kg/m^3 and maximal density of asthenosphere 3310 kg/m^3)
- porosity-density relationship for sediments (Wold, 1995)
- continent-ocean-boundary (seismic refraction data (Table 6.1), AGP (2006))

In areas where no seismic data are available, such as the Arctic Ocean (Figure 6.5, yellow area) grid cell results were interpolated using the results of the adjacent grid cells, with available data. A subsidence model of Moore et al. (2006) was used to define the palaeo-water depth for the Lomonosov Ridge.

Lastly the average sediment thicknesses for each investigated basin north of the Jan Mayen Fracture Zone were calculated for all time slices. The results were compared with theoretical curves for the subsidence of an oceanic basin without sediments, and with linear deposited sediments of 1000 m, 2000 m and 3000 m thickness for the present day configuration. The variation of the seafloor depth is presented relative to the present day conditions.

6.5 Results

6.5.1 Magnetism and age model

In the new aeromagnetic and the Gammaa-5 grids, oceanic crust with anomalies caused by seafloor spreading and magnetic areas with low amplitude and long wavelength, are clearly distinguishable (Figure 6.3). The northern Yermak Plateau and the Morris Jesup Rise appear as pronounced positive anomalies. The Sophia and Lincoln Sea basins do not show seafloor spreading anomalies. The magnetic data along the Spitsbergen Trough, Greenland Spitsbergen Sill, Hovgård Ridge, Greenland Fracture Zone and the Jan Mayen Fracture Zone also do not have a clear signal. Furthermore the north western Boreas Basin shows no clear spreading anomalies. In the Norwegian-Greenland Sea the oldest anomalies are identified in the south western Greenland Basin and in the north eastern Lofoten Basin.

The new aeromagnetic data grid allows the first detailed re-identification of magnetic isochrones in the Boreas Basin, the Molloy Basin and the Lena Trough (Ehlers and Jokat, 2009). In addition, the anomalies in the Norwegian-Greenland Sea and in the Eurasia Basin are re-identified in more detail. The white lines in figure 6.2 represent this detailed re-identification of the magnetic isochrones. Re-identification of anomalies in the Eurasia Basin, east of 60°E, was not possible due to the poor data resolution. The re-identified magnetic anomalies have an average separation of 2.5 Myr and are useful to specify the related angles of rotation (table 6.2). We assume an error of about 0.5 Myr.

Figure 6.6 presents the age of oceanic crust in the northern North Atlantic and the Arctic Ocean (Wold, 1995; Brozena et al. 2003; Ehlers and Jokat, 2009; this study). The age model north of the Jan Mayen Fracture Zone, results in an initial opening time of 54 Ma for the Norwegian-Greenland Sea and the Eurasia Basin. The southern Boreas Basin opened at 38 Ma, whereas the connection between the Norwegian-Greenland Sea and the Boreas Basin east of the Greenland Fracture Zone opened at 21 Ma. The Knipovich Ridge and the Mohns Ridge are a continuous ridge system since 5 Ma. In the northern part of the Boreas Basin seafloor spreading started at about 12 Ma. The Molloy Basin developed from 21 Ma in response to the opening of the Eurasia Basin and the northern North Atlantic. It can thus be deduced that the oceanic basin is 9 Myr older than the southern Lena Trough. According to this kinematic model, seafloor spreading between the Yermak Plateau and the Morris Jesup Rise probably started at 28 Ma.

6.5.2 Palaeobathymetric reconstruction

In the palaeobathymetric reconstruction results we present time slices for every five million years which show the geodynamic evolution of the northern North Atlantic and the Arctic Ocean (Figure 6.7). The results are displayed relative to the corresponding sea level of the particular time slice after Haq et al. (1987) according to the Geological Time Scale 2004 (Gradstein et al., 2004). Palaeobathymetric data are also defined for areas without available data (Figure 6.5, yellow areas). The changes of the sea levels are listed in table 6.3. Figure 6.8 shows the calculated basement topography. Only the results for the

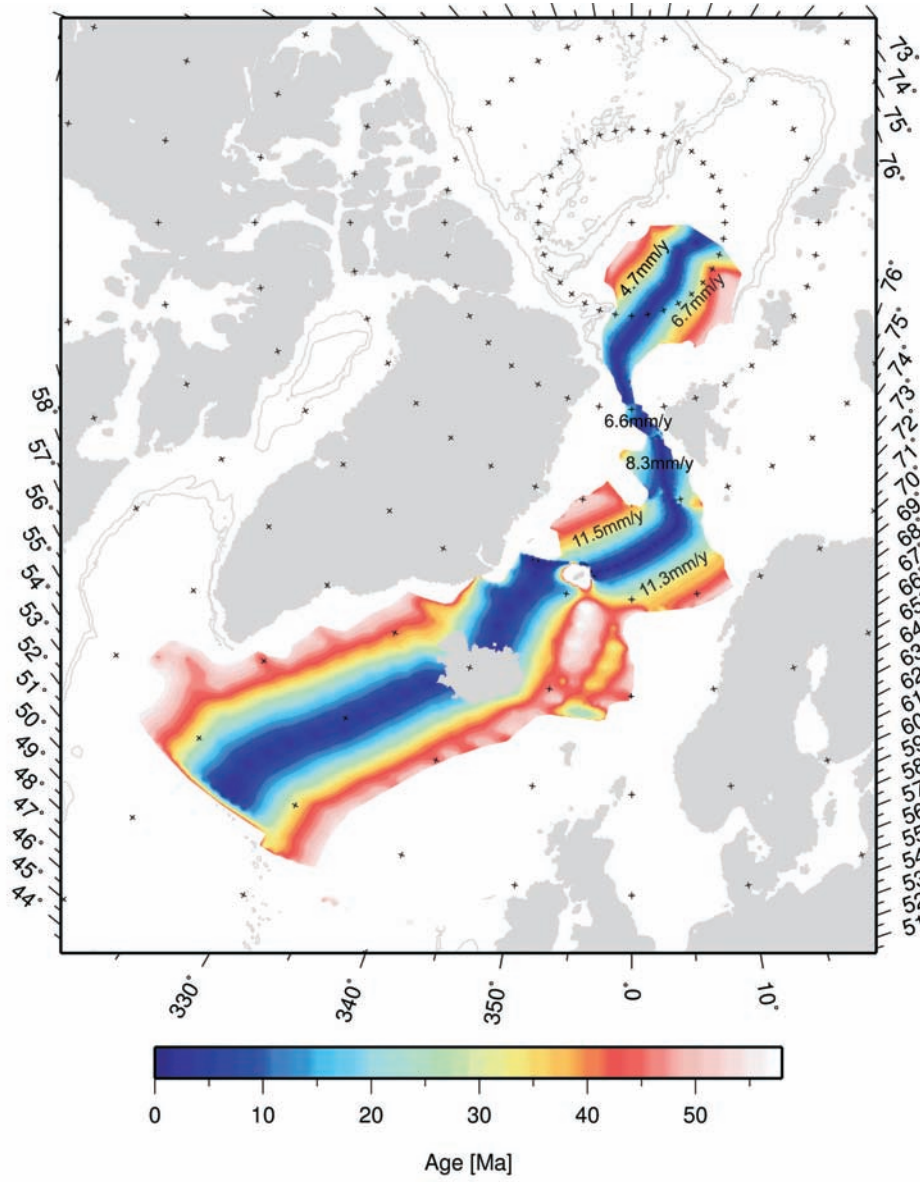


Figure 6.6: Age of oceanic crust for the grid cells with available data. For the area north of the Jan Mayen Fracture Zone, half spreading rates are displayed

available data are displayed here (Figure 6.5, blue and red area). The residual of the basement topography and the seafloor depth, shown in Figure 6.9, represents the decompacted sediment thickness.

age[Ma]	sea level[m]
0	0
5	-57.3
10	-19.1
15	126.9
16	117.6
17	123.3
18	114.9
19	89.1
20	92.9
25	63.4
30	182
35	132.3
40	195.6
45	201.6
50	171.3
55	172.7

Table 6.3: Past sea level for the reconstructed time slices after Haq et al. (1987). The age is modified after the Geological Time Scale 2004 (Gradstein et al., 2004)

Based on the depth-age relationship of Parsons and Sclater (1977) and assuming an inaccuracy of 0.5 Myr for the age model, the depth error can be quantified as circa 180 m for 1 Myr old oceanic crust and circa 25 m for 50 Myr old oceanic crust. Other sources of inaccuracy for the palaeobathymetric reconstruction are the interpolated poles of the rotation angles (table 6.2), depth of the sediment layer and the basement depth derived from the seismic data. The horizontal error for a rotation angle of 0.01° of 55 Myr old crust adds up to 1000 m. The vertical error with respect to the sediment depth is an average of 200 m. These uncertainties are discussed in Berger and Jokat (2008) and Berger and Jokat (2009). Additional palaeobathymetric model errors are introduced through the parameters in the “BalPal v.0.9” software program. It should also be noted that the modelled conditions only consider thermal subsidence and sediment loads, crustal extensions and flexural rigidity are not included.. Uplifts or subsidence of the adjacent land masses and shelf areas which probably influence the palaeobathymetric development of the modelled area, are also not taken into account.

The grid based calculation of the palaeobathymetric model, calculated basement depth and sediment thickness, reduce the resolution of the seafloor and basement depth data. Small structures such as rough basement topography caused by ultra-slow spreading north of the Greenland Fracture Zone (Ehlers and Jokat, 2009) are not resolvable. The distance

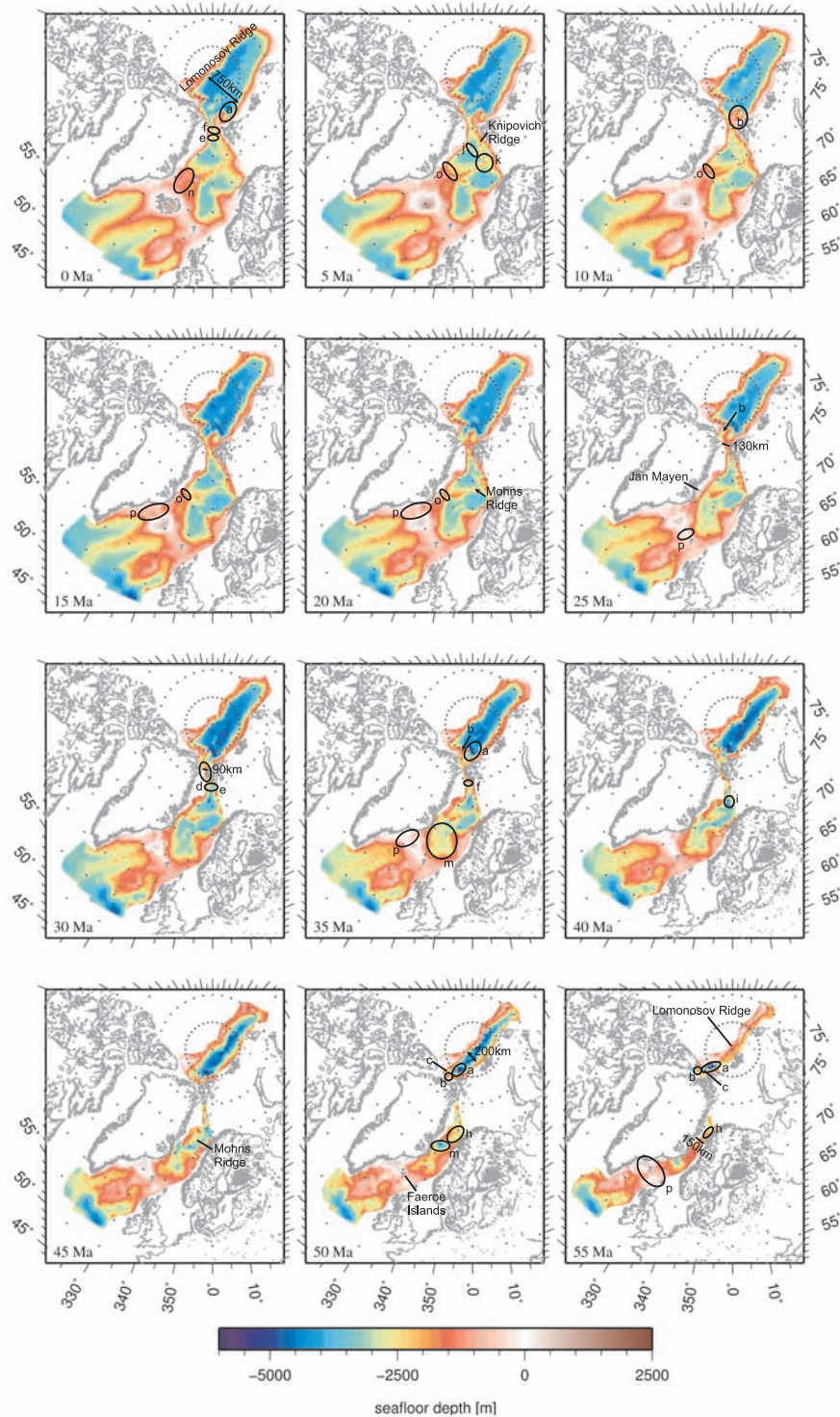


Figure 6.7: Time slices of 5 Myr steps from today backwards to 55 Ma show the results of the palaeobathymetric modelling for the seafloor depth, which is presented relative to the past sea level (Table 6.3)

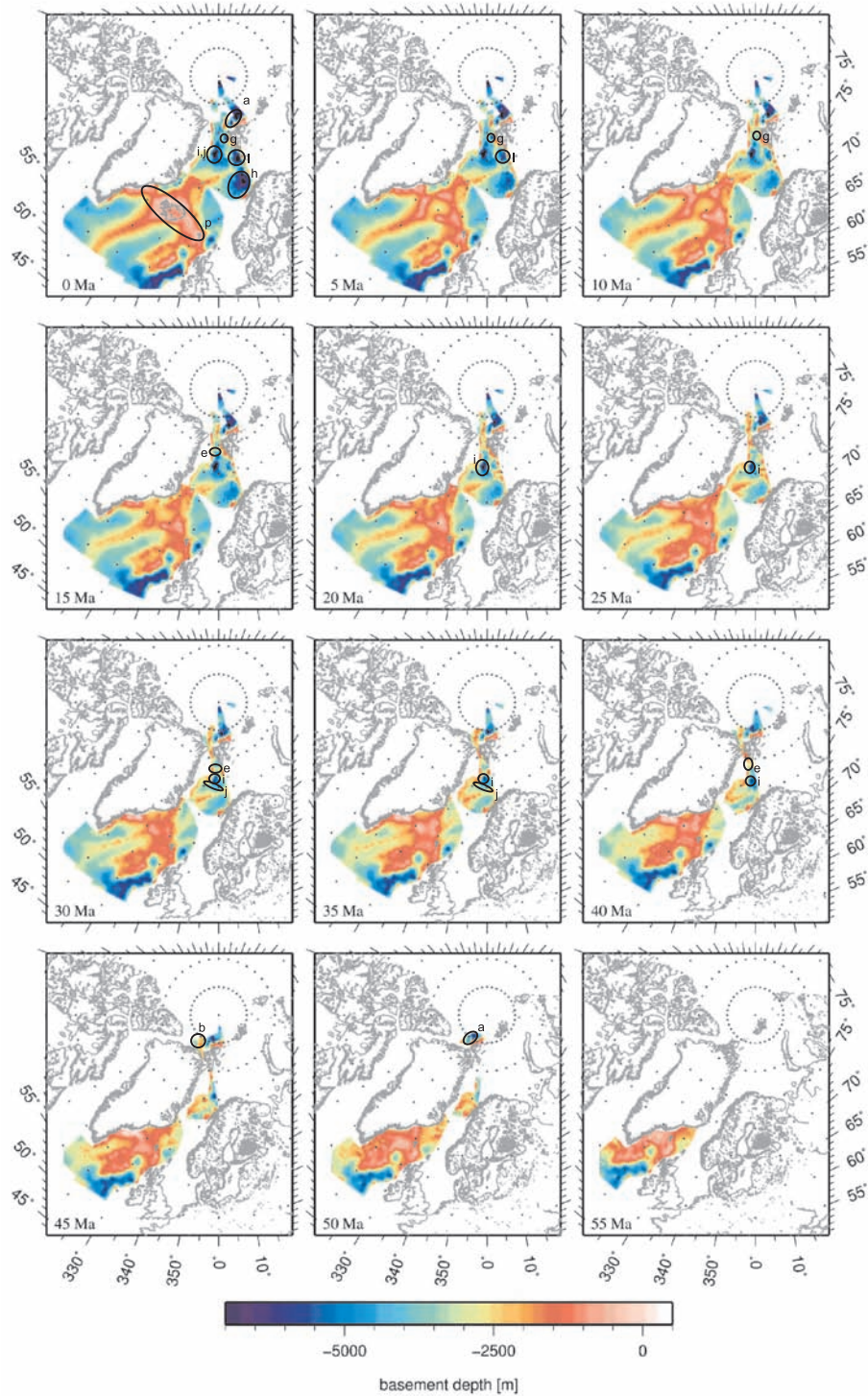


Figure 6.8: Time slices of 5 Myr steps from today backwards to 55 Ma show the results of the palaeobathymetric modelling for the basement depth, which is presented relative to the past sea level (Table 6.3)

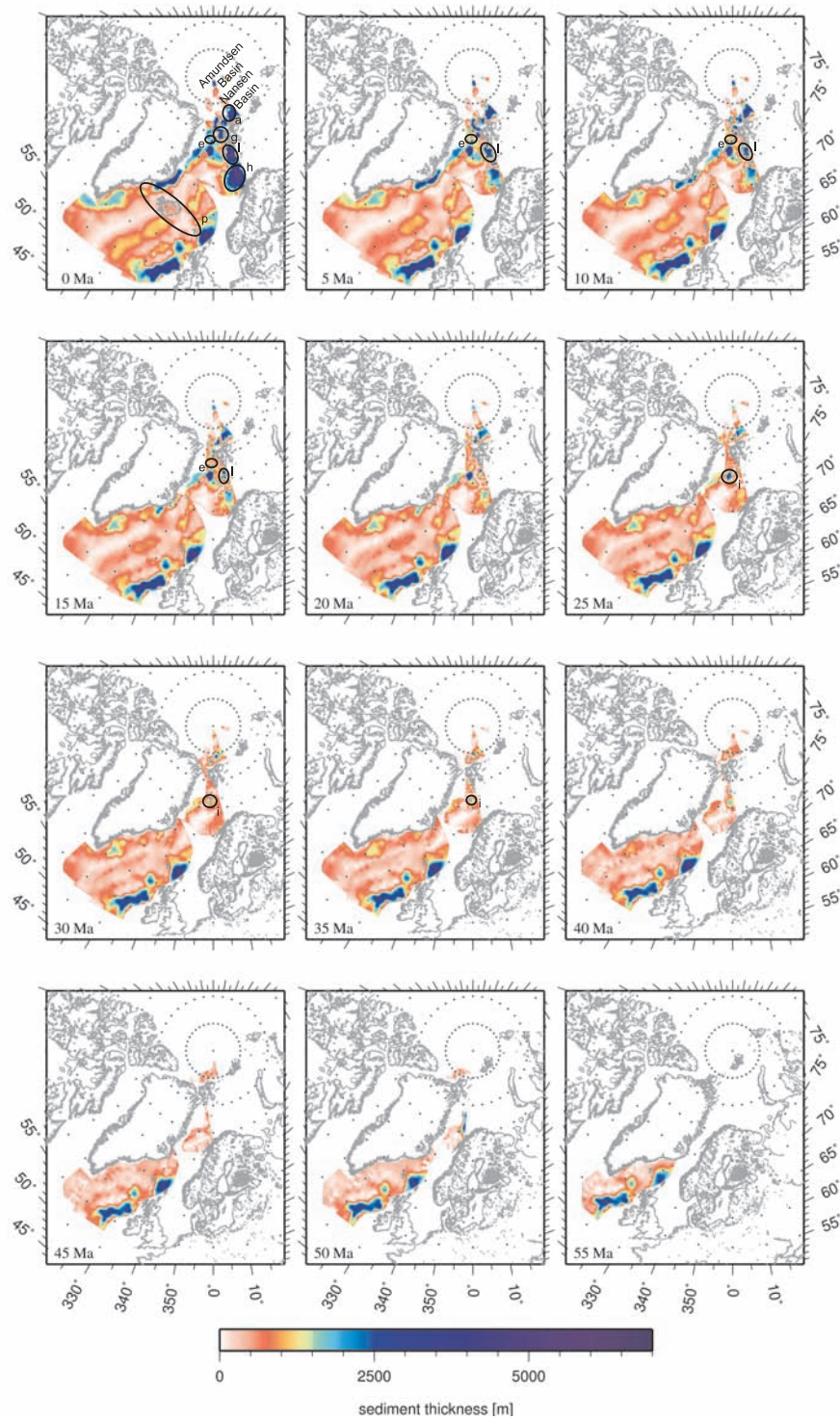


Figure 6.9: Time slices of 5 Myr steps from today backwards to 55 Ma show the results of the palaeobathymetric modelling for the sediment thickness

between the mid points of adjacent grid cells are about 20 km for the most southern part and 4 km for the very northern part, along latitude. In longitude, the distance results in about 110 km in the south (Figure 6.5, blue coloured area) and 55 km (Figure 6.5, red coloured area) in the north.

In the following section, the results of the calculated bathymetry, basement depth and sediment thickness are described according to region and within each region, described according to age.

Lomonosov Ridge, Eurasia Basin, Yermak Plateau and Lena Trough

55 Ma: The time slice of 55 Ma (Figure 6.7) displays the palaeobathymetric situation before the initial seafloor spreading in the Arctic Ocean. Parts of the Lomonosov Ridge lay up to 500 m above the sea level (Moore et al., 2006). The ridge forms a shallow barrier between the young Amundsen Basin and the Makarov Basin.

Between the Nares Strait and the Arctic Ocean the seafloor rises to about 1500 m water depth. In the remaining Arctic Ocean, the Eurasia shelf is still connected to the Lomonosov Ridge. The basin between the northern tip of Ellesmere Island and Svalbard (Figure 6.7, 55 Ma, c) forms the subsequent Sophia Basin.

50 Ma: The Eurasia Basin is up to 200 km wide (Figure 6.7, 50 Ma). At 30°W 85.5°N, the basement between Svalbard and the Lomonosov Ridge is up to 6700 m deep (Figure 6.8, 50 Ma, a). The area north of Ellesmere Island is separated from the Lomonosov Ridge and forms a plateau about 1700 m below sea level (Figure 6.7, 50 Ma, b). A 3000 m deep basin (the Lincoln Sea) developed west of the plateau (Figure 6.7, 50 Ma, c).

45 Ma: The basement of the Yermak Plateau (Figure 6.8, 45 Ma, b) has an average depth of 2000 m, and deepens slightly with time.

35 Ma: The south western Nansen Basin is more than 5000 m deep, reaching maximum water depth since its opening (Figure 6.7, 35 Ma, a). The first evidence of a separation of the Yermak Plateau and the Morris Jesup Rise is observed at 20°W (Figure 6.7, 35 Ma, b).

30 Ma: The connection between the Arctic Ocean and the northern North Atlantic is blocked by shallower seafloor (a less than 1500 m deep), shown in figure 6.10 (30 Ma, d). The distance between Greenland and Svalbard increases from 90 km at 30 Ma, to 130 km at 25 Ma.

25 Ma: The Eurasia Basin opens to the south. The Yermak Plateau and Morris Jesup Rise are entirely separated by a 3000 m deep gateway which runs to the north eastern tip of Greenland (Figure 6.7, 25 Ma, b). The northern North Atlantic and the Arctic Ocean are initially connected by a continuous but narrow channel, circa 9 km wide and at least 1500 m deep (Figure 6.10, 25 Ma, 1). The seafloor depth in the Fram Strait increases to 1650 m and remains constant until 18 Ma (Figure 6.12).

20 Ma–15 Ma: Figure 6.11 presents the opening scenarios of the Fram Strait for 19 Ma, 18 Ma, 17 Ma and 16 Ma. The Eurasia Basin opens to the south. According to the stratigraphic model the Yermak Plateau rises to 1300 m depth. The width of the Lena Trough increases to 30 km but the average depth remains around 1650 m (Figure 6.11, 19 Ma and

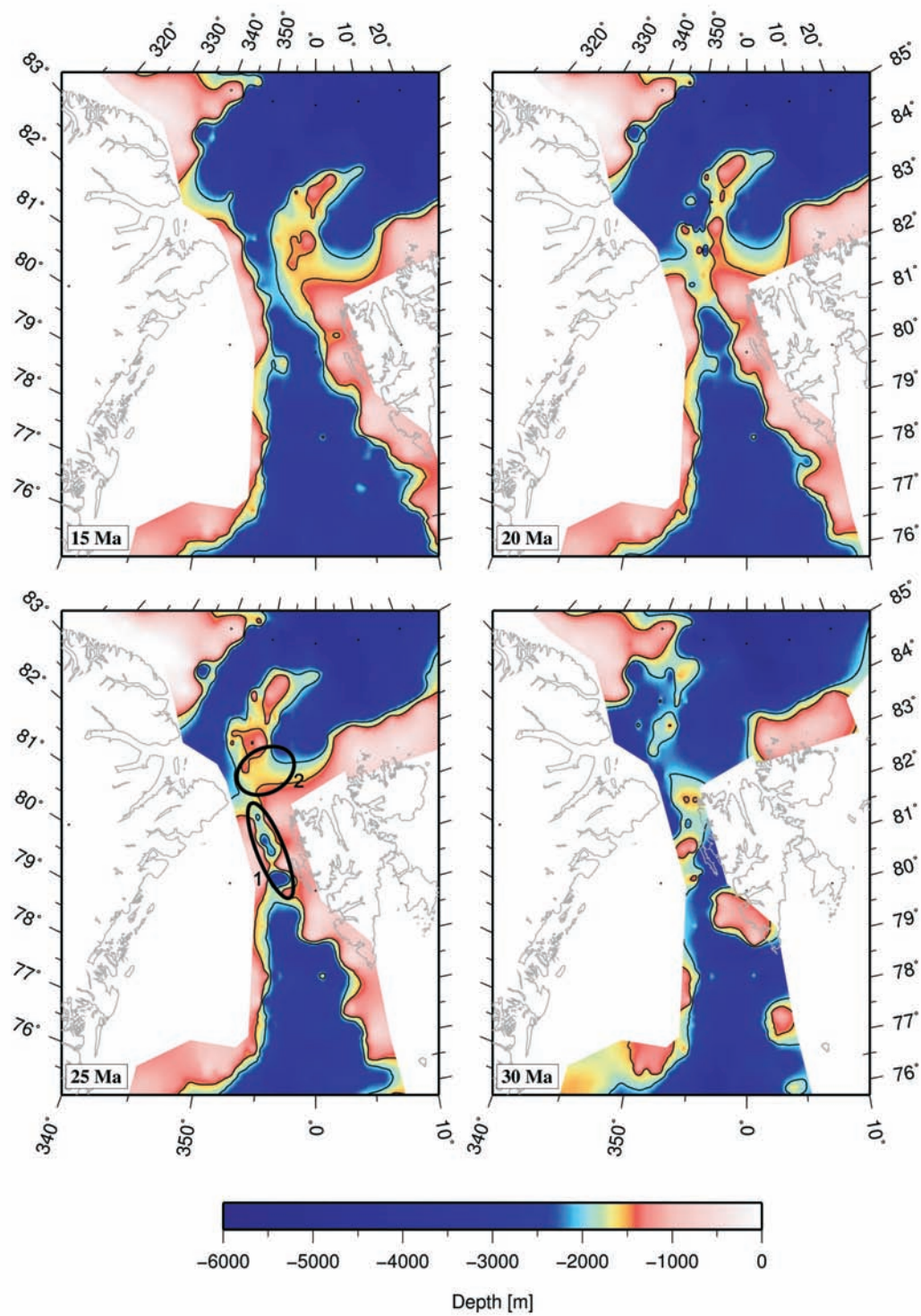


Figure 6.10: Time slices of 5 Myr steps from 15 Ma to 30 Ma show the results of the palaeobathymetric modelling for the seafloor depth (relative to the past sea level) for the Fram Strait area. The black lines display the 1500 m and 2000 m palaeobathymetric contour lines

Figure 6.12) relative to the corresponding sea level. The Lena Trough expands to 10 km width and 20 m depth (Figure 6.11, 18 Ma and Figure 6.12). Between 18 Ma and 17 Ma the width of a >1500 m deep channel increases significantly to 70 km and the depth increases to 1750 m (Figure 6.11, 17 Ma and Figure 6.12). This channel width and depth remains constant for the following 1 Myr (75 km width and 1770 m depth) (Figure 6.11, 16 Ma and Figure 6.12).

10 Ma: The Yermak Plateau becomes a continuous plateau with an average water depth of less than 1500 m (Figure 6.7, 10Ma, b).

0 Ma: The Lomonosov Ridge subsides to about 1500 m below the present sea level. The Eurasia Basin is up to 750 km wide. Due to its average sediment cover of 1850 m thick (Figure 6.9, 0Ma) the 3200 m deep Nansen Basin is about 20 % shallower than the Amundsen Basin, with an average sediment cover of 1150 m. The respective young oceanic crust (Figure 6.8, 0 Ma) close to the Gakkel Ridge is about 3200 m shallower than the 54 Myr old oceanic crust close to the Eurasia shelf and the Lomonosov Ridge.

The deep basin which can be observed at 50 Ma (Figure 6.7 and 6.8, 50 Ma, a), lays east of the Yermak Plateau in the Sophia Basin and the northern extension is at present filled up with about 4000 m of sediments (Figure 6.7–6.9, 0 Ma, a).

Molloy Basin and Hovgård Ridge

40 Ma: The Hovgård Fracture Zone is recognized by two 4300 m deep basement lows (Figure 6.8, 40 Ma, e) still attached to the East Greenland and Barents Sea margins.

35 Ma: First evidence of the development of the Molloy Basin can be observed as a basin with a depth of about 2400 m (Figure 6.7, 35 Ma, f).

30 Ma: The Hovgård Ridge is recognizable west of the most southern tip of Svalbard (Figure 6.7, 30 Ma, e). It moves as a part of the Greenland plate to its present day location. Close to the Hovgård Ridge a 3800 m deep basin grows in east west direction (Figure 6.7 and 6.8, 30 Ma, e).

15 Ma: The basin around the Hovgård Ridge is still found at 78.7°N and from now on is filled up with sediments (Figure 6.7 and 6.8, 15 Ma, e). The sediment thickness increases up to about 2000 m (Figure 6.9, 15 Ma–0 Ma, e).

10 Ma: An up to 5000 m deep depression of the basement is observed along the northwestern shelf of Svalbard (Figure 6.8, 10 Ma–0 Ma, g).

0 Ma: The maximum sediment load with up to 5500 m is found close to the north western shelf of Svalbard (Figure 6.9, 0 Ma, g). Here, the basement today is 25 % deeper (6000 m) than west of the Molloy Ridge (Figure 6.8, 0 Ma, g). The Hovgård Ridge has a shallow bathymetry (2150 m) compared to the adjacent basins (Figure 6.7, 0 Ma, e).

Boreas Basin and Norwegian-Greenland Sea

55 Ma: A basin with a depth of 3600 m is observed (Figure 6.7, 55 Ma, h) before initial seafloor spreading in the Norwegian-Greenland Sea (Figure 6.2). The distance between Norway and northeast Greenland increases to just about 150 km.

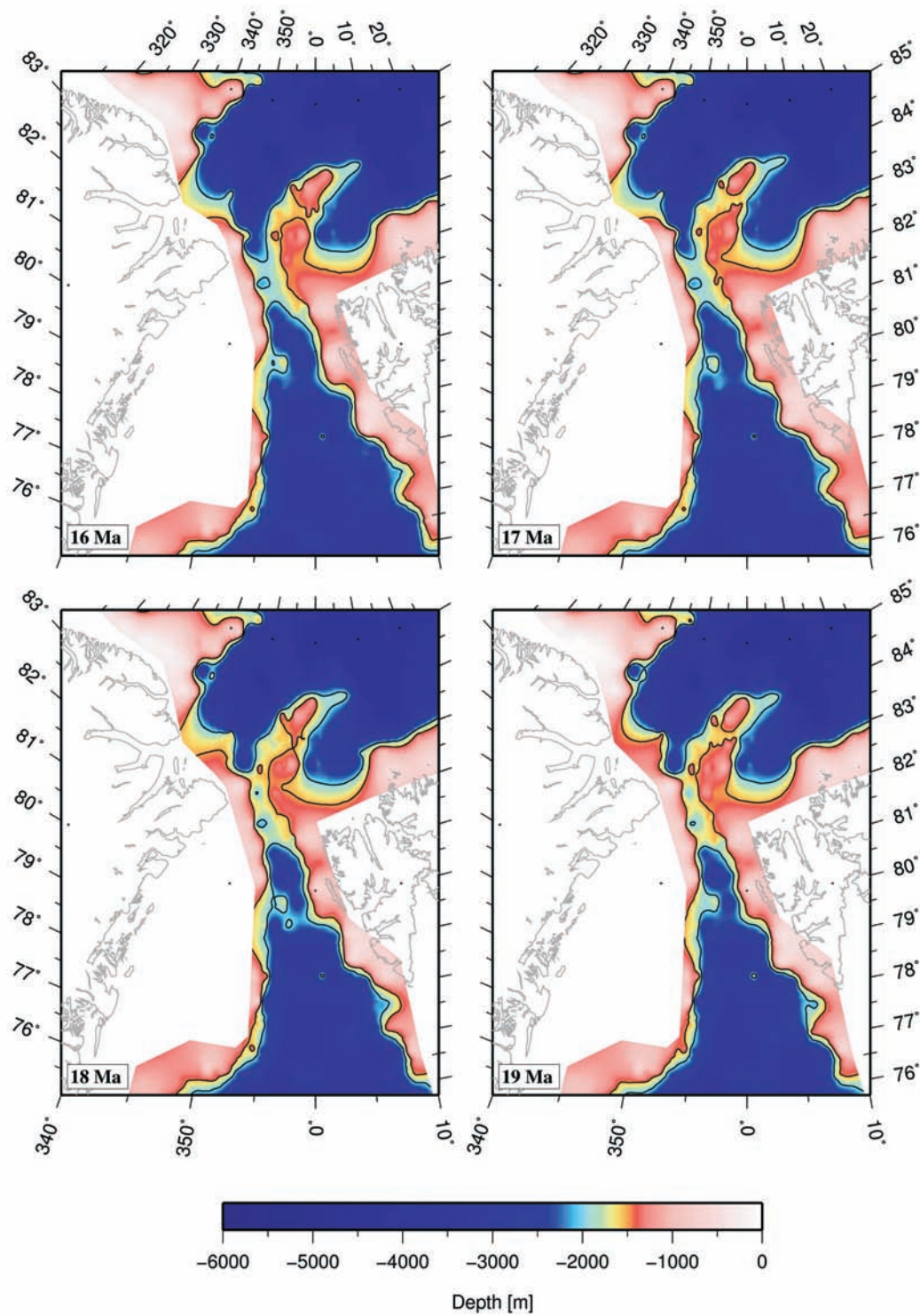


Figure 6.11: Time slices of 1 Myr steps from 16 Ma to 19 Ma show the results of the palaeobathymetric modelling for the seafloor depth (relative to the past sea level) for the Fram Strait area. The black lines display the 1500 m and 2000 m palaeobathymetric contour lines

50 Ma: The Greenland and Norwegian basins deepen. The northern part of the Greenland Basin (2500 m) is up to 300 m deeper than its southern part, whereas within the Lofoten Basin the seafloor has a depth of up to 3000 m (Figure 6.7, 50 Ma, h).

45 Ma: The course of the Mohns Ridge can be reproduced (Figure 6.7, 45 Ma). For the first 25 Myr of the development of oceanic crust the ridge runs from the East Greenland shelf in northwest direction to the Barents Sea shelf.

40 Ma: During its rifting phase the Boreas Basin is up to 3300 m deep (Figure 6.7, 40 Ma, i). It opens between the northern Greenland Basin and the basins around the Hovgård Ridge.

35 Ma: Initial seafloor spreading started in the Boras Basin (Figure 6.2). A sediment load of about 2000 m (Figure 6.9, 35 Ma, i) in the southern Boreas Basin causes a high basement depth of 5900 m (Figure 6.8, 35 Ma, i).

35 Ma–30 Ma: The sedimentation rate and basement depth in the northern Greenland Basin increases from 33 m/Myr to 250 m/Myr (Figure 6.9, 35 Ma–30 Ma, i) and about 33 % to 6000 m (Figure 6.8, 35 Ma–40 Ma, i). The basement lows in the northern Greenland Basin and southern Boreas Basin are separated by the Greenland Fracture Zone (Figure 6.8 and 6.9, 35 Ma–30 Ma, j).

25 Ma: Sedimentation increases at the western Greenland Fracture Zone (Figure 6.9, 25 Ma) to 300 m/Myr and deepens the basement to about 6400 m. The northern Greenland Basin, the western Greenland Fracture Zone and the southern Boreas Basin form a continuous basement low (Figure 6.8, 25 Ma, i).

20 Ma: The average sedimentation rate of 180 m/Myr in the northern Greenland Basin is twice as much as in the southern Boreas Basin. The basement depth increases to 7500 m (northern Greenland Basin) and 6900 m (southern Boreas Basin) (Figure 6.8, 20 Ma, i). The Mohns Ridge propagates to the north towards the Knipovich Ridge (Figure 6.2).

15 Ma: Sediment accumulation starts in the basin east of the Knipovich Ridge (Figure 6.9, 15 Ma–0 Ma, l) with a maximum of 3600 m.

5 Ma: The Mohns and Knipovich ridges form a continuous ridge (Figure 6.2 and Figure 6.7, 5 Ma, k), which separates the Greenland Fracture Zone from the Barents Sea shelf.

0 Ma: Close to the Barents Sea shelf, high sedimentation rates of about 440 m/Myr in the Boreas Basin and 290 m/Myr in the Lofoten Basin are observed between 5 Ma and today (Figure 6.9, 5 Ma and 0 Ma, l).

The older the oceanic crust gets, the deeper is the basement of the basin west and east of the Knipovich Ridge. The basement in the southern Boreas Basin is about 7000 m deep, the northern Greenland Basin even shows a basement depth of 8300 m (Figure 6.8, 0 Ma, i and j). Whereas the basement was deep in the southern Boreas Basin throughout its entire development, the basement in the oldest parts of the basin east of the Knipovich Ridge becomes abruptly deep during the last 5 Myr (Figure 6.8, 5 Ma and 0 Ma, l).

Throughout its evolution the basement in the southern Greenland Basin is about 15 %–20 % shallower than in the Lofoten Basin.

Jan Mayen Fracture Zone, Kolbeinsey Ridge and Aegir Ridge

The palaeobathymetric reconstruction south of the Jan Mayen Fracture Zone down to the Charlie Gibbs Fracture Zone is described by Wold (1995) in detail.

55 Ma: Two basins around the Aegir Ridge with a depth of 3500 m are observed. The basins broaden to about 520 km until 35 Ma (Figure 6.7, 55 Ma–35 Ma, m).

30 Ma: With the termination of the relative movement between Greenland and North America, seafloor spreading at the Aegir Ridge ceased. West of the ridge the Kolbeinsey Ridge developed, which is still an active ridge in the present day configuration. It is noticeable, that the basins evolving at the Kolbeinsey Ridge with a maximum depth of just 2000 m are shallow compared to even younger basins (Figure 6.7, 0 Ma, n).

25 Ma: Jan Mayen is located close to Greenland and moves 490 km away from the coast of East Greenland (Figure 6.7, 25 Ma–0 Ma).

20 Ma–15 Ma: The Jan Mayen Fracture Zone starts to evolve. It has a low sediment accumulation (200 m) and a shallow bathymetry (1200 m).

0 Ma: The basement of the Jan Mayen Fracture Zone and the Kolbeinsey Ridge are shallow with 1400 m, whereas the basement depth of the basins surrounding the Aegir Ridge is comparable to the basins along the Reykjanes Ridge south of Iceland.

Greenland-Faeroe Ridge

55 Ma: The Faeroe Islands and Greenland are connected by the 140 km long Greenland-Faeroe Ridge with an elevation of up to 500 m above sea level (Figure 6.7, 55 Ma, p). Also east of the Faeroe Islands the seafloor has a depth of about 600 m or on occasion lies above the sea level.

50 Ma: The whole area west of the Faeroe Islands lies above the sea level (Figure 6.7, 50 Ma).

35 Ma: A 250 m deep-water connection along the East Greenland shelf evolves (Figure 6.7, 35 Ma, p).

25 Ma: A shallow water connection west of the Faeroe Island is observed (Figure 6.7, 25 Ma). Hence, the land mass, connecting Greenland and the Faeroe Islands, becomes an Island, which departs from Greenland until today and which forms the present-day Iceland.

0 Ma: The sediment thickness along the Greenland-Faeroe Ridge is low with an average of 400 m (Figure 6.9, 0 Ma, p). A huge 5800 m thick sediment package is observed between the Faeroe Islands and the Shetland Islands. The on average 800 m deep basement of the Greenland-Faeroe Ridge (Figure 6.8, 0 Ma, p) is caused by the shallow water depth and a low sediment thickness.

6.6 Discussion

Previous palaeobathymetric reconstructions north of the Jan Mayen Fracture Zone were based only on bathymetric, magnetic and gravimetric data. Here stratigraphic information derived from seismic reflection, seismic refraction and borehole data (Berger and Jokat,

2008, 2009) and a more detailed age model of the oceanic crust in the investigation area (Ehlers and Jokat, 2009; this study) provide an estimate of the palaeo-water depths, palaeo-basement depths as well as palaeo-sediment thicknesses. The tectonic and the palaeobathymetric models produce important insight into the timing of the initial opening of the Fram Strait and of the first exchange of deep-water between the northern North Atlantic and the Arctic Ocean.

An important assumption for a palaeobathymetric model is isostatic equilibrium of oceanic crust. There is crustal thickness data of oceanic crust from seismic refraction data along the East Greenland shelf in the Greenland Basin (Voss et al., 2009). Klingelhöfer et al. (2000) and Ritzmann et al. (2002) found in the Lofoten Basin and around the Molloy and Knipovich ridges a mean thickness of about 4.0 km for the oceanic crust. This means an anomalously thin oceanic crust north of the Jan Mayen Fracture Zone. Beneath basement highs, the crust thickens and is thinner beneath the basins, which implies isostatic compensation (Klingelhöfer et al., 2000). Isostatic compensation is also implied by subsidence calculations in the Boreas, Molloy, Amundsen and Nansen basins (Ehlers and Jokat, 2009). The calculated subsidence corrected for the sediment loads fits in with the observed basement depth and indicates that subsidence calculation can be applied for palaeobathymetric reconstructions.

In general, seafloor depth in oceanic basins decreases with their age. The effective subsidence is dependent on the thermal subsidence (Parsons and Sclater, 1977) and the accumulation of sediments (Allen and Allen, 1990). Figure 6.13 shows theoretical and average curves for the subsidence of the oceanic basins. A positive slope of the theoretical curve means subsidence, a negative slope represents uplift. The highest subsidence rate (1680 m) within 55 Ma is achieved for oceanic crust without a sediment cover. The higher the sediment load, the smaller the theoretical subsidence of the seafloor depth. High sediment accumulation rates even cause uplift for increasing crustal age. Figure 6.13 compares the theoretical curves with the curves resulting from the palaeobathymetric model, which will be described for the investigated basins below. Sediment accumulation rates for every basin are shown in figure 6.14 for intervals of 5 Myr. The oldest stratigraphic age correlation for the oldest basins with high sediment accumulation is made for 15 Ma (table 6.1). We have to assume, that the remaining sediments were accumulated at a constant rate. Hence, the calculation of the sediment mass-age distribution results in an exponential decay due to the increase of the seafloor area (Wold, 1992). To make the results comparable to the deposits of younger ages with detailed stratigraphic information, the average sediment mass for the ages higher than 15 Myr are displayed (Figure 6.14, dotted lines). In addition the total sediment mass, the total grid cell area, the total sediment volume and the total sediment mass per total grid cell area is calculated to make the basins comparable (table 6.4).

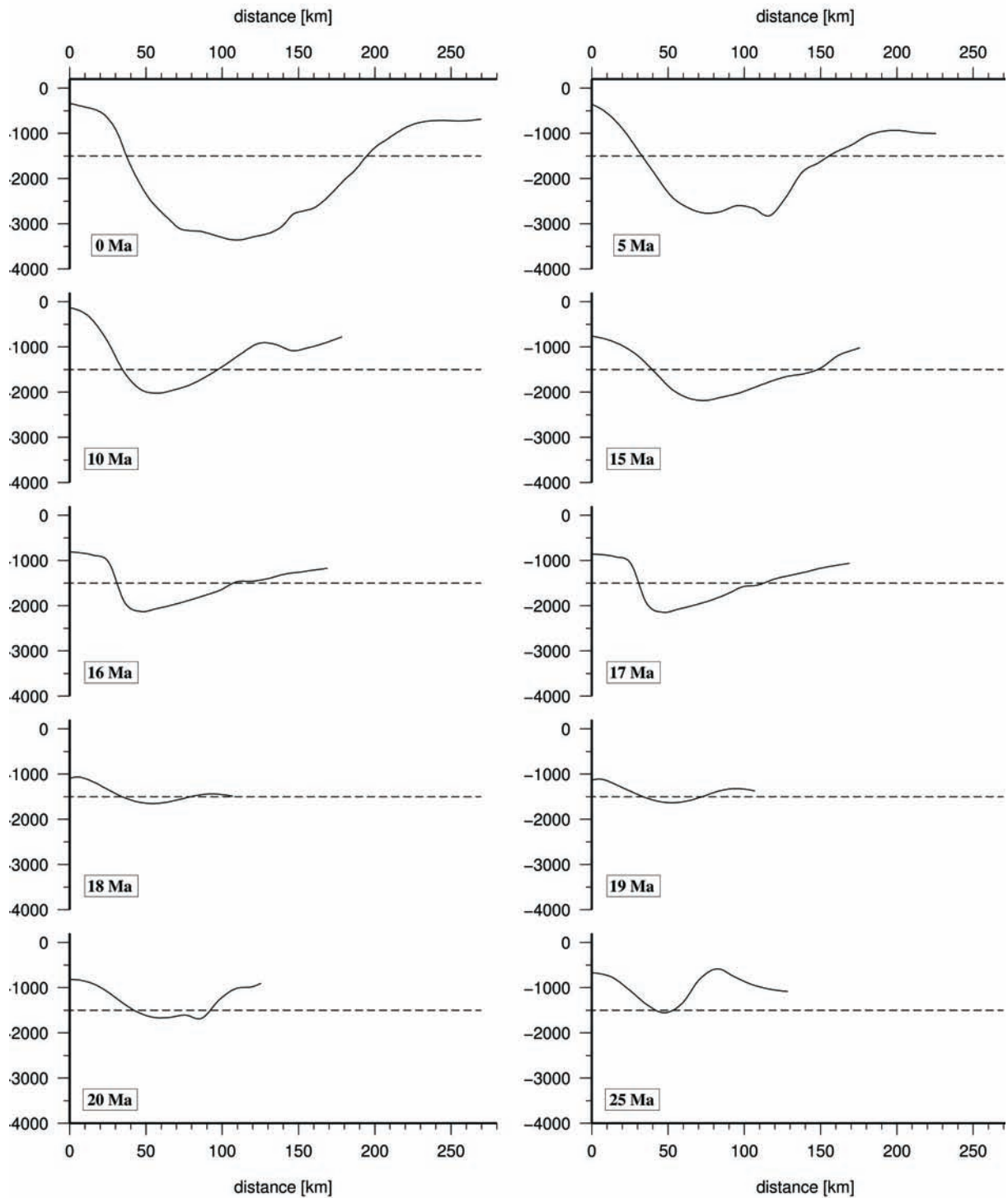


Figure 6.12: Cross sections through the Fram Strait for ages between 0 Ma and 25 Ma representing the water depth and the width of the gateway during its development. The dashed black line displays a water depth of 1500 m (maximum water depth for deep-water circulation (Kristoffersen, 1990))

investigation area	total sediment mass [g]	total grid cell area [km^2]	total sediment volume [km^3]	total sediment mass/grid cell area [g/km^2]
Yermak Plateau	$1.183 \cdot 10^{20}$	$0.327 \cdot 10^5$	$0.696 \cdot 10^5$	$3.61 \cdot 10^{15}$
Lena Trough	$0.149 \cdot 10^{20}$	$0.161 \cdot 10^5$	$0.117 \cdot 10^5$	$0.92 \cdot 10^{15}$
Molloy Basin	$0.912 \cdot 10^{20}$	$0.263 \cdot 10^5$	$0.511 \cdot 10^5$	$3.48 \cdot 10^{15}$
Hovgård Ridge	$0.186 \cdot 10^{20}$	$0.098 \cdot 10^5$	$0.128 \cdot 10^5$	$1.89 \cdot 10^{15}$
Boreas Basin	$1.405 \cdot 10^{20}$	$0.685 \cdot 10^5$	$0.936 \cdot 10^5$	$2.05 \cdot 10^{15}$
Greenland Basin	$2.695 \cdot 10^{20}$	$2.400 \cdot 10^5$	$1.970 \cdot 10^5$	$1.13 \cdot 10^{15}$
Lofoten Basin	$9.627 \cdot 10^{20}$	$2.700 \cdot 10^5$	$5.450 \cdot 10^5$	$3.57 \cdot 10^{15}$

Table 6.4: Total sediment mass, total grid cell area, total sediment volume and total sediment mass/grid cell area for the investigated basins, the plateau and ridge north of the Jan Mayen Fracture Zone

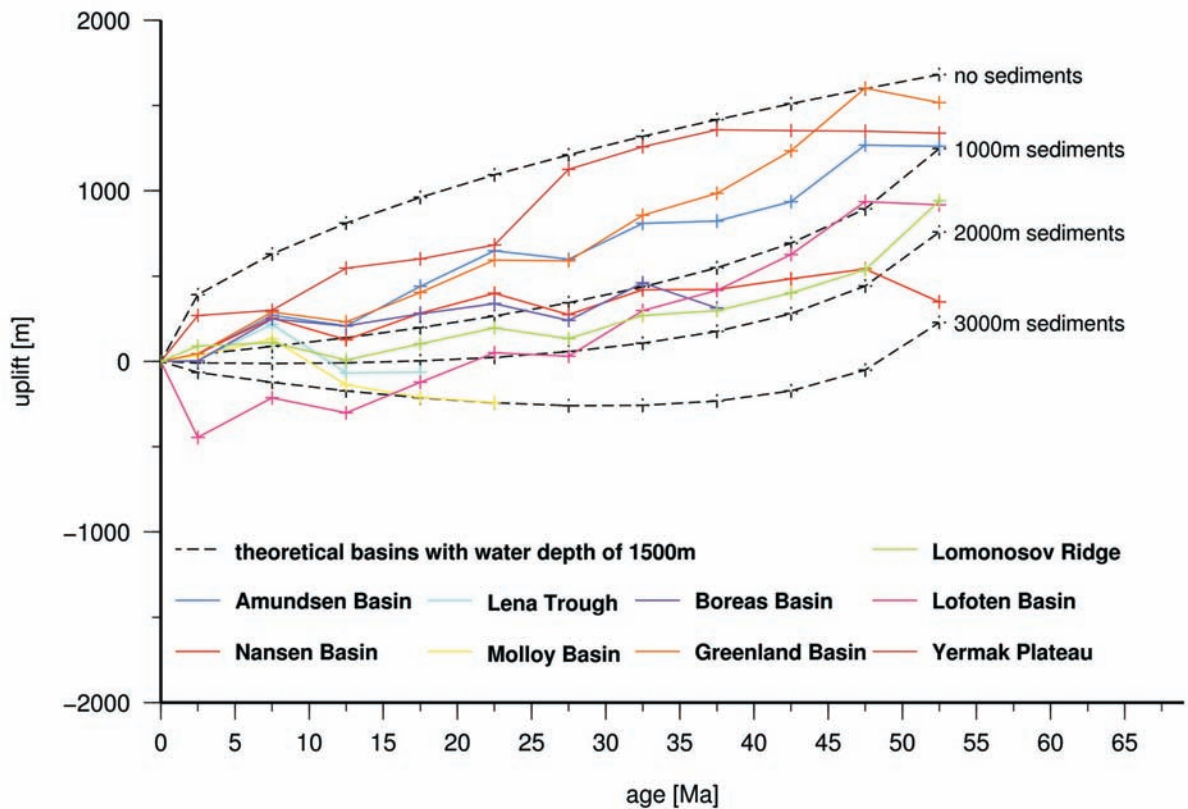


Figure 6.13: Development of the seafloor depth by time presented as a subsidence-age relationship for theoretical basins without a sediment load or linear accumulated 1000 m, 2000 m and 3000 m sediment loads (dashed black lines) and for the investigated basins (colored lines)

6.6.1 Lomonosov Ridge, Eurasia Basin, Yermak Plateau and Lena Trough

Just a few profiles in the Eurasia Basin (Figure 6.4) and the present day seafloor topography derived from the IBCAO data (Jakobsson et al., 2001) (Figure 6.1) provide the data basis

for the palaeobathymetric reconstruction in the Arctic Ocean.

The subsidence curve of Moore et al. (2006) supplies information about the tectonic development of the Lomonosov Ridge. Figure 6.13 shows the resulting subsidence curve. The subsidence with a maximum change of 27 m/Myr is low for the last 35 Myr. Especially after initial seafloor spreading in the Eurasia Basin, we calculated high subsidence rates up to 81 m/Myr. In total the Lomonosov Ridge subsided in average 941 m within the last 55 Myr. Compared to the theoretical subsidence curve (Figure 6.13), the Lomonosov Ridge curve predicts a nearly 2000 m thick sediment cover. The only ground-truthed seismic interpretation from core-seismic interpretation of the ACEX record (Jakobsson et al., 2007) provides a sediment load of about 500 m. This difference in sediment thickness exists due to the underlying continental crust (O'Regan et al., 2008).

In the Amundsen and Nansen basins we observe a different development of sediment accumulation since 15 Ma (Figure 6.7, 15 Ma). The increasing sedimentation in the Eurasia Basin can be explained by large-scale glaciations in the northern Barents Sea during the middle Miocene climate transition (Knies and Gaina, 2008). While the Amundsen Basin adjoins the narrow and sparsely covered Lomonosov Ridge, the Nansen Basin sediment cover is originated from Greenland, the Laptev Sea and the Siberian shelves (Jokat and Micksch, 2004).

The palaeobathymetric reconstruction results in a deep subsided crust in the Sophia Basin and its northern extension (Figure 6.7 and 6.8, a) which existed before seafloor spreading started in the Eurasia Basin (Figure 6.7, 55 Ma, a) and hence, points to a thinning of the continental crust. Furthermore the absence of magnetic spreading anomalies (Figure 6.2) argues for the existence of stretched continental crust. In terms of the adopted tectonic model we assume, that the Sophia Basin and its northern extension developed during the rifting phase of the Eurasia Basin at the triple junction of the North American, the Greenland and the Eurasia plates (Jackson et al., 1984). The strike-slip movement between Eurasia and Greenland caused a pull-apart basin.

The adopted age model for the Arctic Ocean (Brozena et al., 2003, this study) and the palaeobathymetric modelling confirm the continental origin of parts of the Yermak Plateau. The Yermak Plateau was a part of the shelf area north of Ellesmere Island and was connected to the Lomonosov Ridge (Figure 6.7, 55 Ma, b). This observation coincides with seismic refraction data (Ritzmann and Jokat, 2003) that prove stretched continental crust for the western Yermak Plateau. We assume that after the separation of the Yermak Plateau and the Lomonosov Ridge (Figure 6.7, 50 Ma, c) stretched continental crust built the deep rift basin of the Lincoln Sea (Figure 6.1) until seafloor spreading ceased in the Labrador Sea. This hypothesis is based on magnetic data, which give no evidence for the development of oceanic crust in the Lincoln Sea (Figure 6.2). It cannot be proved by the palaeobathymetric reconstruction due to a lack of seismic data.

The modelling of the Yermak Plateau results in an uplift of seafloor until 35 Myr (Figure 6.13). In the model the Yermak Plateau reached the shallowest water depths with an average of 1350 m above the present day mean seafloor depth of 1300 m (Figure 6.7, 35 Ma, b). Regarding the change in sea level (Haq et al., 1987), the plateau shallows about 100 m below sea level. We point out, that the palaeobathymetric reconstruction does not

consider the stretching of continental crust (Ritzmann and Jokat, 2003). Crustal extension intensifies the subsidence of the plateau (Figure 6.13). Our results prove a maximum seafloor depth. The seafloor could have been shallower and even above the sea level at 35 Ma and earlier.

Our model reproduces the beginning of the separation of the Morris Jesup Rise and the Yermak Plateau for 35 Ma (Figure 6.7, 35 Ma, b). The timing of the separation agrees with the results of Feden et al. (1979), but they equalise the separation with the beginning of seafloor spreading. Figure 6.13 displays seafloor subsidence since 35 Ma. We assume that the seafloor subsidence coincides with the increased sedimentation rate (Figure 6.14). Similar to the Eurasia Basin the highest observed sediment accumulation between 15 Ma and present day is caused by glacially eroded material from the uplift to the northern Barents Sea during large-scale glaciations (Knies and Gaina, 2008).

The evolution of the Lena Trough is critical for the final opening of the gateway between the northern North Atlantic and the Arctic Ocean. A deep-water circulation below 1500 m (Kristoffersen, 1990) and a channel width higher than the internal Rossby radius (Jakobsson et al., 2007) are the criteria to change the Arctic Ocean from a land-locked to a ventilated basin. Studies from the Integrated Ocean Drilling Project (IODP) Expedition 302 (ACEX) in 2004 define the first deep-water exchange between the Arctic Ocean and the North Atlantic for 17.5 Ma (Jakobsson et al., 2007). Our study of the modelled seafloor depth confirms the predicted age. The tectonic and sedimentary evolution increases the depth and the width of the Fram Strait gateway significantly between 18 Ma and 17 Ma (Figure 6.11 and 6.12).

Jokat et al. (2008) suppose a limited water exchange between the Arctic Ocean and the North Atlantic already well before the opening of the Fram Strait. The results of our palaeobathymetric reconstruction show, that a limited water exchange between the Arctic Ocean and the northern North Atlantic was possible since 25 Ma (Figure 6.10, 25 Ma, 1). Shallow water masses could have been exchanged through the south eastern Yermak Plateau (Figure 6.10, 25 Ma, 2). Above all, we confirm, that the exchange of warm Atlantic water and cold Arctic water was possible since 17 Ma (Figure 6.11, 17 Ma, Figure 6.12, 17 Ma). The presented deep-water exchange, which was enabled before initial seafloor spreading in the Lena Trough (Figure 6.2) can be explained by continental rifting and crustal extension.

6.6.2 Molloy Basin and Hovgård Ridge

The exchange of deep-water between the Arctic Ocean and the North Atlantic also depends on the evolution of the Molloy Basin and the Hovgård Ridge. The palaeobathymetric reconstruction results in a deep continental rift basin (Figure 6.7, 35 Ma, f) before initial seafloor spreading started at the Molloy Ridge (Figure 6.2). Glacial deposits are found since 2.5 Ma along the Svalbard and Barents Sea margins (Solheim et al., 1998) and since 15 Ma along the East Greenland margin (Berger and Jokat, 2008). 2–3 times higher sedimentation rates are observed along the Svalbard and Barents Sea margins. In addition the opening of the Fram Strait allows the transport of glacial deposits from the Barents Sea

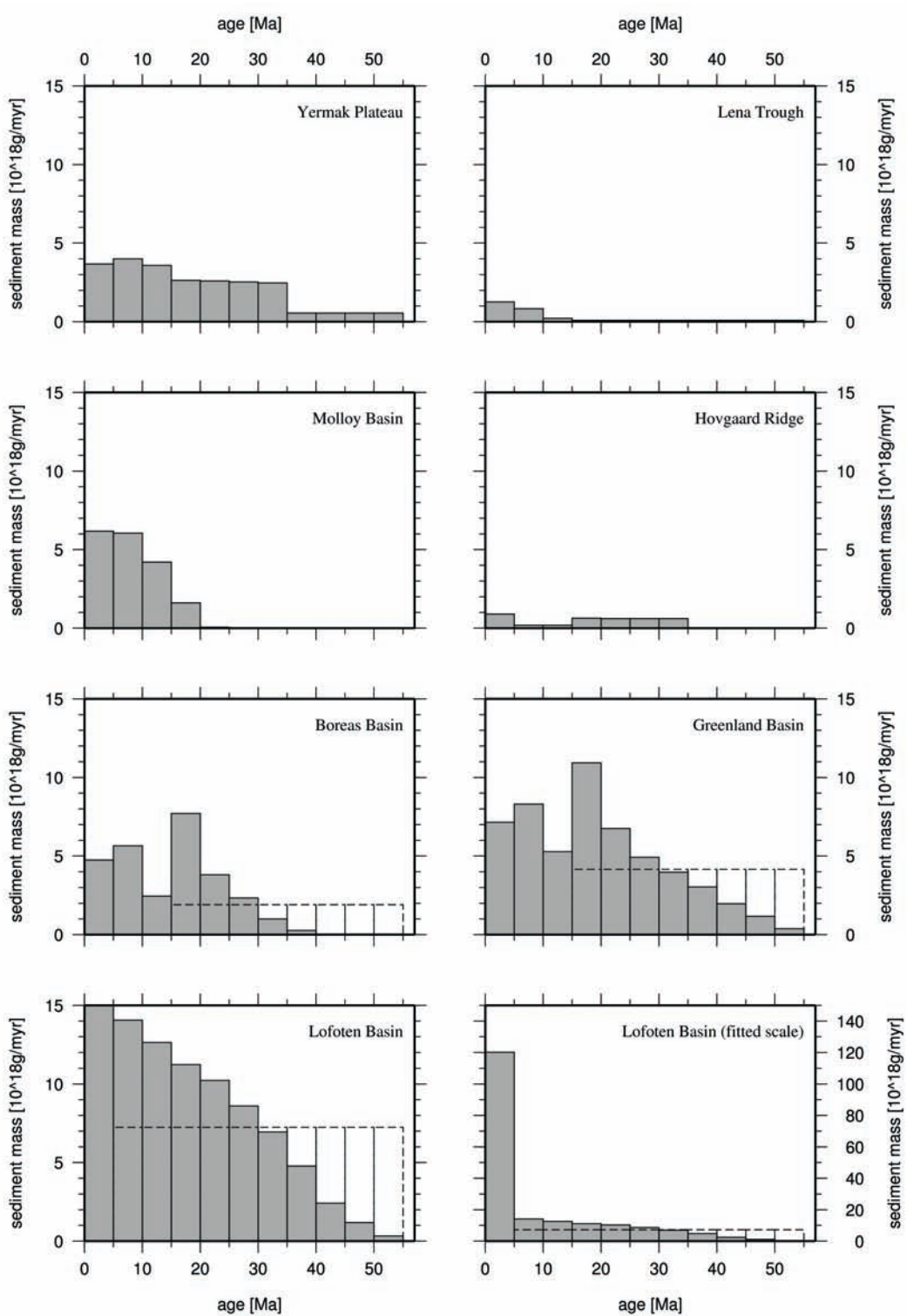


Figure 6.14: Sediment mass accumulation for the investigated basins during 1 Myr observed in 5 Myr intervals. The dashed black lines show a average sediment accumulation for sediments without age correlation

(Knies and Gaina, 2008). All sources of sediment deposits are reflected in the increasing sediment rate (Figure 6.14) since 15 Ma and have influence on the development of the Molloy Basin. Hence, the high subsidence of the basement (Figure 6.8, 10 Ma–0 Ma, g) close to the Svalbard Margins is explained by the sediment load (Figure 6.9, 0 Ma, g).

Furthermore the palaeobathymetric reconstruction gives evidence, that the Hovgård Ridge is originated at the southern tip of Svalbard (Myhre et al., 1982). We cannot conclude, whether the basins close to the Hovgård Ridge (Figure 6.7, 30 Ma–0 Ma, e) are either of oceanic or continental origin. But due to the low amplitude of the magnetic data (Figure 6.3) we assume, that the crust around the Hovgård Ridge consists of stretched continental crust.

The reconstruction results in a very low sedimentation of the Hovgård Ridge (Figure 6.14). Between 5 Ma and now the sedimentation rate increases from $0.19 \cdot 10^{18}$ g/Myr to $0.90 \cdot 10^{18}$ g/Myr. We presume, that this increase correlates with the northward propagation of the Knipovich Ridge (Figure 6.2 and 6.7, 5 Ma and 0 Ma).

6.6.3 Boreas Basin and Norwegian-Greenland Sea

Today the basement depth in parts of the Boreas Basin and of the Norwegian-Greenland Sea is considerable (Figure 6.8, 0 Ma, i, l, h). The analysis of the development of the basement depth in the palaeobathymetric reconstruction points up the different evolution of the basins. Similar to the eastern Molloy Basin, the basement depth increases in the eastern Boreas Basin and in the Lofoten Basin for the last 5 Myr (Figure 6.8, 5 Ma–0 Ma, l, h). Again, the high basement subsidence correlates with high sedimentation rates (Figure 6.14) caused by glacial deposits (Solheim et al., 1998). Especially the high sediment accumulation of $120 \cdot 10^{18}$ g/Myr in the Lofoten Basin for the last 5 Myr (Figure 6.14) even causes the highest uplift (450 m) of seafloor depth (Figure 6.13) in the investigated area.

By contrast, the reconstruction yields high basement depth in the southern Boreas Basin before initial seafloor spreading started at the Knipovich Ridge. Hence, we assume, that a continental rift basin (Figure 6.8, 4 Ma, i) was the preliminary stage of the oceanic Boreas Basin (Figure 6.2 and 6.3). It is after that, that the northern Greenland Basin basement depth increases due to sediment accumulation and the Greenland Fracture Zone evolves as a barrier between the Boreas Basin and the Greenland Basin (Figure 6.9, 6.9, 30 Ma–25 Ma, i, j). An increasing sediment load resulting in a increasing basement depth at the western Greenland Fracture Zone connects the southern Boreas Basin and the northern Greenland Basin basement lows since 25 Ma (Figure 6.8, 25 Ma, i).

In the northern Greenland Basin, magnetic anomalies show a slightly different pattern than in the remaining southern basin (Figure 6.2 and 6.3). If we assume, that the re-identified anomalies in the southern Greenland Basin cross the northern Greenland Basin, the corresponding anomalies in the oldest part of the Lofoten Basin would continue north into the Barents Sea shelf. The great basement depth of this part of the Greenland Basin can probably be explained by the development of a self-contained basin during or before the evolution of the southern part. Continental rifting is followed by seafloor spreading.

The sedimentation rate of the Boreas and the Greenland basins (Figure 6.14) represent

similar sequences of glacial deposition. We observe the highest rates between 10 Ma and 5 Ma. These sediments are assumed to be of glacial origin since 15 Ma (Berger and Jokat, 2008) and are presented in our subsidence investigations (Figure 6.13). Between 10 Ma and 5 Ma the seafloor depth of both basins even decreased because of the high sediment deposits, and subsidence was low with just 4m in the Boreas Basin and about 50 m in the Greenland Basin within the last 5 Myr.

6.6.4 Jan Mayen Fracture Zone, Kolbeinsey Ridge and Aegir Ridge

Based on the tectonic model south of the Jan Mayen Fracture Zone, the Kolbeinsey Ridge is an active mid ocean ridge since about 35 Ma. Compared to the above described oceanic basins both the seafloor and the basement are very shallow. The older basins along the Aegir Ridge show an expected depth for subsided and sediment covered basins. The shallow seafloor and basement depth are accompanied by a thick crust north of Iceland. Until now it has not been resolved, why the thick crust does not continue north of the Jan Mayen Fracture Zone. The reconstruction confirms that the Jan Mayen Fracture Zone is apparently a north-south linear feature separating the Iceland Plateau from the Norwegian-Greenland Sea (Wold, 1995).

6.6.5 Greenland-Faeroe Ridge

In the present day configuration the source of the deep-water overflow along the Greenland-Faeroe Ridge does not originate at the bottom of the Norwegian-Greenland Sea but at a water depth of about 1000 m (Peterson and Rooth, 1976). Hence, the palaeobathymetric reconstruction confirms, that between 20 Ma and 15 Ma the seafloor depth of the Greenland-Faeroe Ridge subsides up to 1000 m in the Denmark Strait between Greenland and Iceland (Figure 6.7, 20 Ma and 15 Ma). The timing of initial overflow correlates with the timing of a first deep-water exchange through the Fram Strait.

6.6.6 Comparison of the basins north of the Jan Mayen Fracture Zone

The palaeobathymetric reconstruction shows, that the development of the seafloor and the basement depth during the basin evolution is highly influenced by the deposition of sediments and the underlying crust.

The sediment accumulation rates are calculated for the basins of the northern North Atlantic north of the Jan Mayen Fracture Zone (Figure 6.14). In addition the total sediment masses, the size of the grid cell area used for the calculation, the total sediment volume and the total sediment mass per grid cell area is listed in table 6.4. The highest sedimentation rate is found for the Yermak Plateau and the adjacent Sophia Basin followed by the Lofoten Basin and the Molloy Basin.

6.7 Conclusions

A detailed age model combined with new and existing seismic stratigraphy data for the first time makes a palaeobathymetric reconstruction from the Jan Mayen Fracture Zone up to the Arctic Ocean possible. The reconstruction yields an insight into the development of the seafloor depth, the basement depth and the sediment thickness during the entire basin evolution.

The results of modelling the seafloor depth show the history of subsidence of the northern North Atlantic and Arctic Ocean, which is dependent on the sedimentation rates of the basins. Low sedimentation rates cause seafloor subsidence whereas high sedimentation rates even entail seafloor uplift.

The highest sedimentation rates are observed along the Svalbard and Barents Sea margins during the last 5 Ma. They are caused by large-scale glaciations in the Barents Sea. Along the East Greenland margin, glacial sedimentation started earlier (15 Ma) but did not reach such a high sediment accumulation. Larger basement depth confirms the evolution along the Svalbard and Barents Sea margin.

Resulting from thermal subsidence and sediment accumulation, the palaeobathymetric model shows the onset of a channel with a depth of well below 1500 m since 17 Ma. It confirms that around 17 Ma the Arctic Ocean changed from a “land-locked” ocean to a ventilated stage by an exchange of deep-water between the Arctic Ocean and the northern North Atlantic. Approximately during this period subsidence of the Greenland-Faeroe Ridge reaches a water depth which allows an initial overflow of deep-water from the Norwegian-Greenland Sea to the North Atlantic. Before the deep-water exchange, since 25 Ma shallow water masses could be exchanged east of the Yermak Plateau.

Deep basement structures are observed well before initial seafloor spreading in the oceanic basins started. We assume that they are originated by stretched continental crust during the rifting phase and are filled up by sediments today. Stretched continental crust is also responsible for the Fram Strait opening. The deep-water gateway opened before seafloor spreading started in the Lena Trough.

The palaeobathymetric model of the northern North Atlantic and the Arctic Ocean derived from this study confirms the correlation between the timing of the Fram Strait opening and climate changes in the northern polar region. More detailed magnetic, seismic and stratigraphic data would improve this model especially in the Arctic Ocean. The results of this study are useful for future oceanographic and climate research.

Acknowledgements

We thank Tim Minshull, Carmen Gaina and an anonymous reviewer for their helpful reviews, which improved this manuscript very much. Furthermore, thanks is given to Ansa Lindeque and Hans Mürkens for improving the English of the manuscript.

Bibliography

- Allen, P. A. and Allen, J. R. (1990). Basin analysis principles & applications, Blackwell Science Publications, 272 pp.
- Arctic Gravity Project (2006). <http://earth-info.nga.mil/GandG/wgs84/agp>.
- Berger, D. and Jokat, W. (2008). A seismic study along the East Greenland margin from 72°N to 77°N, *Geophysical Journal International*, doi: 10.1111/j.1365-246X.2008.03794.x.
- Berger, D. and Jokat, W. (2009). Sediment deposition in the northern basins of the North Atlantic and characteristic variations in shelf sedimentation along the East Greenland margin, *Marine and Petroleum Geology*, doi: 10.1016/j.marpetgeo.2009.04.005.
- Brozena, J.M., Childers, V.A., Lawver, L.A., Gahagan, L.M., Forsberg, R., Faleide, J.I. and Eldholm, O. (2003). New aerogeophysical study of the Eurasia Basin and Lomonosov Ridge: Implications for basin development, *Geology*, 31, 825–828.
- Bott, M. H. P., Nielsen, P. H. and Sutherland, J. (1976). Converted P-waves originated at the continental margin between the Iceland Phaeroe Ridge and the Phaeroe Bank, *Journal of the Royal Astronomical Society*, 44, 229–238.
- Czuba, W., Ritzmann, O., Nishimura, Y., Grad, M., Mjelde, R., Guterch, a. and Jokat, W. (2005). Crustal structure of the northern Spitsbergen along the deep seismic transect between the Molloy Deep and Nordaustlandet, *Geophysical Journal International*, 161, 347–364.
- Ehlers, B.-M. and Jokat, W. (2009). Subsidence and crustal roughness of ultra-slow spreading ridges in the northern North Atlantic and the Arctic Ocean, *Geophysical Journal International*, 177, 451–462, doi: 10.1111/j.1365-246X.2009.04078.x.
- Eldholm, O., Karasik, A. M. and Reksnes, P. A. (1990). The North American plate boundary, in *The Arctic Ocean region*, Band L of *The Geology of North America*, eds Grantz, A., Johnson, L. and Sweeney, J. F., Geological Society of America, Boulder, Colorado, 171–184.
- Engen, Ø, Faleide, J. I., Dyreng, T. K. (2008). Opening of the Fram Strait gateway: A review of plate constraints, *Tectonophysics*, 450, 51–69.

BIBLIOGRAPHY

- Faleide, J. I., Solheim, A., Fiedler, A., Hjelstuen, B. O., Andersen, E. S. and Vanneste, K. (1996). Late Cenozoic evolution of the western Barents Sea-Svalbard continental margin, *Global and Planetary Change*, 12, 53–74.
- Feden, R. H., Vogt, P. R. and Flemming, H. S. (1979). Magnetic and bathymetric evidence for the ‘Yermak Hot Spot’ northwest of Svalbard in the Arctic Basin, *Earth planet. Sci. Lett.*, 44, 18–38.
- Fiedler, A. and Faleide, J. I. (1996). Cenozoic sedimentation along the northwestern Barents Sea margin in relation to uplift and erosion of the shelf, *Global and Planetary Change*, 12, 75–93.
- Gaina, C., Roest, W. R. and Müller, R. D. (2002). Late Cretaceous - Cenozoic deformation of northeast Asia, *Earth and Planetary Science Letter*, 197, 273–286.
- Geissler, W. H. and Jokat, W. (2004). A geophysical study of the northern Svalbard continental margin, *Geophysical Journal International*, 158, 50–66.
- Gradstein, F., Ogg, J. and Smith, A. (eds) (2004). *A Geological Time Scale 2004*, Cambridge University Press.
- Haq, B. U., Hardenbol, J. and Vail, P.R. (1987). Chronology of fluctuating sea level since the Triassic, *Science*, 235, 1156–1167.
- Jackson, H. R., Johnson, G. L., Sundvor, E. and Myhre, A. M. (1984). The Yermak Plateau: formed at a triple junction, *Journal of Geophysical Research*, 89 (B5), 3223–3232.
- Jakobsson, M. and IBCAO Editorial Board Members (2001). Improvement to the International Bathymetric Chart of the Arctic Ocean (IBCAO): Updating the Data Base and the Grid Model, *EOS, Trans. Am. Un.*, 82 (47), Fall Meet. Suppl., Abstract OS11B-0371.
- Jakobsson, M., Backman, J., Rudels, B., Nycander, J., Frank, M., Mayer, L., Jokat, W., Sangiorgi, F., O’Regan, M., Brinkhuis, H., King, J., Moran, K. (2007). The early Miocene onset of a ventilated circulation regime in the Arctic Ocean, *Nature*, vol. 447, 986–990.
- Jokat, W. and Micksch, U. (2004). Sedimentary Structure of the Nansen and Amundsen basins, Arctic Ocean, *Geophysical Research Letters*, vol. 31.
- Jokat, W., Geissler, W. and Voss, M. (2008). Basement structure of the north-western Yermak Plateau, *Geophysical Research Letters*, vol. 35.
- Klingelhöfer, F., Gèli, L., Matias, L., Steinsland, N. and Mohr, J. (2000). Crustal structure of a super/slow spreading centre: a seismic refraction study of Mohns Ridge, 72°N, *Geophysical Journal International*, 141, 509–526.
- Knies, J. and Gaina, C. (2008). Middle Miocene ice sheet expansion in the Arctic > View from the Barents Sea, *G3 - Geochemistry Geophysics Geosystems*, vol. 9, number 2.

- Kristoffersen, Y. (1990). On the tectonic evolution and palaeoceanographic significance of the Fram Strait gateway, *Geological History of the Polar Oceans: Arctic Versus Antarctic*, Bleil, U. and Thiede, J. (eds.), Kluwer Academic Publishers, 63–76.
- Leinweber, V. T. (2006). Abschätzung von Sedimentmächtigkeiten in der Framstraße anhand magnetischer Daten, Diploma thesis Karl-Franzens-University Graz, 96pp.
- Ljones, F., Kuwano, A., Mjelde, R., Breivik, A., Shimamura, H., Murai, Y. and Nishimura, Y. (2004). Crustal transect from the North Atlantic Knipovich Ridge to the Svalbard Margin west of Hornsund, *Tectonophysics*, 378, 17–41.
- Moore, T. C. and the Expedition 302 Scientists (2006). Sedimentation and subsidence history of the Lomonosov Ridge, in *Proceedings of the Integrated Ocean Drilling Program, 302*, edited by Backman, J., Moran, K., McInroy, D. B., Mayer, L. A. and the Expedition 302 Scientists, College Station, TX (Integrated Ocean Drilling Program Management International, Inc.).
- Moran, K. et al. (2006). The Cenozoic palaeoenvironment of the Arctic Ocean, *Nature*, 441, 601–605.
- Myhre, A. M., Eldholm O. and Sundvor, E. (1982). The margin between Senja and Spitsbergen Fracture Zones: Implications from Plate Tectonics, *Tectonophysics*, 89, 33–50.
- Myhre, A. M., Thiede, J., Firth, J. V. and shipboard scientific party (1995). *Proceedings of the Ocean Drilling Program; initial reports; North Atlantic-Arctic gateways I; covering Leg 151 of the cruises of the drilling vessel JOIDES Resolution, St. John's Harbour, Newfoundland, to Reykjavik, Iceland, sites 907–913, 24 July-24 September, Proceedings of the Ocean Drilling Program, Part A: Initial Reports, vol. 151, 926.*
- O'Regan, M., Moran, K., Backman, J., Jakobsson, M., Sangiorgi, F., Brinkhuis, H., Pockalny, R., Skelton, A., Stickley, C., Koç, N., Brumsack, H.-J. and Willard, D. (2008). Mid-Cenozoic tectonic and paleoenvironmental setting of the central Arctic Ocean, *Paleoceanography*, vol. 23, doi 10.1029/2007PA001559.
- Parsons, B. and Sclater, J. G. (1977). An analyses of the variation of ocean floor bathymetry and the heat flow with age, *Journal of Geophysical Research*, 82(5), 803–827.
- Peterson, W. H. and Rooth, C. G. H. (1976). Formation and exchange of deep water in the Greenland and Norwegian Seas, *Deep-Sea Research*, 23, 273–283.
- Ritzmann, O., Jokat, W., Mjelde, R. and Shimamura, H. (2002). Crustal structure between the Knipovich Ridge and the Van Mijenfjorden (Svalbard), *Marine Geophysical Research*, 23, 379–401.
- Ritzmann, O. and Jokat, W. (2003). Crustal structure of northwestern Svalbard and the adjacent Yermak Plateau: Evidence for Oligocene simple shear rifting and non-volcanic break-up, *Geophysical Journal International*, 152, 139–159.

BIBLIOGRAPHY

- Ritzmann, O., Jokat, W., Czuba, W., Guterch, A., Mjelde, R. and Nishimura, Y. (2004). A deep seismic transect from Hovgård Ridge the northwestern Svalbard across the continental-ocean transition: A sheared margin study, *Geophysical Journal International*, 157, 683–702.
- Roest, W. R. and Srivastava, S. P. (1989). Seafloor spreading history I: Magnetic anomalies along track', in J. S. Bell (ed.), *East Coast Basin Atlas Series: Labrador Sea*, Geological Survey Canada, Map Sheet L17-1.
- Sclater, J. G., Hellinger, S. and Tapscott, C. (1977). The palaeobathymetry of the Atlantic Ocean from the Jurassic to the present, *Journal of Geology*, vol. 85, no. 5, 509–552.
- Solheim, A., Faleide, J. I., Andersen, E. S., Elverhøl, A., Forsberg, C. F., Vanneste, K., Unzelmann-Neben, G. and Channell, J. E. T. (1998). Late Cenozoic seismic stratigraphy and glacial geological development of the East Greenland and Svalbard-Barents Sea continental margins, *Quaternary Science Reviews*, vol. 17, 155–184.
- Srivastava, S. P. (1985). Evolution of the Eurasian Basin and its implications to the motion of Greenland along Nares Strait, *Tectonophysics*, 114, no. 1–4, pp. 29–53.
- Srivastava, S. P. and Tapscott, C.R. (1986). Plate kinematics of the North Atlantic, in: Vogt, P. R. and Tucholke, B. E. (ed.), *The Western North Atlantic Region*, Geological Society of America, 379–404.
- Steckler, M.S. and Watts, A.B. (1978). Subsidence of the Atlantic-type continental margin off New York, *Earth and Planetary Science Letters*, 41, 1–13.
- Talwani, M. and Eldholm, O. (1973). The boundary between continental and oceanic crust at the margin of rifted continents, *Nature*, 241, 325–330.
- Talwani, M. and Eldholm, O. (1977). Evolution of the Norwegian-Greenland Sea, *Geol. Soc. Am. Bull.* 88, 969–999.
- Tsikalas, F., Eldholm, O. and Faleide, J. I. (2005). Crustal structure of the Lofoten-Vesterålen continental margin, off Norway, *Tectonophysics*, 404, 151–174.
- U.S. Department of Commerce, National Oceanic and Atmospheric Administration, National Geophysical Data Centre (NGDC), 2006. 2-minutes Gridded Global Relief Data (ETOPO2v2), <http://www.ngdc.noaa.gov/mgg/fliers/06mgg01.html>.
- Verhoef, J., Macnab, R., Roest, W., Arjani-Hamed, J. and the project team (1996). Magnetic anomalies of the Arctic and North Atlantic and adjacent land areas. GAMMA5 (Gridded Aeromagnetic and Marine Magnetics of the North Atlantic and Arctic, 5km), Geological Survey of Canada, Open File 3125a (CD-Rom).

- Vogt, P. R., Taylor, P. T., Kovacs, L. C. and Johnson, G. L. (1979). Detailed Aeromagnetic Investigation of the Arctic Basin, *Journal of Geophysical Research*, vol. 84, B3, 1071–1089.
- Voss, M., Schmidt-Aursch, M. and Jokat, W. (2000). Variations in magmatic processes along the East Greenland volcanic margin, *Geophysical Journal International*, 177, 755–782, 10.1111/j.1365-246X.2009.04077.x.
- Weigelt, E. and Jokat, W. (2001). Peculiarities of roughness and thickness of oceanic crust in the Eurasian Basin, Arctic Ocean, *Geophysical Journal International*, 145, 505–516.
- Wold, C. N. (1992). Palaeobathymetry and Sediment Accumulation in the northern North Atlantic and southern Greenland-Iceland-Norwegian Sea, Dissertation, Christian-Albrechts-Universität zu Kiel.
- Wold, C. N. (1995). Palaeobathymetric reconstruction on a gridded database: the northern North Atlantic and southern Greenland-Iceland-Norwegian sea, from Scrutton, R. A., Stoker, M. S., Shimmiel, G. B. and Tudhope, A. W. (eds), *The Tectonics, Sedimentation and Palaeoceanography of the North Atlantic Region*, Geological Society Special Publication No. 90, 271–302.
- Wright, J. O. and Miller, K. G. (1996). Control of North Atlantic deep water circulation by the Greenland-Scotland Ridge, *Palaeoceanography*, 11(2), 157–170.

BIBLIOGRAPHY

Chapter 7

A palaeoceanographic modelling study of the Cenozoic northern North Atlantic and the Arctic Ocean

Birte-Marie Ehlers¹, Martin Butzin^{1,2}, Klaus Grosfeld¹ and Wilfried Jokat¹

¹Alfred Wegener Institute for Polar and Marine Research, Am Alten Hafen 26,
27568 Bremerhaven, Germany

²University of Bremen, MARUM-Center for Marine Environmental Sciences,
P.O. Box 33 04 40, 28334 Bremen, Germany

Global and Planetary Change
submitted 2008 December 17

7.1 Summary

The tectonic evolution of the northern North Atlantic, especially the opening of the Fram Strait, influences the ocean circulation. Today, deep-water formation in the northern North Atlantic and in the Arctic Ocean is a key driver for the global thermohaline circulation and hence, on global climate. Until now it is speculative, if there is a causal relationship between the Fram Strait opening, the northern North Atlantic and Arctic Ocean deep-water formation and Middle Miocene climate changes.

This study presents results from uncoupled ocean circulation simulations for time slices from the Middle Eocene until present day, which are based on palaeobathymetric reconstruction data. The model results indicate that the bathymetric evolution caused significant changes in the Cenozoic circulation of the northern North Atlantic.

Starting from a land-locked Arctic Ocean in the Middle Eocene (45 Ma), we found in the Early Miocene (20 Ma) that saline and warm Atlantic Water is imported to the Arctic

Ocean through the Fram Strait at about 1000 m water depth, which warms the Arctic Ocean until the Middle Miocene (15 Ma).

An interaction of the increased depth and width of the Fram Strait and the northward propagation of Atlantic surface water between Early and Middle Miocene seems to be responsible for the fully ventilation of the Arctic Ocean. The expansion of the ocean basins between the Greenland-Faeroe Ridge and the Fram Strait allowed a re-circulation of Atlantic Water and hence, enhanced the deep-water formation in the northern North Atlantic. The Middle Miocene simulation (15 Ma) results in the onset of Arctic Ocean deep-water export. Based on our ocean model runs we propose that a relationship between the Fram Strait opening, the onset of deep-water exchange and the onset of the global Middle Miocene climate optimum is likely.

Key words: Arctic region, Atlantic Ocean, Cenozoic, Ocean modelling, Tectonic and climate interactions

7.2 Introduction

The global climate has undergone significant changes during the last 60 Myr (Zachos et al., 2001). The Cenozoic climate evolution is characterised by two main characteristics: a general cooling trend, which started about 50 Ma, and the occurrence of relatively rapid changes between warmer and colder periods. Tectonic changes may have led to reorganisations in the global ocean circulation, which in turn may have had significant climatic effects. Especially, the extent and depth of the gateways between the main ocean basins have been influenced by continental movements.

Deep-water formation in the northern North Atlantic and the Arctic Ocean is a key driver of the thermohaline circulation and hence also of global climate (Aagaard et al., 1985). The only possibility to exchange deep-water between the northern North Atlantic and the Arctic Ocean is through the Fram Strait (Figure 7.1) which is today about 200 km wide and up to 3000 m deep (Jakobsson et al., 2001).

Studies about a core from the crest of the Lomonosov Ridge (Figure 7.1) in the central Arctic Ocean (IODP Expedition 302, Moran et al. (2006)) show that the change in ventilation history in the Arctic Ocean was completed about 17.5 Ma (Jakobsson et al., 2007). Furthermore, a palaeobathymetric reconstruction of the Fram Strait shows a first shallow water connection since 25 Ma and a deep-water connection since 17 Ma (Ehlers and Jokat, 2008).

The proposed timing of the opening of the Fram Strait deep-water connection (Jakobsson et al., 2007; Ehlers and Jokat, 2008) coincides with the onset of the Middle Miocene Climate Optimum (Zachos et al., 2001). Until now it is still speculative, if there exists a causal relationship between the tectonic and bathymetric evolution of the northern North Atlantic and the Arctic Ocean, the development of oceanic circulation and the global climate cooling since the Middle Miocene.

In this study, we attempt to shed light on the relationship between bathymetry, ocean

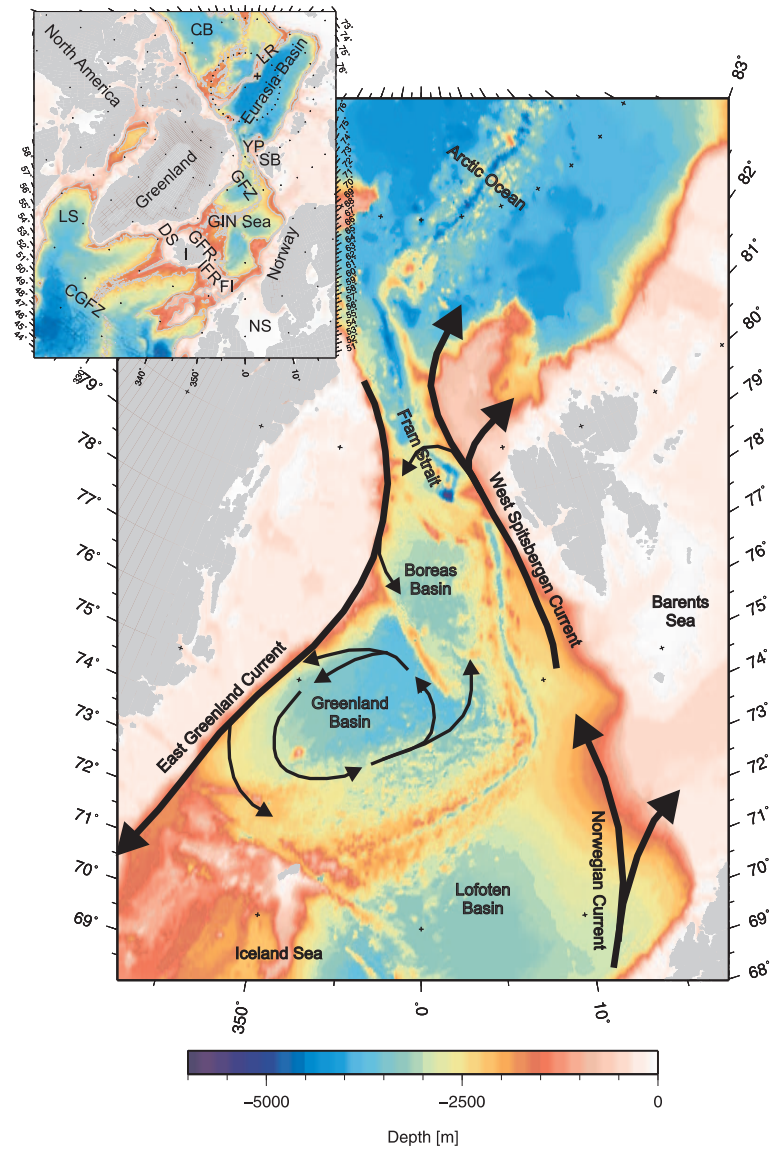


Figure 7.1: Bathymetry map of the international bathymetric chart of the Arctic Ocean (IBCAO) (Jakobsson et al., 2001) and ocean currents (after Aagaard et al. (1985) and Rudels et al. (2002)) in the northern North Atlantic. Top left: Bathymetry (Jakobsson et al., 2001). The grey lines show the 1000 m and 2000 m bathymetric contour lines. The grid points have a distance of 3° . CB: Canada Basin, CGFZ: Charlie Gibbs Fracture Zone, DS: Denmark Strait, FI: Faeroe Islands, GFR: Greenland-Faeroe Ridge, GFZ: Greenland Fracture Zone, GIN Sea: Greenland-Iceland-Norwegian Sea, I: Iceland, IFR: Iceland Faeroe Ridge, LB: Lofoten Basin, LR: Lomonosov Ridge, LS: Labrador Sea, NS: North Sea, SB: Svalbard, YP: Yermak Plateau. The black cross marks the location of the core from the IODP Expedition 302 (Moran et al., 2006).

circulations and climate changes. For this purpose we used a palaeobathymetric reconstruction (Ehlers and Jokat, 2008) as a basis for a palaeoceanographic modelling sensitivity study for the northern North Atlantic and the Arctic Ocean.

Ocean circulation in the North Atlantic and the Arctic Ocean

The global ocean circulation is responsible for a substantial part of the equator-to-pole heat transport through its meridional overturning circulation (MOC) (e.g. IPCC (2007) and references therein). At the present day, deep-water formation occurs in the North Atlantic and (to lesser extent) in the Southern Ocean. Hence, the North Atlantic and the adjacent Fram Strait and Arctic Ocean play an important role in the global ocean circulation due to its exchange of water masses, heat and salt.

The present status of the circulation in the Fram Strait area (Figure 7.1) is largely derived from hydrographic measurements and observations of ice motion, whereas the ice drift appears to be decoupled from the circulation below a few tens of meters of water depth (Aagaard, 1989). The circulation between the northern North Atlantic and the Arctic Ocean consists of the northward flowing Norwegian Current (NC), which mixes with dense, saline water leaving the Barents Sea, resulting in the West Spitsbergen Current (WSC) (Quadfasel et al., 1987) and the southward flowing East Greenland Current (EGC) (Figure 7.1). Volume transports add up to 9.5 ± 1.4 Sv ($1 \text{ Sv} = 1 \cdot 10^6 \text{ m}^3 \text{ s}^{-1}$) to the north and 1.1 ± 1.7 Sv to the south in the monthly average (Fahrback et al., 2001).

Warm and saline Atlantic Water (AW) flows into the Arctic Ocean and cools by heat loss to the atmosphere and freshens mainly by river inflow and by mixing with Pacific waters. The mixing forms a fresh and shallow outflow of Polar waters in the upper 1500 m (Holland et al., 2001; Curry and Mauritzen, 2005). Furthermore, the Arctic Ocean today is not simply a passive recipient of ventilated water from the south, but an important source of dense water, which is exported southward through the Fram Strait (Aagaard et al., 1985). Schauer and Fahrback (2004) characterise North Atlantic deep-water (NADW) as water below 700 m. North of the Greenland-Faeroe Ridge (Figure 7.1) the source of the southward flowing current, which crosses the Ridge to the North Atlantic, is not water from the bottom of the Norwegian-Greenland Sea but from a depth close to 1000 m (Peterson and Rooth, 1976).

The complicated bathymetry of the Fram Strait leads to a splitting of the WSC in at least three branches (Quadfasel et al., 1987). One branch follows the shelf edge and enters the Arctic Ocean north of Svalbard. It crosses the Yermak Plateau. Here, the flow is limited to the Yermak Plateau depth of approximately 600 m (Schauer and Fahrback, 2004). The second branch flows northward along the north western slope of the Yermak Plateau. The third one re-circulates immediately in the Fram Strait between 78°N and 80°N (Perkin and Lewis, 1984; Bourke et al, 1988; Gascard et al., 1995). This Re-circulated Atlantic Water (RAW) merges with the Polar Water from the north and flows in the EGC southward to the southern tip of Greenland (Swift and Aagaard, 1981). The size and strength of the three northward flowing branches largely determine the input of the oceanic heat to the Arctic Ocean (Schauer and Fahrback, 2004).

The formation of sea ice in the Arctic Ocean increases the salinity and hence, the density of the seawater. As a consequence Arctic Intermediate Water (AIW) sinks and merges with inflowing AW. Saline deep-water is transported by the EGC through the Fram Strait to the south (Schauer and Fahrback, 2004). This Fram Strait overflow affects the water mass modification in the Greenland-Iceland-Norwegian (GIN) Sea. Young and oxygen-rich intermediate water flows through the Denmark Strait and across the Iceland-Faeroe Ridge and contributes a major portion to the North Atlantic Deep Water (NADW), which ventilates the entire Atlantic Ocean (Aagaard et al., 1985; Johannessen, 1986).

For this study we outline the most important characteristics of the northern North Atlantic and Arctic Ocean circulation which probably have significant influence on the present day climate:

- the northward flowing Norwegian and West Spitsbergen currents with warm and saline Atlantic Water
- the Atlantic Water re-circulation in the Fram Strait and south of the Fram Strait
- the latitude of sinking of dense Atlantic Water beneath colder and low-saline Arctic Water and hence, the possibility of absorption of oxygen of the Atlantic Water
- the outflow of cold and low-saline Arctic Water through the Fram Strait
- the formation of sea-ice in the Arctic Ocean which increases the density of surface water
- the merging of fresh Arctic Water and Atlantic Water in the Arctic Ocean forming deep-water
- the outflow of deep-water from the Arctic Ocean through the Fram Strait
- the southward flowing East Greenland Current
- the outflow of oxygen-rich water of the East Greenland Current through the Denmark Strait to the Atlantic Ocean

Here, we compare the present day circulation with simulations for time slices from the Middle Eocene (45 Ma), the Early Miocene (20 Ma) and the Middle Miocene (15 Ma).

7.3 Palaeobathymetry data

For a palaeoceanographic study global palaeobathymetric data are required to simulate the influences to global ocean circulations. Müller et al. (2008) provide palaeobathymetric data for the oceanic crust of the world oceans (Figure 7.2). The missing sediment cover of the shallow continental margins required to assume an artificial depth setting for the palaeobathymetry of 200 m below sea level during the Eocene and Miocene. Additionally, we assume a depth of the land masses as 1000 m above the present day sea level.

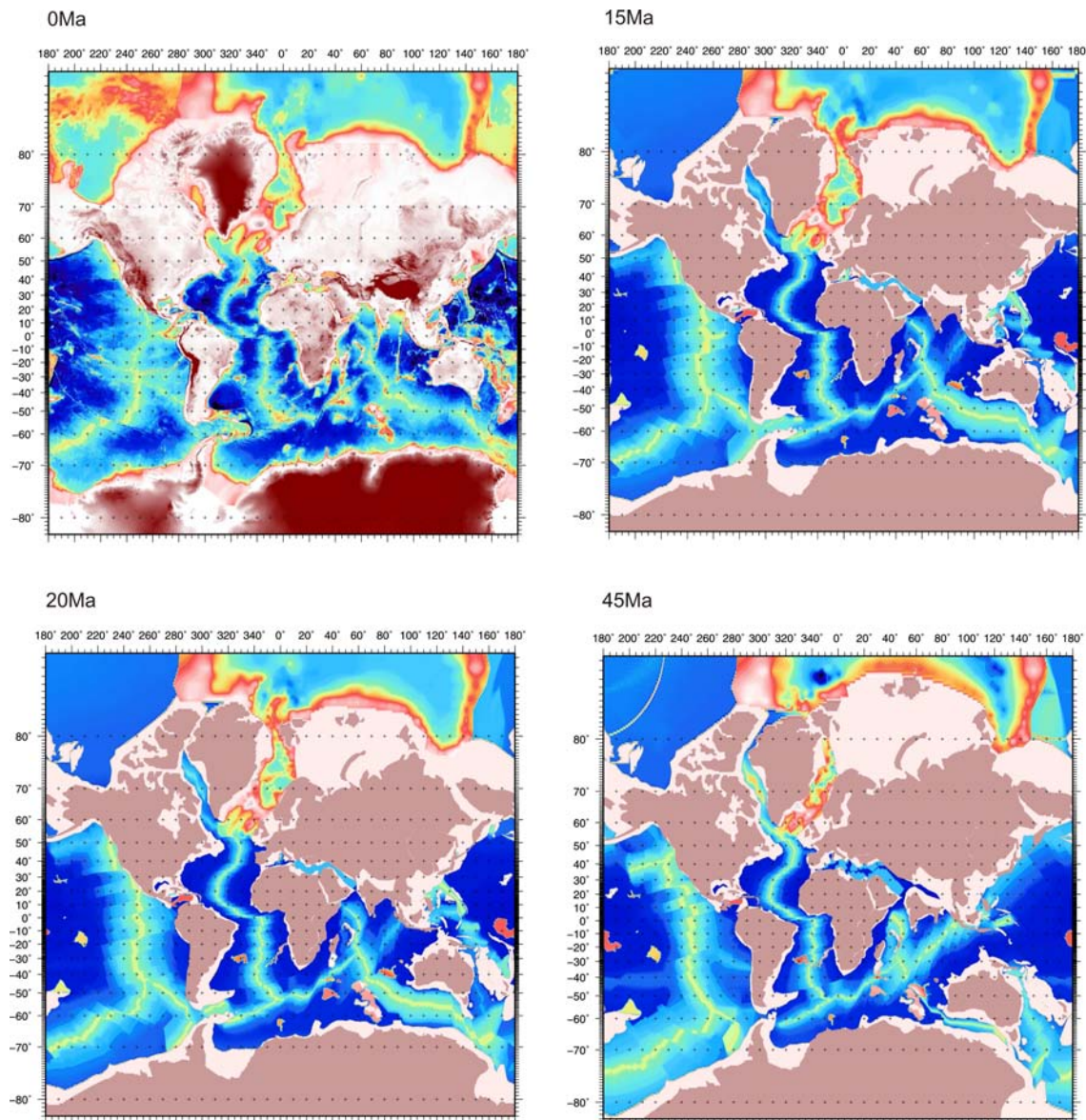


Figure 7.2: Palaeobathymetric reconstruction for 0 Ma, 15 Ma, 20 Ma and 45 Ma (Ehlers and Jokat, 2008) included into the palaeobathymetric data of Müller et al. (2008). The modelled seafloor depth is the basis for the palaeoceanographic modelling.

In this study we focus on the Fram Strait region. A more detailed palaeobathymetric reconstruction for the northern North Atlantic and the Eurasia Basin is available for the investigation area (Ehlers and Jokat, 2008). This reconstruction is based on new magnetic and seismic data and shows detailed seafloor depths from the Charlie Gibbs Fracture Zone to the Eurasia Basin, which is bounded by the European and Asia margins and the Lomonosov Ridge. Compared to the global palaeobathymetry data (Müller et al., 2008),

the palaeobathymetric data in the Fram Strait area have a high resolution ($1^\circ \times 1^\circ$ and $0.5^\circ \times 0.5^\circ$). These palaeobathymetric data (Ehlers and Jokat, 2008) are nested into the global data set (Müller et al., 2008) for four time slices: present day, Middle Miocene (15 Ma), Early Miocene (20 Ma) and Middle Eocene (45 Ma) (Figure 7.2). Since we do not have any atmospheric forcing data for our time slices older than present day, we take the present day configuration for a control run in order to investigate the principal flow pattern and hydrography of our set-up. The older time slices of 15 Ma and 20 Ma should point to the onset of deep-water exchange while the time slice of 45 Ma should show the status of the land-locked Arctic Ocean.

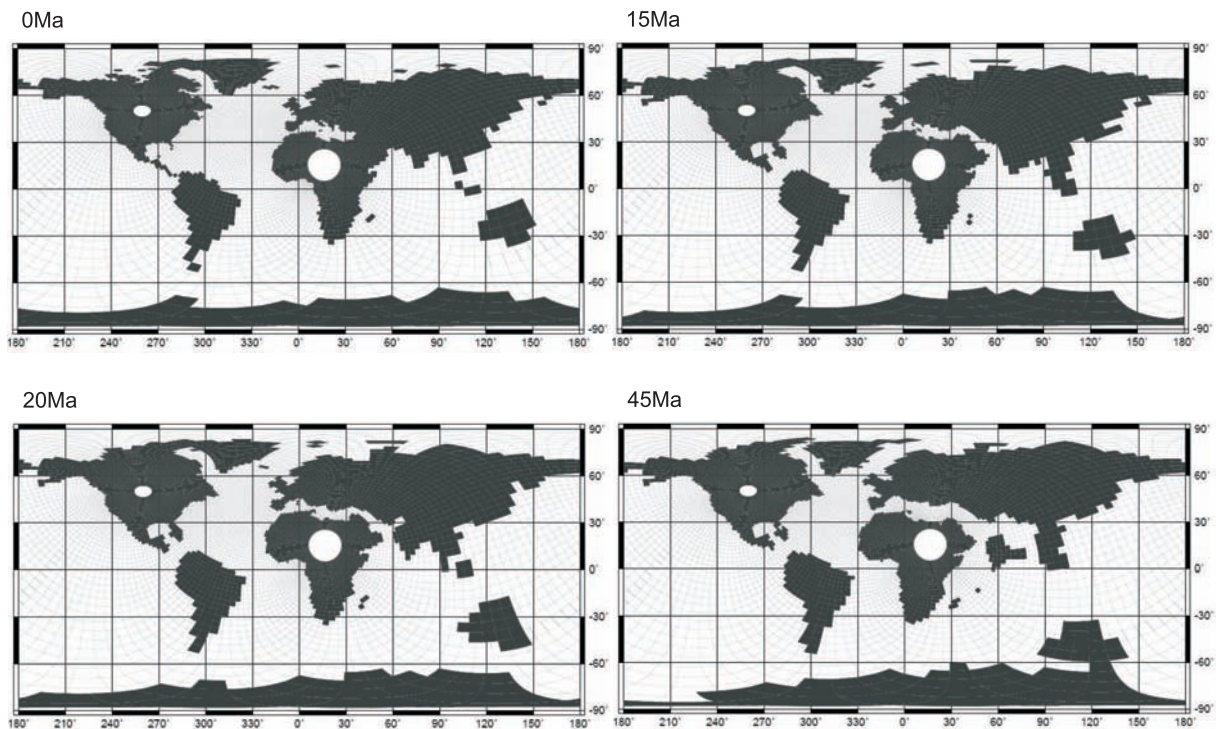


Figure 7.3: Land-sea masks for the modelled time slices with the chosen poles in North America and North Africa. The black lines show the distribution of the model grid cells.

7.4 Model

The selected palaeobathymetric reconstruction is taken as input fields for an ocean circulation model. In this study we use version 1.3 of the global Max-Planck-Institute ocean model (MPIOM 1.3) (Marsland et al., 2003). The formal horizontal resolution is 3° (longitude) and 1.8° (latitude) on an Arakawa C-grid (Arakawa and Lamb, 1977). The MPIOM 1.3 model uses a bipolar orthogonal spherical coordinate system (Marsland et al., 2003), which allows to shift the poles. In this study we positioned the poles on North America and

North Africa to enhance the resolution in the North Atlantic compared to traditional configurations having one pole on Antarctica (Figure 7.3). The vertical resolution is 20 levels in water depth from 10 m to 5350 m. The model is integrated for 1000 years to quasi steady state conditions. This might not be true for the deep ocean, but for shallow and intermediate water depth.

In all experiments the model is forced with climatological data for the present day (OMIP forcing; Röske (2006)). This implies that the model results mirror the response of the ocean circulation to tectonic forcing only, but do not capture the adjustment to presumed changes in palaeoclimate.

The model experiments are analysed for zonal and meridional velocities, for the salinity and temperature and for salinity-depth and temperature-depth distributions in the northern North Atlantic and the Arctic Ocean. Additionally, the Atlantic MOC between 15°S and 85°N is calculated.

7.5 Results

For a detailed analysis of the evolution of the ocean circulation in the northern North Atlantic and the Arctic Ocean we present bathymetric maps for the present day (Jakobsson et al., 2001) and the Cenozoic (Ehlers and Jokat, 2008; Müller et al., 2008) with resulting ocean flow directions for different water depths. Figures 7.4, 7.5 and 7.6 show the direction of modelled currents at water depths of 400 m, 1125 m, 1400 m and 1750 m for the present day bathymetry and the palaeobathymetry of 15 Ma and 20 Ma.

In addition we show modelled salinities at the sea surface (Figures 7.7, 7.8 and 7.9) and modelled salinity and temperature distributions along sections representing the West Spitsbergen Current (WSC) and the East Greenland Current (EGC) for present day conditions and for 15 Ma and 20 Ma (Figures 7.10–7.11, 7.12, 7.13, 7.14 and 7.15). We also analyse vertical profiles of salinities and temperatures for all four time slices along the WSC (Figure 7.16) and the EGC (Figure 7.17) and in the Arctic Ocean (Figure 7.18).

Present day control simulation

The present day control experiment shows a northward flowing water mass with a salinity of up to 35 PSU along the Norwegian Margin (Figure 7.7), which represents the Norwegian Current (NC) and is originated in the Atlantic Ocean. Saline inflow of surface water corresponds to the WSC and reaches the Arctic Ocean through the eastern Fram Strait. Another branch transports water to the Barents Sea north of Norway. We find a layer of saline (35–35.2 PSU) and warm ($\sim 5^\circ\text{C}$) AW with a thickness of up to 500 m in the GIN Sea (Figures 7.10 and 7.16). Figures 7.4 and 7.7 show that the modelled WSC reaches up to 80°N at the surface and at 400 m water depth (Figures 7.7, 7.10 and 7.16).

In the GIN Sea and in the Fram Strait we find a pronounced re-circulation at the surface and at a water depth of 400 m (Figure 7.4). Parts of the northward flowing WSC turn west and completely re-circulate (as RAW) into the EGC. With increasing depth the

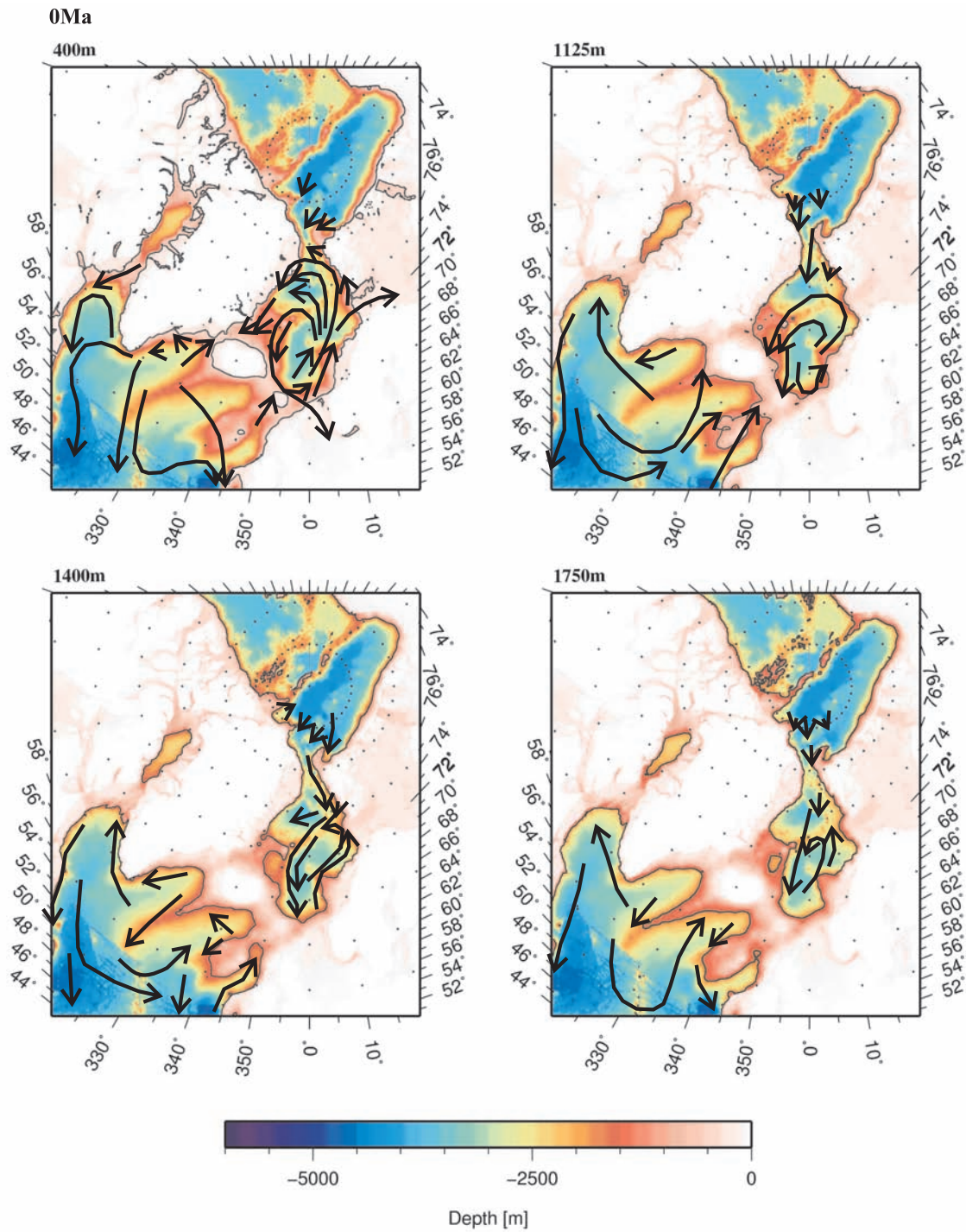


Figure 7.4: Present bathymetric map with modelled ocean current directions for 400 m, 1125 m, 1400 m and 1750 m water depth. The black line shows the respective contour line.

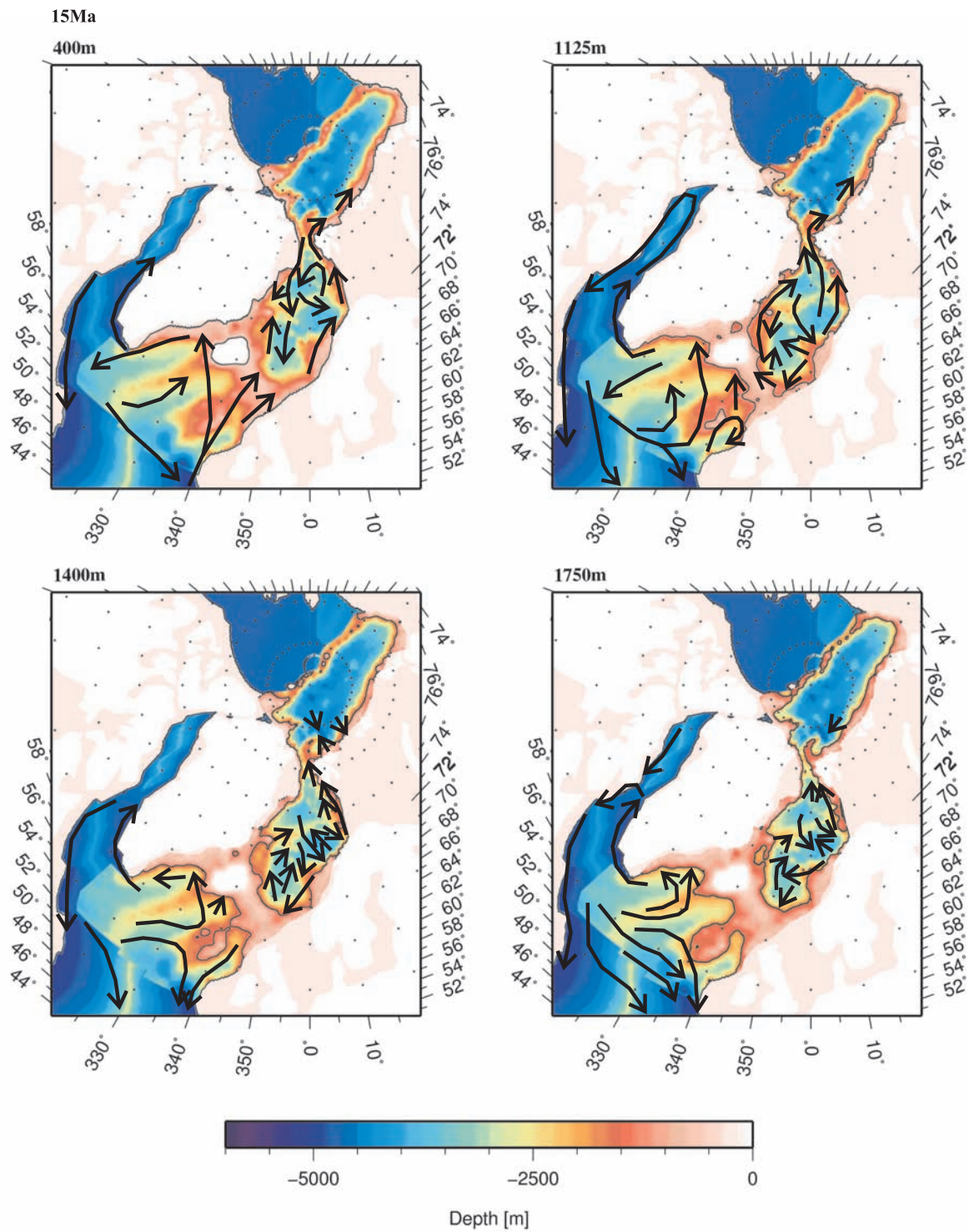


Figure 7.5: Palaeo-bathymetric map for Middle Miocene (15 Ma) with modelled ocean current directions for 400 m, 1125 m, 1400 m and 1750 m water depth. The black line shows the respective contour line.

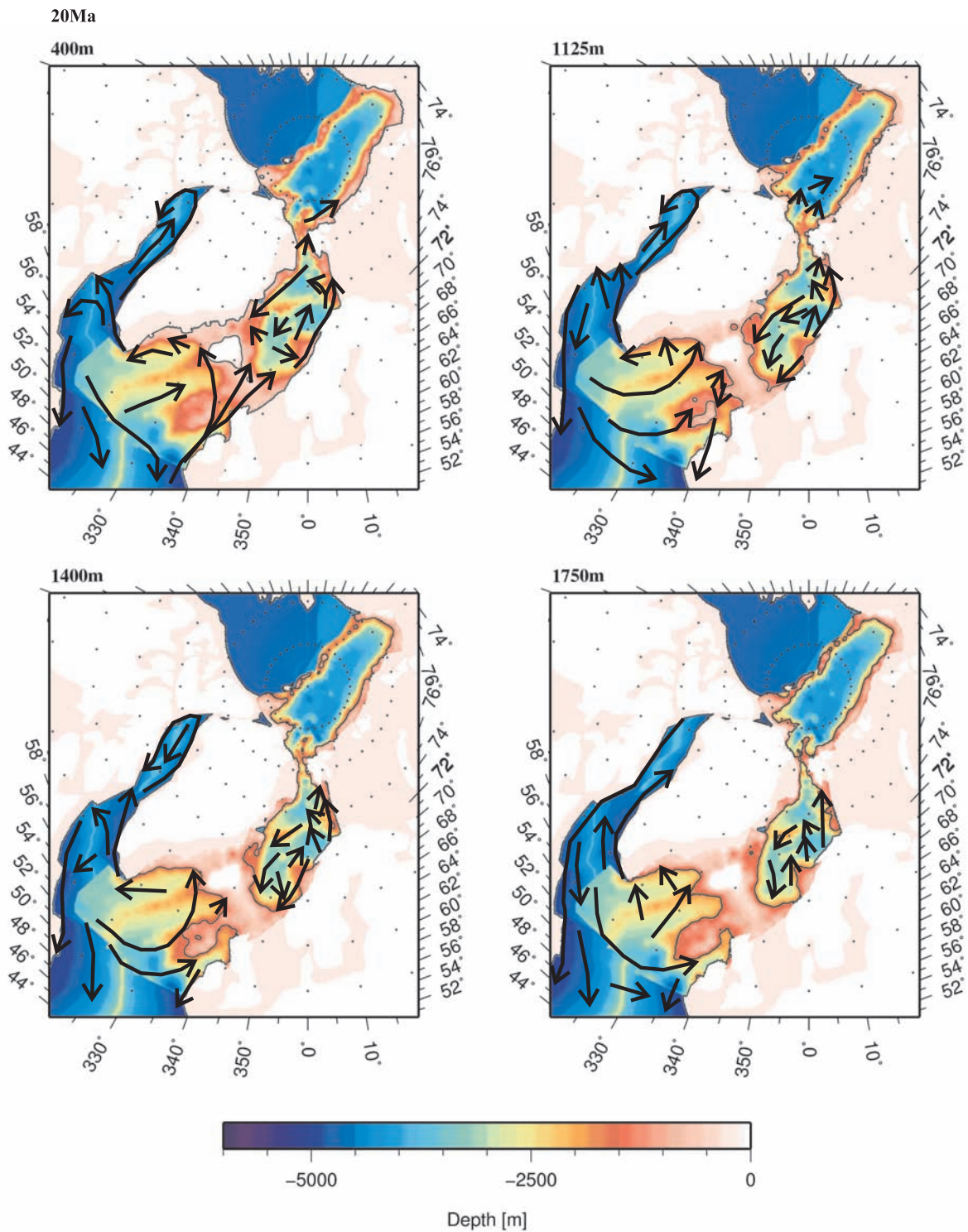


Figure 7.6: Palaeo-bathymetric map for Early Miocene (20 Ma) with modelled ocean current directions for 400 m, 1125 m, 1400 m and 1750 m water depth. The black line shows the respective contour line.

radius of re-circulation decreases. Below 1125 m a re-circulation is confined to the Lofoten Basin and to the eastern Iceland Sea (Figure 7.4).

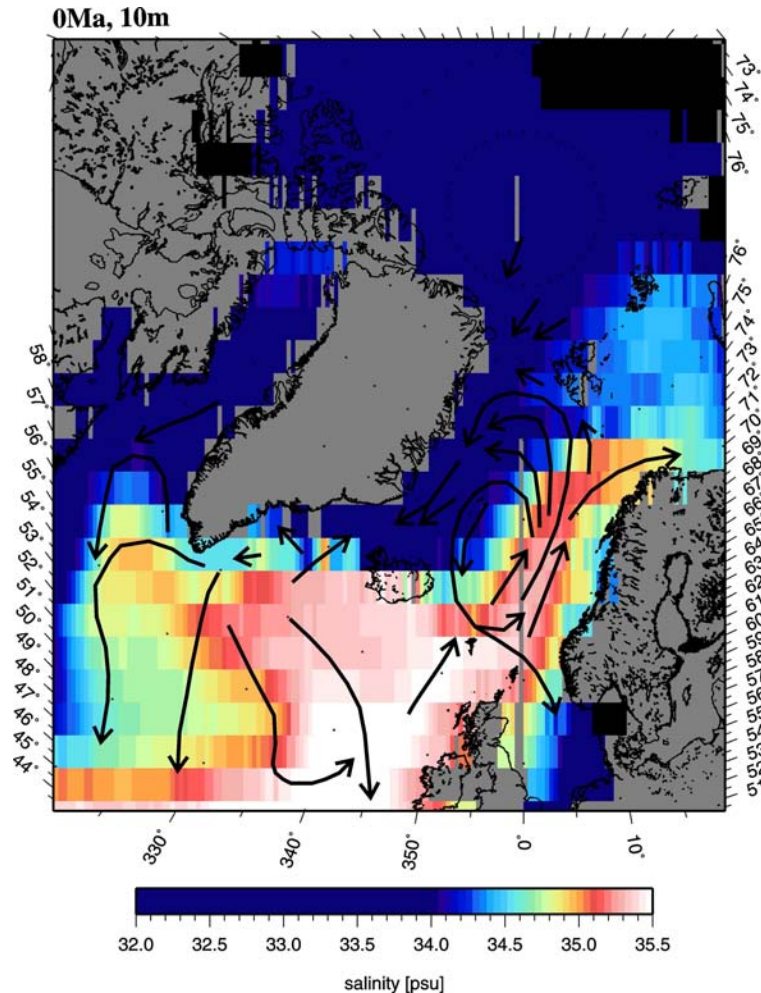


Figure 7.7: Modelled salinities and currents in 10 m depth for the present day condition.

We find outflow of cold (-1°C) and low-saline ($<34\text{PSU}$) water in the upper 600 m of the western Fram Strait (Figure 7.13 and 7.10), which is associated with the EGC. In the Eurasia Basin salinity is constant at about 34.8 PSU and temperature is slightly decreasing from 1.5°C to 0.4°C , which indicates a vertical mixing of the lower water column (Figure 7.18).

Moreover, we observe a NADW outflow from the Arctic Ocean through the Fram Strait (Figure 7.4, 1400 m and 1750 m). This outflow crosses the Boreas Basin and merges with RAW. Figure 7.10, 7.13 and 7.17 also indicate salinity and temperature distributions, which can be associated with the outflow of deep-water.

The EGC follows the bathymetry of the East Greenland shelf to the Greenland-Faeroe Ridge (Figure 7.4). South of 80°N salinity and temperature are increased (Figure 7.13).

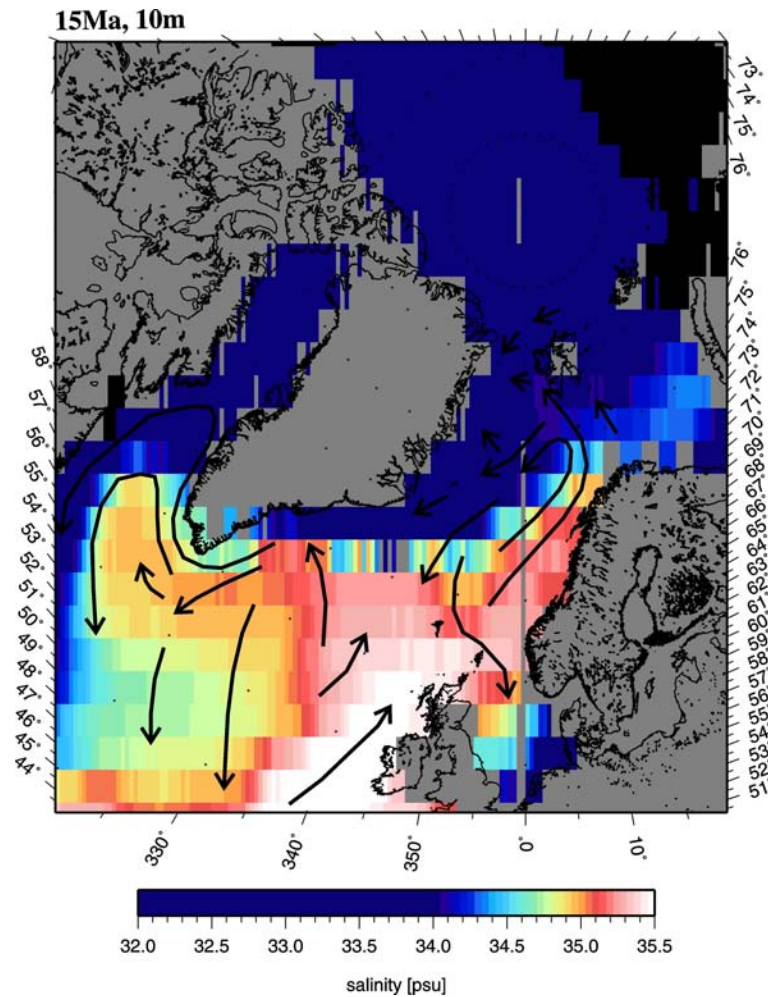


Figure 7.8: As for Figure 7.7, but for Middle Miocene (15 Ma).

Below 500 m a layer with a salinity of ~ 35 PSU and a temperature of about 3°C is observed (Figure 7.17), which results from the merging with the RAW. This experiment results in an outflow of surface-water (Figure 7.7) and water with a depth up to 400 m (Figure 7.4) transported by the EGC through the Denmark Strait.

The Atlantic meridional overturning circulation (Atlantic MOC) for present day conditions shows a maximum volume transport of 18 Sv located south of the Greenland-Faeroe Ridge between 500 m and 1700 m water depth (Figure 7.19(a)). Compared to the results by Marsland et al. (2003), we find a higher volume transport north of 70°N . The difference might be due to differences in the model grid setup.

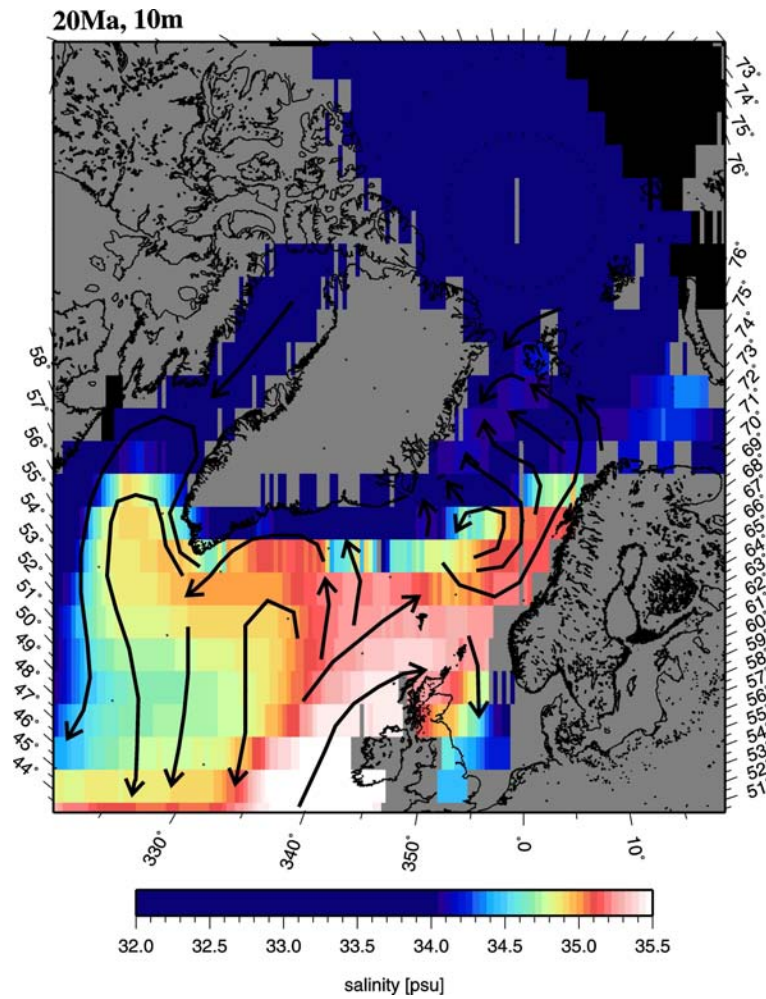


Figure 7.9: As for Figure 7.7, but for Early Miocene (20 Ma).

Cenozoic scenarios

In this section we describe the results of the Cenozoic time slice experiments. The description begins with the Middle Eocene and steps forward in time following Earth's history.

Middle Eocene (45Ma):

The Atlantic MOC exhibits a maximum volume transport of about 5 Sv north of 60°N between 300 m and 750 m depth (Figure 7.19(d)). There is no deep-water formation but southward export of intermediate water with a rate of 3 Sv.

In the Arctic Ocean salinities are low (33.2 PSU) at the sea surface and increase with depth up to 34.7 PSU (2200 m). Analogously, water temperatures increase with depth from -1.9°C at the sea surface to 0.6°C close to the bottom (Figure 7.18). According to the bathymetric reconstruction for this time slice the deep Arctic Ocean is land-locked there

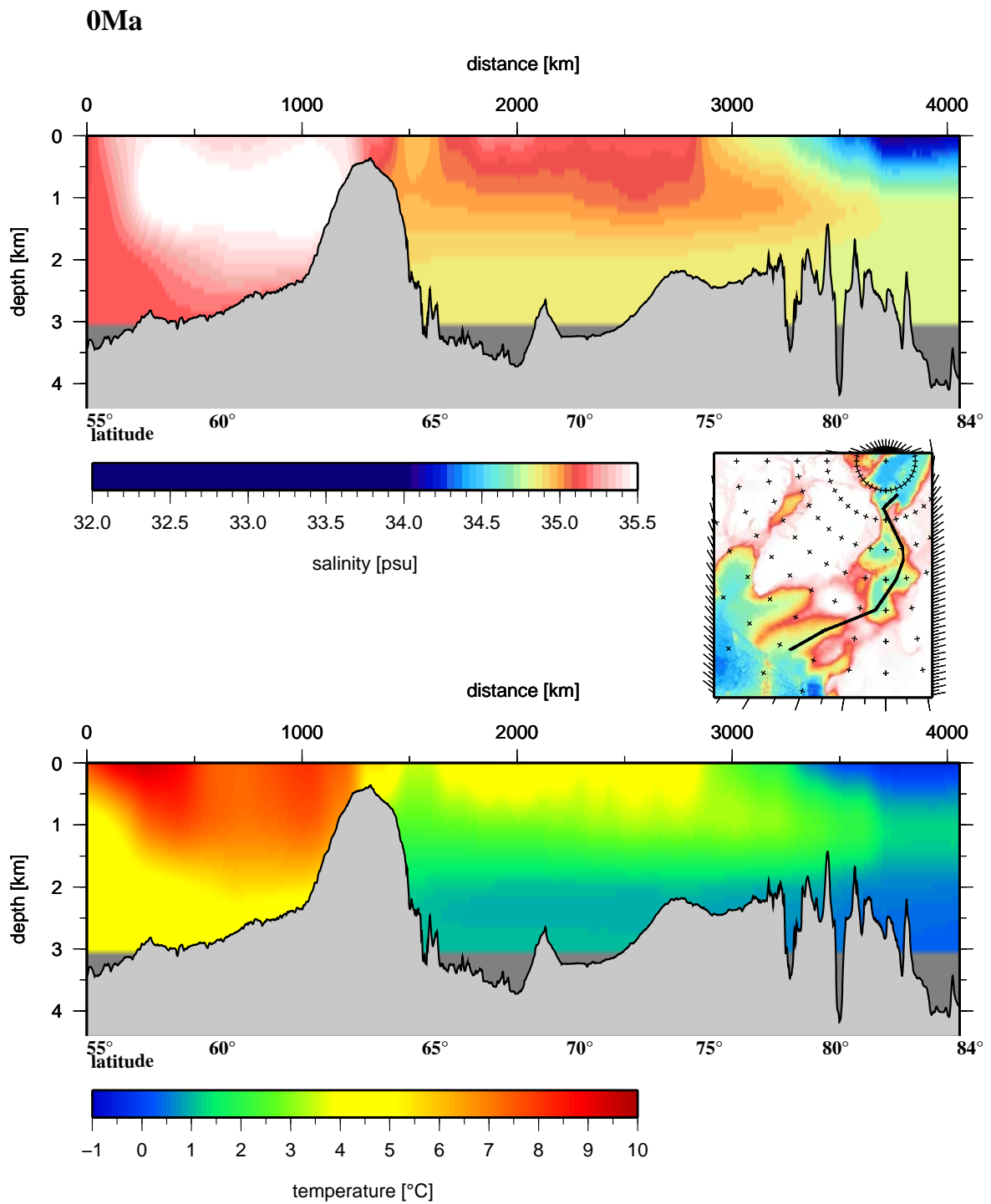


Figure 7.10: Modelled salinity (top) and temperature (bottom) of the West Spitsbergen Current for the present day conditions. Right: bathymetry map with presented profile.

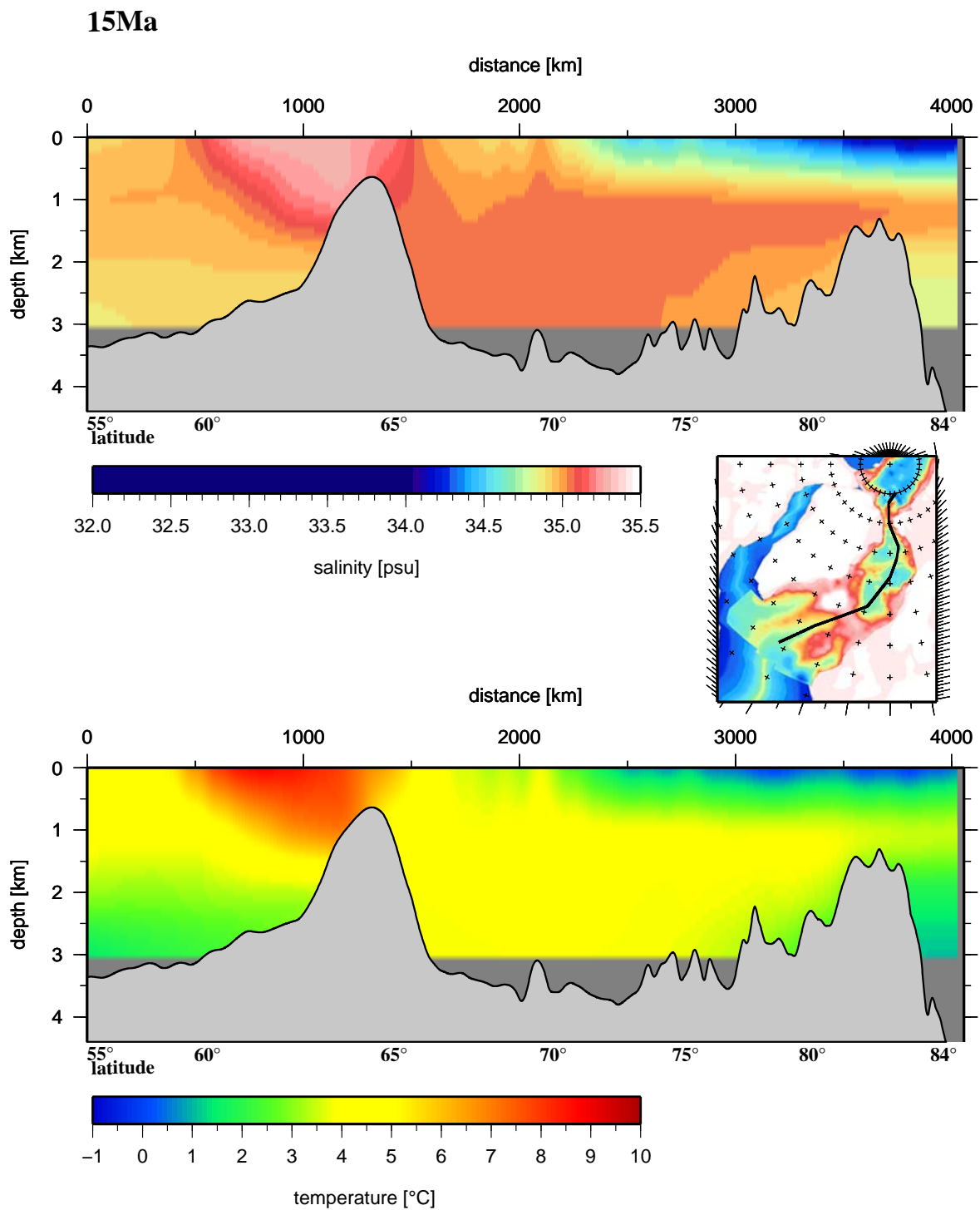


Figure 7.11: As for Figure 7.10, but for Middle Miocene (15 Ma). Right: bathymetry map with section leg.

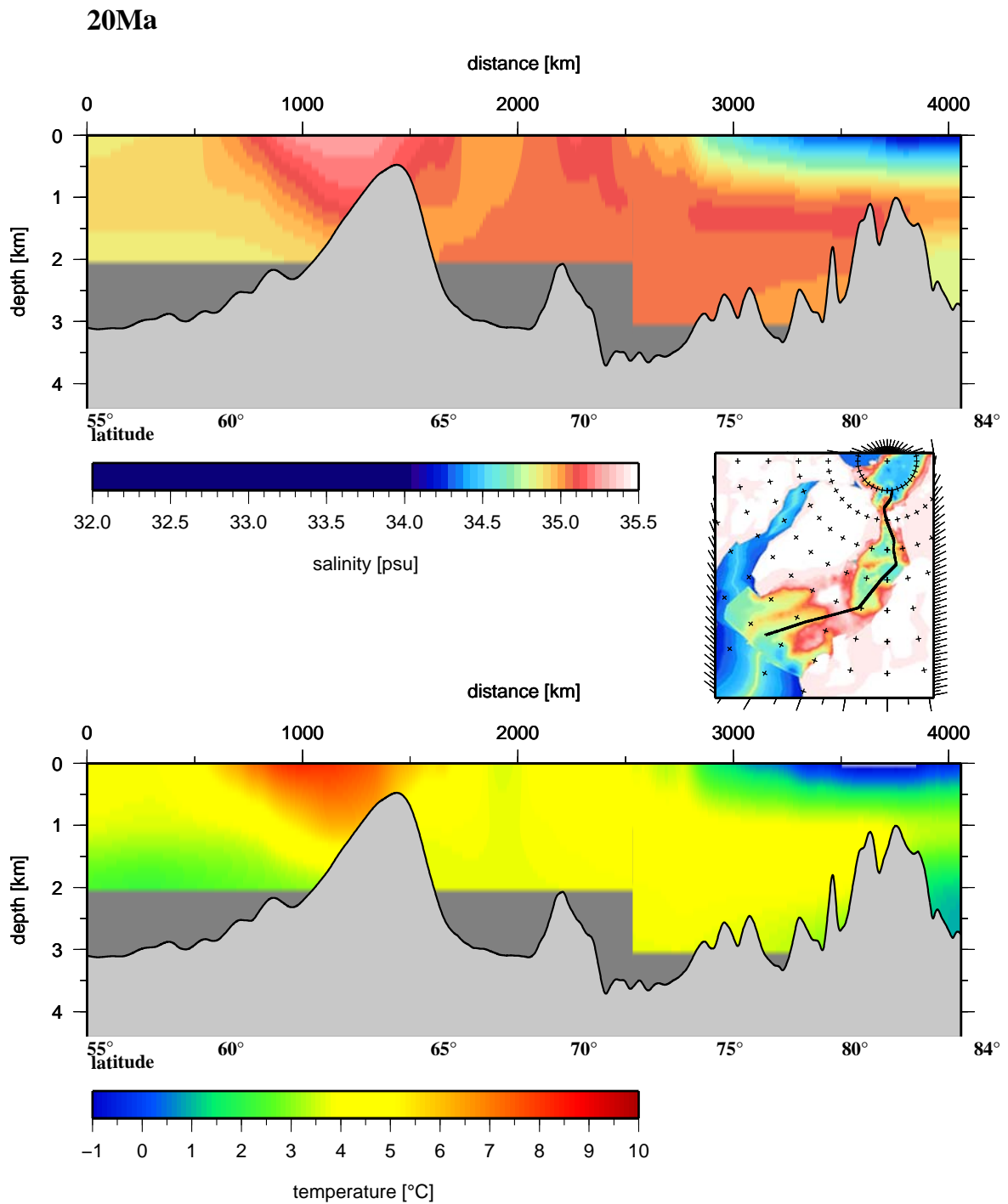


Figure 7.12: As for Figure 7.10, but for Early Miocene (20 Ma). Right: bathymetry map with section leg.

is no deep-water exchange between the northern North Atlantic and the Arctic Ocean. Hence, we do not show any profile data for this time slice.

Early Miocene (20 Ma):

The Atlantic MOC displays a maximum overturning rate of about 12 Sv at about 80 °N and modest deep-water formation. Southward deep-water export amounts about 7 Sv (Figure 7.19(c)).

The model shows at the sea surface northward flowing water with salinities of up to 35.25 PSU along the Norwegian Margin. The surface flow ceases at 75 °N at the sea surface (Figure 7.9). At a depth of 400 m water from the south crosses the Fram Strait towards the Arctic Ocean (Figure 7.6). Figure 7.12 indicates that in a water depth of 1000 m saline and warm water is transported into the Arctic Ocean. Below 1125 m there is no evidence for a water exchange between the northern North Atlantic and the Arctic Ocean (Figure 7.6).

Figure 7.9 shows a narrow re-circulation of Atlantic surface water at about 70 °N. North of 70 °N the flow is towards the East Greenland Margin. We find a weak re-circulation in 400 m water depth (Figure 7.6) at 75 °N. Below 1125 m the simulation reveals a northward current along the northern Norwegian and the Barents Sea margins. North of 70 °N we do not observe AW at the surface, but at a depths below 500 m (Figure 7.9 and 7.12).

In the eastern Fram Strait, surface-water leaves the Arctic Ocean as a 500 m thick layer and flows south to about 75 °N (Figure 7.12). The western Fram Strait is crossed by cold (-1 °C) and low-saline (34 PSU) water with salinities and temperatures increasing to the south (Figure 7.15).

Between 500 m and 1000 m water depth we find a salinity of 35 PSU and a temperature of 3.5 °C (Figure 7.18). Both, salinity and temperature in this depth are significant increased compared to the remaining water column.

Figures 7.12 and 7.15 do not indicate a deep-water export from the Arctic Ocean. The model results show that surface-water from the Arctic is transported to the Denmark Strait, where a weak overflow to the North Atlantic exists (Figure 7.15). Although we do not find re-circulation of AW in deeper layers, saline (35.1 PSU) and warm (5.5 °C) water (Figure 7.15) flows to the south (Figure 7.6) along the East Greenland Margin.

Middle Miocene (15 Ma):

The Atlantic MOC exhibits a maximum volume transport of about 13 Sv north of 70 °N, and southward deep-water fluxes of up to 10 Sv (Figure 7.19(b)). Compared to 20 Ma deep-water formation intensifies in terms of water fluxes and convection depths.

Northward flowing water with salinities of up to 35 PSU is found along the Norwegian Margin (Figure 7.8). One branch of the flow turns east to the Barents Sea north of Norway. A small lower-saline branch (~34.25 PSU) flows northward towards the Spitsbergen Margin. We do not observe an outflow of saline surface-water to the Arctic Ocean. Flow of saline surface-water reaches about 77 °N. Figure 7.11 indicates sinking of AW between 70 °N and 75 °N in the GIN Sea. In a depth of 1000 m warm (up to 5 °C) and saline (up to 35 PSU) water is transported through the Fram Strait to the Arctic Ocean (Figure 7.5).

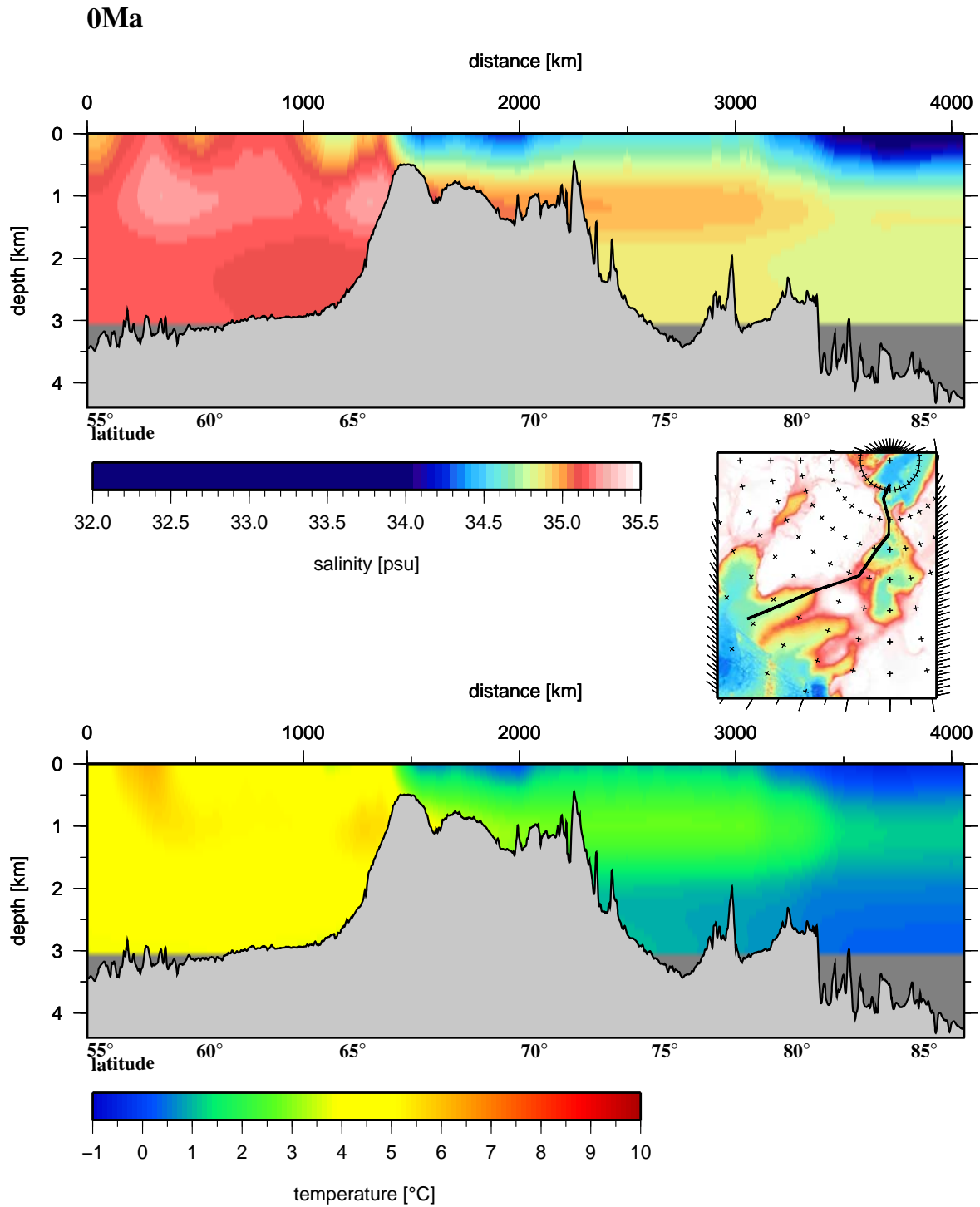


Figure 7.13: Modelled salinities (top) and temperatures (bottom) along a section following the modern East Greenland Current, present day control simulation. Right: bathymetry map with section leg.

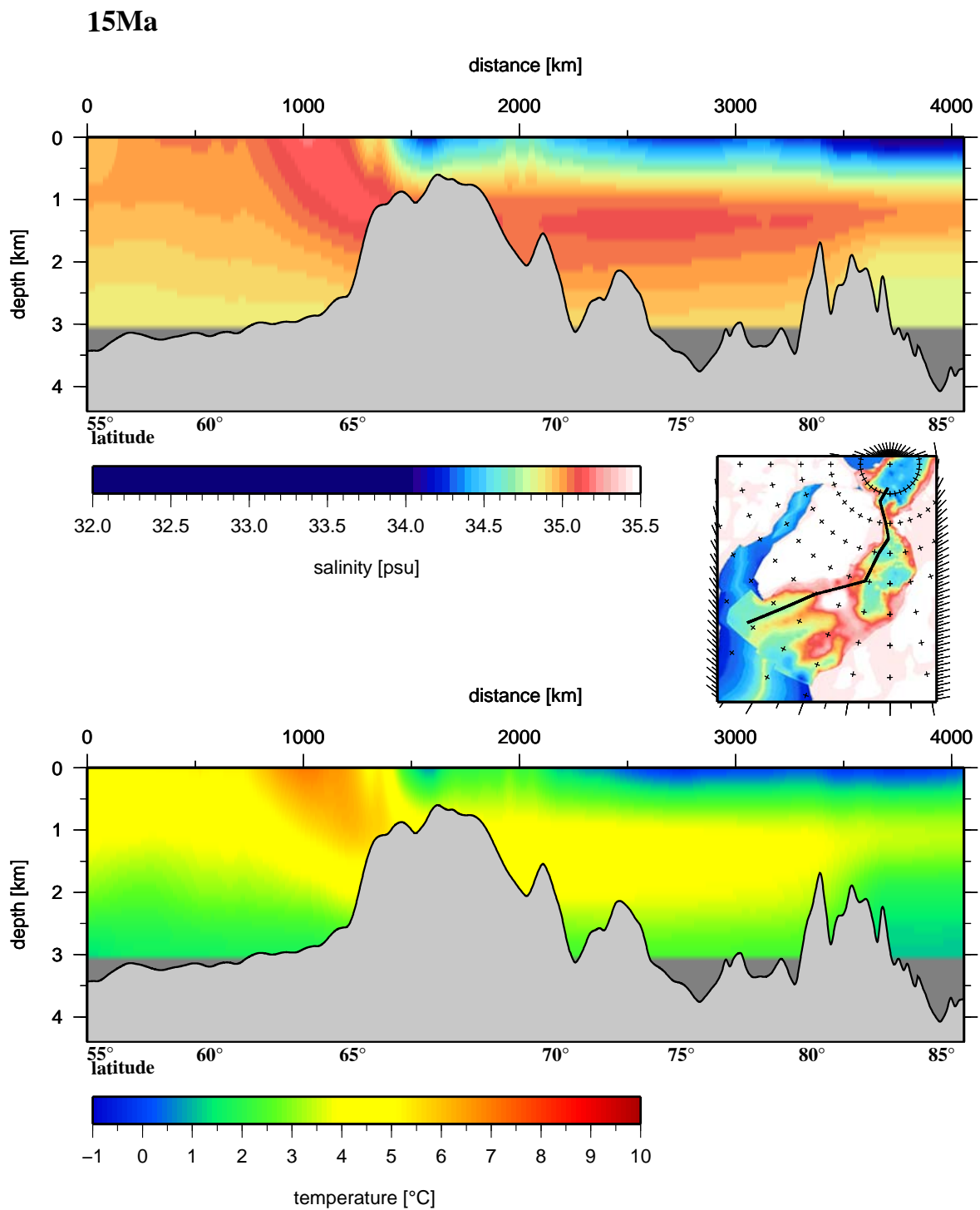


Figure 7.14: As for Figure 7.13, but for Middle Miocene (15 Ma). Right: bathymetry map with section leg.

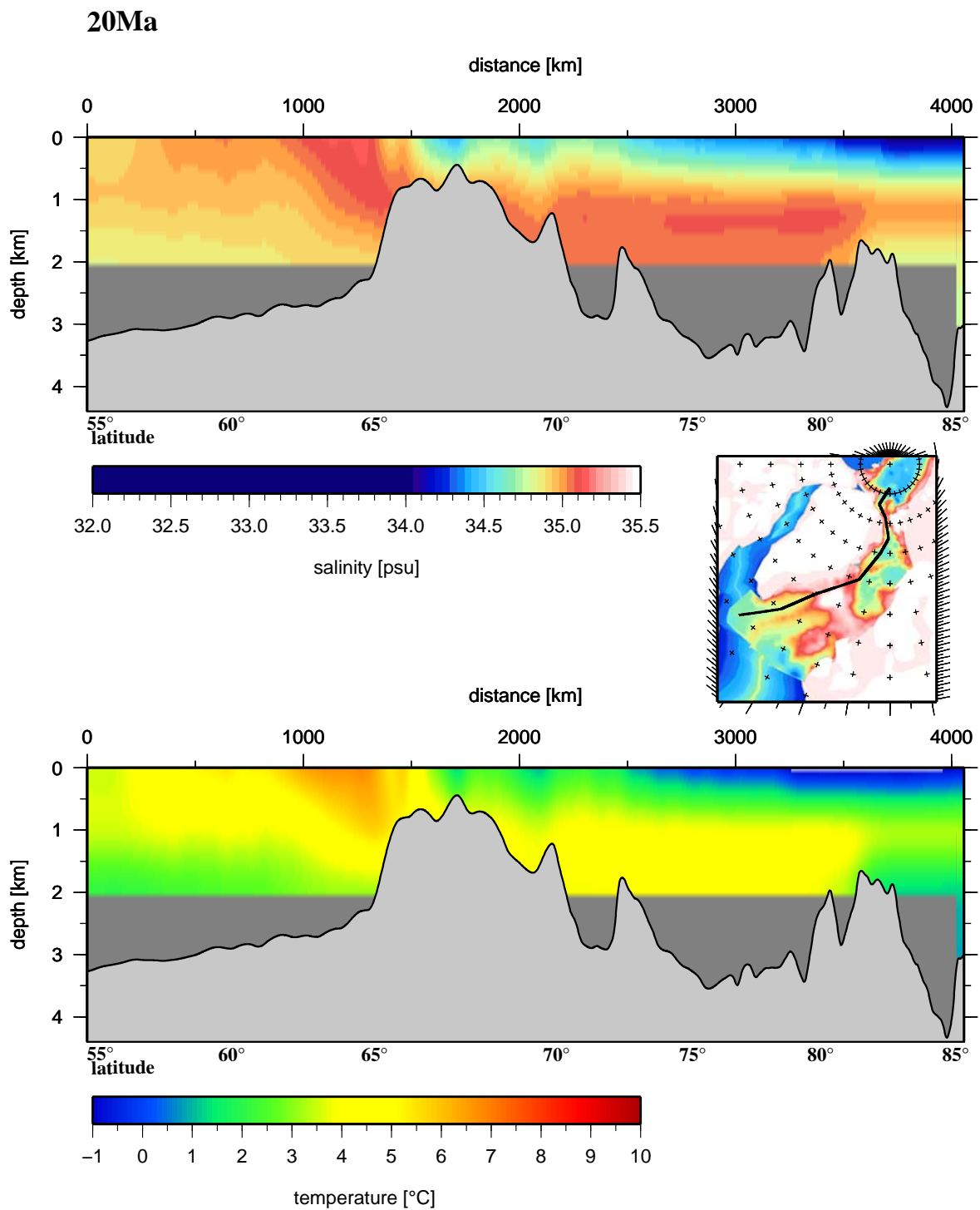


Figure 7.15: As for Figure 7.13, but for Early Miocene (20 Ma). Right: bathymetry map with section leg.

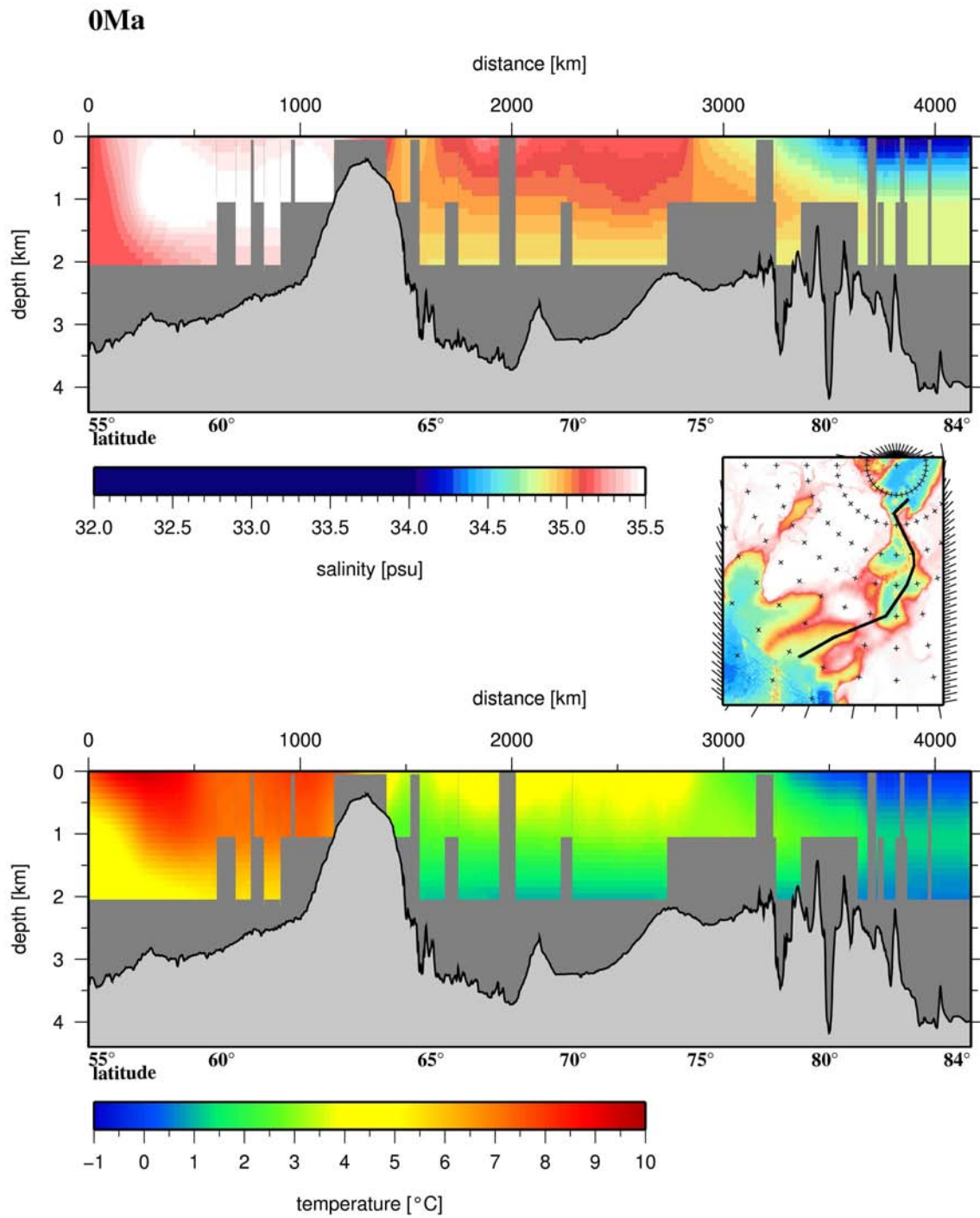


Figure 7.16: Vertical profiles of salinities and temperatures averaged along the West Spitsbergen Current for the present day (0 Ma), Middle Miocene (15 Ma), Early Miocene (20 Ma) and Middle Eocene (45 Ma).

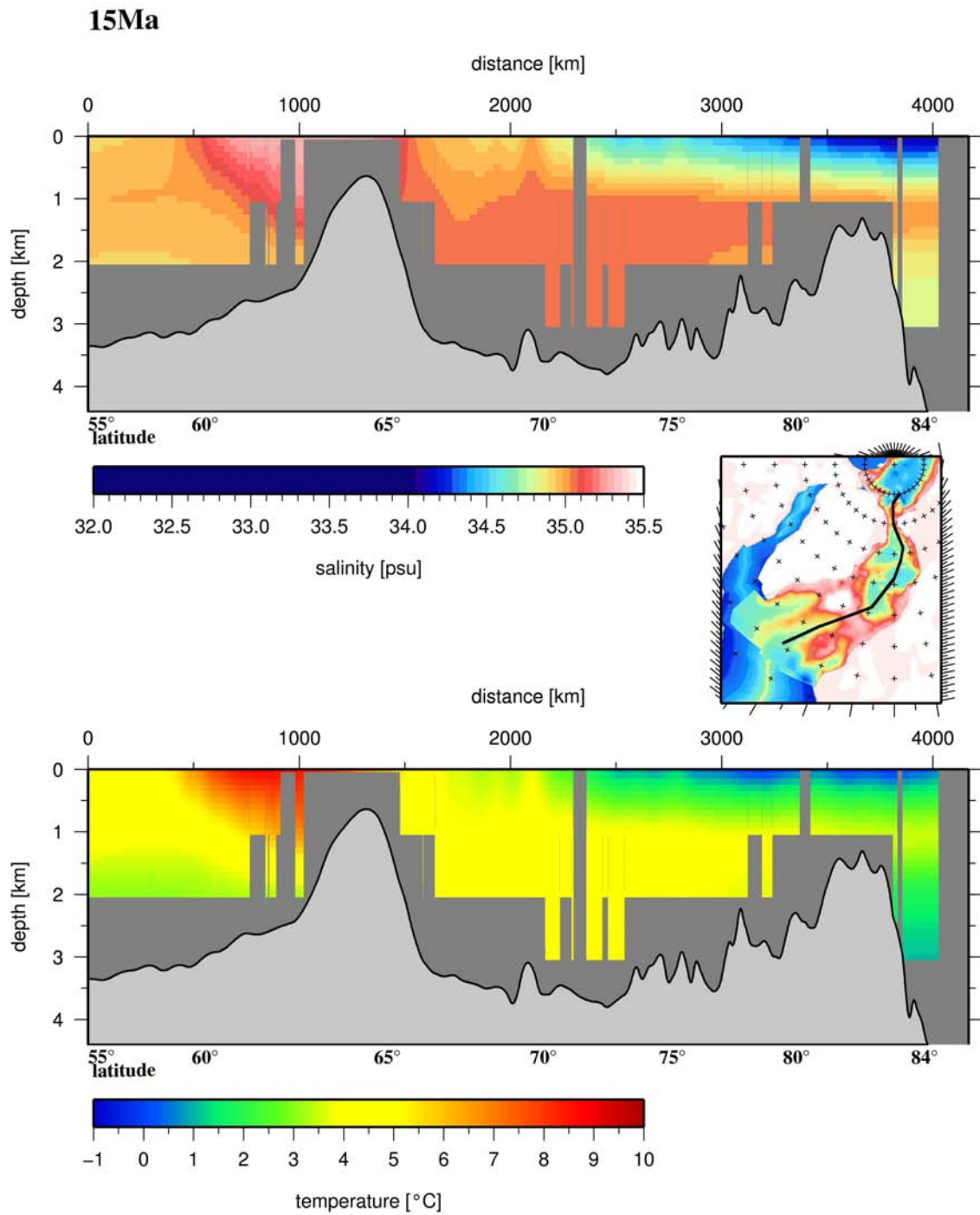


Figure 7.17: As Figure 7.16, but for the East Greenland Current.

Below 1400 m the simulation gives no evidence for a water exchange.

Re-circulation of AW is observed at the sea surface (Figure 7.8) and in 400 m water

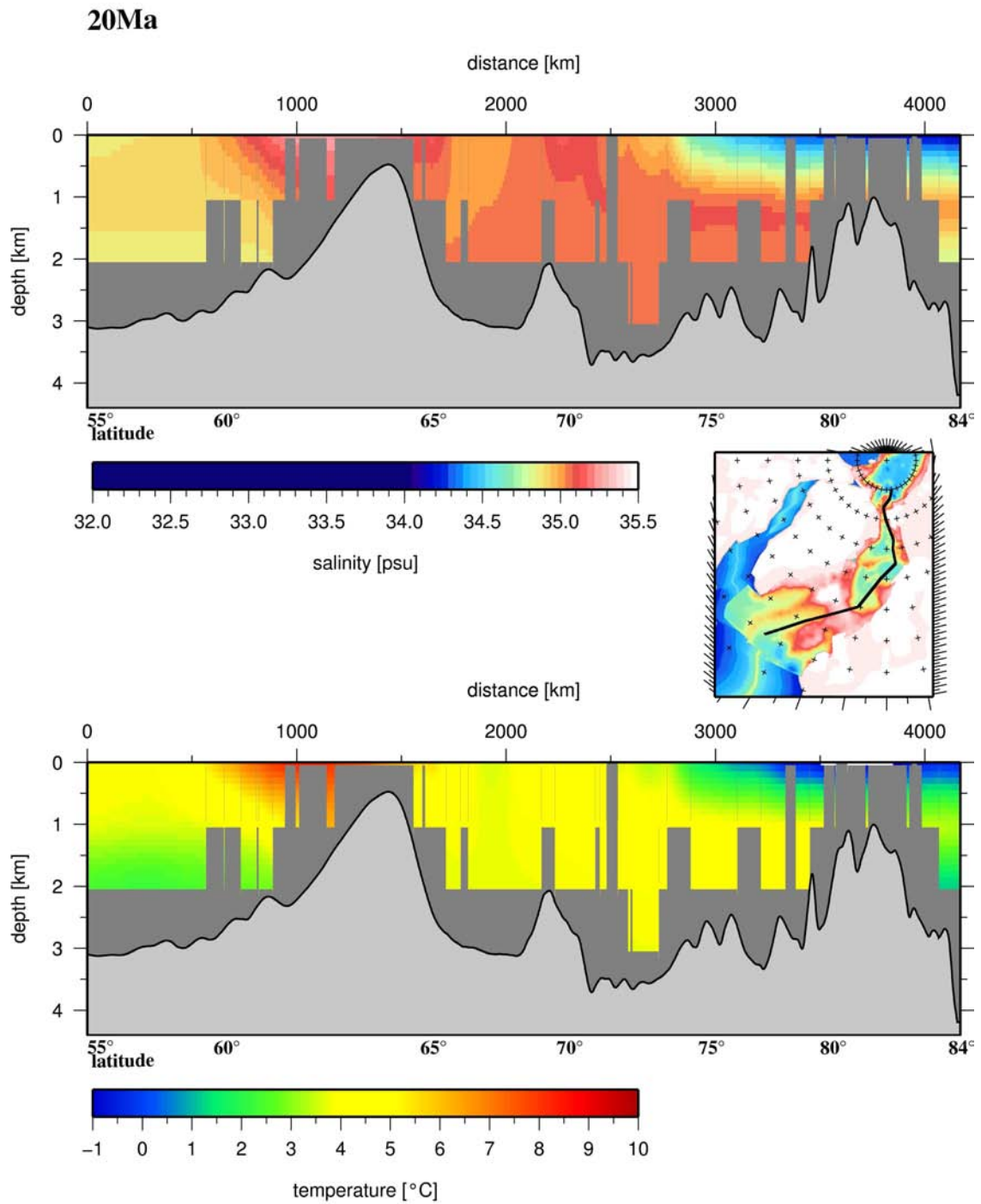


Figure 7.18: As Figure 7.16, but for the Eurasia Basin.

depth in the Boreas Basin (Figure 7.5). The northernmost re-circulation is at about 77°N. Surface-water in the Fram Strait (80°N) turns west towards the East Greenland shelf.

There is no re-circulation in deeper water layers (Figure 7.5, 1125 m and 1400 m).

Surface-water from the Arctic Ocean with temperatures of about -1°C and salinities of about 34 PSU or less flows southward through the Fram Strait (Figure 7.5 and 7.17). The cold and low-saline surface water reaches 70°N in the Lofoten Basin and the Denmark Strait through the western GIN Sea (Figures 7.11 and 7.14). In the Eurasia Basin, the highest temperatures for 15 Ma are found between 500 m and 1000 m (Figure 7.18). The model run results in salinities of about 35 PSU below 500 m, which decrease to 34.8 PSU in 2200 m depth (Figure 7.18).

Figures 7.16 and 7.17 show similar salinity and temperature values as for the 20 Ma model experiment and do not give evidence for an outflow of deep-water from the Arctic Ocean. However, figures 7.11 and 7.14 show a decreased salinity and little decreased temperature south of the Fram Strait between 75°N and 80°N .

Along the East Greenland Margin the simulation shows a southward current in the upper 500 m (Figures 7.5 and 7.14). Salinities and temperatures are decrease south of 75°N . Below 500 m, comparatively warm (5.5°C) and saline (35.1 PSU) AW flows northward (Figures 7.5 and 7.14, 1125 m). We do not observe a southward deep-water transport along the East Greenland Margin. On the other hand, temperature and salinity distributions suggest overflow through the Denmark Strait (Figure 7.14). Arctic surface-water reaches the incoming AW at the southern end of the Denmark Strait.

7.6 Discussion

The results of our control simulation with present day bathymetry are largely in line with oceanographic observations of the northern North Atlantic and the Arctic Ocean (e.g. Aagaard et al. (1985); Quadfasel et al. (1987); Fahrbach et al. (2001); Schauer and Fahrbach (2004)). Due to its limited resolution the model does not resolve all details of the observed currents. However, the model reproduces the re-circulation of RAW south of the Fram Strait (Figures 7.4, 7.10 and 7.13), the mixing of water masses in the GIN Sea and in the Arctic Ocean (Figures 7.13 and 7.18), the inflow of AW of the WSC through the Fram Strait (Figures 7.10 and 7.13), the outflow of colder surface and deep PW from the Arctic Ocean through the Fram Strait to the EGC (Figures 7.4, 7.10 and 7.13) and the overflow of water from the GIN Sea to the Atlantic through the Denmark Strait. We propose that our model experiments for the other time slices provide a first guess of the response of Arctic Ocean currents to Cenozoic changes in tectonic movements and sediment accumulation (Ehlers and Jokat, 2008). While this sensitivity study was carried out using present day climate forcing fields, further insight into the Cenozoic history of Arctic Ocean currents and water masses could be gained from simulations with coupled atmosphere-ocean circulation models.

Atlantic meridional overturning circulation (MOC)

Our time slice experiments suggest that the Atlantic MOC (and the associated polewards

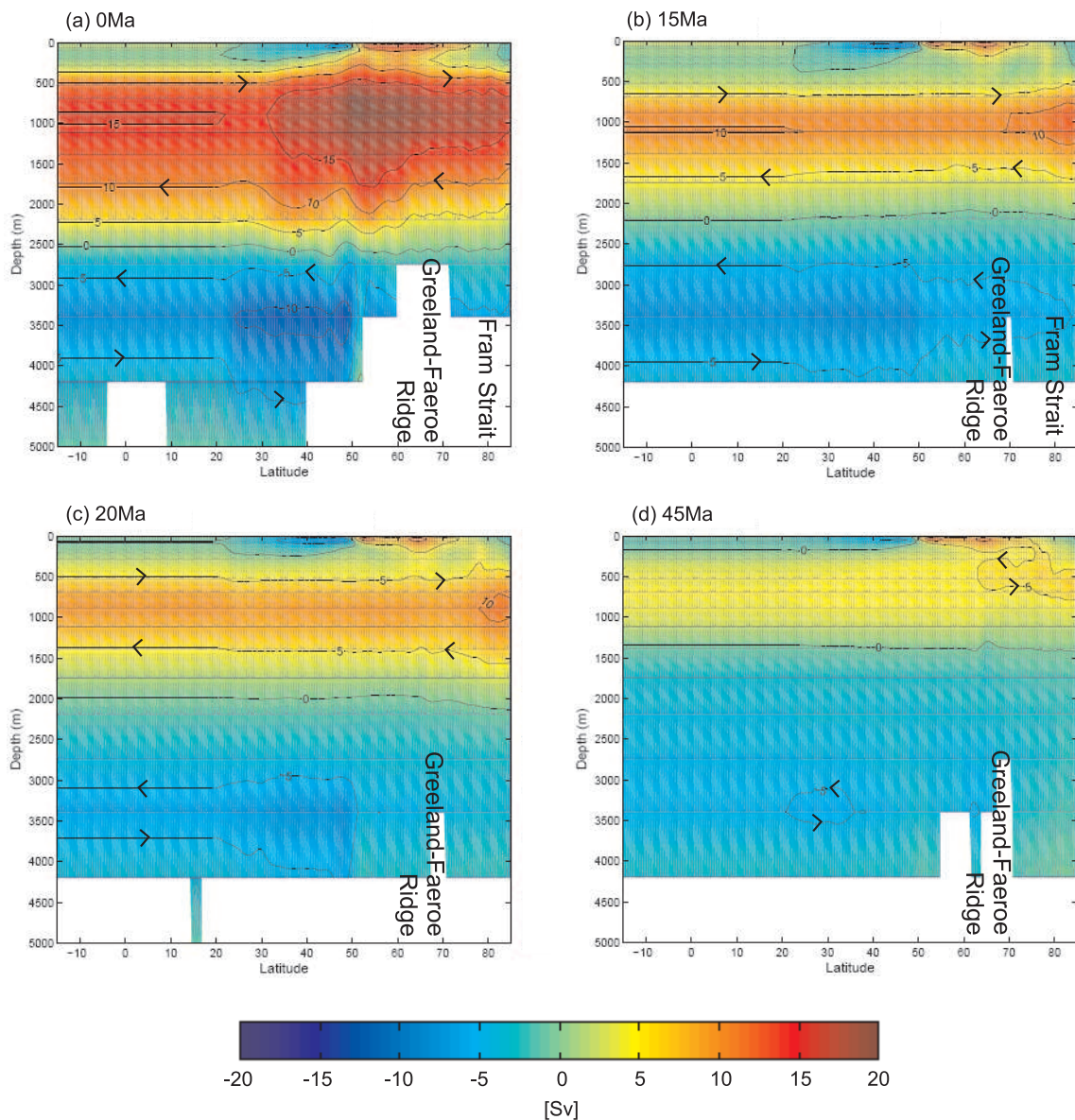


Figure 7.19: Atlantic meridional overturning circulation between 15°S and 85°N for (a) the present day, (b) Middle Miocene (15 Ma), (c) Early Miocene (20 Ma) and (d) Middle Eocene (45 Ma).

heat transport) was significantly changed during various Cenozoic periods. The thickness of the volume transport in the GIN Sea higher than 5 Sv increased for 122 % from the Middle Eocene to the Early Miocene. The simulation results in an expansion of 20 % until Middle Miocene (Figure 7.19(b)–7.19(d)).

Future work has to investigate, if this outcome is solely caused by tectonic and bathymetric changes in the Fram Strait area, or if the Atlantic MOC weakening can also be

attributed to the gradual closing of the Panama Seaway (Haug and Tiedemann, 1998).

Evolution of ocean circulation in the northern North Atlantic and in the Arctic Ocean

Our model results indicate that the Cenozoic changes in bathymetry may have had a significant influence on past ocean currents. Today, the basins south of the Fram Strait are wide enough to allow the geostrophic re-circulation of AW in the whole water column. At 77°N the ocean basins deeper than 1500 m are 440 km wide. In the Early Miocene (20 Ma) these basins were about 90 km smaller, which probably impeded the re-circulation of deep-water. Hence, at 15 Ma and 20 Ma re-circulation occurred only in the upper water column, with the northernmost re-circulating currents being in the northern Boreas Basin (15 Ma) and in the Greenland Fracture Zone (20 Ma).

On the basis of our model results we propose that the modern NC and WSC had precursors in the Early and Middle Miocene. The flow into the Arctic seas with the Early Miocene-WSC (EMWSC) and of the Middle Miocene-WSC (MMWSC) varied in thickness and strength and submerged underneath the cold Arctic Ocean outflow. The water layer with salinity higher than 35 PSU, which reaches the Arctic Ocean north of the Fram Strait in a depth of 1000 m–1500 m, is three times thicker in the Middle Miocene than in the Early Miocene.

For a ventilation of the Miocene Arctic Ocean (Jakobsson et al., 2007) the inflow of AW has to be oxygen-rich. The only location for oxygen absorption is the sea surface. According to our model results the sinking region of AW shifted northward during the Cenozoic, from about 70°N during the Early Miocene to about 77°N in the Middle Miocene and to about 80°N for the present day. We propose that this latitudinal shift of 7° between 20 Ma and 15 Ma is responsible for the onset of the ventilation of the Arctic Ocean. This is in line with Jakobsson et al. (2007), who found that the change in ventilation history in the Arctic Ocean was completed about 17.5 Ma.

Besides the import of saline and warm AW to the Arctic Ocean, the outflow of dense water, which results from mixing of AW and fresh Arctic Water, plays also an important role in ocean current changes (Aagaard et al., 1985). Today, we observe a strong outflow of deep-water from the Arctic Ocean which is transported to the North Atlantic by the EGC. The model experiment shows an Early Miocene-EGC (EMEGC) for a water depth of 400 m, but no deep-water outflow was established 20 Ma. This was primarily due to the shallow and narrow Fram Strait (Ehlers and Jokat, 2008). The model run for 15 Ma (Figures 7.11 and 7.14) gives evidence for the beginning of an exchange in both directions. We find a deep-water inflow by the MMWSC and a deep-water outflow by the Middle Miocene-EGC (MMEGC).

Zachos et al. (2001) found the onset of a climate optimum in the Middle Miocene. While our simulations are uncoupled, it is interesting to note that our model temperatures in the Eurasia Basin (Figure 7.18) are in line with the climate record in that the highest temperatures are obtained for 15 Ma.

7.7 Conclusions

The presented model scenarios result in a sensitivity study of the ocean circulations in the northern North Atlantic and the Arctic Ocean regarding the palaeobathymetric reconstructions. The model runs show a correlation between the opening of the Fram Strait and the development of deep-water exchange through the Fram Strait. This was probably a crucial factor for the global climate cooling after the Middle Miocene climate optimum.

Our oldest investigated time slice (45 Ma) shows a land-locked Middle Eocene Arctic Ocean without water exchange between the Arctic Ocean and the northern North Atlantic. This situation changed in the Early Miocene (20 Ma), for which we find inflow of surface water through the Fram Strait warming the Arctic Ocean. For the Middle Miocene (15 Ma) our model indicates deep-water outflow through the Fram Strait.

The northward propagation of the latitude of the sinking of warm and saline Atlantic Water from 70°N to 77°N between 20 Ma and 15 Ma influenced the oxygen concentration of the Arctic Ocean and provided for the ventilation of the Arctic Ocean. As the outflow of deep-water through the Fram Strait correlates with its deepening and widening, our findings support views that the onset of the deep-water exchange through the Fram Strait played an important role in the Earth's climate history since the Miocene.

Bibliography

- Aagaard, K. (1989). A synthesis of the Arctic Ocean circulation, *Rapp. P. V. Reun. Cons. Int. Explor. Mer.*, 188(1), 11–22.
- Aagaard, K., Swift, J. H. and Carmack, E. C. (1985). Thermohaline Circulation in the Arctic Mediterranean Seas, *Journal of Geophysical Research*, 90 (C3), 4833–4846.
- Arakawa, A. and Lamb, V. R. (1977). Computational design of the basic dynamical processes of the UCLA general circulation model, *Methods Compu. Phys.*, 17. 173–265.
- Bourke, R. H., A. M. Weigel and R. G. Paquette (1988). The Westward Turning Branch of the West Spitsbergen Current, *Journal Geophysical Research*, 93, 14,065–14,077.
- Curry, R. and Mauritzen, C. (2005). Dilution of the northern North Atlantic Ocean in recent decades, *Science*, 308, 1772–1773.
- Ehlers, B.-M. and Jokat, W. (submitted 2008). Palaeobathymetric study of the North Atlantic and the Eurasia Basin, *Geophysical Journal International*.
- Fahrbach, E., Meicke, J., Østerhus, S., Rohardt, G., Schauer, U., Tverberg, V. and Verduin, J. (2001). Direct measurements of volume transports through Fram Strait, *Polar Research*, 20(2), 217–224.
- Gascard, J. C., C. Richez and C. Rouault (1995). New insights on largescale oceanography in Fram Strait: The West Spitsbergen Current, in *Arctic Oceanography: Marginal Ice Zones and Continental Shelves*, Coastal Estuarine Stud., vol. 49, edited by W. Smith and J. Grebmeier, 131-182, AGU, Washington D. C.
- Haug, G. H. and Tiedemann, R. (1998). Effect of the formation of the Isthmus of Panama on the Atlantic Ocean thermohaline circulation, *Nature*, 393, 673–676.
- Holland, M. M., Bitz, C. M., Eby, M. and Weaver, A. J. (2001). The role of ice-ocean interactions in the variability of the North Atlantic thermohaline circulation, *Journal of Climate*, 14, 656–675.
- Intergovernmental Panel on Climate Change (IPCC) (2007). *Climate Change 2007: The Physical Science Basis. Contribution of Working Group I to the Fourth Assessment Report of the Intergovernmental Panel on Climate Change*, Solomon, S., D. Qin, M.

BIBLIOGRAPHY

- Manning, Z. Chen, M. Marquis, K.B. Averyt, M. Tignor and H.L. Miller (eds.), Cambridge University Press, Cambridge, United Kingdom and New York, NY, USA, 996 pp.
- Jakobsson, M. and IBCAO Editorial Board Members (2001). Improvement to the International Bathymetric Chart of the Arctic Ocean (IBCAO): Updating the Data Base and the Grid Model, EOS, Trans. Am. Un., 82 (47), Fall Meet. Suppl., Abstract OS11B-0371.
- Jakobsson, M., Backmann, J., Rudels, B., Nycander, J., Frank, M., Mayer, L., Jokat, W., Sangiorgi, F., O'Regan, M., Brinkhuis, H., King, J. and Moran, K. (2007). The early Miocene onset of a ventilated circulation regime in the Arctic Ocean, *Nature*, 447, doi:10.1038/nature05924.
- Johannessen, O. M. (1986). Brief overview of the physical oceanography, in: Hurdle, B. G. (ed), *The Nordic Seas*, 103–127, Springer, New York.
- Marsland, S. J., Haak, H., Jungclaus, J. H., Latif, M. and Röske, F. (2003). The Max-Planck-Institute global ocean/sea ice model with orthogonal curvilinear coordinates, *Ocean Modelling*, 5, 91–127.
- Moran, K., Backman, J., Brinkhuis, H. and al. (2006). The Cenozoic palaeoenvironment of the Arctic Ocean, *Nature*, 441, doi:10.1038/nature04800.
- Müller, R. D., Sdrolias, M., Gaina, C. and Roest, W. R. (2008). Age, spreading rates, and spreading asymmetry of the world's ocean crust, *Geochemistry, Geophysics, Geosystems*, 9(4), doi:10.1029/2007GC001743.
- Perkin, R. G. and E. L. Lewis (1984). Mixing in the West Spitsbergen Current, *Journal Phys. Oceanogr.*, 14(8), 1315- 1325.
- Peterson, W. H. and Rooth, C. G. H. (1976). Formation and exchange of deep water in the Greenland and Norwegian Seas, *Deep-Sea Research*, 23, 273–283.
- Quadfasel, D., Gascard, J.-C. and Koltermann, K.-P. (1987). Large-scale oceanography in Fram Strait during the 1984 Marginal Ice Zone Experiment, *Journal of Geophysical Research*, 92, 6719–6728.
- Röske, F. (2006). A global heat and freshwater forcing dataset for ocean models, *Ocean Modelling*, 11, 235–297.
- Rudels, B., Fahrbach, E., Meincke, J., Budèus, G. and Eriksson, P. (2002). The East Greenland Current and its contribution to the Denmark Strait overflow, *Journal of Marine Science*, 59, 1133–1154, doi: 10.1006/jmsc.2002.1284.
- Schauer, U. and Fahrbach, E. (2004). Arctic warming through the Fram Strait: Oceanic heat transport from 3 years of measurements, *Journal of Geophysical Research*, 109, doi:10.1029/2003JC001823.

- Swift, J. H. and Aagaard, K. (1981). Seasonal transitions and water mass formation in the Iceland and Greenland seas, *Deep-Sea Research*, 28, 1107–1129.
- Zachos, J., Pagani, M., Sloan, L., Thomas, E. and Billups, K. (2001). Trends, Rhythms, and Aberrations in Global Climate 65 Ma to Present, *Science*, 292, 686–693.

BIBLIOGRAPHY

Chapter 8

Tectonic models

This chapter shows some additional tectonic studies. The existing bathymetry, magnetic and gravity data are rotated due to the plate tectonic reconstruction. The rotations are applied for the northern North Atlantic north of the Jan Mayen Fracture Zone and the Eurasia Basin including the Lomonosov Ridge. Whereas the bathymetry data show high variations during the development of the oceanic basins, the magnetic and gravity data in the oceanic basins stay nearly constant since initial seafloor spreading until present day conditions. The rotation parameters (Euler pole of rotation, angle of rotation) are listed in table B.1. Furthermore a tectonic model of bathymetry data is shown for 5 Myr in the future.

8.1 Tectonic model of bathymetric data

The bathymetry data of the IBCAO grid (Jakobsson et al., 2001) are rotated after table B.1 (Figures 8.1, 8.2, 8.3). In the following description, the rotated data are compared to the results of the palaeobathymetric reconstruction (Figure 6.7 and A.1–A.16).

Even the time slice for 5 Ma (Figure 8.1, 5 Ma) differs from the results of the palaeobathymetric reconstruction. Especially the high sedimentation rates within the last 2.5 Myr along the Barents Sea and the Svalbard margins cause a deeper seafloor in the palaeobathymetric reconstruction. On the other hand the Lena Trough increases the seafloor depth in the reconstructed model. The rotated present day bathymetry data result in an initial opening between 20 Ma and 15 Ma for the Fram Strait. It is not possible to estimate, when the Fram Strait was deep enough for a deep-water exchange between the North Atlantic and the Arctic Ocean. Furthermore this rotated bathymetry data cannot provide evidence on a shallow water exchange, because the vertical movement of the Yermak Plateau and the adjacent basins is not modelled. The rotated bathymetry data display the separation of the Yermak Plateau and the Morris Jesup Rise (Figure 8.2, 35 Ma), but does not verify the continental origin of the Yermak Plateau (Figure 6.7 and 8.3, 50 Ma).

Hence, the comparison of the rotated bathymetry data with the palaeobathymetric reconstruction demonstrates, that the rotation of bathymetry data does not reproduce the

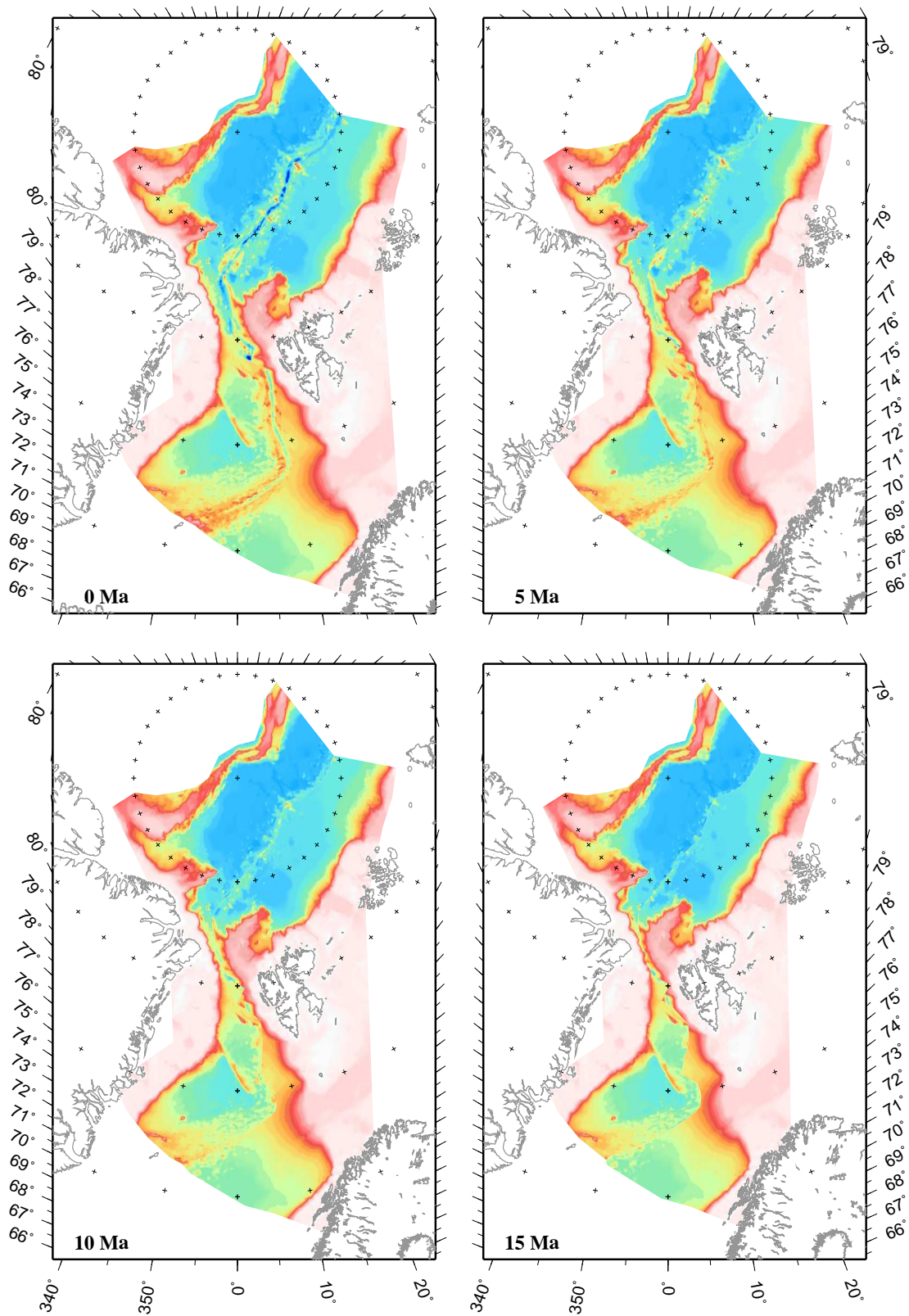


Figure 8.1: Rotated bathymetric data, 0Ma–15Ma

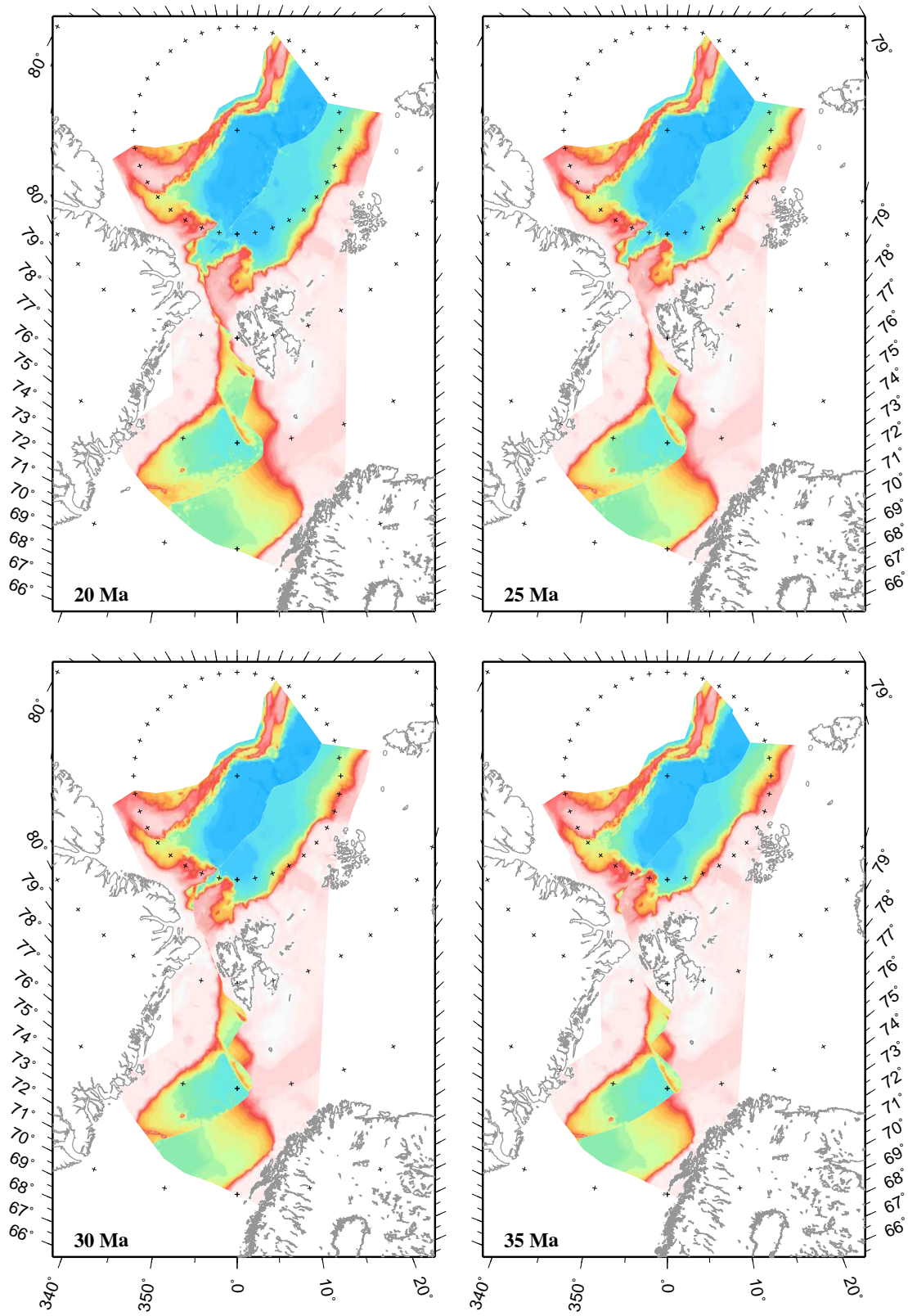


Figure 8.2: Rotated bathymetric data, 20Ma–35Ma

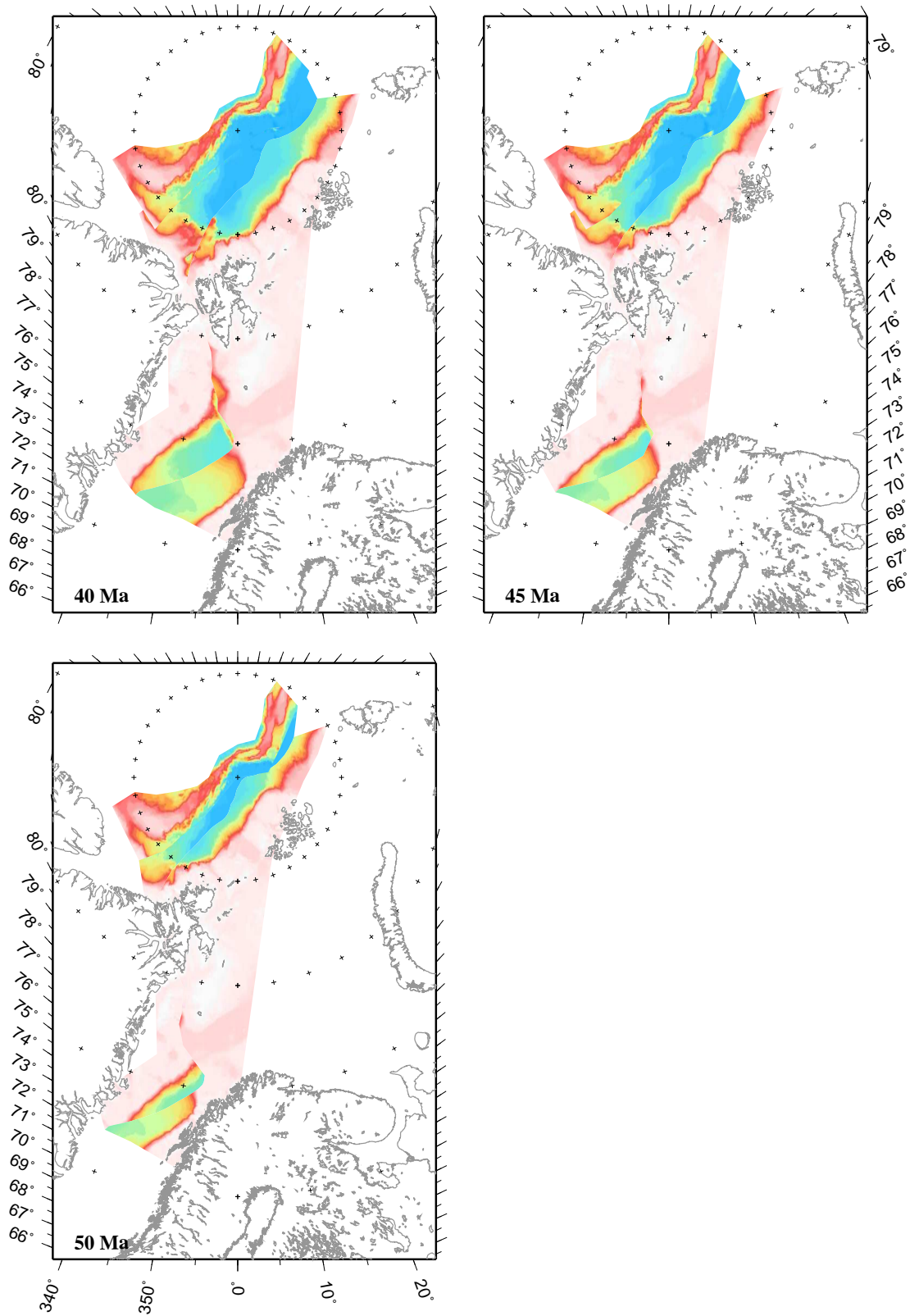


Figure 8.3: Rotated bathymetric data, 40Ma–50Ma

evolution of oceanic basins and its margins. In the investigated area, thermal subsidence and sediment deposits cause a significant change in the bathymetry by time (Figure 6.7). It is essential to consider subsidence calculations, sediment corrections and isostatic balance to a palaeobathymetric model. A further advantage of included subsidence calculations and sediment corrections is the analysis of the basement depth which provides evidence for the oceanic basin evolution before initial seafloor spreading starts. With rotated present day bathymetry data, stretched continental crust cannot be verified.

8.2 Tectonic model of magnetic data

The magnetic data of the Gammaa5-grid (Verhoef et al., 1996) combined with the new aeromagnetic data grid (Leinweber, 2006) are rotated for time slices from 5 Ma to 50 Ma in 5 Myr steps after the rotation parameters of table B.1. The results are presented in figure 8.4, 8.5 and 8.6.

Oceanic crust with anomalies caused by seafloor spreading and magnetic calm or magnetic anomalies areas along the fracture zones and the continental margins are clearly distinguishable. Hence, a magnetic tectonic model illustrates the timing of initial seafloor spreading in the oceanic basins (Figures 8.4, 8.5, 8.6).

Spreading anomalies can be noticed since 10 Ma in the Lena Trough (Figure 8.4 (10 Ma)). Along the Molloy Ridge spreading anomalies are recognisable since 20 Ma (Figure 8.5 (20 Ma)). Again, the final opening of the deep-water gateway in the Fram Strait region does not coincide with initial seafloor spreading. A tectonic model of magnetic data cannot give evidence for the initial exchange of deep-water between the Arctic Ocean and the North Atlantic.

Spreading anomalies along the Knipovich Ridge are mostly diffuse. The rotation of the magnetic data grids shows that the Mohns and the Knipovich ridges were connected since at least 5 Ma (Figure 8.4 (5 Ma)). Before 5 Ma the Greenland Fracture Zone separated both ridges.

The northern part of the Yermak Plateau and the Morris Jesup Rise are clearly observed by high magnetic anomalies. Jackson et al. (1984) assume, that those anomalies are caused by volcanic material. The northernmost basement segment of the Yermak Plateau is of volcanic origin and was formed during the final separation of the Morris Jesup Rise and the Yermal Plateau. This final separation is proved by the rotated magnetic data. 20 Ma the youngest spreading anomaly is found between the Yermak Plateau and the Morris Jesup Rise (Figure 8.5 (20 Ma)). 25 Ma seafloor spreading at the Gakkel Ridge did not propagate south but the magnetic anomalies of the northern Yermak Plateau and the Morris Jesup Rise are still separated (Figure 8.5 (25 Ma)). 30 Ma the anomalies are connected (Figure 8.5 (30 Ma)).

The evolution of the Yermak Plateau includes, that the magnetic anomalies from the present measurements represent realistic conditions since 20 Ma for the Yermak Plateau and the Morris Jesup Rise. Before the formation of the volcanic segment, the high magnetic anomalies probably were absent. Before 30 Ma during the separation of the Morris Jesup

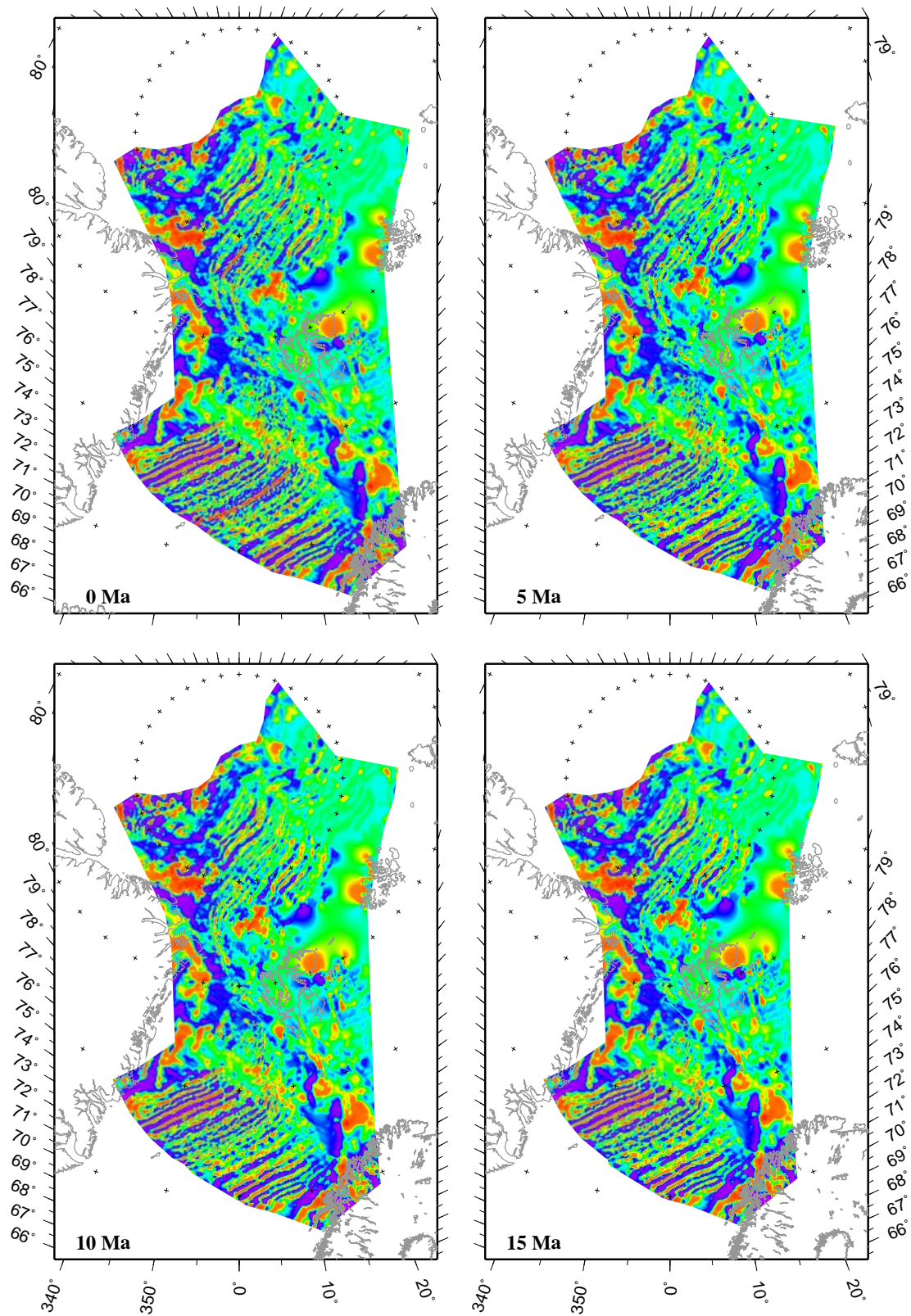


Figure 8.4: Rotated magnetic data, 0Ma–15Ma

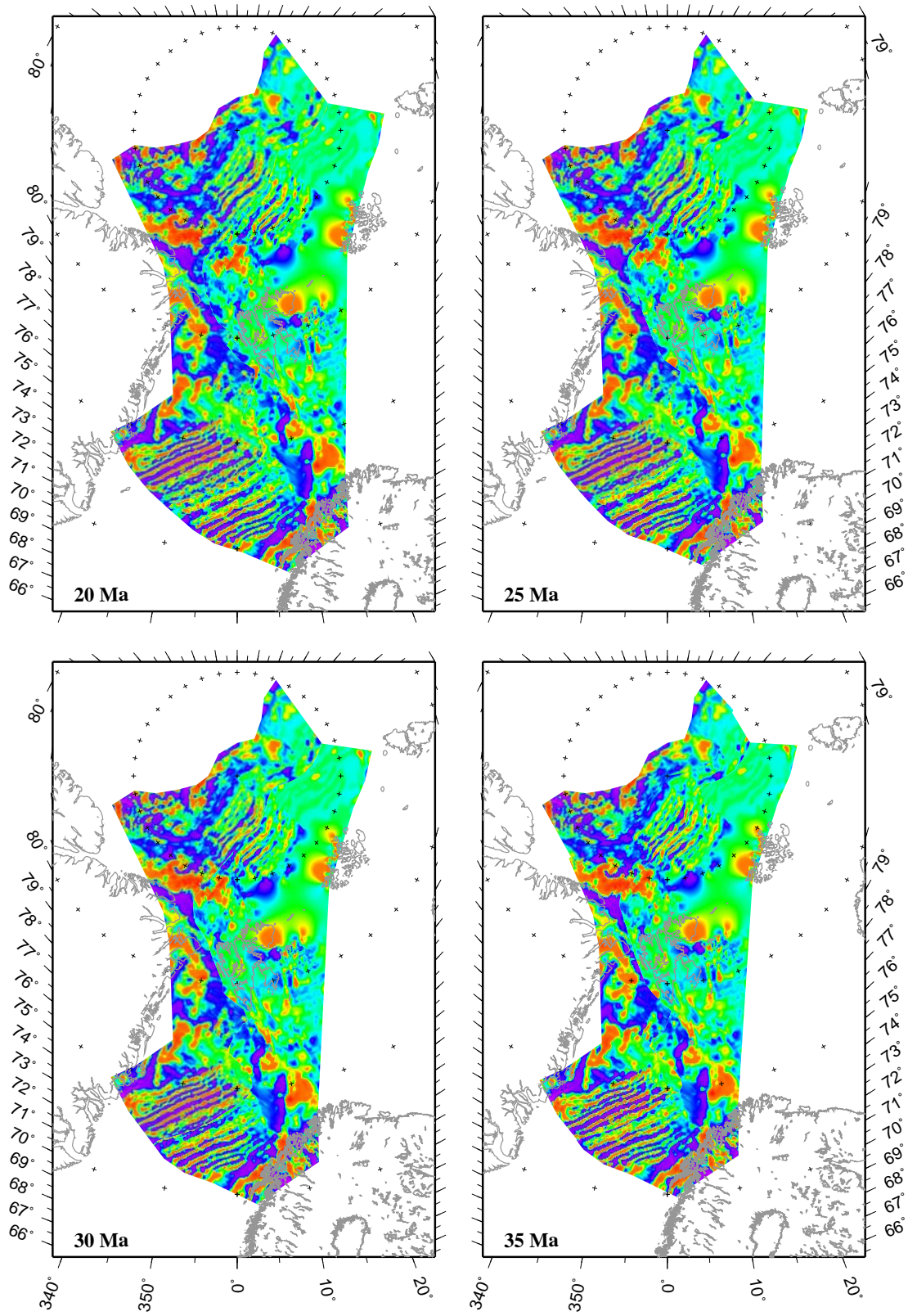


Figure 8.5: Rotated magnetic data, 20Ma–35Ma

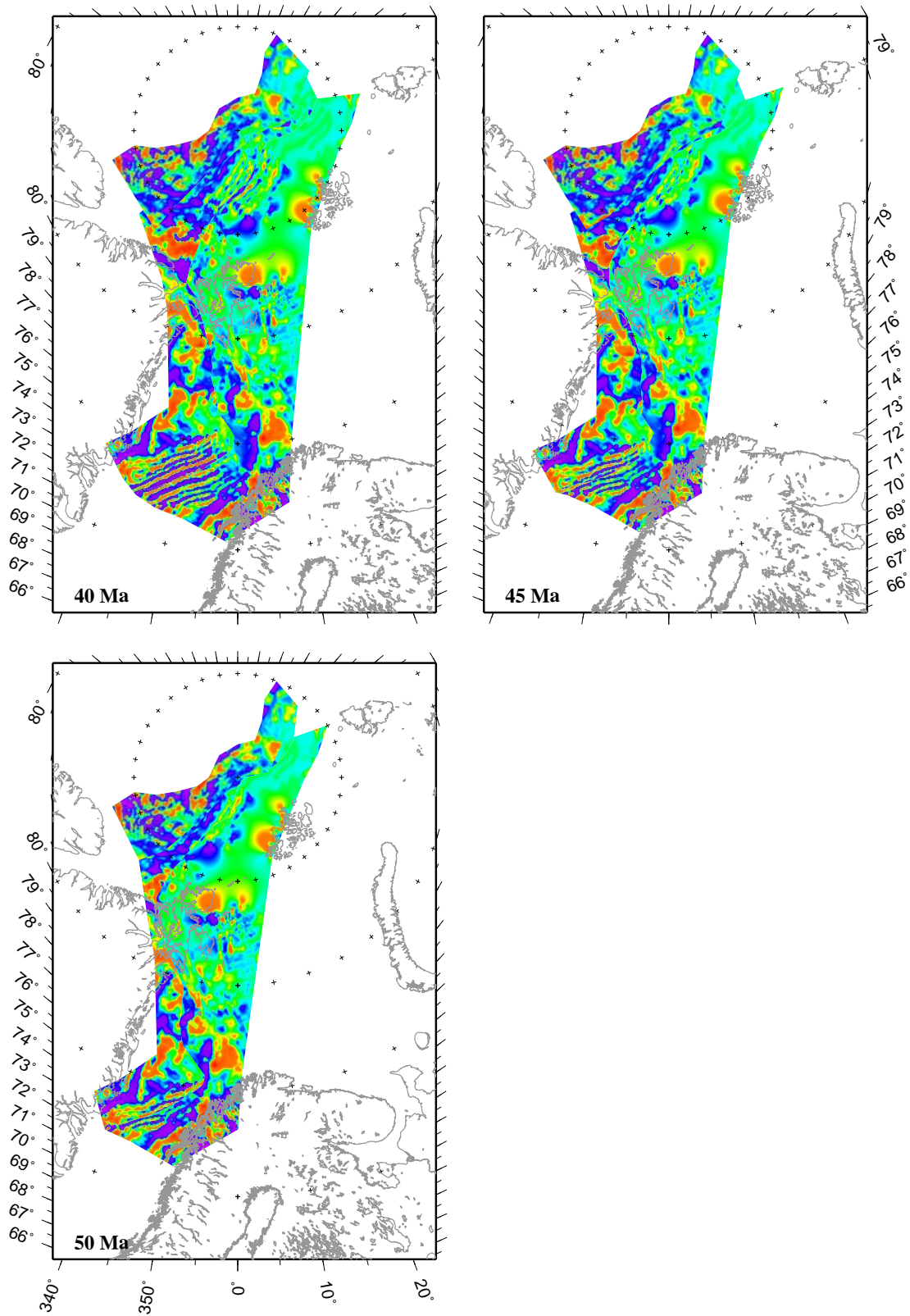


Figure 8.6: Rotated magnetic data, 40Ma–50Ma

Rise and the Yermak Plateau, stretching is not considered in the magnetic tectonic model.

Figure 8.6 just shows seafloor spreading in the Eurasia Basin and in the Norwegian-Greenland Sea. The other parts of the northern North Atlantic show the present magnetic anomalies of the continental margins which were originated during this time of rifting continental margins.

The rotation of the magnetic data provides an evidence for the tectonic movements of oceanic crust in the northern North Atlantic and in the Arctic Ocean.

8.3 Tectonic model of gravity data

The gravity data of the Arctic Gravity Project (AGP, 2006) are also rotated for time slices from 5 Ma to 50 Ma in 5 Myr steps after the rotation parameters of table B.1. The results are presented in figure 8.7, 8.8 and 8.9. In the present day data, the shelf break and the spreading ridges are clearly identifiable (Figure 8.7 (0 Ma)). The gravity anomalies of the ridge adjacent areas are recognised until 15 Ma (Figure 8.7 (15 Ma)). The gravity anomaly probably existed along the ridges since the initial seafloor spreading. This anomaly is missing in the older time slices possibly due to a sediment cover in the older parts of the basins. The anomalies along the shelf break are constant through time since seafloor spreading came off the continental rifting phase. In the Lena Trough the shelf break anomalies begin to connect latest 20 Ma (Figure 8.8 (20 Ma)). The free air anomaly is influenced by the present day sediment load.

The high gravity anomalies on the Yermak Plateau and the Morris Jesup Rise lay on the transition from the Plateau and Rise respectively to the Lena Trough. The transitions to the Lincoln Sea and to the Sophia Basin do not show such positive gravity anomalies. This supports the assumption, that no seafloor spreading took place in the Lincoln Sea and in the Sophia Basin. The positive anomalies along the northern Yermak Plateau and Morris Jesup Rise are connected latest 35 Ma (Figure 8.8 (35 Ma)). During this time probably volcanic activity built the northern Yermak Plateau and the Morris Yesup Rise (Jackson et al., 1984). Hence, the rotated anomalies prior 35 Ma only show the present gravity anomalies.

The Greenland Fracture Zone separates the Greenland Basin from the Boreas Basin. Today the Mohns Ridge and the Knipovich Ridge are connected but already 5 Ma the gravity anomaly of the ridges indicate a disconnection of these two ridges (Figure 8.7 (5 Ma)).

Similar to the rotated magnetic data, the rotated gravity data confirm the initial seafloor spreading of oceanic basins in the northern North Atlantic and in the Arctic Ocean. It does not give evidence about the evolution and the initial opening of the deep-water connection.

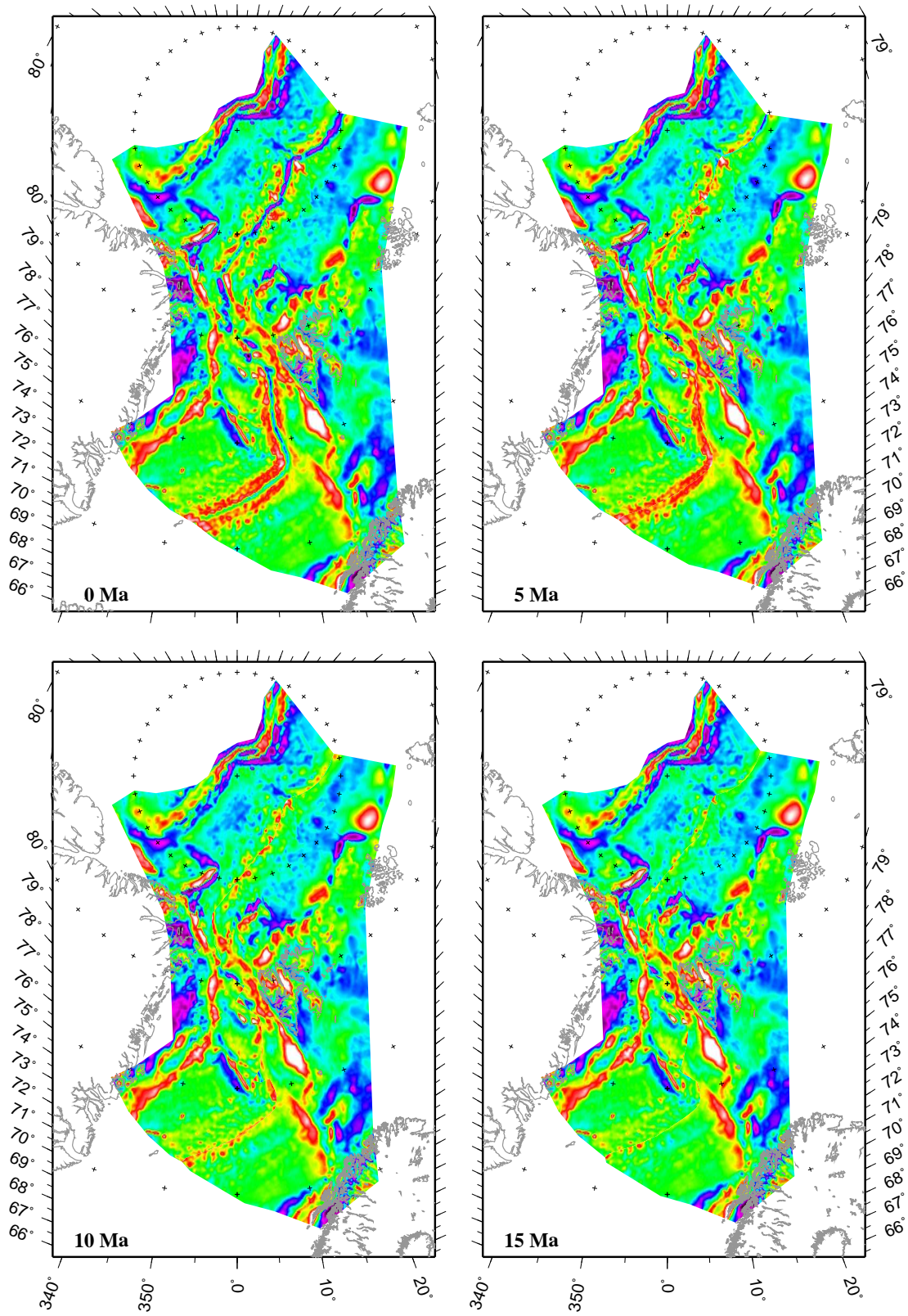


Figure 8.7: Rotated gravity data, 0Ma–15Ma

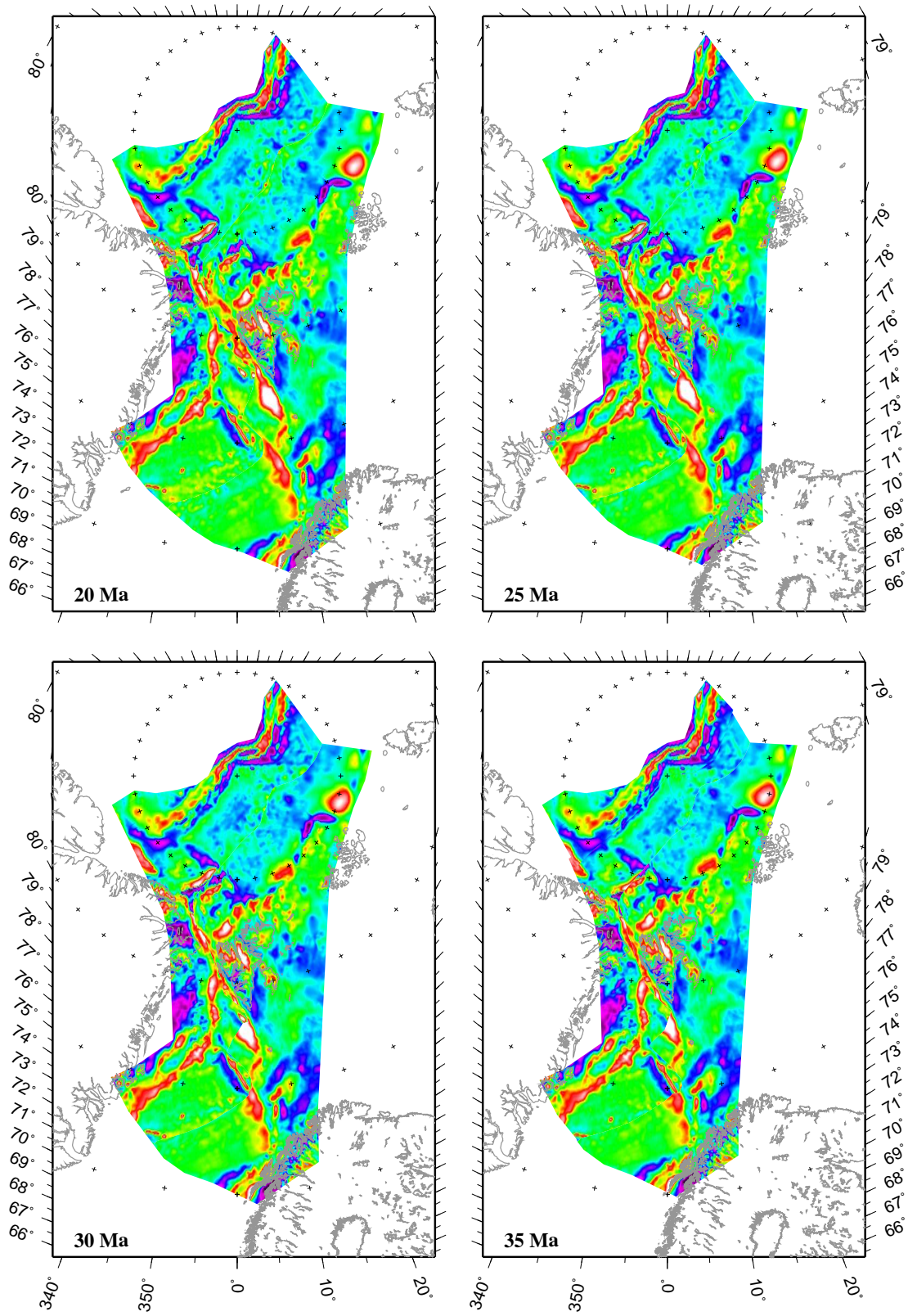


Figure 8.8: Rotated gravity data, 20Ma–35Ma

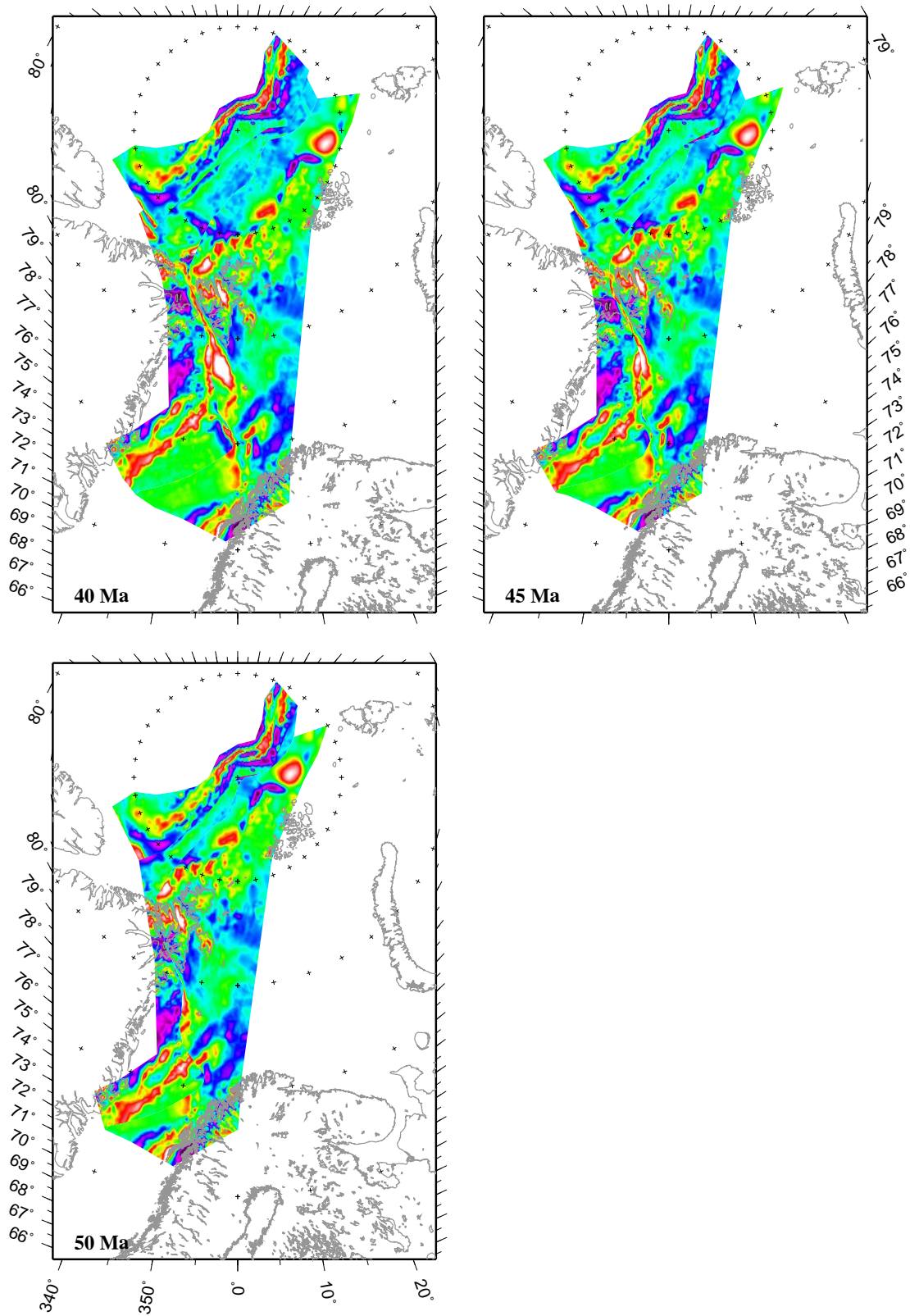


Figure 8.9: Rotated gravity data, 40Ma–50Ma

8.4 Future tectonic model of bathymetry data

The study of the past geodynamic evolution raises the question, how the basins in the northern North Atlantic and in the Arctic Ocean will develop in the future. The answer of the question is highly speculative. A lot of assumptions have to be made. Figure 8.10 shows the simplest model for 5 Myr in future and compares it with the present day data. The future ridge depth is set to the present day ridge depth.

Based on the poles of rotation (table 6.2) the following rotation parameters are assumed:

longitude[°]	latitude[°]	angle[°]	age[Myr]
132.98	66.44	1	5

Table 8.1: Extrapolated pole of rotation and rotation angle for 5Myr in future (Eurasia - North America)

This rotation parameters expect, that the present day tectonic movement between Eurasia and North America stays constant for the next 5 Myr.

Furthermore the sediment thickness and the resulting subsidence and uplift, respectively, is not included. Except for the Lofoten Basin, which showed an uplift for the last 5 Myr (Figure 6.13), all basins will probably subside because of thermal subsidence and sediment accumulation. This is dependend on the future sedimentation rate and therefore, the future climate. Figure 8.10 illustrates a minimum depth of the northern North Atlantic and the Arctic Ocean. Also future sea level changes are not considered. A rising sea level will cause a higher subsidence than a falling sea level.

All basins enlarge and this study especially brings the Fram Strait area into focus. Present day the channel deeper than 1500 m is 140 m wide (Figure 8.10, 0 Myr (right)). The future model proposes, that it will open for 40 km to a width of 180 m (8.10, 5 Myr (right)) within the next 5 Myr. This advanced gateway opening will influence the ocean currents and probably will change future climate conditions.

The listed headwords point the weakness of the future tectonic model up:

- present day depth of ridge axis
- no future sediment accumulation
- no thermal and sediment corrected subsidence
- constant rotation
- no sea level changes

Therefore, the presented model just gives an indication of the future development of the northern North Atlantic and the Arctic Ocean.

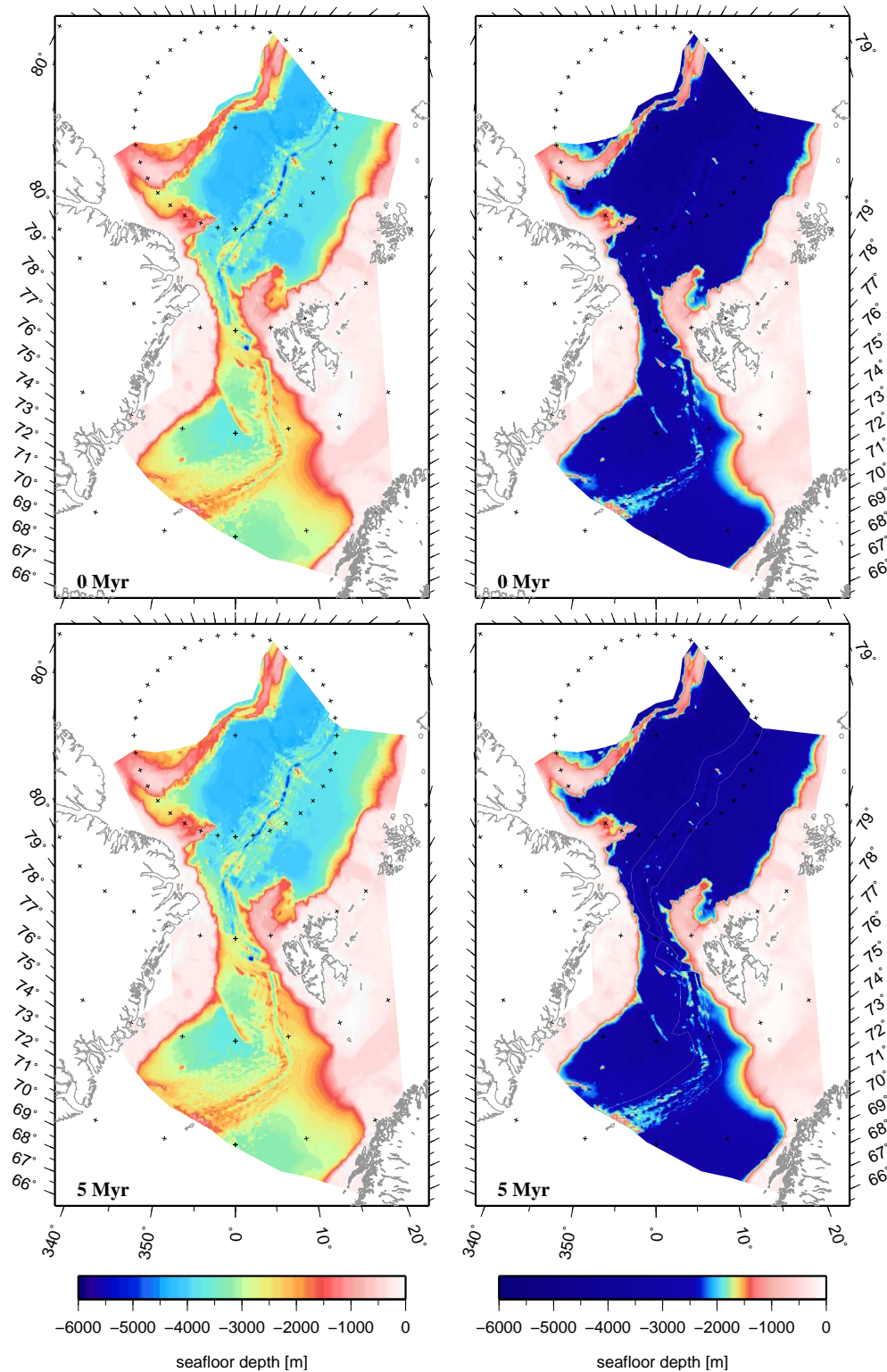


Figure 8.10: Present day bathymetry data and rotated bathymetry data for 5 Myr in future with different colour scales. Left: details of the seafloor depth, right: the Fram Strait channel width with seafloor deeper than 1500 m.

Chapter 9

Discussion and conclusions

The Fram Strait region is an important area to determine the relationship between the bathymetric development of ocean basins, the resulting changes in ocean circulations and the changes in the long-term climate. An important event to verify this relationship is the timing of the Fram Strait tectonic opening, and the resulting onset of the deep-water exchange through the Fram Strait. This study is engaged in the understanding of the tectonic and geological history, and the history of the ocean circulations, and their impact on the climate history. The analysis of the geodynamic evolution of the northern North Atlantic and the Arctic Ocean is possible due to new aeromagnetic and seismic data gathered by the Alfred Wegener Institute (AWI) during the last years. The additional AWI data provide a basis for a detailed crustal age model of the northern North Atlantic and the Eurasia Basin, and allows subsidence and crustal roughness calculations, as well as a palaeobathymetric reconstruction. These investigations result in a model of palaeo-seafloor depth, which is the key information for a palaeoceanographic model experiment. Hence, this study solves various problems in the understanding of the development of the northern North Atlantic and the Arctic Ocean, which are described in chapter 1. The following sections discuss and conclude the results of this study, presented in the scientific articles of chapter 5, 6 and 7.

Subsidence and roughness calculations

The crustal age model yields the timing of initial seafloor spreading for the oceanic basins (Table 9.1). Since initial seafloor spreading started, the basins in the study area show ultra-slow spreading rates north of the Greenland Fracture Zone until present. This makes the region globally quite unique. The crustal age model is an essential basis for subsidence calculations and for the palaeobathymetric reconstruction.

Seismic profiles combined with results from sediment cores in the northern North Atlantic and in the Eurasia Basin provide an insight into the sediment thickness, the seismic stratigraphy, and the basement depth.

In the Eurasia, Boreas and Molloy basins, the sediment corrected thermal subsidence predicts the general trend of the observed basement, and hence, confirms thermal cooling

region	age [Ma]
Eurasia Basin	54
southern Gakkel Ridge	28
Lena Trough	12
Molloy Basin	21
northern Boreas Basin	12
southern Boreas Basin	38
east of Greenland Fracture Zone	21
Norwegian-Greenland Sea	54

Table 9.1: Timing of the initial seafloor spreading north of the Jan Mayen Fracture Zone

and isostatic equilibrium of the oceanic crust. The basement depth developed as the theory of subsidence predicts. This analyses indicate that subsidence calculations can be used to describe the evolution of the bathymetry from the onset of seafloor spreading until today through palaeobathymetric reconstruction.

The global data set of the RMS roughness has been updated with new values for the ultra-slow spreading systems based on roughness calculations of seismic reflection profiles in the Arctic Ocean, the northern North Atlantic and the Fram Strait. Until recently, the global data set of RMS roughness has lacked data from ultra-slow spreading centres. This study found two new curve fits, which separate axial valley-adjacent and axial high-adjacent roughness values. The curves describe the relationship of seafloor spreading rate, RMS roughness and ridge morphology. The analysis north of the Greenland Fracture Zone show a significant correlation between spreading rates, roughness and morphology, and provide a better insight into the evolution of the spreading rates, and the axial ridge morphology in the northern North Atlantic and in the Arctic Ocean.

Palaeobathymetry

The palaeobathymetric reconstruction results of the seafloor depth, the basement depth and the sediment thickness of the last 55 Myr, contributes to a better understanding, of the entire basin evolution north of the Charlie Gibbs Fracture Zone. The past seafloor depth model shows the subsidence evolution of the north Atlantic and the Arctic Ocean, which is dependend on the sediment rates and the crustal age. Low sedimentation rates cause seafloor subsidence, high sedimentation rates entail even uplift. The basement depth correlates with the sediment loads. A deep basement before initial seafloor spreading is originated by stretched continental crust. Today these deep basins are filled up with sediments.

The results of this study correlate with the analysis of a core from the crest of the Lomonosov Ridge (Moran et al., 2006). The palaeobathymetric reconstruction results in

a first continuous channel between the North Atlantic and the Arctic Ocean some 25 Ma. Shallow water masses could be exchanged east of the Yermak Plateau. A first channel with a depth of obviously below 1500 m exists since 17 Ma. This result confirms that the “land-locked” Arctic Ocean changed to a ventilated stage via an exchange of deep-water between the Arctic Ocean and the North Atlantic. An overflow at the Greenland-Faeroe Ridge started approximately during the same time. These results assume a correlation between the timing of the Fram Strait opening, and long term climate changes in the northern North Atlantic.

To test the correlation between the investigated bathymetric changes and changes in the long-term climate, this study uses the palaeobathymetric results for a palaeobathymetric model experiment.

Palaeoceanography

On the basis of the calculated palaeobathymetric reconstruction of this study and an available global palaeobathymetric data set, a palaeoceanographic model experiment indicates a relationship between bathymetry, the ocean circulations and long-term climate changes. Due to the time limitation of this study, four model scenarios are calculated. The model run for the present day bathymetry is a test run to compare the model experiment results with present day observations. The calculated ocean circulation model scenarios for 15 Ma, 20 Ma and 45 Ma give evidence, that the Arctic Ocean changed from a land-locked to a ventilated ocean in the Middle Miocene. In Early Miocene times, a warm and saline inflow from the Atlantic Ocean reaches the Arctic Ocean and increases its salinity and temperature. During Middle Miocene an outflow of deep-water from the Arctic Ocean to the northern North Atlantic is shown by the model run due to the expanding Fram Strait. The onset of the Fram Strait two-way deep-water exchange correlates with the onset of a global cooling trend. It strongly suggests a relationship between the tectonic and geological development of the northern North Atlantic and the Arctic Ocean, the changes of the ocean circulations in the model scenarios and established long-term climate changes.

This study supports views that the onset of the deep-water exchange through the Fram Strait played an important role in the earth climate history since the Miocene.

Chapter 10

Outlook

This study gives an overview of the tectonic and geological evolution of the northern North Atlantic and the Arctic Ocean. It constrains the timing of the Fram Strait opening and the timing of the initial deep-water exchange through the Fram Strait, and gives evidence to link these events and changes in the long-term climate.

Continuous research in the northern North Atlantic and in the Arctic Ocean can confirm the presented results, and are important to varify the evolution history of the adjacent areas. This study concentrates on the region between the Charlie Gibbs Fracture Zone in the south and the Lomonosov Ridge in the north. To get a complete understanding of the Arctic Ocean tectonic, bathymetric, oceanographic and climate development, a detailed study of the Canada Basin is essential. Furthermore, the palaeobathymetric reconstruction and the palaeoceanographic modelling can be a basis for studies in various disciplines, like climate research or even marine biology.

The following outlook is devided into sections basend on the three scientific manuscripts of this study.

Subsidence and roughness calculations

Subsidence calculations were implemented for five profiles located in the Boreas, the Molloy and the Eurasia basins. Only oceanic basins were investigated. It is useful, to include detailed subsidence observations from features underlain by continental crust, for example the Yermak Plateau and the Hovgård Ridge. Fracture zones, plateaus and the shelf areas also play an important role in the bathymetric system and need to be investigated in more detail. Subsidence calculations for continental crust should be amended by continental stretching.

Additionally, subsidence calculations and roughness analyses in the Canada Basin (Figure 10.1) should provide an indication of its tectonic and geological evolution. A classification of continental and oceanic crust and a reliable crustal age model are required for the Canada Basin.

The investigated constant ultra-slow spreading rates during the formation and the basin evolution of the northern North Atlantic and the Arctic Ocean, and their relationship with

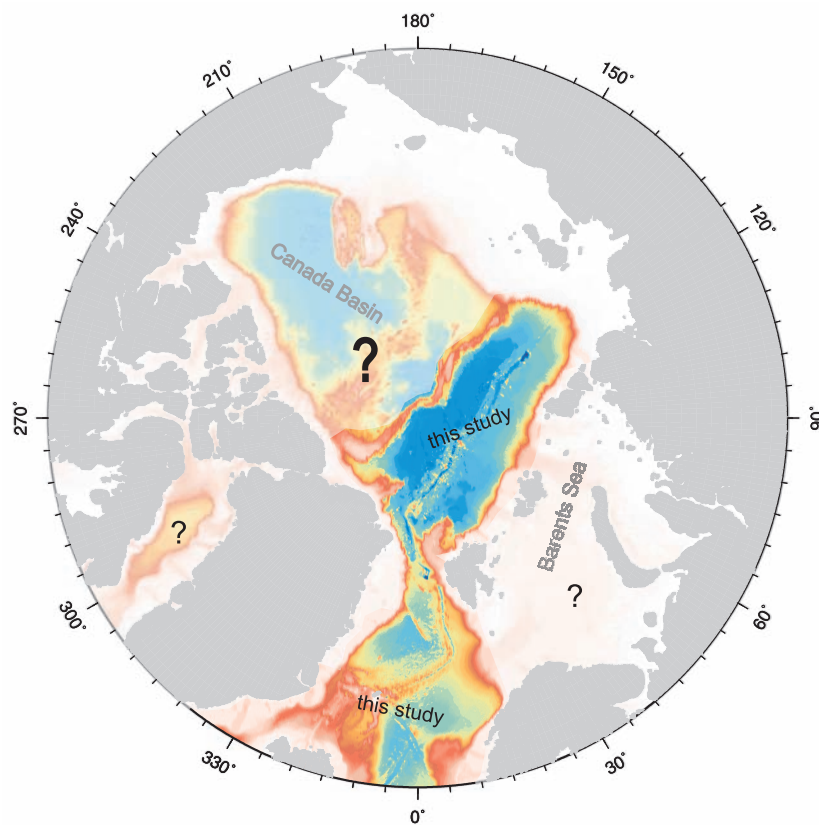


Figure 10.1: Arctic regions of interest for future palaeobathymetric reconstructions, in particular the Canada Basin and the Barents Sea.

the axial-valley morphology and high roughness values are of special interest for future research in geodynamixs and plate tectonics.

Palaeobathymetry

The palaeobathymetric reconstruction is limited to the available data. Especially seismic stratigraphy data have an influence on the sediment corrected subsidence calculations in the reconstruction. To enhance the reconstruction, additional sediment cores would deliver an improved seismic stratigraphy and an advanced investigation of the continent ocean transition zone is needed.

The investigated region should be enlarged to the entire Arctic Ocean (Figure 10.1). This requires a complete data base of geophysical data such as magnetics, seismics and gravity in the remaining parts of the Eurasia Basin, and especially in the Canada Basin.

The software package “BalPal v.0.9” for the palaeobathymetric reconstruction should include models for subsidence of continental crust. Continental stretching plays an important role before initial saefloor spreading started, but this is not included into the software package “BalPal v.0.9” until now. A subsidence analysis of continental crust makes it pos-

sible to include the Barents Sea Shelf, which probably also plays an important role in the shallow-water exchange between the northern North Atlantic and the Arctic Ocean. Hence, informations about the history of the northern hemisphere glaciation are required, because of the glacial influence on the subsidence evolution and palaeobathymetric reconstruction.

An interesting future study is the reconstruction of the continental topography above sea level. The palaeo-topography probably had a significant impact on the atmosphere and hence, on the climate, on glaciations and the subsidence evolution.

Palaeoceanography

The palaeoceanographic model experiment of this study is calculated by an uncoupled ocean circulation model. The study can be probably improved by applying an ocean circulation model run with past atmosphere forcing, which does not exist until now. To run a coupled model, it is essential to compile a palaeotopography grid of the continents. Changes in topography have a significant influence on the atmosphere forcings.

Improved global palaeobathymetry data will result in detailed changes in ocean circulations. For example, a consideration of the Barents Sea Shelf evolution can be interesting for the surface and intermediate water exchange between the northern North Atlantic and the Arctic Ocean.

For this study it was not possible to calculate oceanic circulation model scenarios for further time slices due to the time limitation and software problems. The development of ocean circulations, salinity and temperature between 15 Ma and present day is very interesting to understand the development of ocean circulations from the onset of the deep-water exchange through the Fram Strait until today.

This study concentrates on the results of the ocean circulation model run in the northern North Atlantic and in the Arctic Ocean, especially in the Eurasia Basin. The circulation model provides a correlation between the ocean circulation changes and the climate changes. Due to global bathymetric changes, ocean circulations are modified in all world oceans. For example, the closing of the Panama gateway and the Mediterranean Sea effects the ocean circulation in the Atlantic and Pacific oceans (Figure 10.2) and hence, the inflow to the northern North Atlantic. A future study can probably compare the impact of the opening of the Fram Strait deep-water gateway to the impact of global interactions of ocean circulations to long-term climate changes.

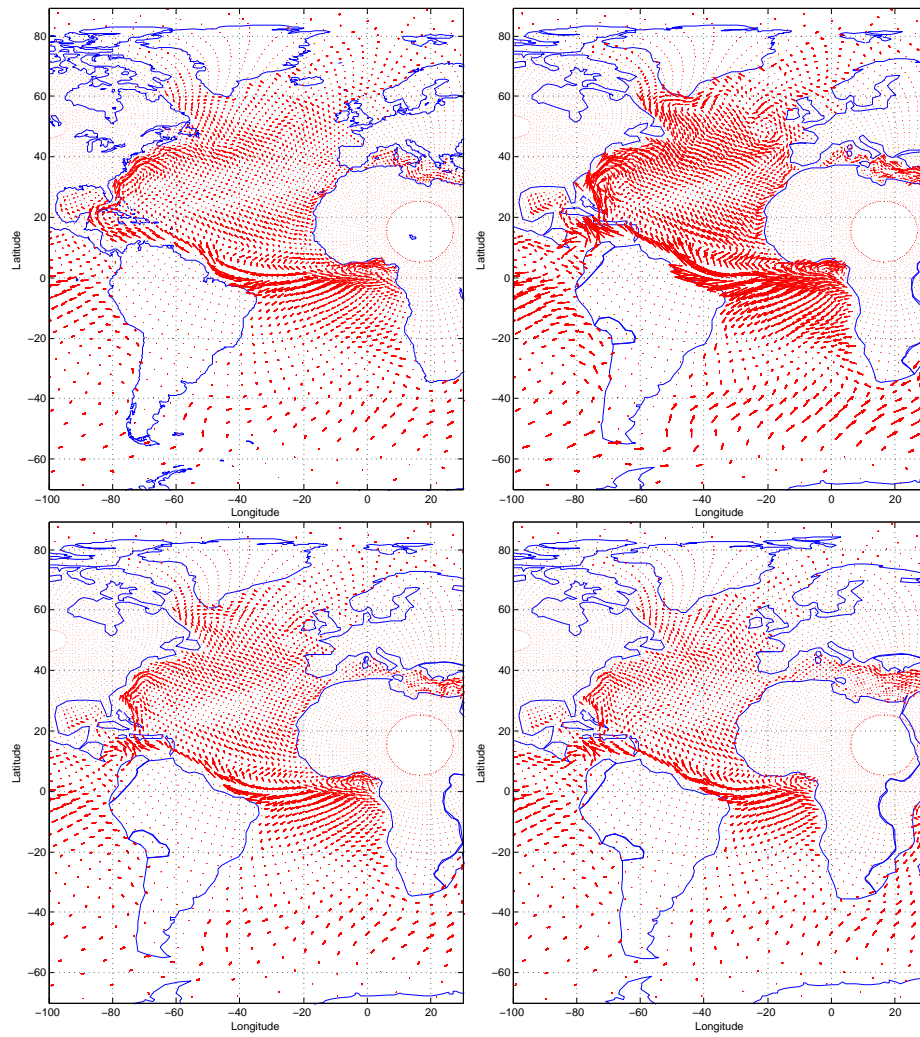


Figure 10.2: Ocean currents in the Atlantic Ocean. top: 0 Ma (left), 15 Ma (right), bottom: 20 Ma (left), 45 Ma (right)

Bibliography

- Aagaard, K., Swift, J. H. and Carmack, E. C. (1985). Thermohaline Circulation in the Arctic Mediterranean Seas, *Journal of Geophysical Research*, 90 (C3), 4833–4846.
- Aagaard, K., Foldvik, A. and Hillmann, S. R. (1987). The West Spitsbergen Current: Disposition and water mass transformation, *Journal of Geophysical Research*, 92, 3778–3784.
- Aagaard, K. (1989). A synthesis of the Arctic Ocean circulation, *Rapp. P. V. Reun. Cons. Int. Explor. Mer.*, 188(1), 11–22.
- Arctic Gravity Project (2006). <http://earth-info.nga.mil/GandG/wgs84/agp>.
- Allen, P. A. and Allen, J. R. (1990). *Basin analysis principles & applications*, Balckwell Science Publications, 272 pp.
- Arakawa, A. and Lamb, V. R. (1977). Computational design of the basic dynamical processes of the UCLA general circulation model, *Methods Compu. Phys.*, 17, 173–265.
- Ben-Avraham, Z. and von Herzen, R. P. (1987). Heat flow and continental break-up, *Journal of geophysical Research*, 92, 1407–1416.
- Berger, D. and Jokat, W. (2008). A seismic study along the East Greenland margin from 72°N to 77°N, *Geophysical Journal International*, 174, 733–748.
- Boebel, T. (2000). Flugzeuggestützte Topographie- und Schweremessung: Meßsystem und Anwendung afu die Region Framstraße, Spitzbergen und Nordostgrönland, *Berichte zur Polarforschung*, 366.
- Bourke, R. H., Weigel, A. M. and Paquette, R. G. (1988). the westard Turning Branch of the West Spitsbergen Current, *Journal Geophysical Research*, 93, 14065–14077.
- Bowen, J. W. and White, R. S. (1994). Variation with spreading rate of oceanic crustal thickness and geochemistry, *Earth and Plaetary Science Letters*, 121(3-4), 435–449.
- Brozena, J. M., Childers, V. A., Gahagan, L. M., Forsberg, R., Faleide, J. I. and eldholm, O. (2003). New aerogeophysical study of the Eurasia Basin and Lomonosov Ridge: Implications for basin development, *Geology*, 31, 825–828.

BIBLIOGRAPHY

- Burchfiel, B. C. (1980). Tectonics of non-collisional regimes - the modern Andes and the Mesozoic Cordilleran orogen of the western United States, in Burchfiel, B. C. (eds), *Continental Tectonics*, National Academy of Sciences, Washington D.C., p. 65–72.
- Courtillot, V. (1982). Propagating rifts and continental breakup, *Tectonics*, 1, 239–256.
- Courtillot, V. and Vink, G. E. (1983). How continents break up, *Sci. Am.*, 249(1), 40–47.
- Davidson, A. and Rex, D. C. (1980). Age of volcanism and rifting in south western Ethiopia, *Nature*, 283, 657–658.
- Dick, H. J. B., Lin, J. and Schouten, H. (2003). An ultraslow-spreading class of ocean ridge, *Nature*, 405–412.
- Dietrich, G., Kalle, K., Krauss, W. and Siedler, G. (1980). *General Oceanography* 2nd ed., Wiley-Interscience, New York.
- Eldholm, J. I., Myhre, A. M. and Thiede, J. (1994). Cenozoic tectono-magmatic events in the Northern Atlantic: Potential paleoenvironmental implications, in *Cenozoic Plants and Climates of the Arctic*, NATO ASI Series, vol. 27, edited by Boulter, M. . and Fischer, H. C., Springer-Verlag, Berlin, pp. 35–55.
- Eldrett, J. S., Harding, I. C., Wilson, P. A., Butlere, E. and Roberts, A. P. (2007). Continental ice in Greenland during the Eocene and Oligocene, *Nature*, 446, 176–179.
- Engen, Ø., Faleide, J. I. and Dyreng, T. K. (2008). Opening of the Fram Strait gateway: A review of plate constraints, *Tectonophysics*, 450, 51–69.
- Fahrbach, E., Meicke, J., Østerhus, S., Rohardt, G., Schauer, U., Tverberg, V. and Verduin, J. (2001). Direct measurements of volume transports through Fram Strait, *Polar Research*, 20(2), 217–224.
- Feden, R. H., Vogt, P. R. and Flemming, H. S. (1979). Magnetic and bathymetric evidence for the ‘Yermak Hot Spot’ northwest of Svalbard in the Arctic Basin, *Earth planet. Sci. Lett.*, 44, 18–38.
- Fronval, T. and Jansen, E. (1996). Late Neogene paleoclimates and paleoceanography in the Iceland-Norwegian Sea: Evidence from the Iceland and Vøring plateaus, ODP Leg 151 and 104, in *Proceedings of the Ocean Drilling Program, Scientific Results*, vol. 151, edited by J. Thiede et al., Ocean Drilling Program, College, Station, TX, pp. 455–468.
- Gaina, C., Roest, W. R. and Müller, R. D. (2002). Late Cretaceous - Cenozoic deformation of northeast Asia, *Earth and Planetary Science letter*, 197, 273–286.
- Gascard, J. C., Richez, C. and Rouault, C. (1995). New insight on large-scale oceanography in Fram Strait: The West Spitsbergen Current, in *Arctic Oceanography: Marginal Ice Zones and Continental Shelves*, Coastal Estuarine Stud., vol. 49, Smith, W. and Grebmeier, J. (eds), 131–182, AGU, Washington D.C.

- Geissler, W. H. and Jokat, W. (2004). A geophysical study of the northern Svalbard continental margin, *Geophysical Journal International*, 158, 50–66.
- Goff, J. A., Ma, Y., Shah, A., Cochran, J. R. and Sempéré (1997). Stochastic analysis of seafloor morphology on the flank of the Southeast Indian Ridge: The influence of ridge morphology on the formation of abyssal hills, *Journal of Geophysical Research*, vol. 102, no. B7, 15521–15534
- Gradstein, F., Ogg, J. and Smith, A. (eds) (2004). *A Geological Time Scale 2004*, Cambridge University Press.
- Håkansson, E. and Pedersen, S. A. S. (1982). Late Paleozoic to Tertiary tectonic evolution of the continental margin in North Greenland, in *Arctic Geology and Geophysics*, eds Embry, A. F. & Balkwill, H. R., *Memoirs of the Canadian Society of Petroleum Geologists*, 8, 331–348.
- Haq, B. U., Hardenbol, J. and Vail, P. R. (1987). Chronology of fluctuating sea level since the Triassic, *Science*, 235, 1156–1167.
- Haug, G. H. and Tiedemann, R. (1998). Effect of the formation of the Isthmus of Panama on the Atlantic Ocean thermohaline circulation, *Nature*, vol. 393, p. 673–676.
- Hayes, D. E. and Kane, K. A. (1991). The dependence of seafloor roughness on spreading rate, *Geophysical Research Letters*, 18(8), 1425–1428.
- Hey, R. N., Kleinrock, M. C., Miller, S. P., Atawater, T. M. and Searle, R. C. (1986). Sea Beam/Deep-Tow investigation of an oceanic propagating rift system, *Journal Geophysical Research*, 91, 3369–3393.
- Helland, P. E. and Holms, M. A. (1997). Surface textural analysis of quartz sand grains from ODP Site 918 off the southeast coast of Greenland suggests glaciation of southern Greenland at 11 Ma, *Palaeogeography, Palaeoclimatology, Palaeoecology*, 135, 109–121.
- Hibler, W. D. (1979). A dynamic thermodynamic sea ice model, *J. Phys. Oceanogr.*, 9, 815–846.
- Hoffman, P., Burke, K. C. A. and Dewey, J. F. (1974). Aulacogens and their genetic relation to geosynclines, with a Proterozoic example from Great Slave Lake, Canada, in Dott, R. H. and Shaver, R. H. (eds), *Modern and Ancient Geosyncline Sedimentation*, Soc. econ. Pal. Mineral. Spec. Pub. 19, 38–55.
- Hooper, P. R. (1990). The timing of crustal extension and the eruption of continental flood basalts, *Nature*, 345, 246–249.
- Jackson, H. R., Johnson, G. L., Sundvor, E. and Mhyre, A. M. (1984). The Yermol Plateau: formed at a triple junction, *Journal of Geophysical Research*, vol. 89, B5, 3223–3232.

BIBLIOGRAPHY

- Jakobsson, M. and IBCAO Editorial Board Members (2001). Improvement to the International Bathymetric Chart of the Arctic Ocean (IBCAO): Updating the Data Base and the Grid Model, EOS, Trans. Am. Un., 82(47), Fall Meet. Suppl., Abstract OS11B-0371.
- Jakobsson, M., Backmann, J., Rudels, B., Nycander, J., Frank, M., Mayer, L., Jokat, W., Sangiorgi, F., O'Regan, M., Brinkhuis, H., King, J. and Moran, K. (2007). The early Miocene onset of a ventilated circulation regime in the Arctic Ocean, *Nature*, vol. 447, doi:10.1038/nature05924.
- Jansen, E. and Sjøholm (1991). Reconstruction of glaciation over the past 6 Myr from ice-borne deposits in the Norwegian Sea, *Nature*, 349 (6310), 600–603.
- Jokat, W., Ritzmann, O., Schmidt-Aursch, M., Drachev, S., Gauger, S. and Snow, J. (2003). Geophysical evidence for reduced melt production on the super-slow Gakkel Ridge (Arctic Ocean), *Nature*, 423, 962 - 965.
- Jokat, W. (ed) (2003). The expedition ARKTIS XVIII/2 of RV "Polarstern" in 2002: contributions of the participants, Reports on polar and marine research, 449, Alfred-Wegener-Institut für Polar- und Meeresforschung.
- Jokat, W. (ed) (2004). The expedition ARKTIS XIX/4 of the research vessel POLARSTERN in 2003: reports of legs 4a and 4b, Reports on polar and marine research, 475, Alfred-Wegener-Institut für Polar- und Meeresforschung.
- Jokat, W., Geissler, W. and Voss, M. (2008). Basement structure of the northwestern Yermak Plateau, *Geophysical Research Letters*, vol. 35, doi:10.1029/2007GL032892.
- Keary, P. and Vine, F. J. (1996). *Global Tectonics* (2nd edn), Blackwell Scientific Publications, Oxford.
- Knies, J. and Gaina, C. (2008). Middle Miocene ice sheet expansion in the Arctic: Views from the Barents Sea, *Geochemistry, Geophysics, Geosystems*, vol. 9, nr. 2, doi:10.1029/2007GC001824.
- Kristoffersen, Y. (1990). On the tectonic evolution and palaeoceanographic significance of the Fram Strait gateway, *Geological History of the Polar Oceans: Arctic Versus Antarctic*, Bleil, U. and Thiede, J. (eds.), Kluwer Academic Publishers, 63–76.
- Kusznir, N. J. and Park, R. G. (1984). Intraplate lithosphere deformation and the strength of the lithosphere, *Geophysical Journal Royal astr. Society*, 79, 513–538.
- Lawver, L. A., Müller, R. D., Srivastava, S. P. and Roest, W. (1990). The opening of the Arctic Ocean, *Geological History of the Polar Oceans: Arctic Versus Antarctic*, Bleil, U. and Thiede, J. (eds.), Kluwer Academic Publishers, 29–62.
- Leinweber, V. T. (2006). Abschätzung von Sedimentmächtigkeiten in der framstraße anhand magnetischer Daten, Diploma thesis Karl-Franzens-University Graz, 96pp.

- Livermore, R., Nankivell, A., Eagles, G., Morris, P. (2005). Paleogene opening of Drake Passage, *Earth and Planetary Science Letters*, 236, p. 459–470.
- Ma, L. Y. and Cochran, J. R. (1997). Bathymetric roughness of the Southeast Indian Ridge: Implications for crustal accretion at intermediate spreading rate mid-ocean ridges, *Journal of Geophysical Research*, vol. 102, no. B8. 17697–17711.
- Malinverno, A. (1991). Inverse square-root dependence of mid-ocean ridge flank roughness on spreading rate, *Nature*, 352, 58–60.
- Malinverno, A. and Cowie, P. A. (1993). Normal faulting and the topographic roughness of mid-ocean ridge flanks, *Journal of Geophysical Research*, 98(B10), 17921–17939.
- Marsland, S. J., Haak, H., Jungclaus, J. H., Latif, M. and Röske, F. (2003). The Max-Planck-Institute global ocean/sea ice model with orthogonal curvilinear coordinates, *Ocean Modelling*, 5, 91–127.
- Miller, K.G., Kominz, M.A., Browning, J.V., Wright, J.D., Mountain, G.S., Katz, M.E., Sugarman, P.J., Cramer, B.S., Christie-Blick, N. and Pekar, S.F. (2005). The Phanerozoic record of global sea-level change, *Science*, vol.310, 1293–1298.
- Moore, T. C. and the Expedition 302 Scientists (2006). Sedimentation and subsidence history of the Lomonosov Ridge, in *Proceedings of the Integrated Ocean Drilling Program, 302*, edited by Backmann, J., Morean, K., McInroy, D. B., Mayer, L. A. and the Expedition 302 Scientists, College Station, TX (Integrated Ocean Drilling Program Management International, Inc.).
- Moran, K., Backman, J., Brinkhuis, H. and al. (2006). The Cenozoic palaeoenvironment of the Arctic Ocean, *Nature*, 441, doi:10.1038/nature04800.
- Morgan, J. P. (1983). Hotspot tracks and the early rifting of the Atlantic, *Tectonophysics*, 94, 123–139.
- Morgan, J. P. and Chen, Y. J. (1993). Dependence of ridge-axis morphology on magma supply and spreading rate, *Nature*, vol. 364, no. 6439, 706–708.
- Mudie, P. J. and Helgason, J. (1983). Palynological evidence for Miocene climatic cooling in eastern Iceland about 9.8 Myr ago, *Nature*, 303 (5919), 689–692.
- Müller, R. D., Sdrolias, M., Gaina, C. and Roest, W. R. (2008). Age, spreading rates, and spreading asymmetry of the world’s ocean crust, *Geochemistry, Geophysics, Geosystems*, vol. 9, no. 4, doi:10.1029/2007GC001743.
- Myhre, A. M. and Eldholm, O. (1988). The Western Svalbard margin (74°-80°N), *Marine and Petroleum Geology*, vol. 5, p. 134–156.

BIBLIOGRAPHY

- Mhyre, A. M., Thiede, J., Firth, J. V. and Shipboard Scientific Party (1995). North Atlantic-Arctic Gateways, Proc. ODP Init. Rep., 151.
- Neumann, E. R. and Ramberg, I. B. (1978). Palaeorifts - concluding remarks, in Neumann, E. R. and Ramberg, I. B. (eds), *Tectonics and Geophysics of Continental Rifts*, D. Reidel, Dodrecht, p. 409–424.
- Parsons, B. and Sclater, J. G. (1977). An analyses of the variation of the ocean floor bathymetry and the heat flow with age, *Journal of Geophysical Research*, 82(5), 803–827.
- Perkin, R. G. and Lewis, E. L. (1984). Mixing in the West Spitsbergen Current, *Journal Physical Oceanography*, 14(8), 1315–1325.
- Peterson, W. H. and Rooth, C. G. H. (1976). Formation and exchnage of deep water in the Greenland and Norwegian Seas, *Deep-Sea Research*, 23, 273–283.
- Price, J. F. and Baringer, M. (1994). Outflows and deep water productions by marginal seas, *Progress in Oceanography*, 33, 161–200.
- Quadfasel, D., Gascard, J. C., Koltermann, K. P. (1987). Large-scale oceanography in Fram Strait during the 1984 Marginal Ice-Zone Experiment, *Journal of Geophysical Research*, 92, 6719–6728.
- Reid, I. and Jackson, H. R. (1981). Oceanic spreading rate and crustal thickness, *Marine Geophysical Researches*, 5, 165–172.
- Röske, F. (2006). A global heat and freshwater forcing dataset for ocean models, *Ocean Modelling*, 11, 235–297.
- Roest, W. R. and Srivastava, S. P. (1989). Seafloor Spreading history I: Magnetic anomalies along track, in J. S. Bell (ed.), *East Coast Basin Atlas Series: Labrador Sea*, Geol. Survey Can., Map Sheet L17-1.
- Rudels, B., Fahrbach, E., Meincke, J., Budèus, G. and Eriksson, P. (2002). The East Greenland Current and its contribution to the Denmark Strait overflow, *Journal of Marine Science*, 59, 1133–1154, doi: 10.1006/jmsc.2002.1284.
- Schauer, U. and Fahrbach, E. (2004). Arctic warming through the Fram Strait: Oceanic heat transport from 3 years of measurements, *Journal of Geophysical research*, vol. 109, doi:10.1029/2003JC001823.
- Snow, J. E. and Edmonds. H. N. (2007). Ultraslow-Spreading Ridges Rapid Paradigm Chages, *Oceanography*, vol. 20, no. 1, 90–101.

- Solheim, A., Faleide, J. I., Andersen, E. S., Elverhøl, A., Forsberg, C. F., Vanneste, K., Uenzelmann-Neben, G. and Channell, J. E. T. (1998). Late Cenozoic seismic stratigraphy and glacial geological development of the East Greenland and Svalbard-Barents sea continental margins, *Quaternary Science Reviews*, vol. 17, p. 155–184.
- Srivastava, S. P. and Roest, W. R. (1989). Seafloor spreading history II-IV, in J. S. Bell (ed.), *East Coast Basin Atlas Series: Labrador Sea*, Geol. Survey Can., Map Sheets L17-2–L17-6.
- Steckler, M. S. and Watts, A. B. (1978). Subsidence of the Atlantic-type continental margin off New York, *Earth and Planetary Science Letters*, 41, 1–13.
- Steele, M., Morley, R. and Ermold, W. (2001). A global ocean hydrography with a high-quality arctic ocean, *J. Climate*, 14(9), 2079–2087.
- Stein, R. (ed) (2005). Scientific cruise report of the Arctic expedition ARK-XX/3 of RV “Polarstern” in 2004: Fram Strait, Yermak Plateau and East Greenland continental margin, *Reports on polar and marine research*, 517, Alfred-Wegener-Institut für Polar- und Meeresforschung.
- Stewart, R. H. (2007). Introduction to Physical Oceanography, Texas A & M University, http://oceanworld.tamu.edu/resources/ocng_textbook/contents.html.
- Stickley, C. E., Brinkhuis, H., Schellenberg, S. A., Sluijs, A., Röhl, U., Fuller, M., Grauert, M., Huber, M., Wamaar, J. and Williams, G. L. (2004). Timing and nature of the deepening of the Tasmanian Gateway, *Paleoceanography*, vol. 19, doi: 10.1029/2004PA001022.
- Talwani, M. and Eldholm, O. (1977). Evolution of the Norwegian-Greenland Sea, *Geol. Soc. Am. Bull.* 88, 969–999.
- Thiede, J. (ed) (2002). POLARSTERN ARKTIS XVII/2 : Cruise Report: AMORE 2001 (Arctic Mid-Ocean Ridge Expedition), *Reports on polar and marine research*, 421, Alfred-Wegener-Institut für Polar- und Meeresforschung.
- U.S. Department of Commerce, National Oceanic and Atmospheric Administration, National Geophysical Data Center (NGDC) (2006). 2-minutes Gridded Global Relief Data (ETOPO2v2), <http://www.ngdc.noaa.gov/mgg/fliers/06mgg01.html>.
- Verhoef, J., Macnab, R., Roest, W., Ariani-Hamed, J. and the project team (1996). Magnetic anomalies of the Arctic and North Atlantic and adjacent land areas, GAMMA5 (Gridded Aeromagnetic and Marine Magnetics of the North Atlantic and Arctic, 5km), Geological Survey of Canada, Open File 3125a (CD-Rom).
- Vogt, P. R., Taylor, P. T., Kovacs, L. C. and Johnson, G. L. (1979). Detailed Aeromagnetic Investigation of the Arctic Basin, *Journal of Geophysical Research*, vol. 84, B3, 1071–1089.

BIBLIOGRAPHY

- Vogt, P. R., Jung, W.-Y. and Brozena, J. (1998). Arctic margin gravity highs remain puzzling, *Eos, Transaction, American Geophysical Union*, vol. 79, no. 49, 605–606.
- Winkler, A., Wolf-welling, T. C. W., Stattegger, K and Thiede, J. (2002). Clay mineral sedimentation in high northern latitude deep-sea basins since the Middle Miocene (ODP Leg 151, NAAG), *International Journal of Earth Science*, 91, 133–148.
- Wold, C. N. (1995). Palaeobathymetric reconstruction on a gridded database: the northern North Atlantic and southern Greenland-Iceland-Norwegian sea, from Scrutton, R. A., Stoker, M. S., Shimmield, G. B. and Tudhope, A. W. (eds), *The Tectonics, Sedimentation and Palaeoceanography of the North Atlantic Region*, Geological Society Special Publication No. 90, 271–302.
- Wolf-Welling, T. C. W., Cremer, M., O'Connell, S., Winkler, A. and Thiede, J. (1996). Cenozoic Arctic Gateway paleoclimate variability: indications from changes in coarse-fraction composition (ODP Leg 151), in *Proceedings of the Ocean Drilling Program, Scientific Results*, vol. 151, edited by J. Thiede et al., Ocean Drilling Program, College Station, TX, pp. 515–567.
- Wright, J. D. and Miller, K. G. (1996). Control of North Atlantic Deep Water circulation by the Greenland-Scotland Ridge, *Paleoceanography*, vol.11, no. 2, 157–170.
- Zachos, J., Pagani, M., Sloan, L., Thomas, E. and Billups, K. (2001). Trends, Rhythms, and Aberrations in Global Climate 65 Ma to Present, *Science*, vol. 292, 686–693.

Appendix A

Additional figures

A.0.1 Reconstruction of palaeobathymetry

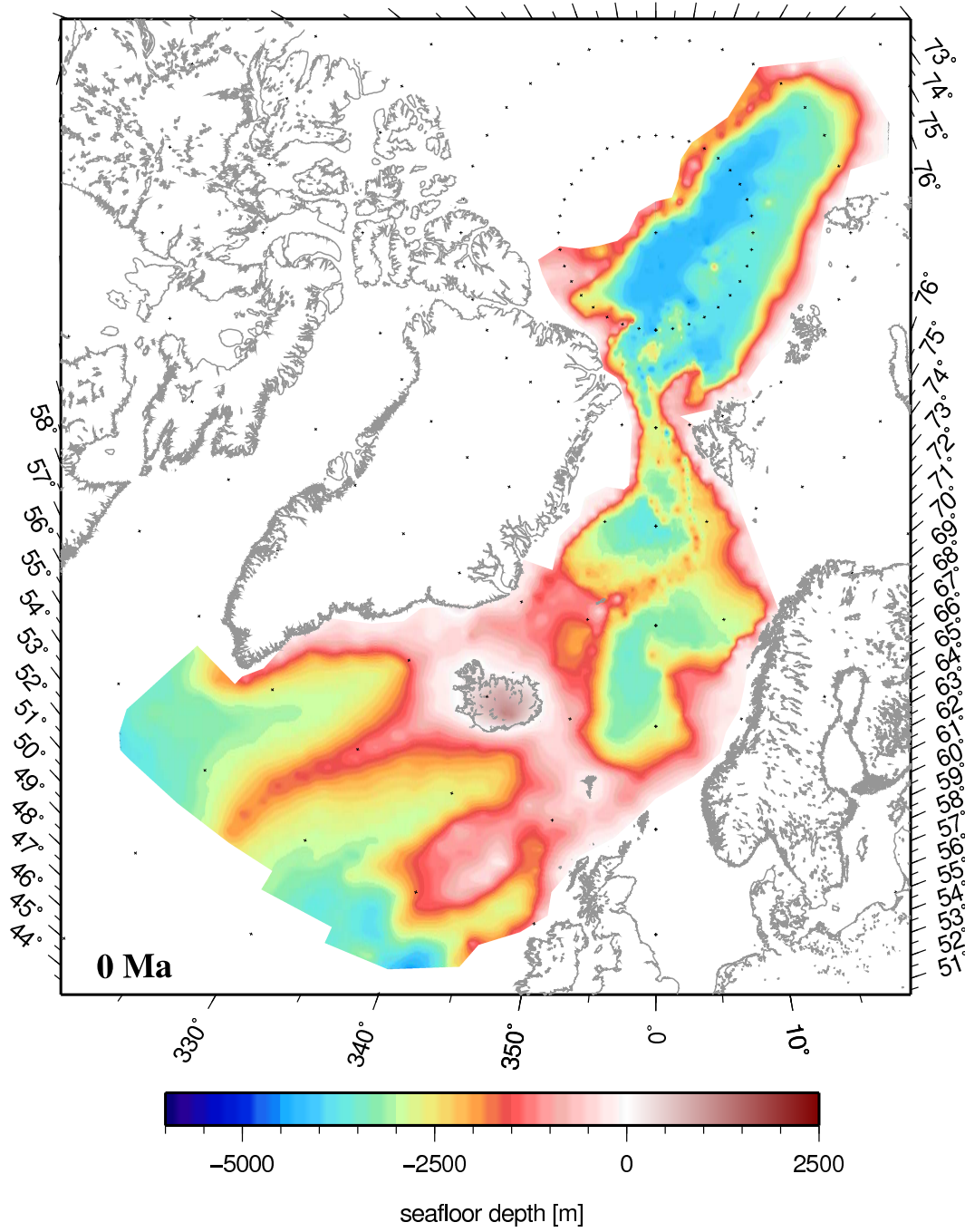


Figure A.1: Palaeobathymetric reconstruction for 0 Ma

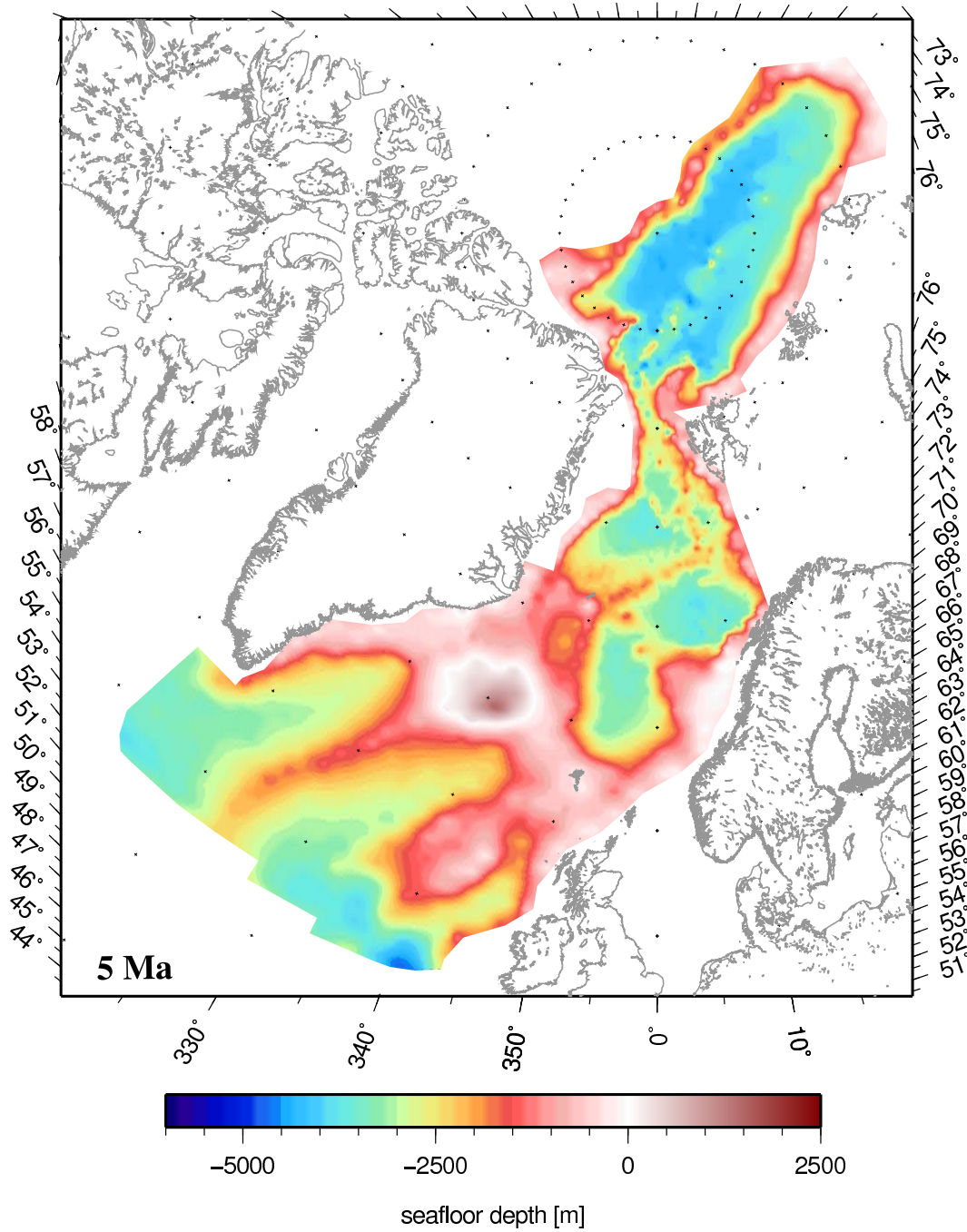


Figure A.2: Palaeobathymetric reconstruction for 5 Ma

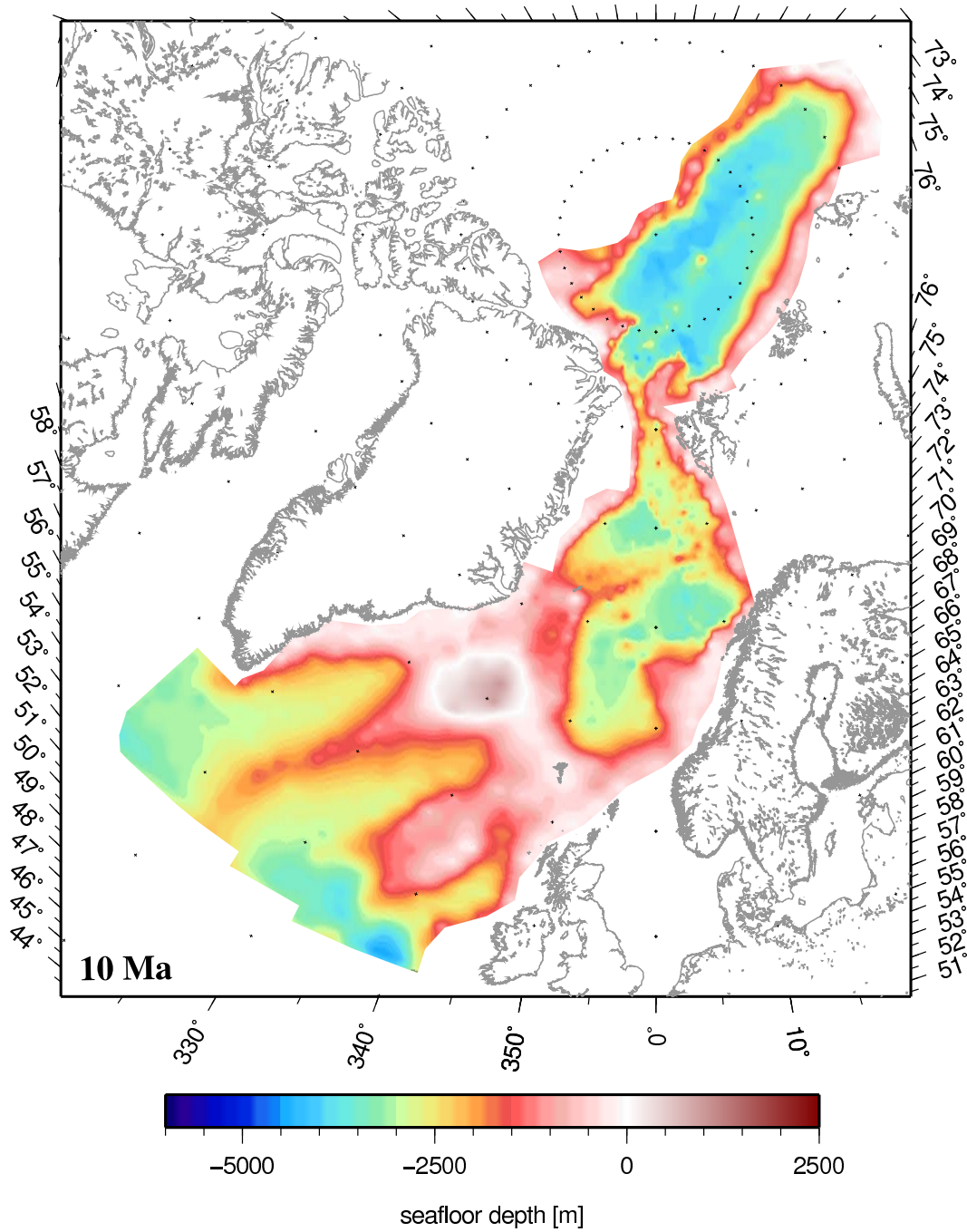


Figure A.3: Palaeobathymetric reconstruction for 10 Ma

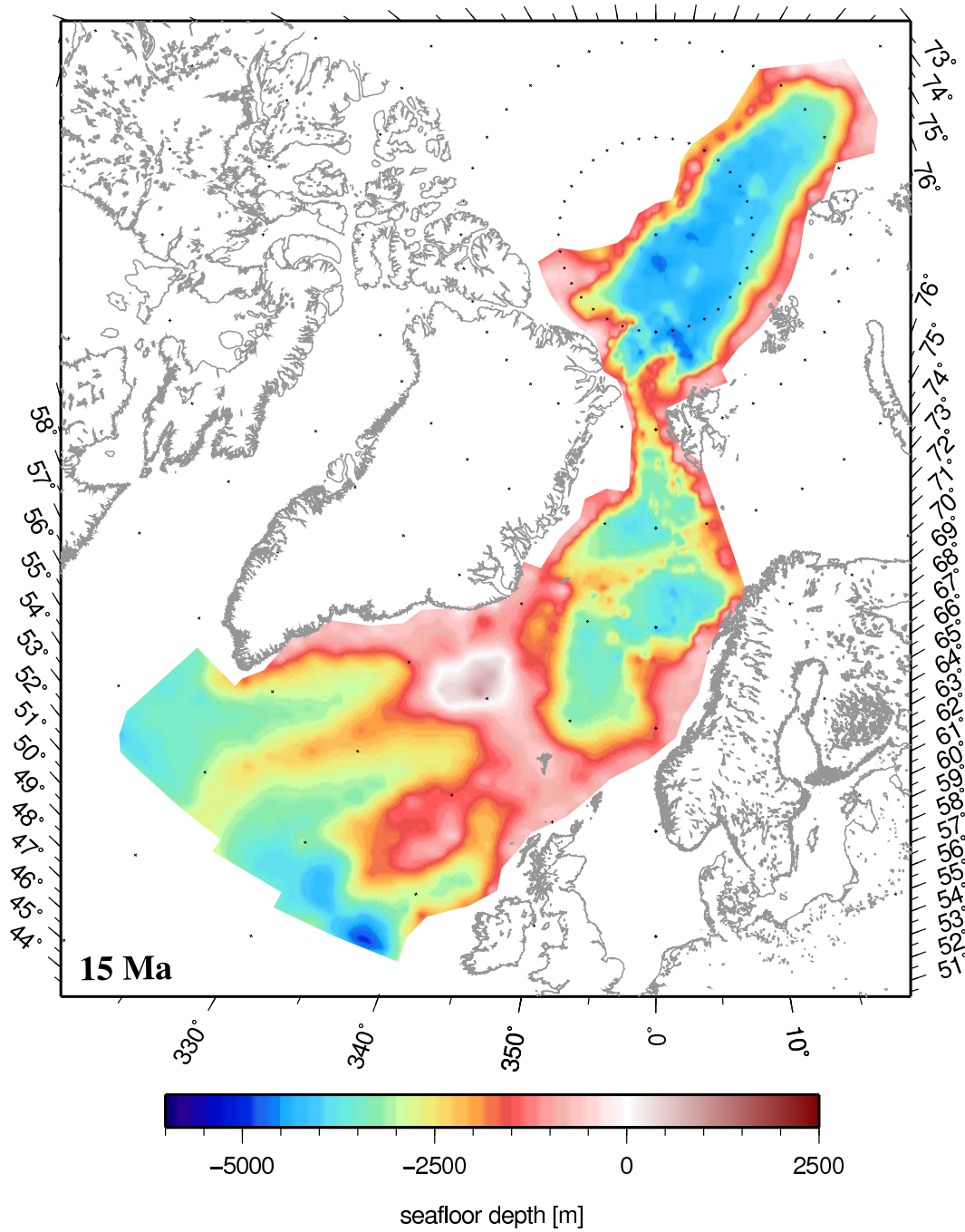


Figure A.4: Palaeobathymetric reconstruction for 15 Ma

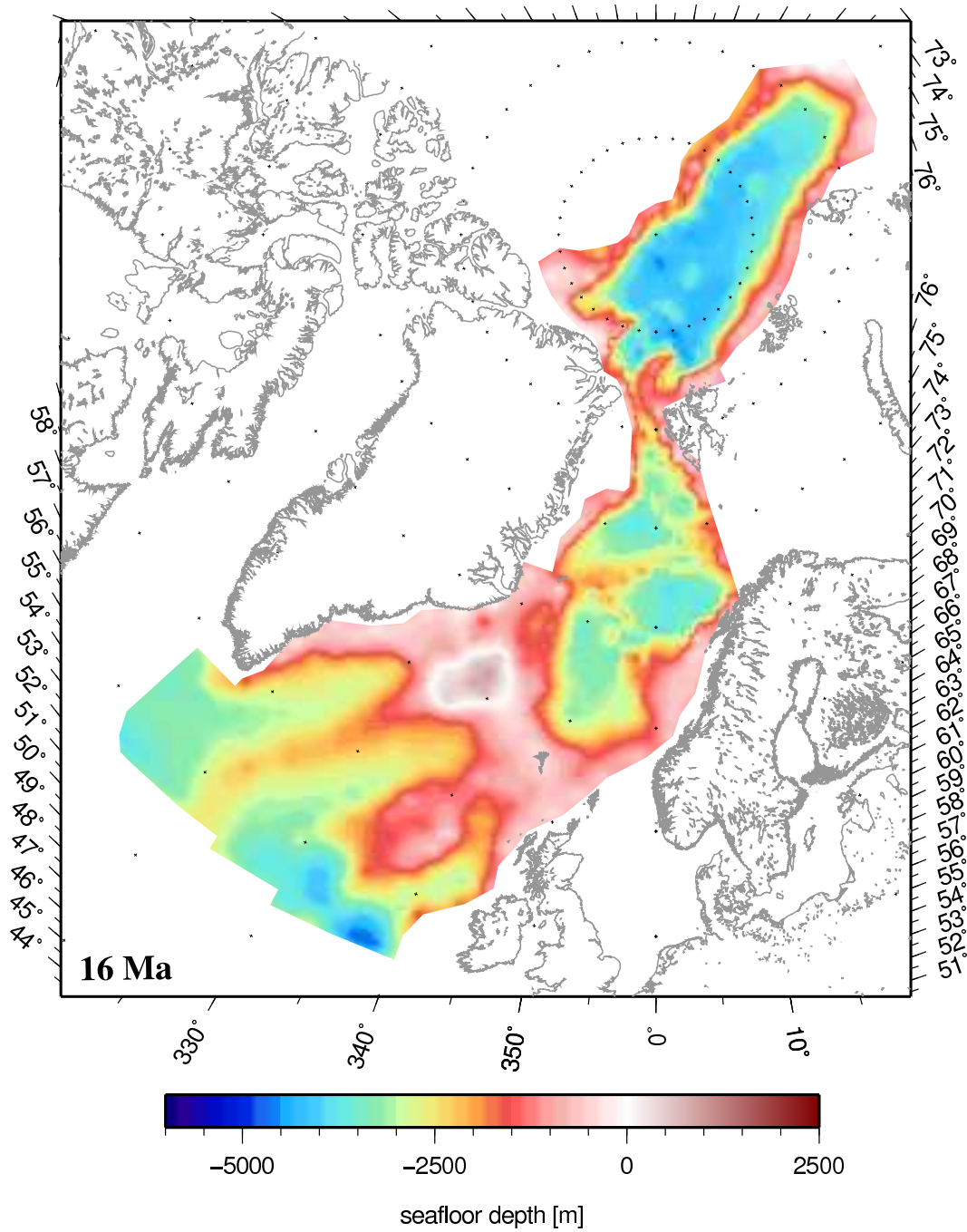


Figure A.5: Palaeobathymetric reconstruction for 16 Ma

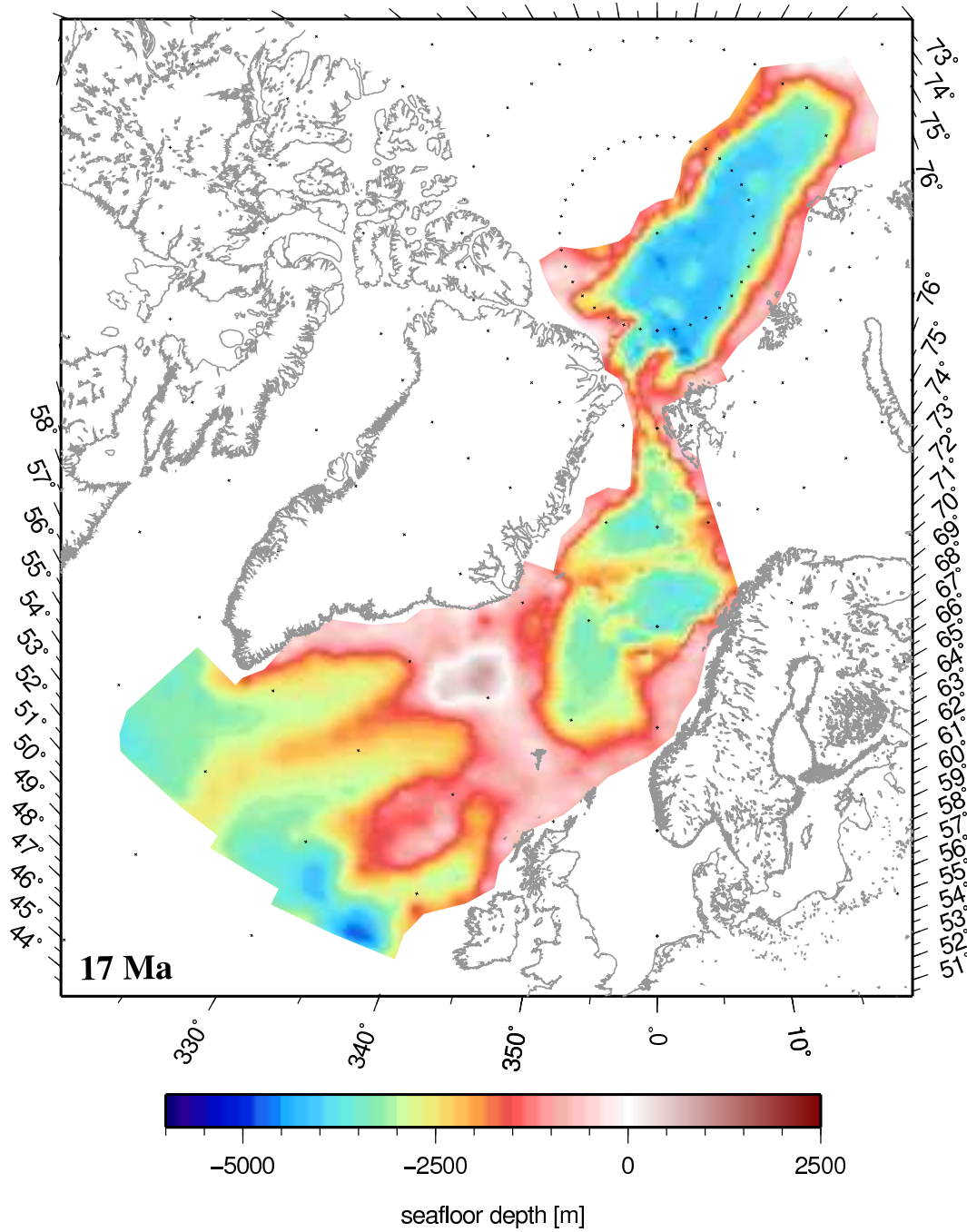


Figure A.6: Palaeobathymetric reconstruction for 17 Ma

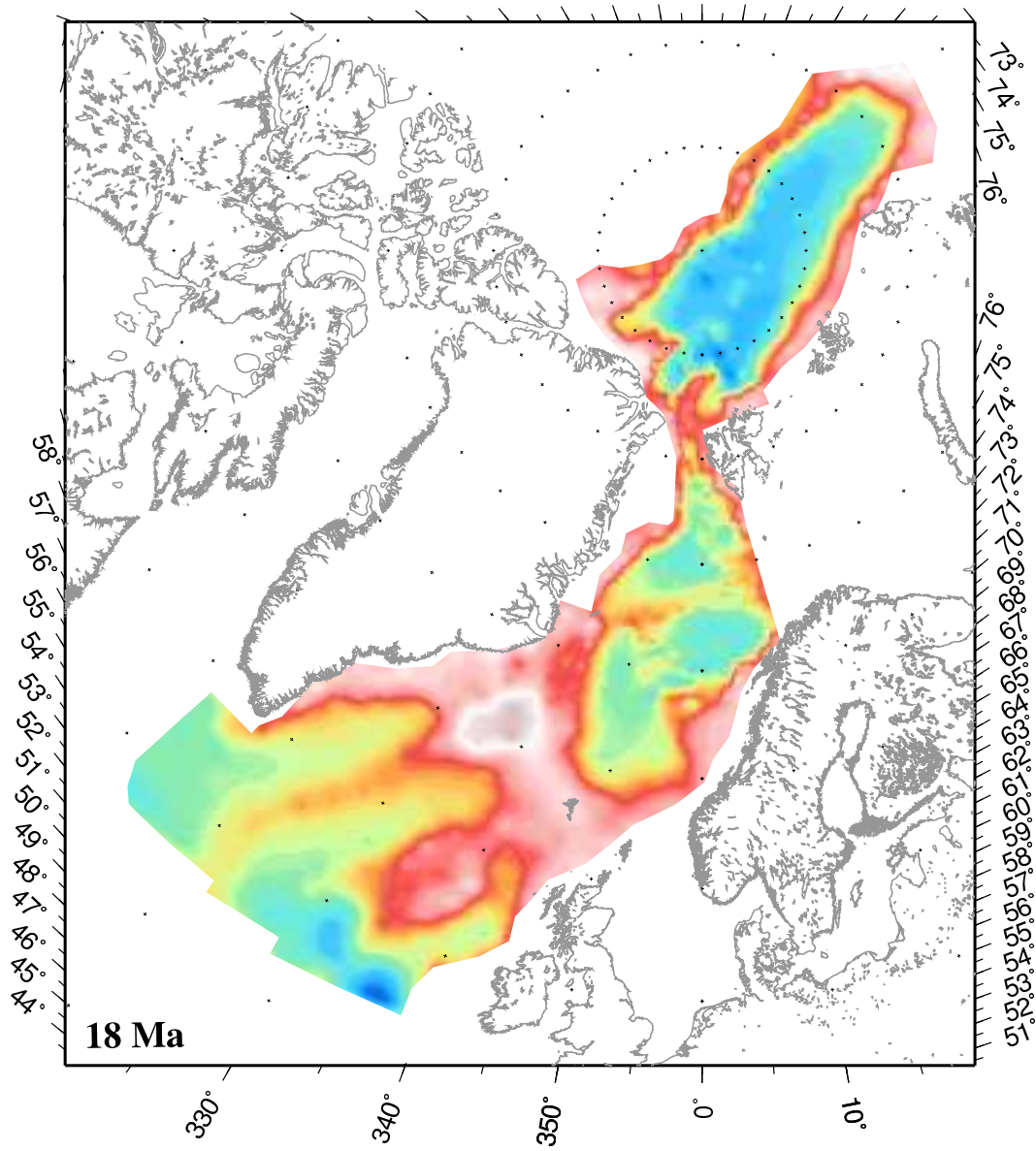


Figure A.7: Palaeobathymetric reconstruction for 18 Ma

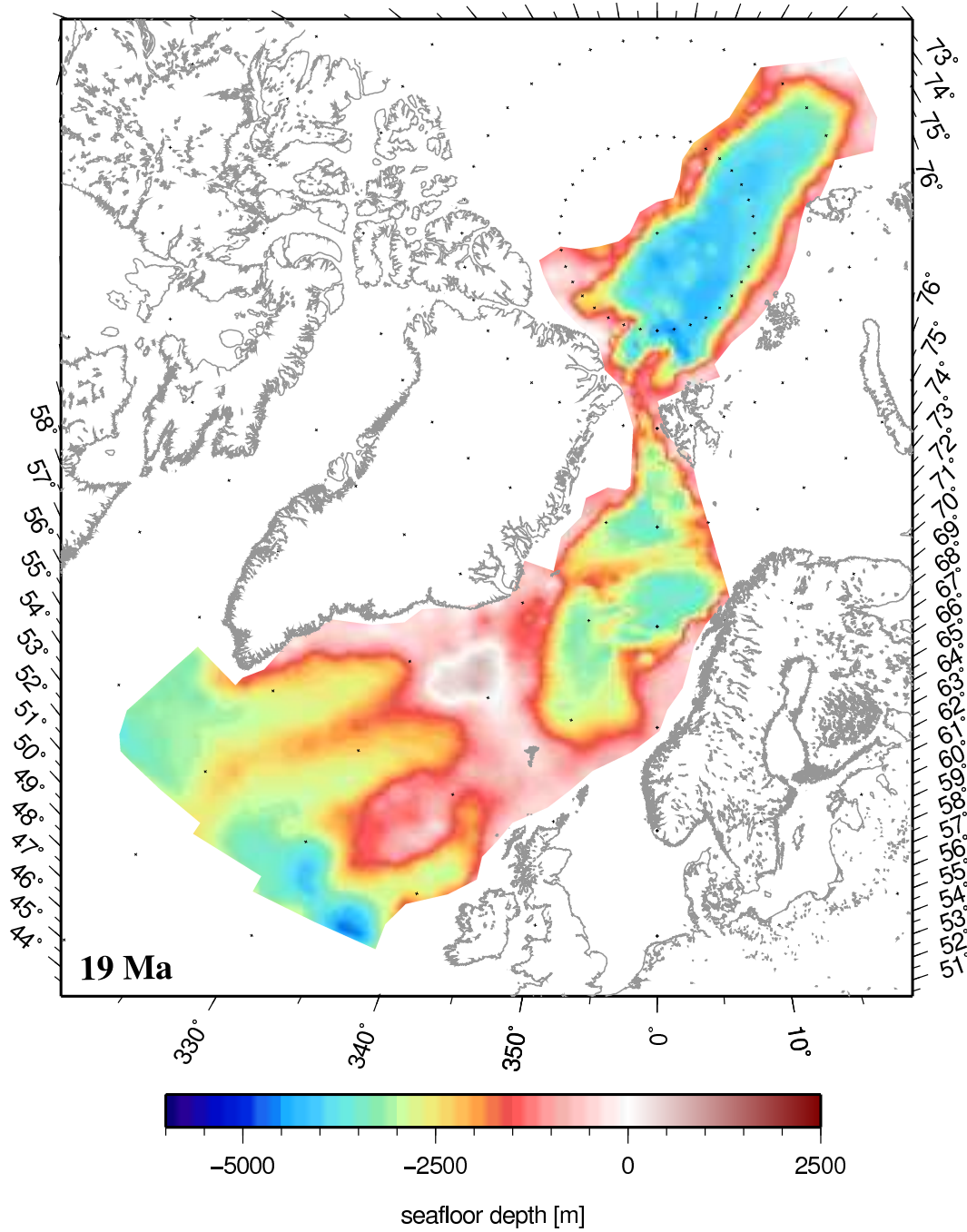


Figure A.8: Palaeobathymetric reconstruction for 19 Ma

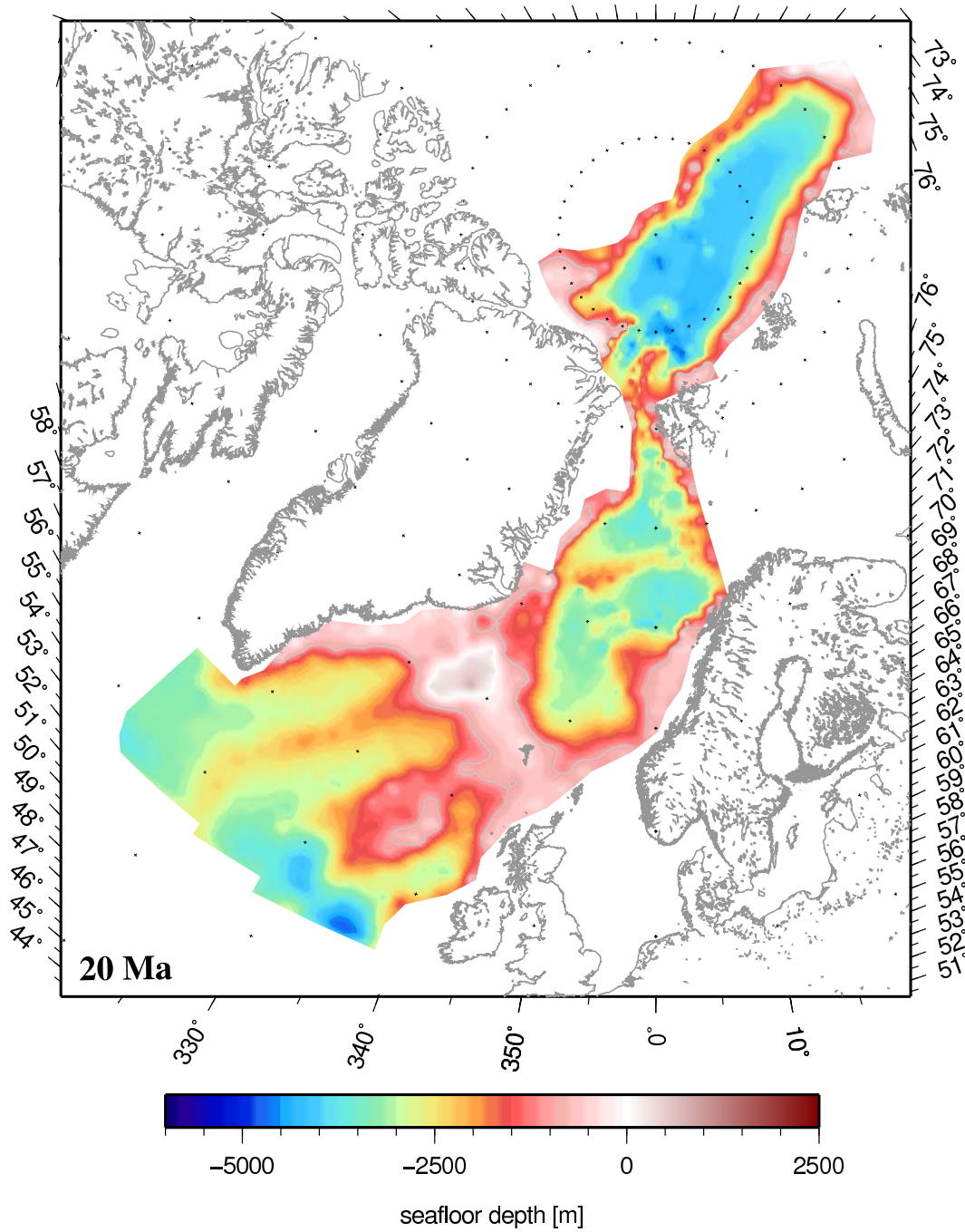


Figure A.9: Palaeobathymetric reconstruction for 20 Ma

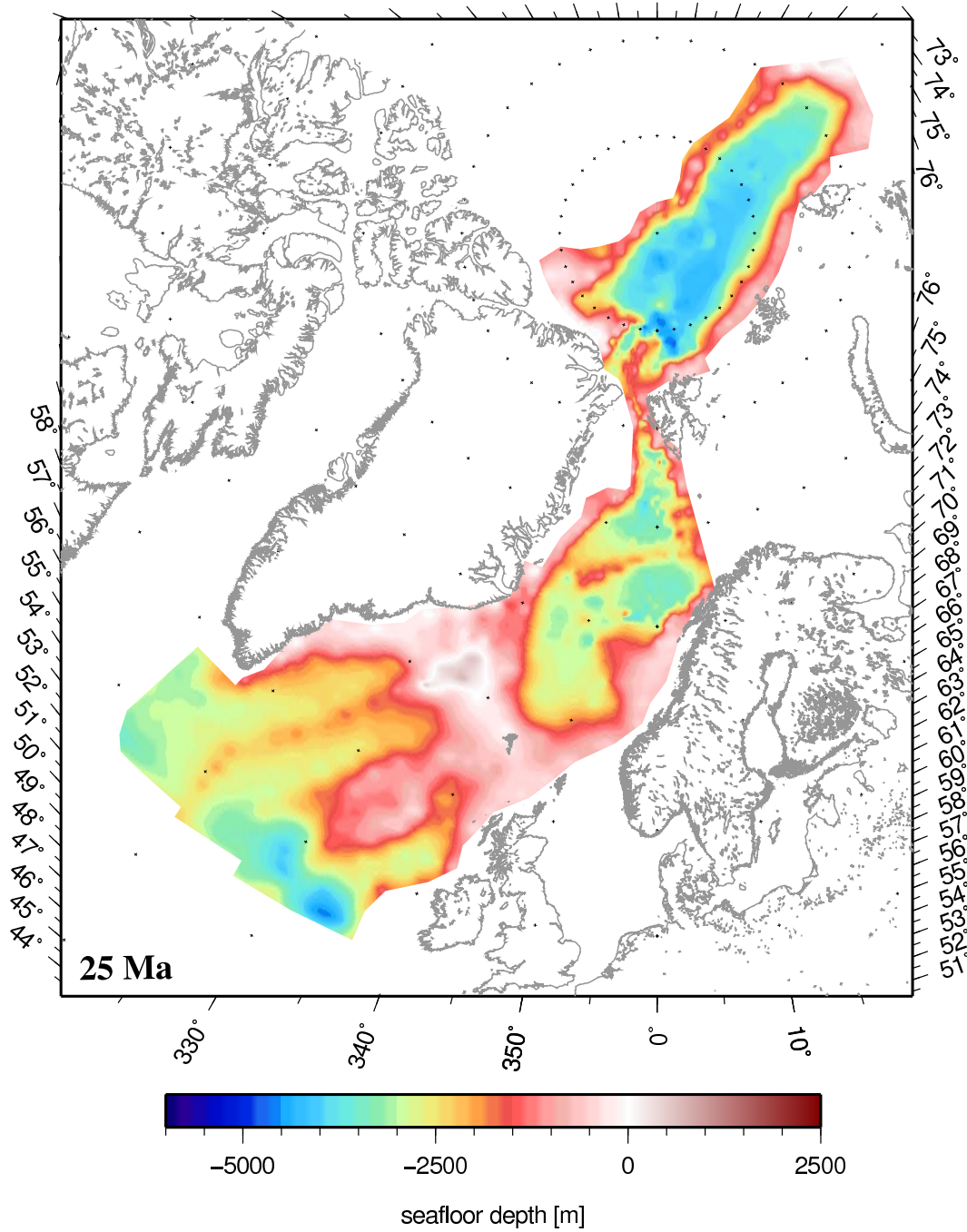


Figure A.10: Palaeobathymetric reconstruction for 25 Ma

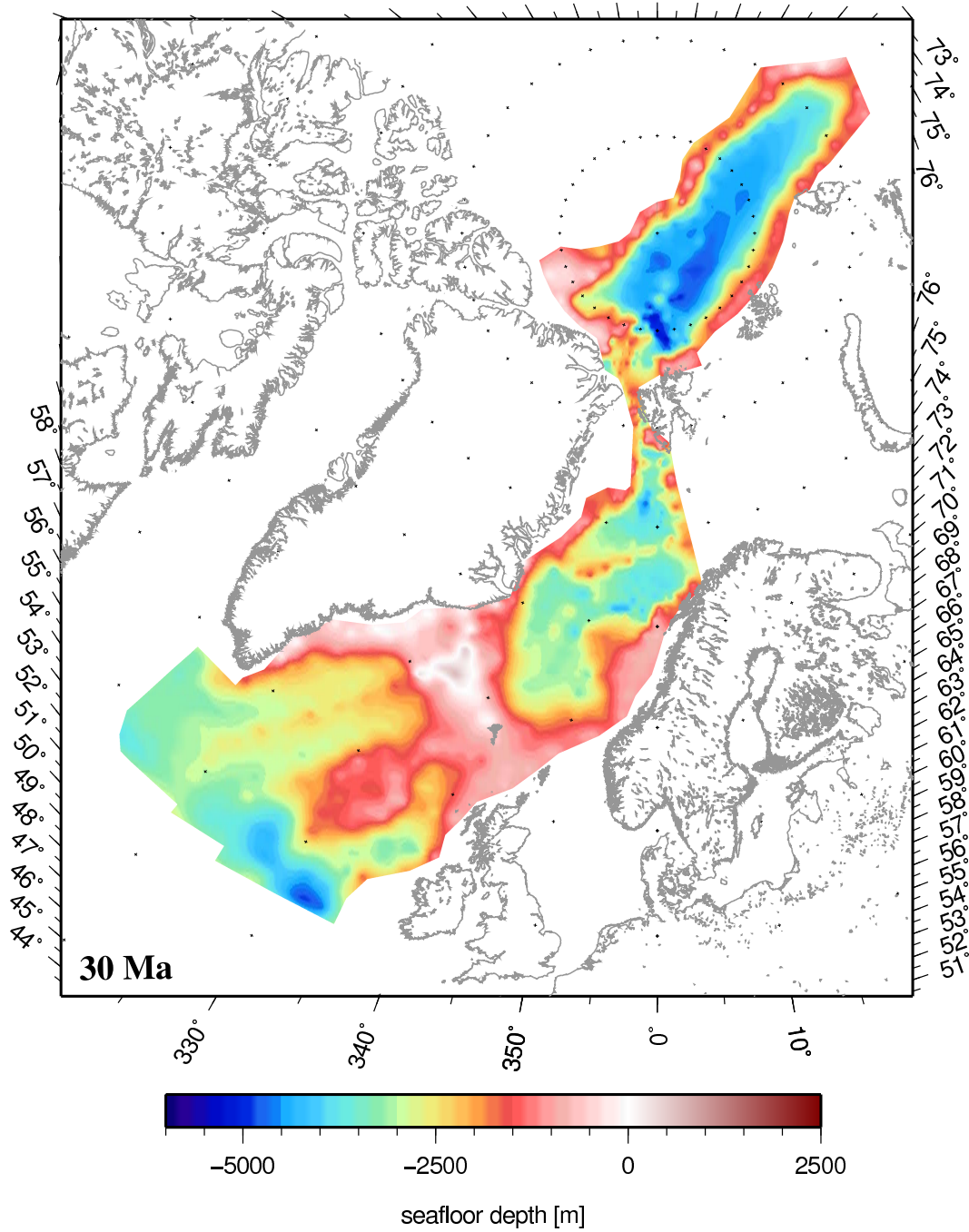


Figure A.11: Palaeobathymetric reconstruction for 30 Ma

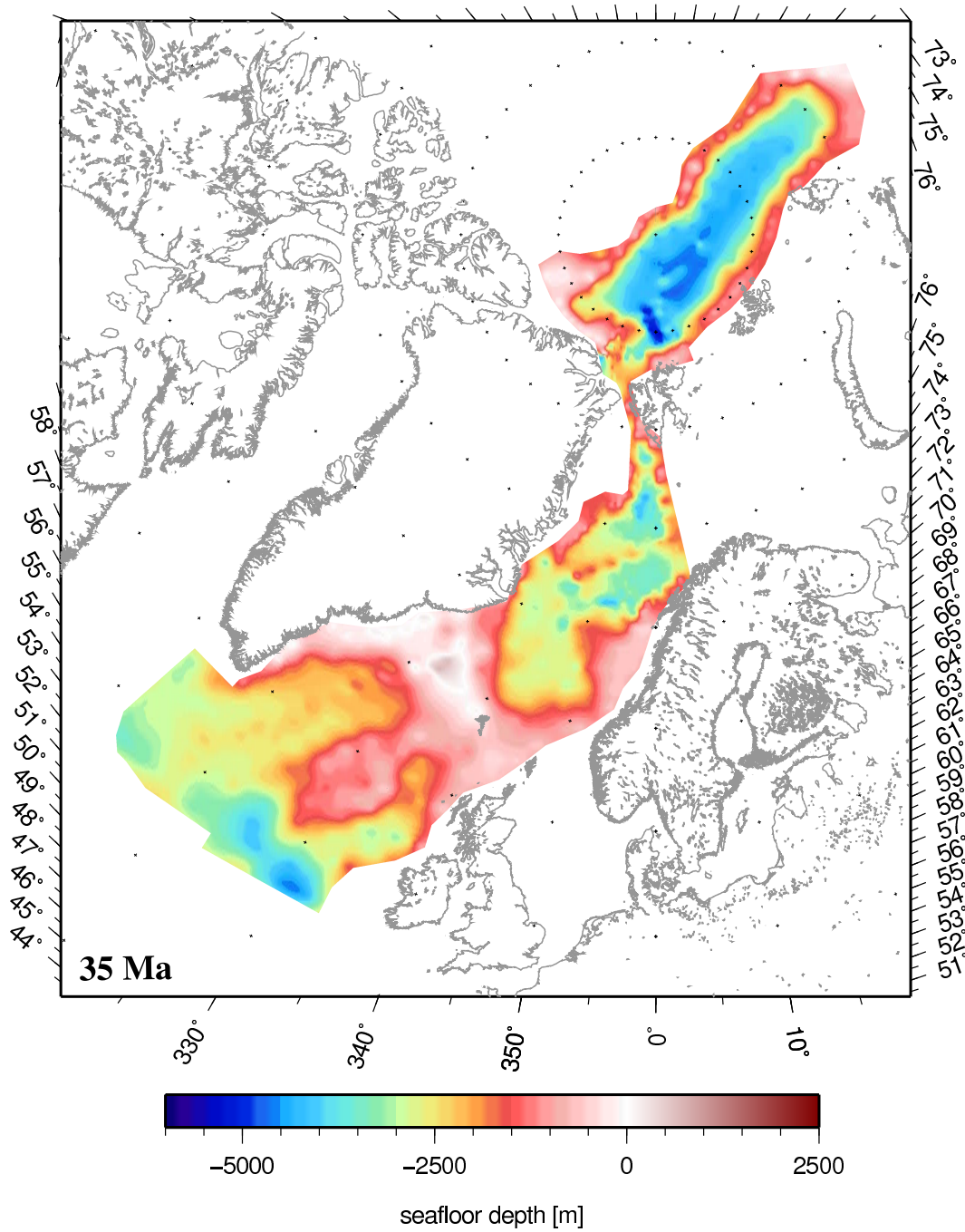


Figure A.12: Palaeobathymetric reconstruction for 35 Ma

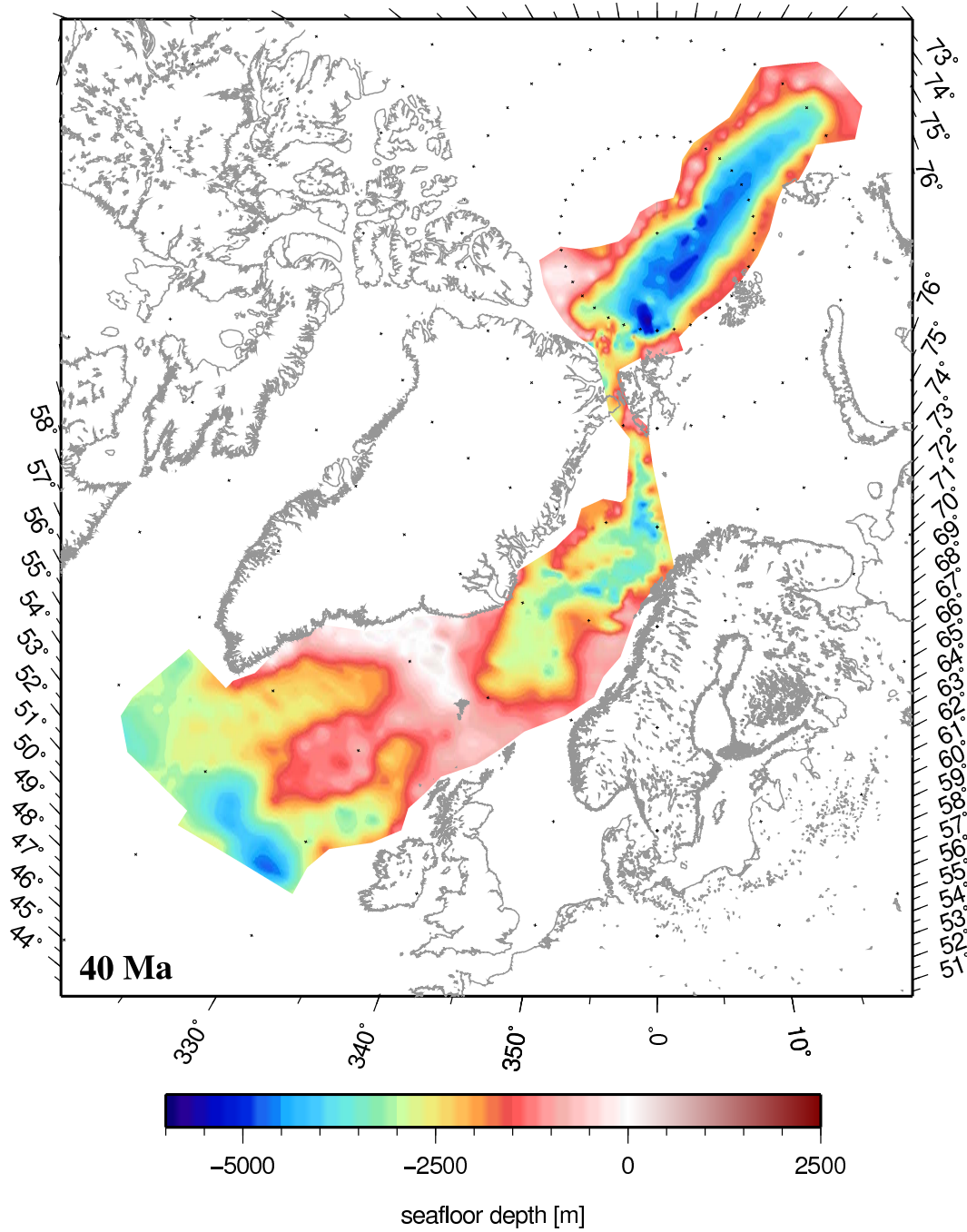


Figure A.13: Palaeobathymetric reconstruction for 40 Ma

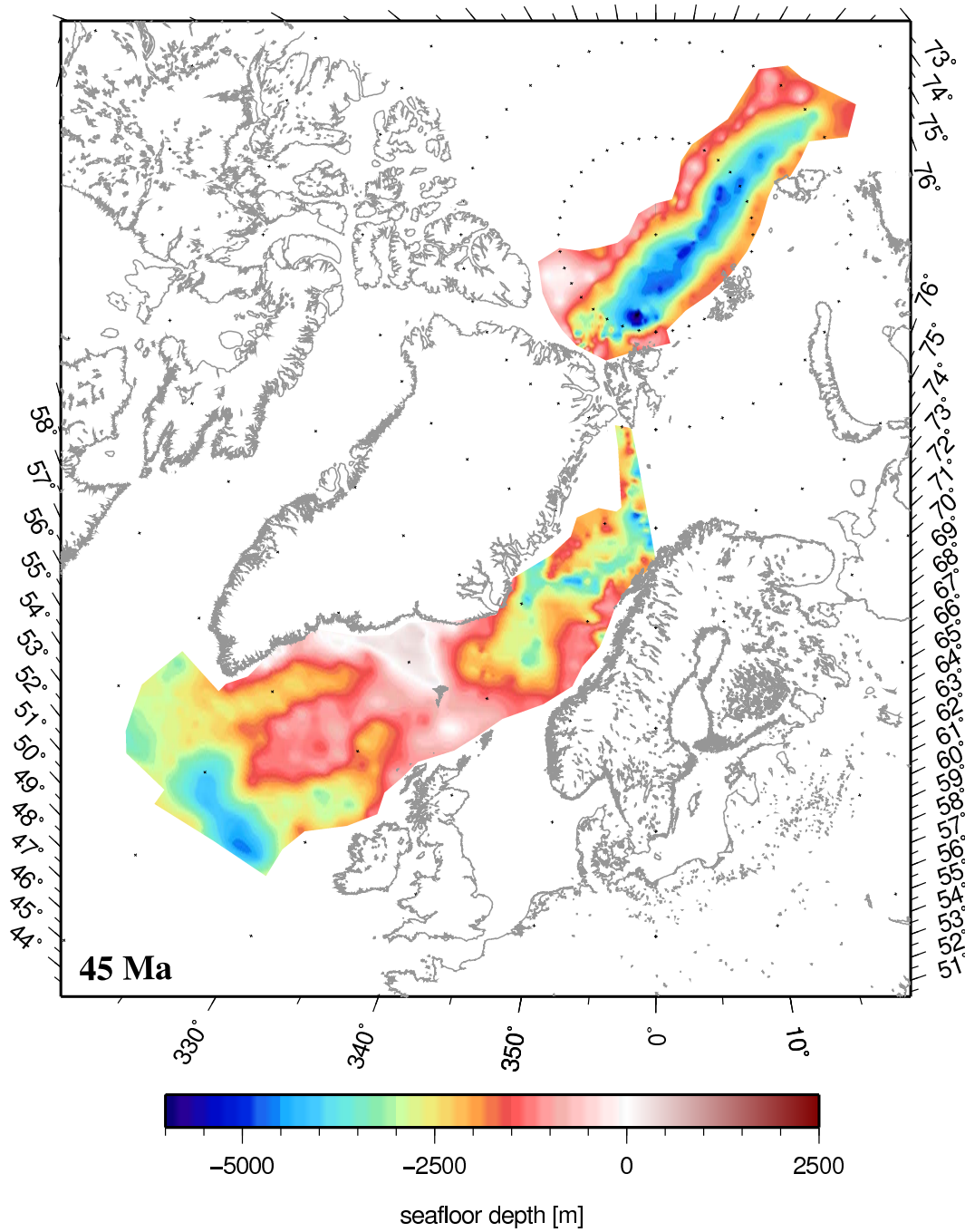


Figure A.14: Palaeobathymetric reconstruction for 45 Ma

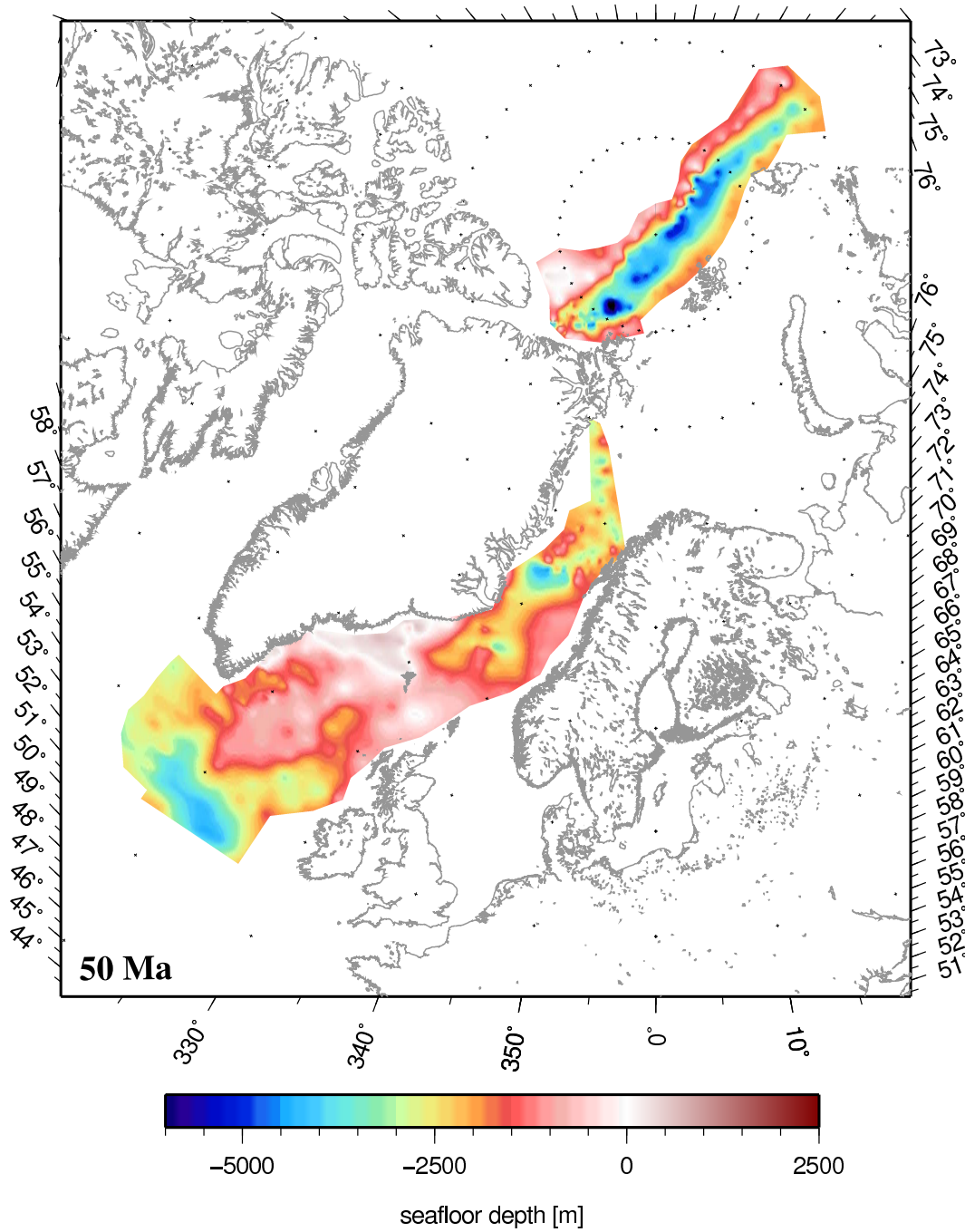


Figure A.15: Palaeobathymetric reconstruction for 50 Ma

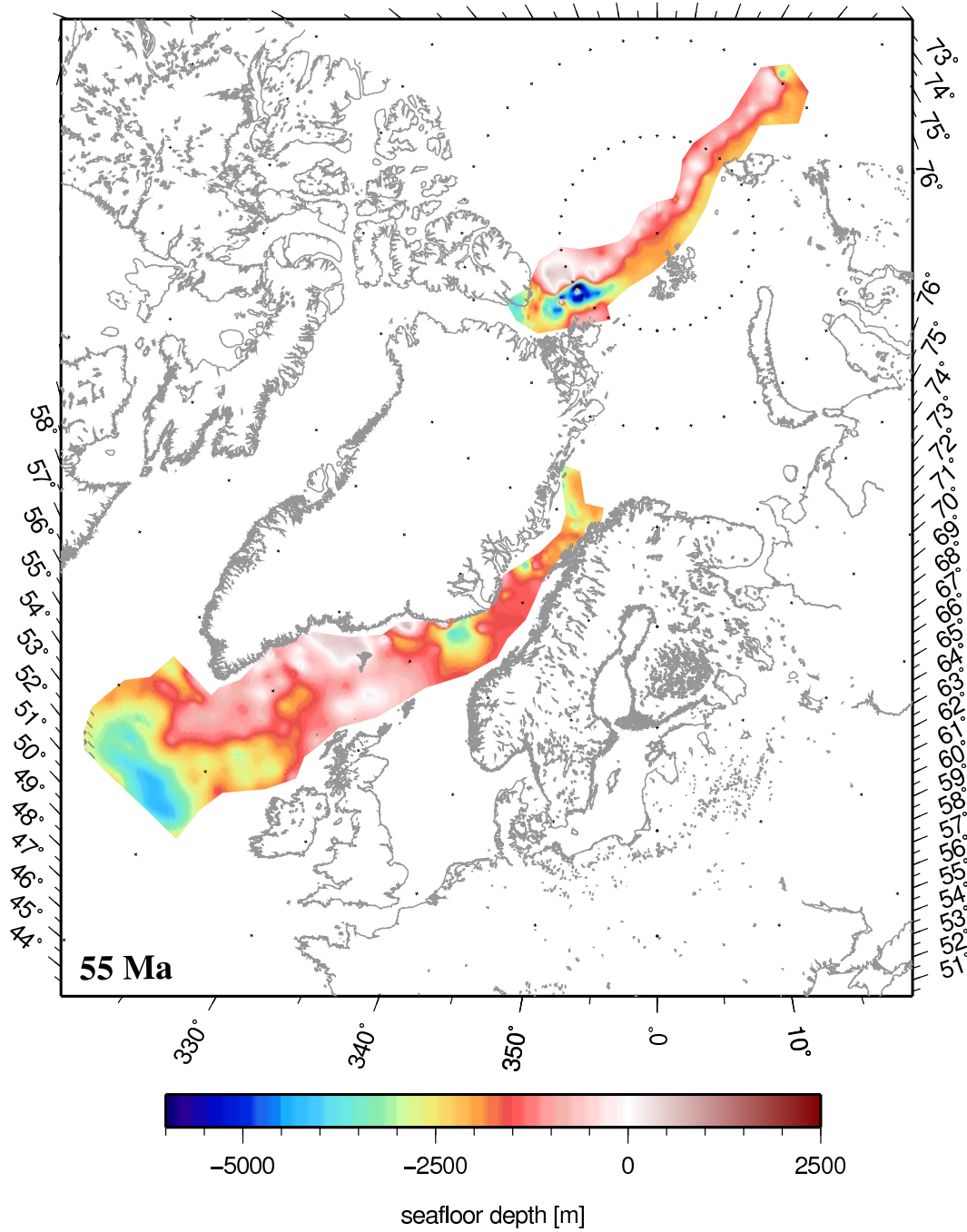


Figure A.16: Palaeobathymetric reconstruction for 55 Ma

A.0.2 Reconstruction of palaeo-basement depth

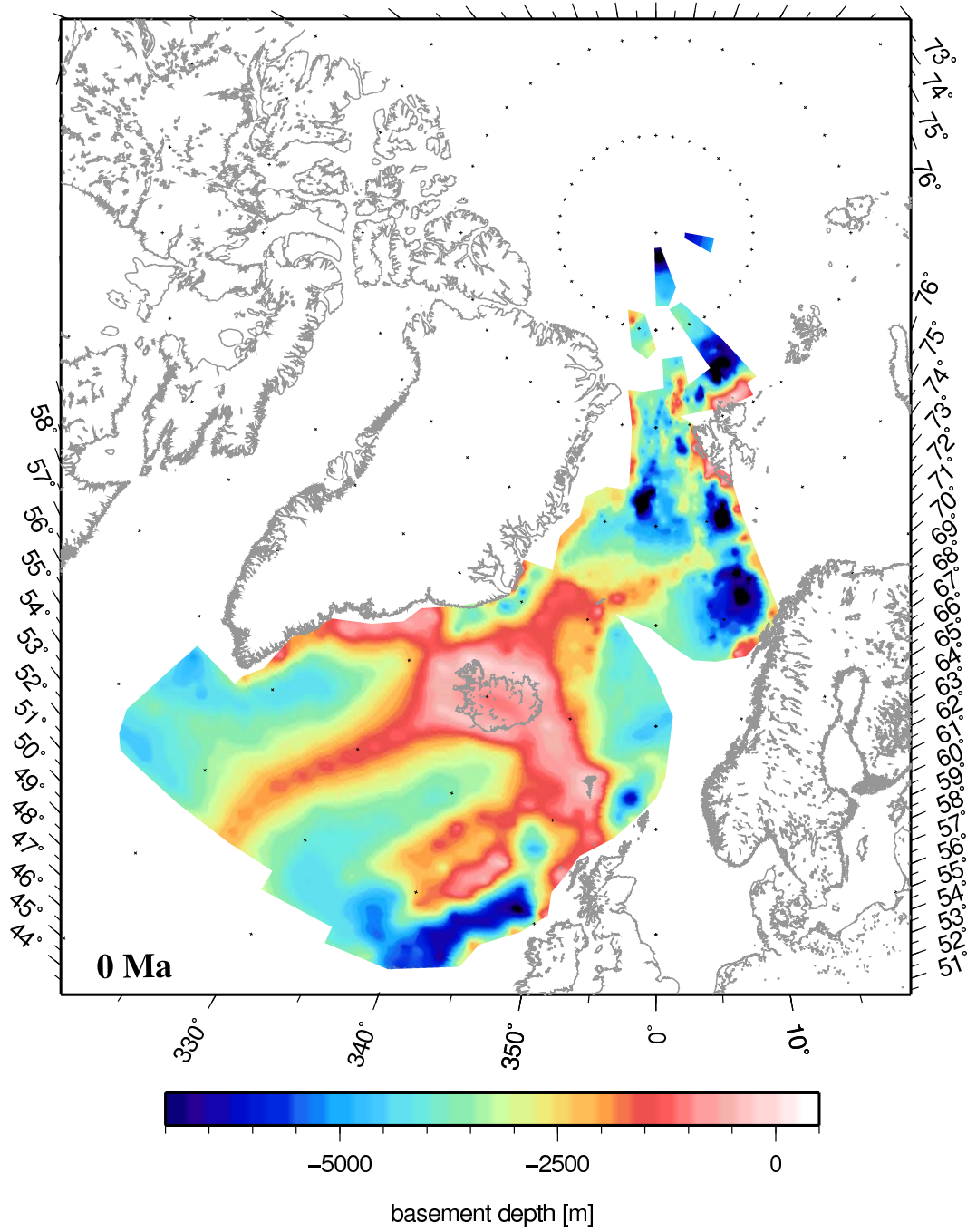


Figure A.17: Palaeo-basement reconstruction for 0 Ma

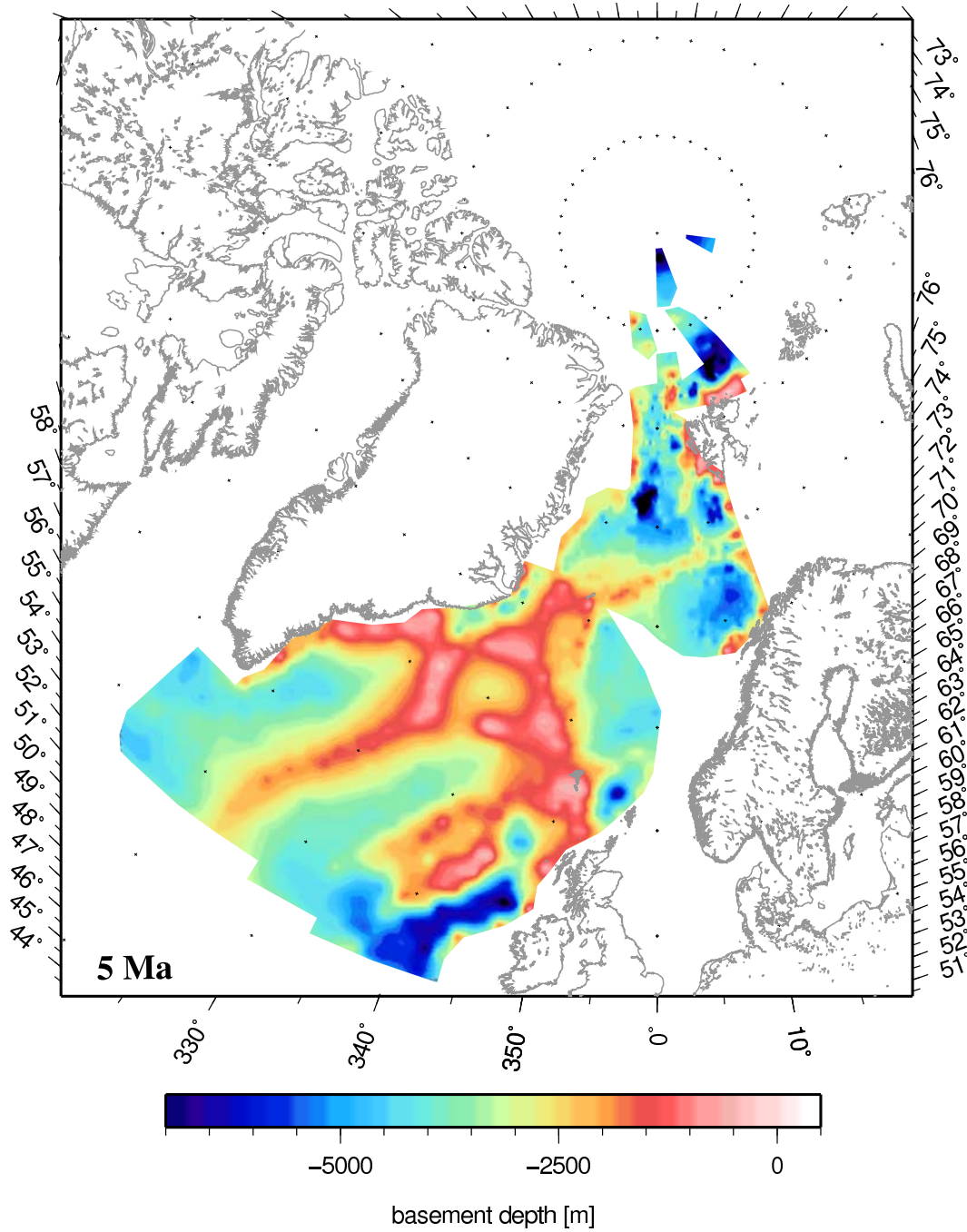


Figure A.18: Palaeo-basement reconstruction for 5 Ma

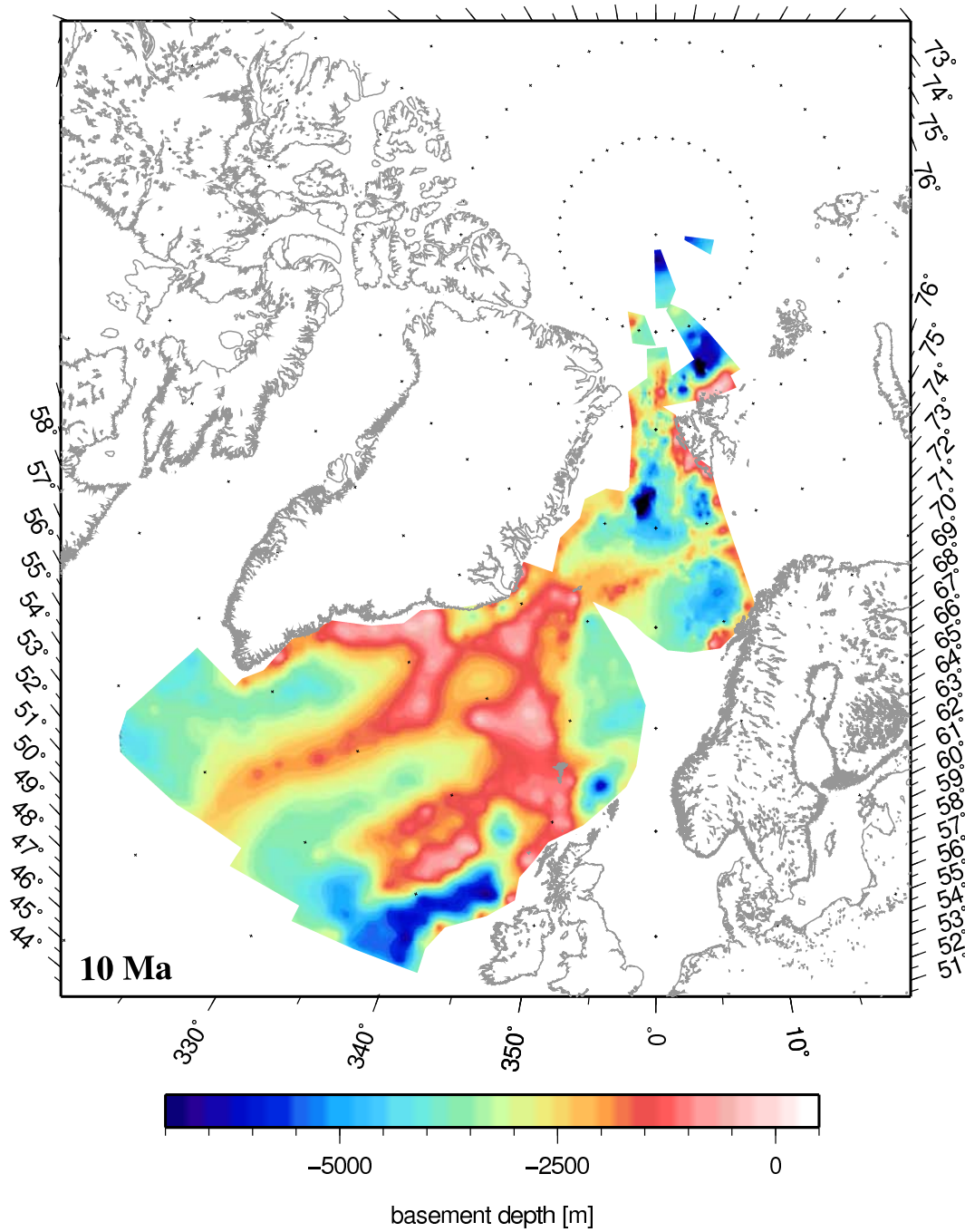


Figure A.19: Palaeo-basement reconstruction for 10 Ma

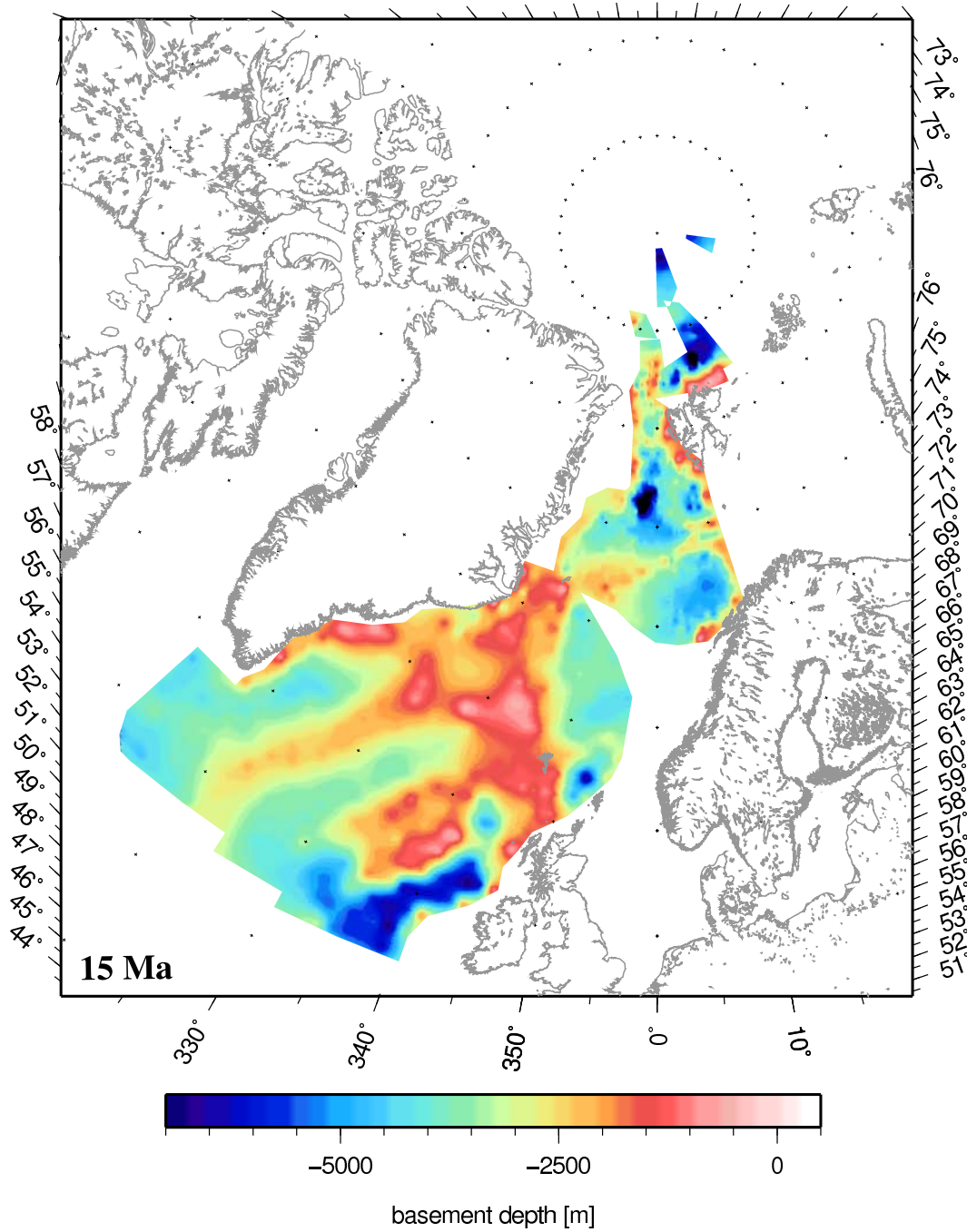


Figure A.20: Palaeo-basement reconstruction for 15 Ma

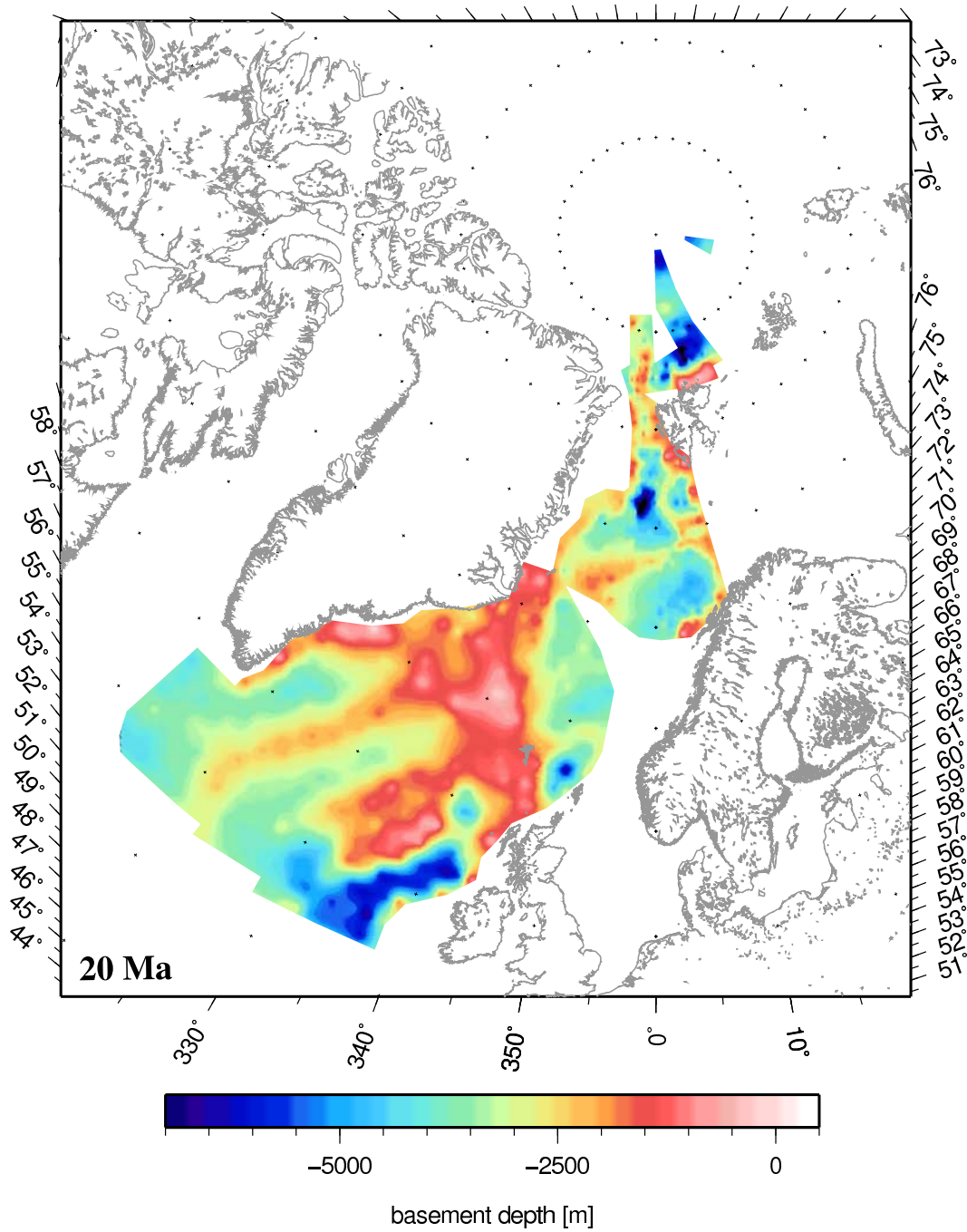


Figure A.21: Palaeo-basement reconstruction for 20 Ma

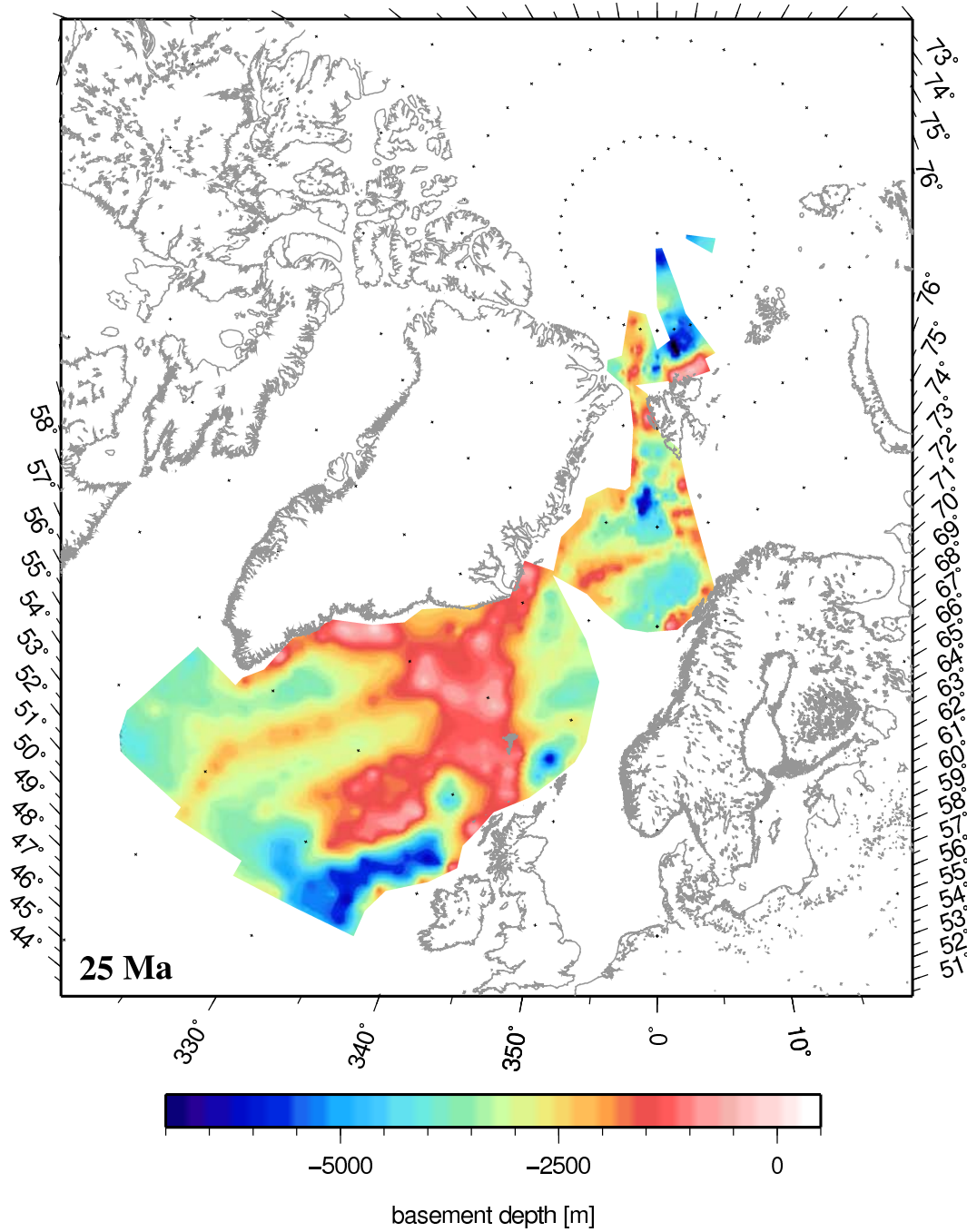


Figure A.22: Palaeo-basement reconstruction for 25 Ma

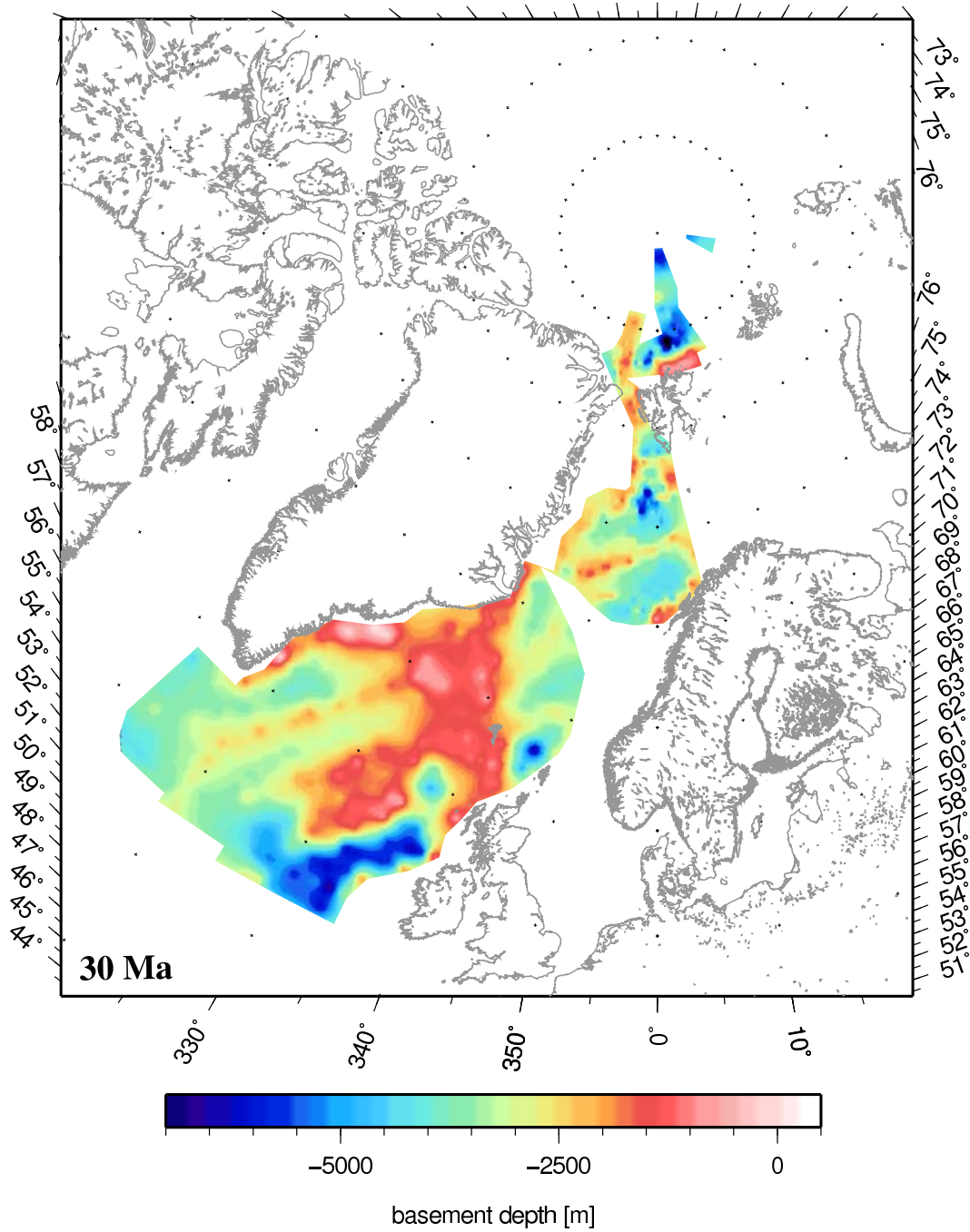


Figure A.23: Palaeo-basement reconstruction for 30 Ma

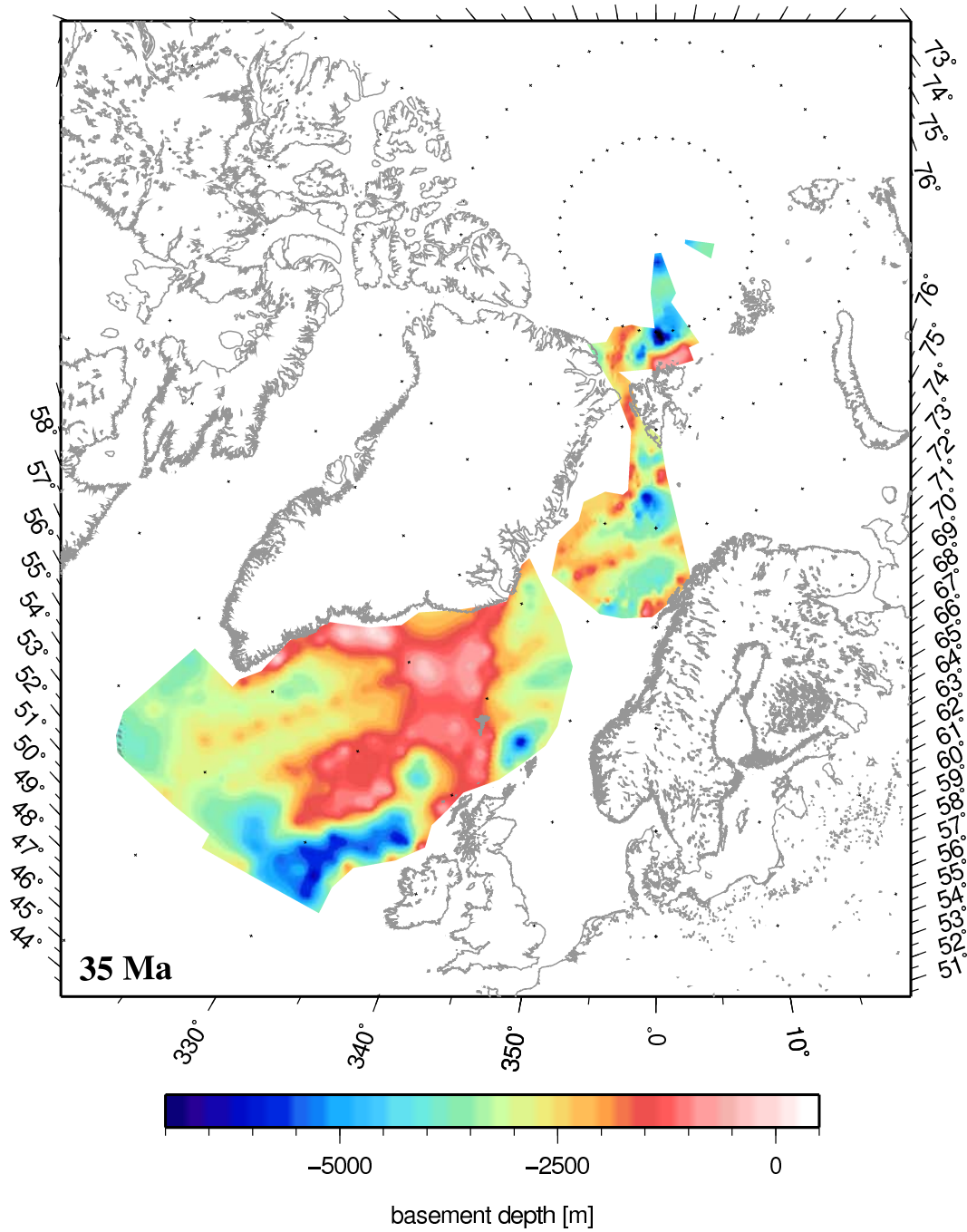


Figure A.24: Palaeo-basement reconstruction for 35 Ma

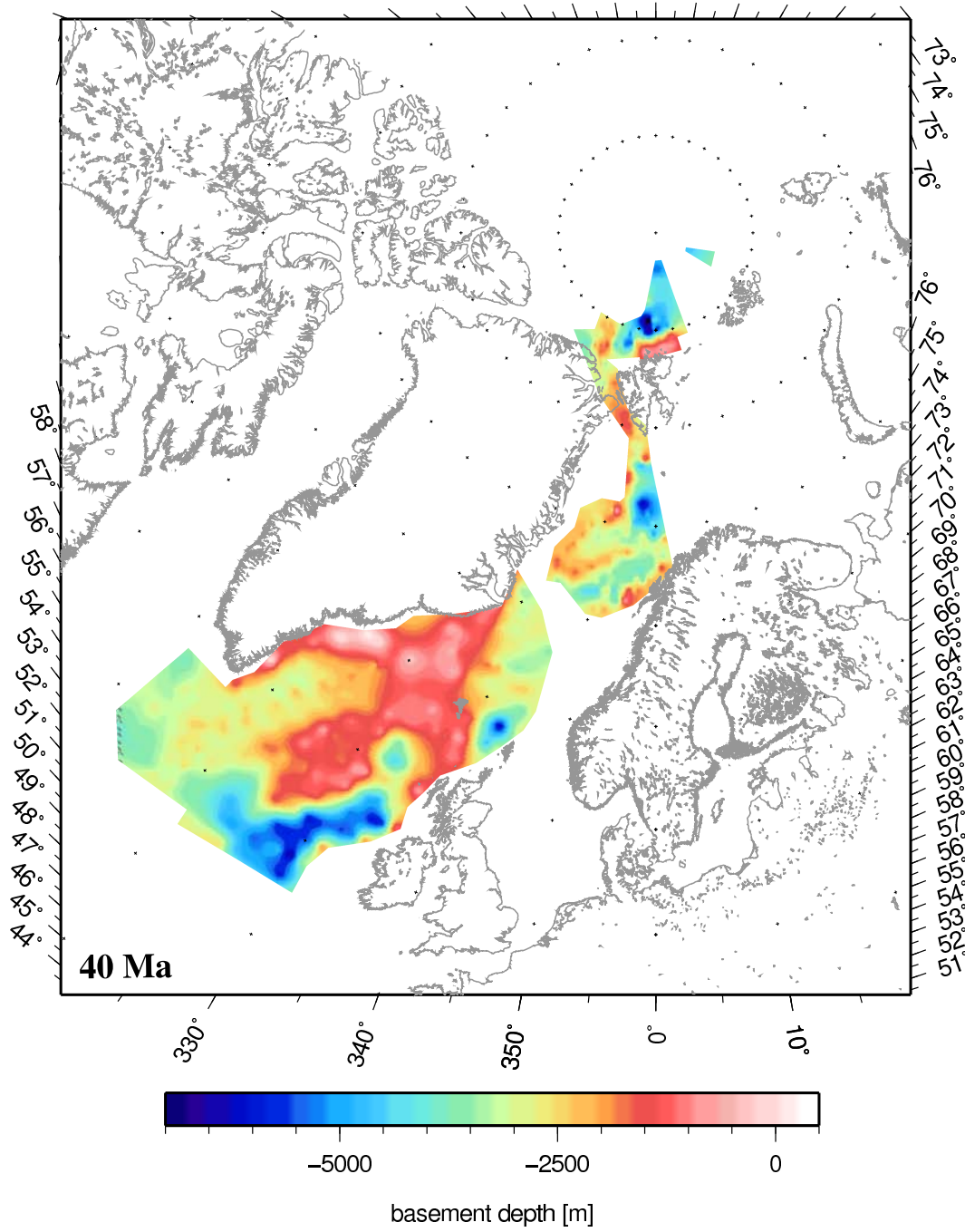


Figure A.25: Palaeo-basement reconstruction for 40 Ma

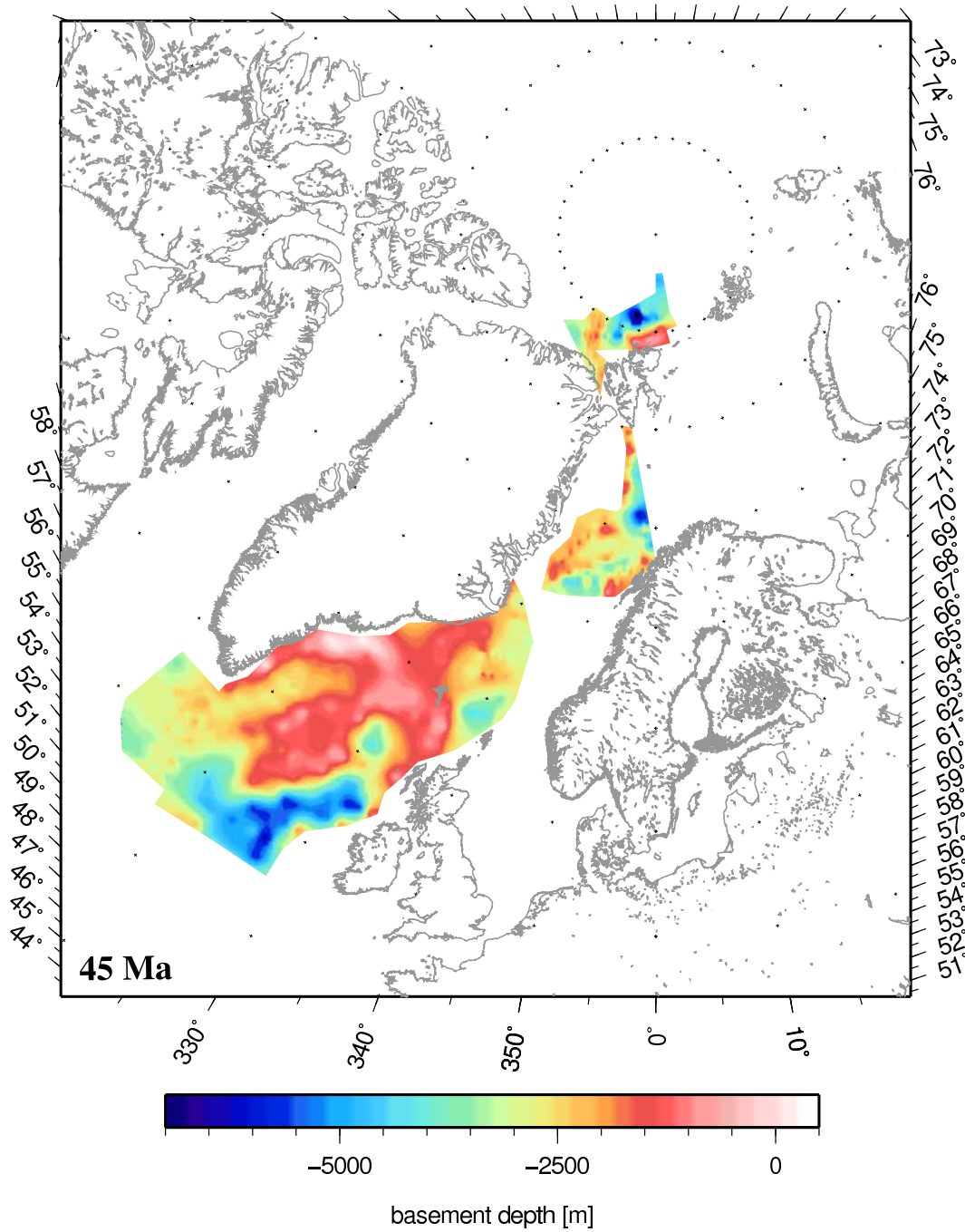


Figure A.26: Palaeo-basement reconstruction for 45 Ma

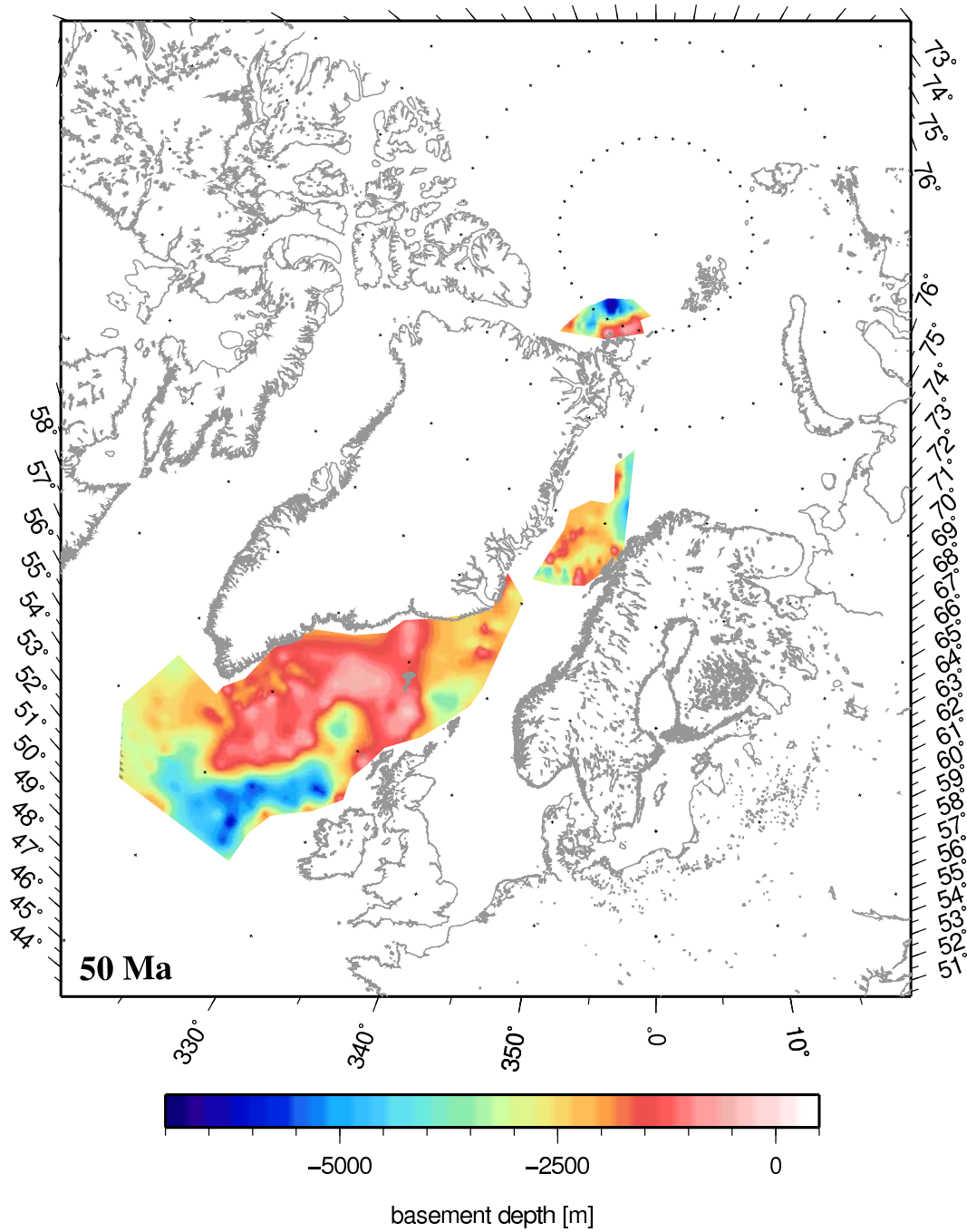


Figure A.27: Palaeo-basement reconstruction for 50 Ma

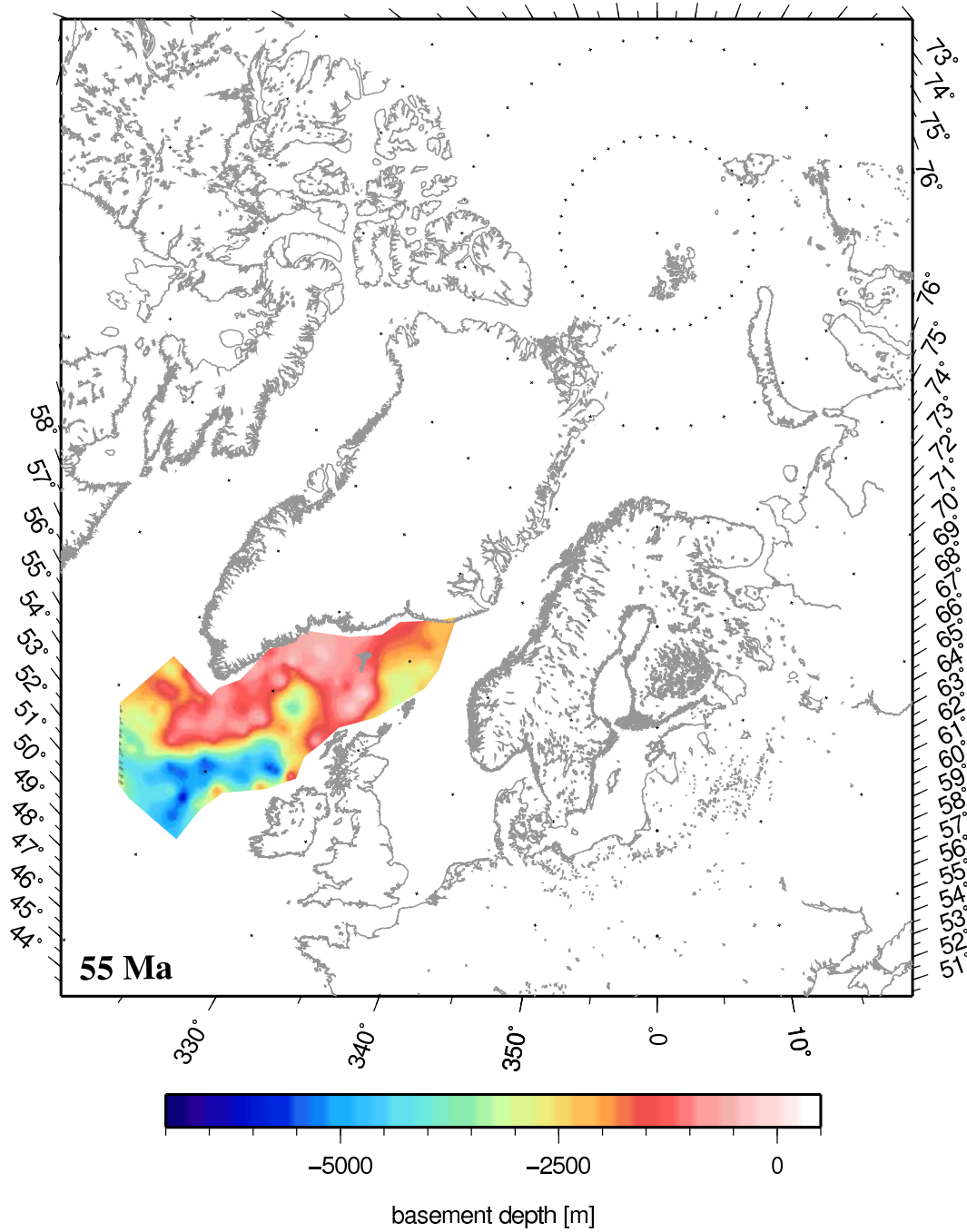


Figure A.28: Palaeo-basement reconstruction for 55 Ma

A.0.3 Reconstruction of palaeo-sediment thickness

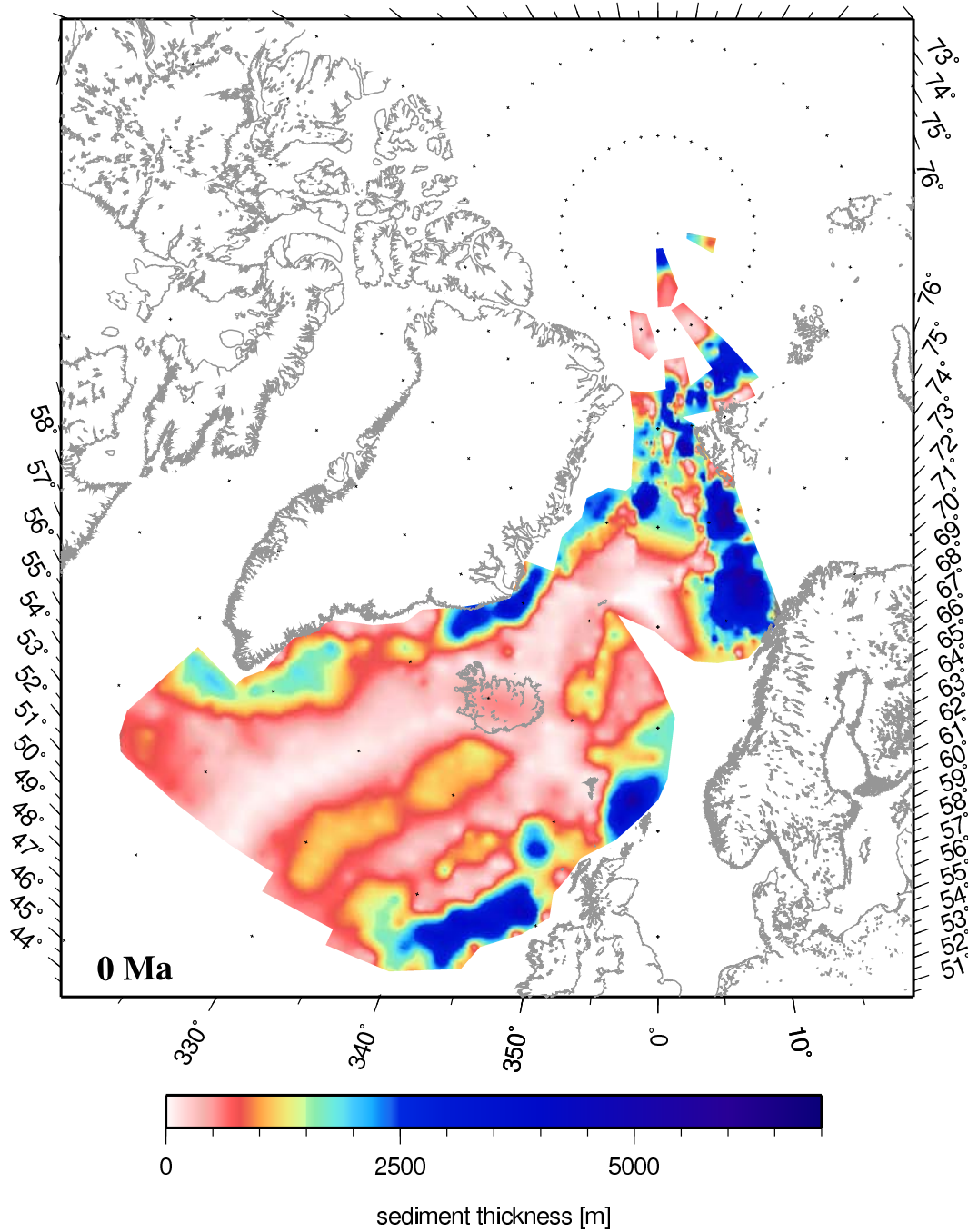


Figure A.29: Palaeo-sediment thickness reconstruction for 0 Ma

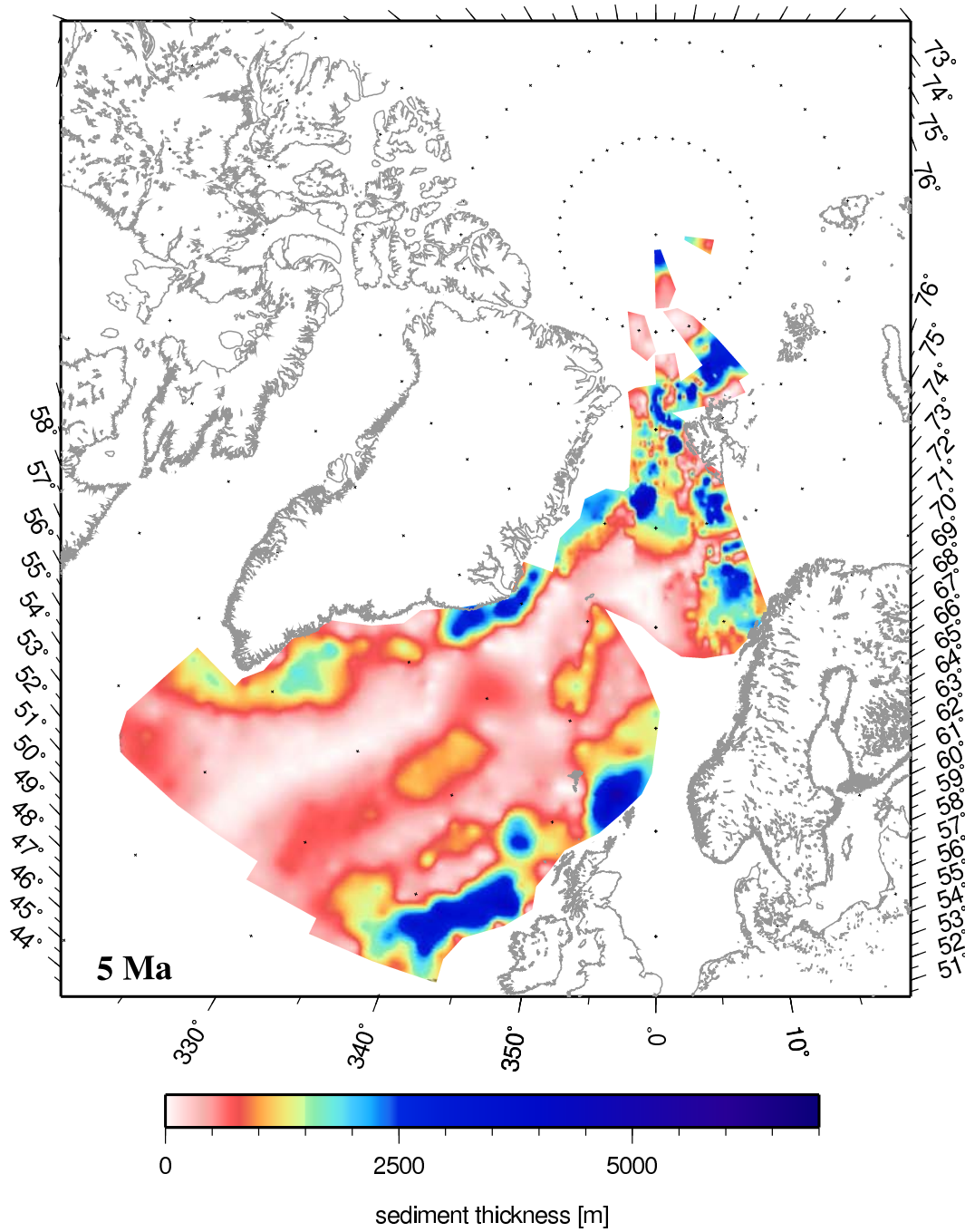


Figure A.30: Palaeo-sediment thickness reconstruction for 5 Ma

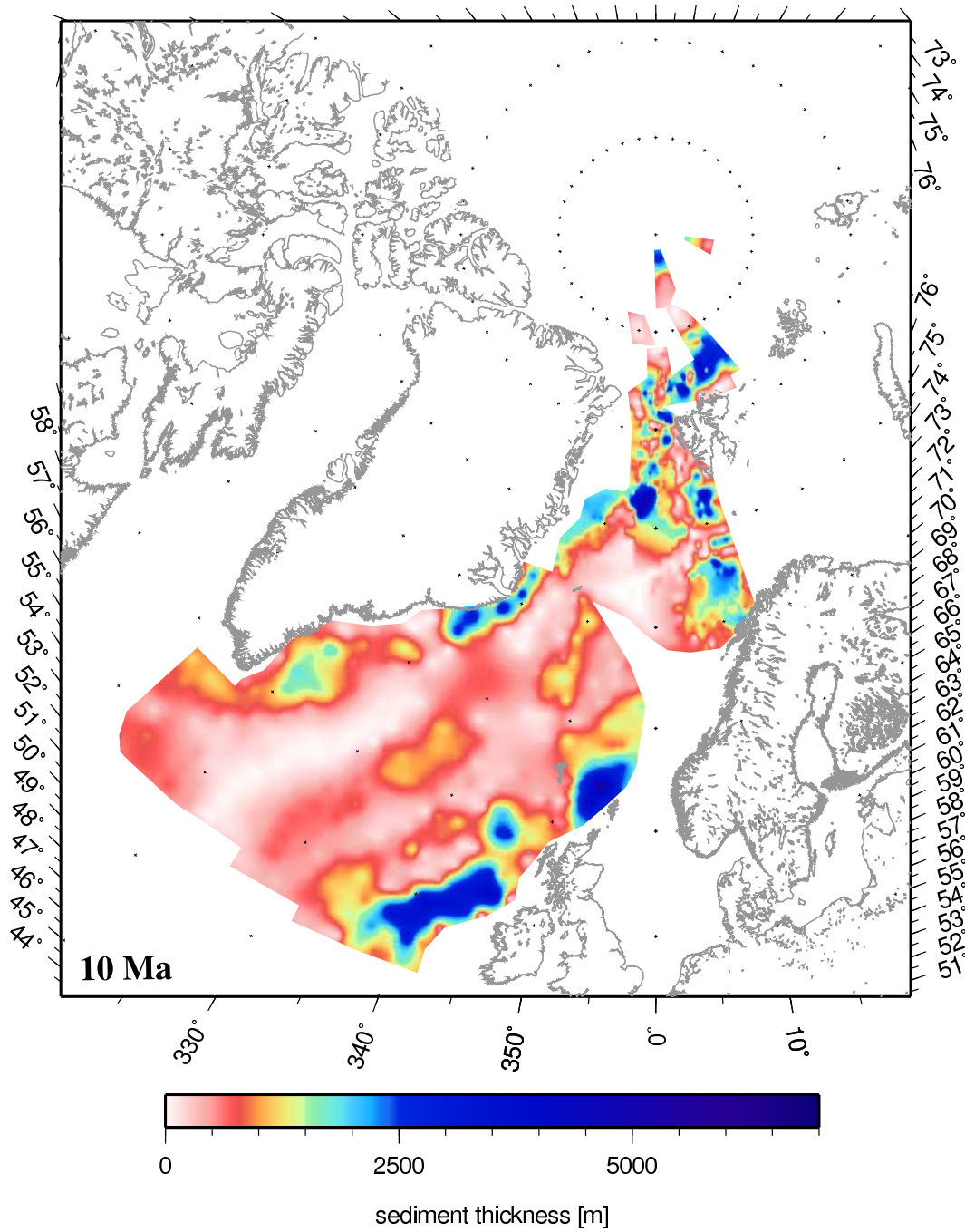


Figure A.31: Palaeo-sediment thickness reconstruction for 10 Ma

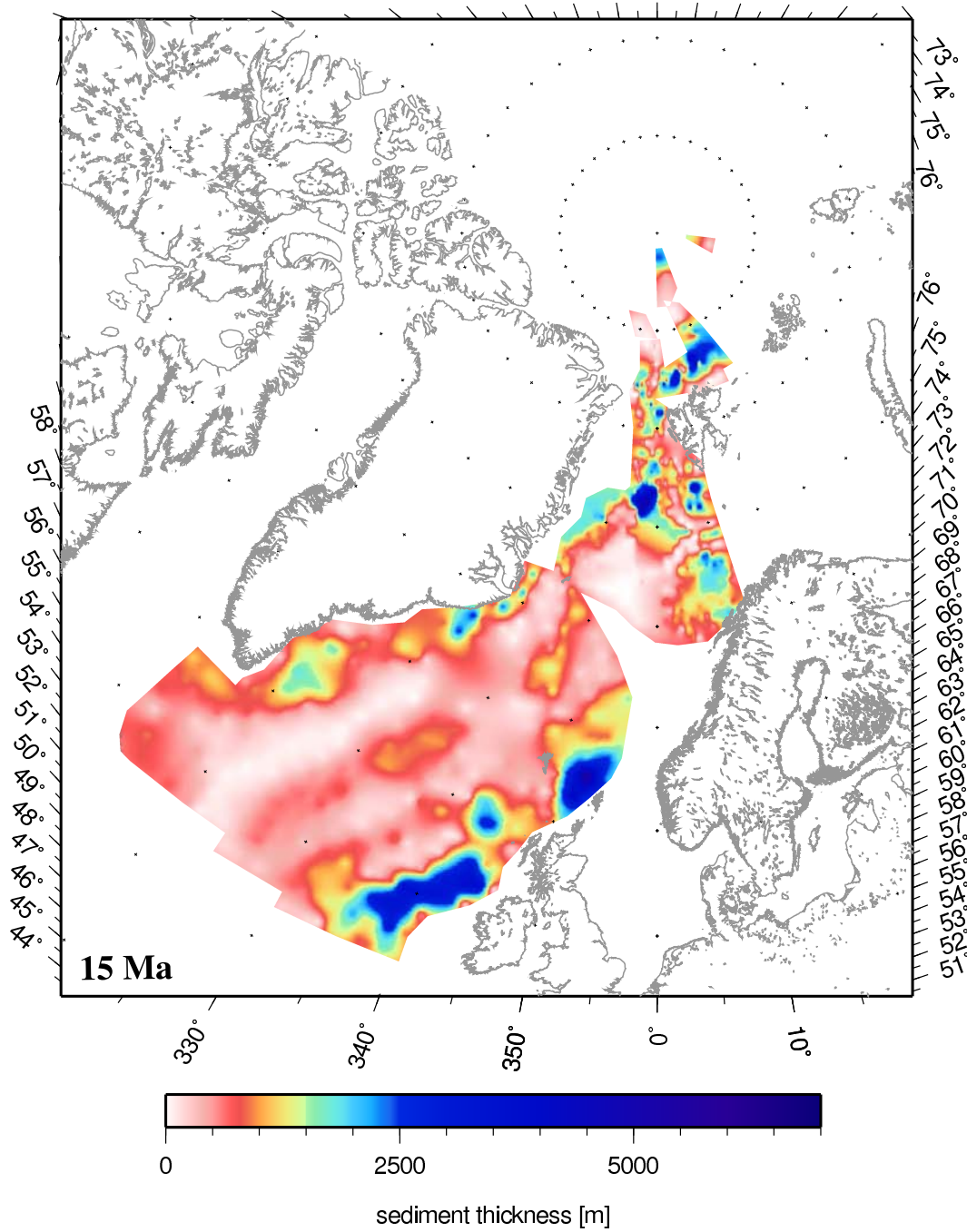


Figure A.32: Palaeo-sediment thickness reconstruction for 15 Ma

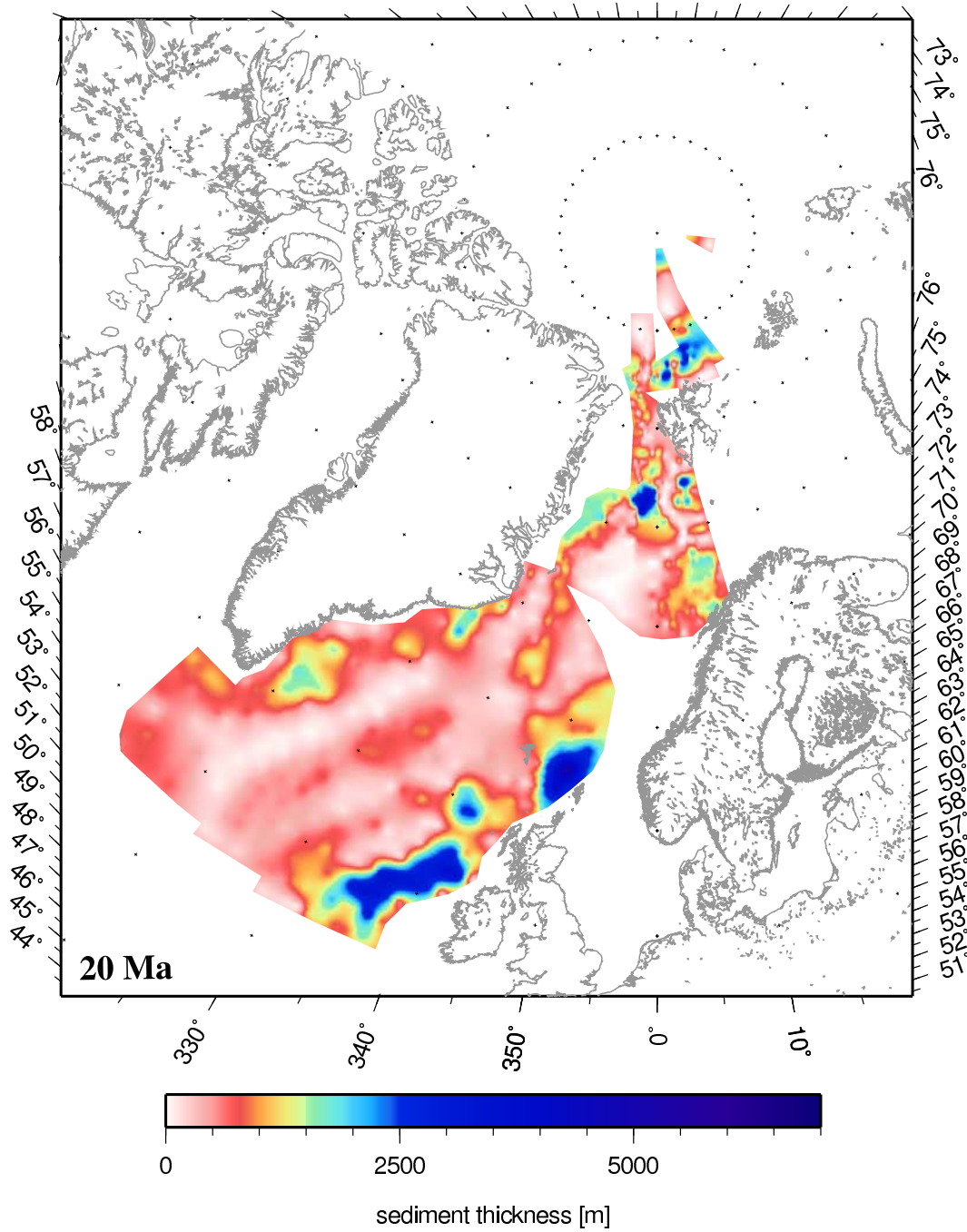


Figure A.33: Palaeo-sediment thickness reconstruction for 20 Ma

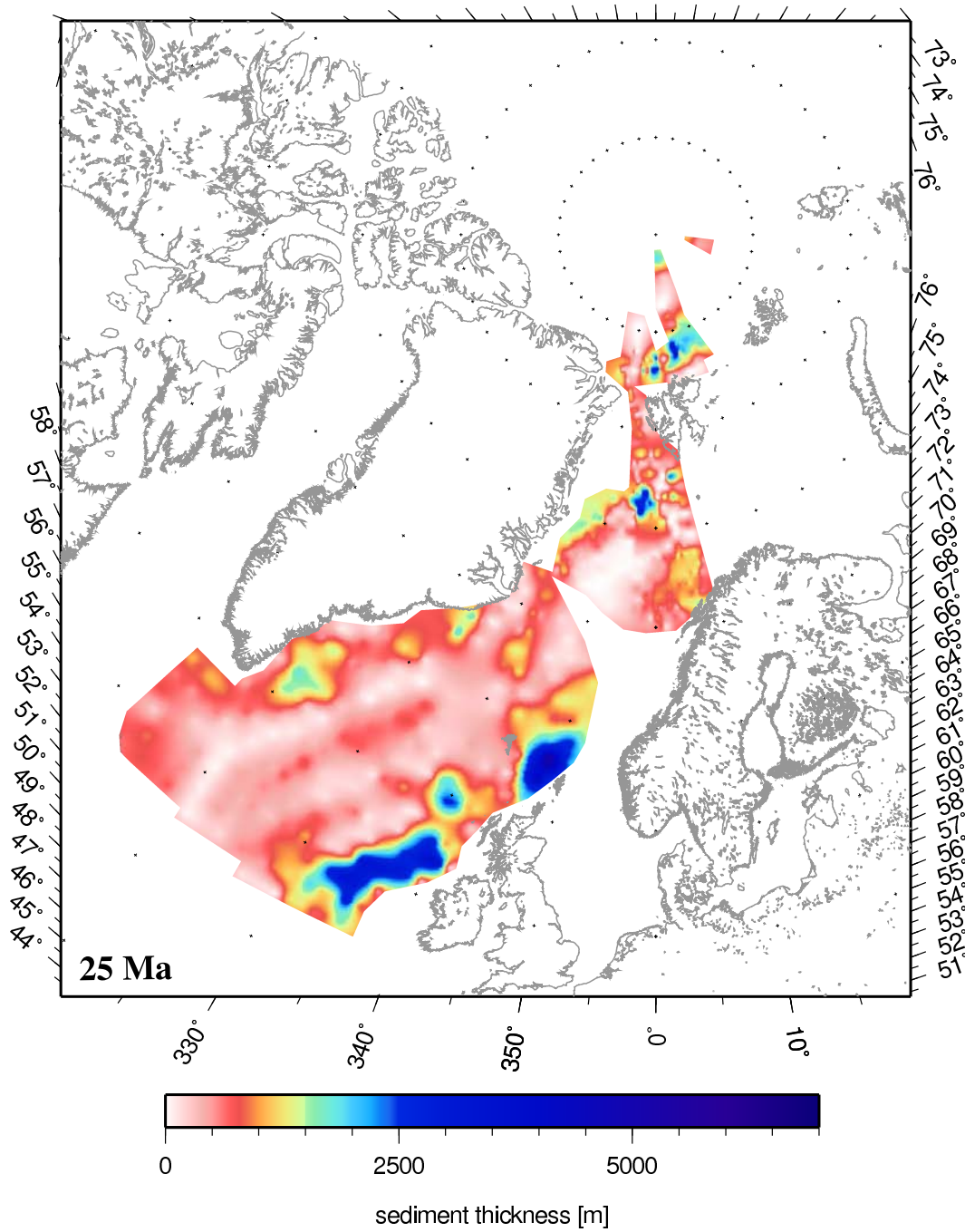


Figure A.34: Palaeo-sediment thickness reconstruction for 25 Ma

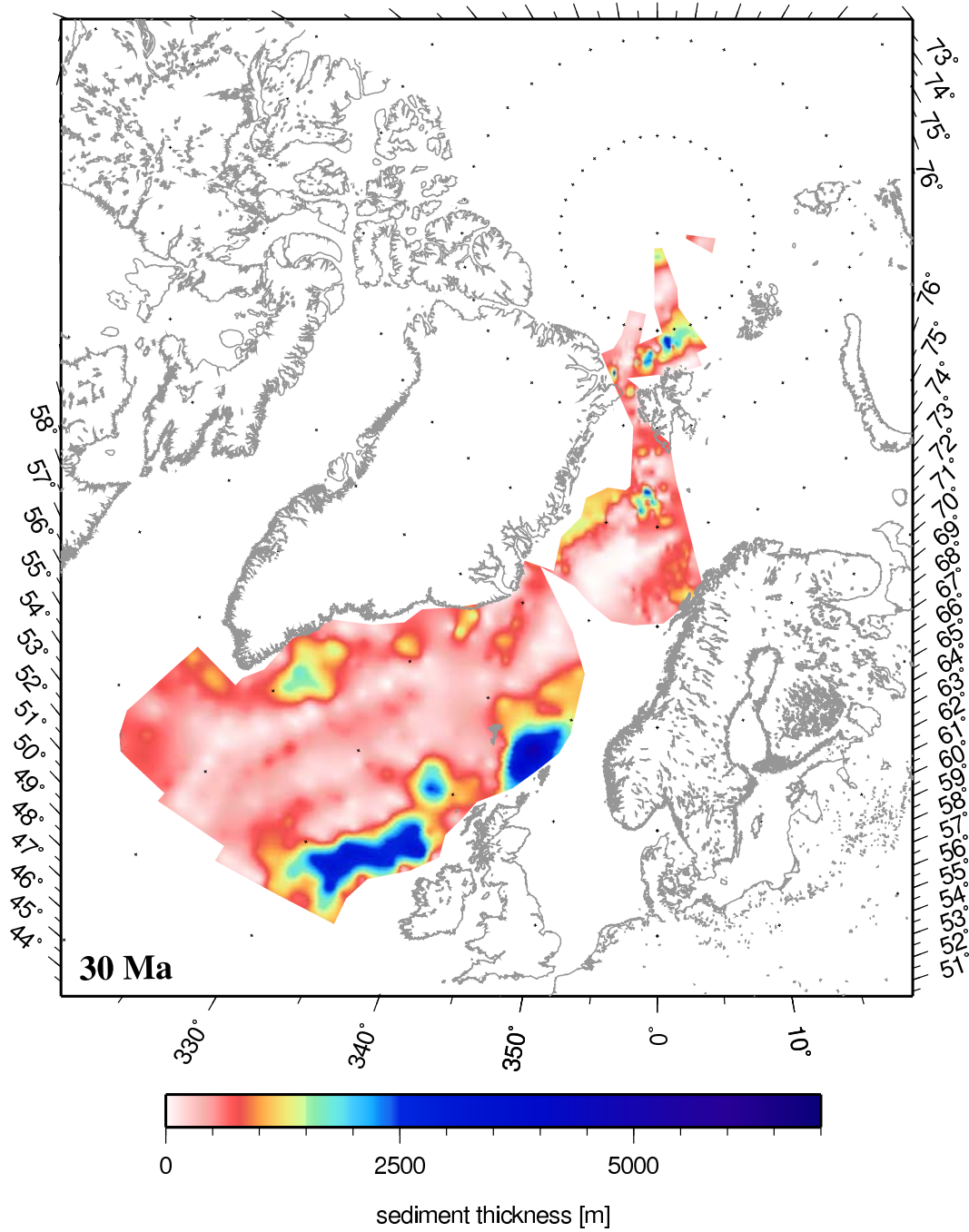


Figure A.35: Palaeo-sediment thickness reconstruction for 30 Ma

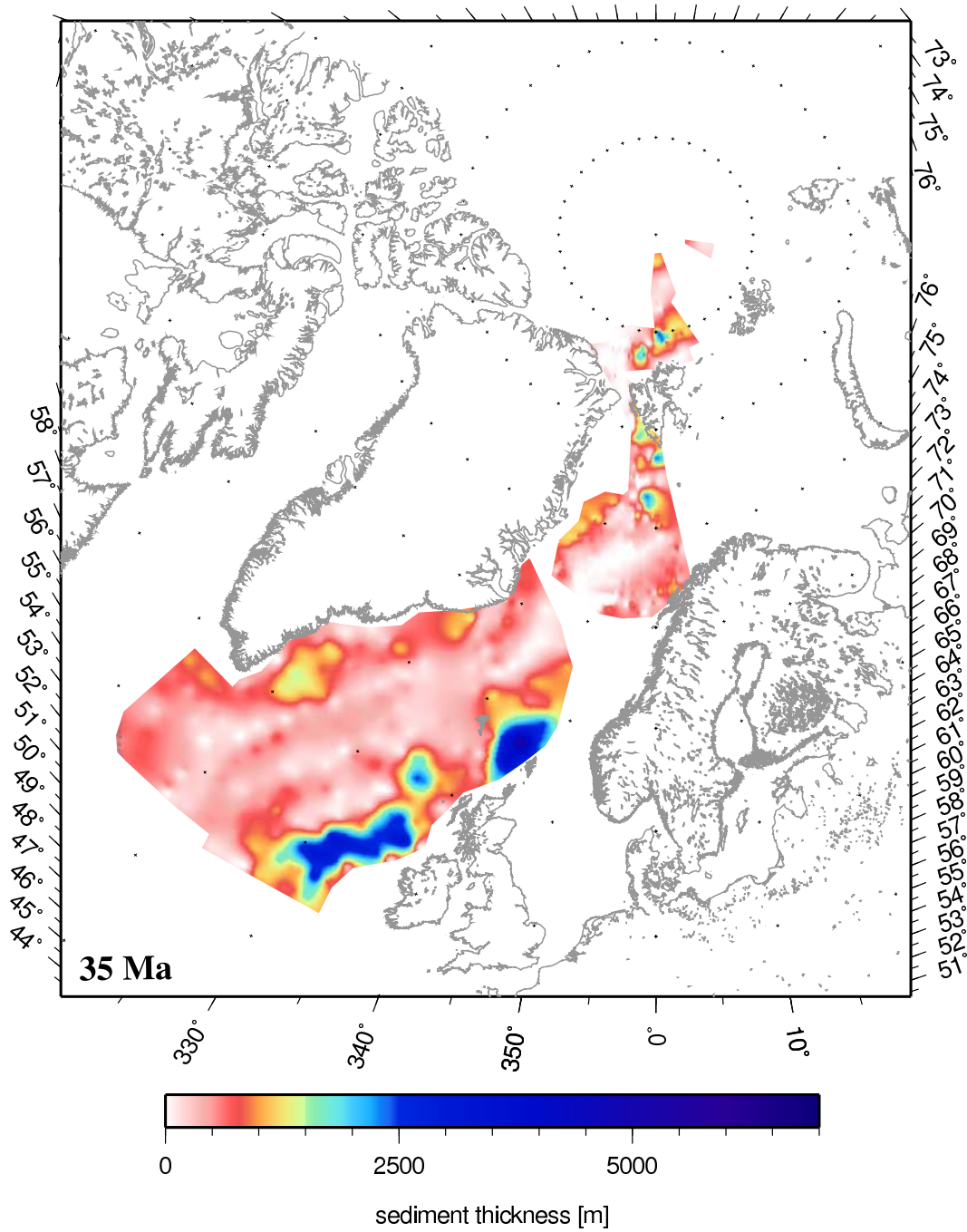


Figure A.36: Palaeo-sediment thickness reconstruction for 35 Ma

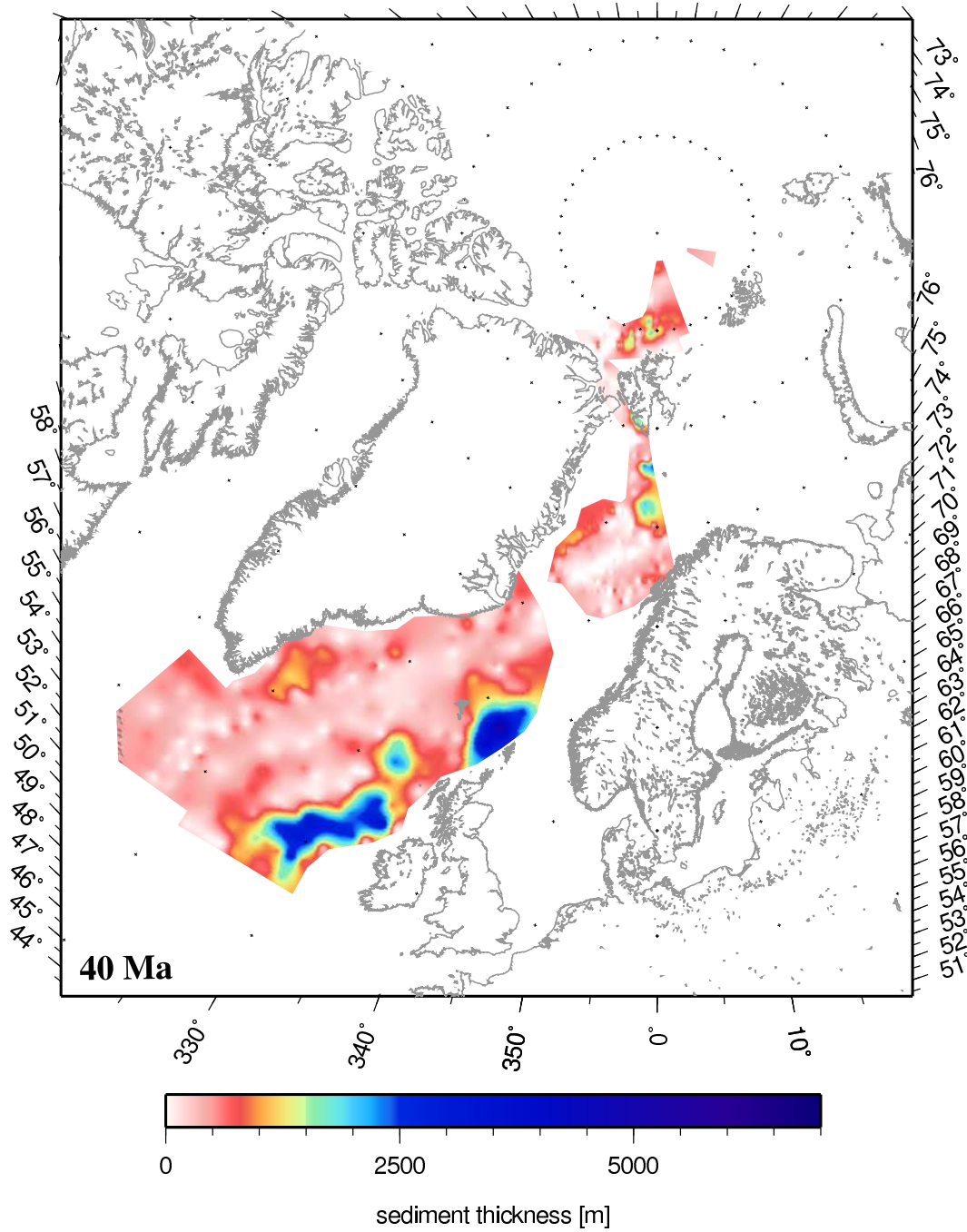


Figure A.37: Palaeo-sediment thickness reconstruction for 40 Ma

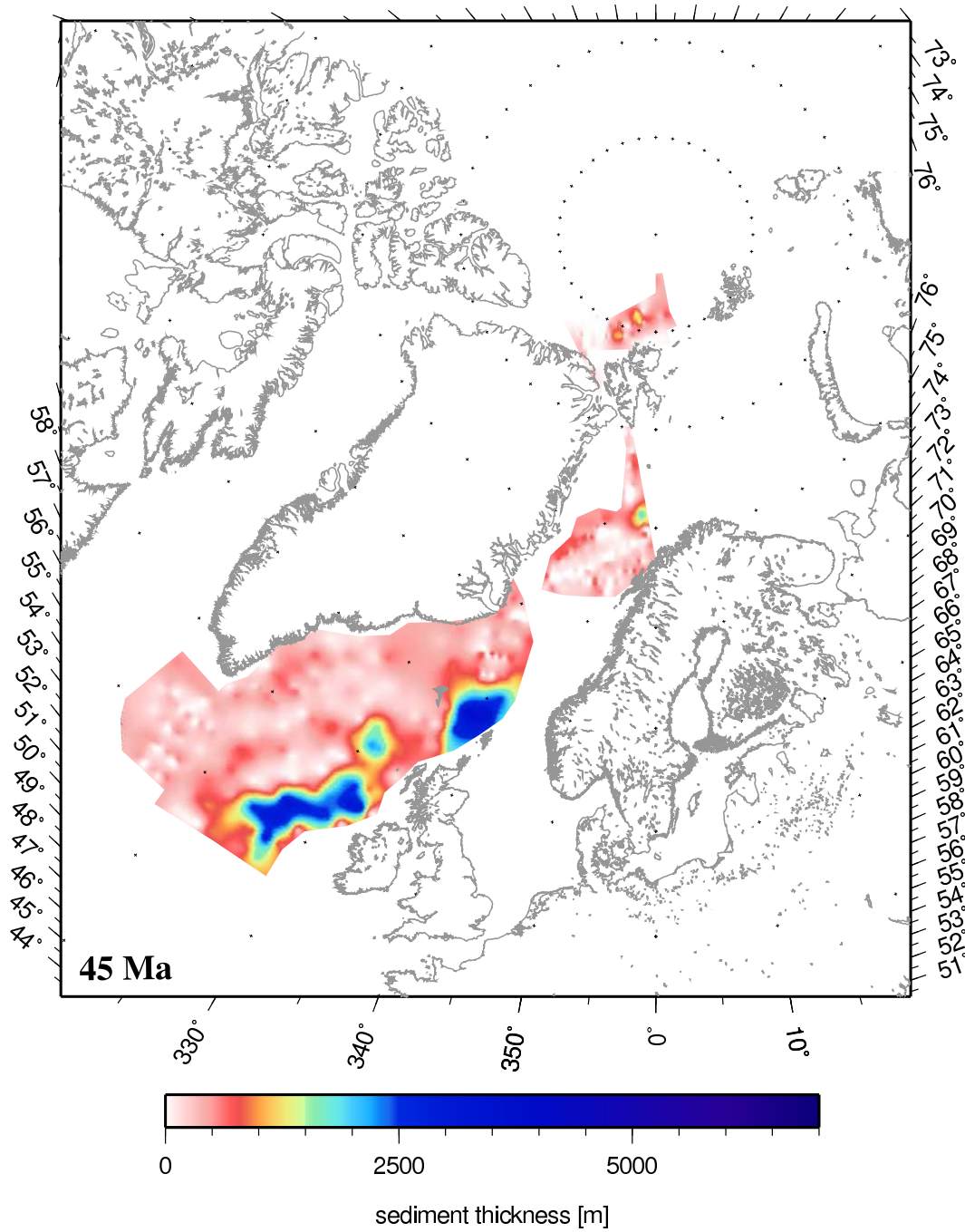


Figure A.38: Palaeo-sediment thickness reconstruction for 45 Ma

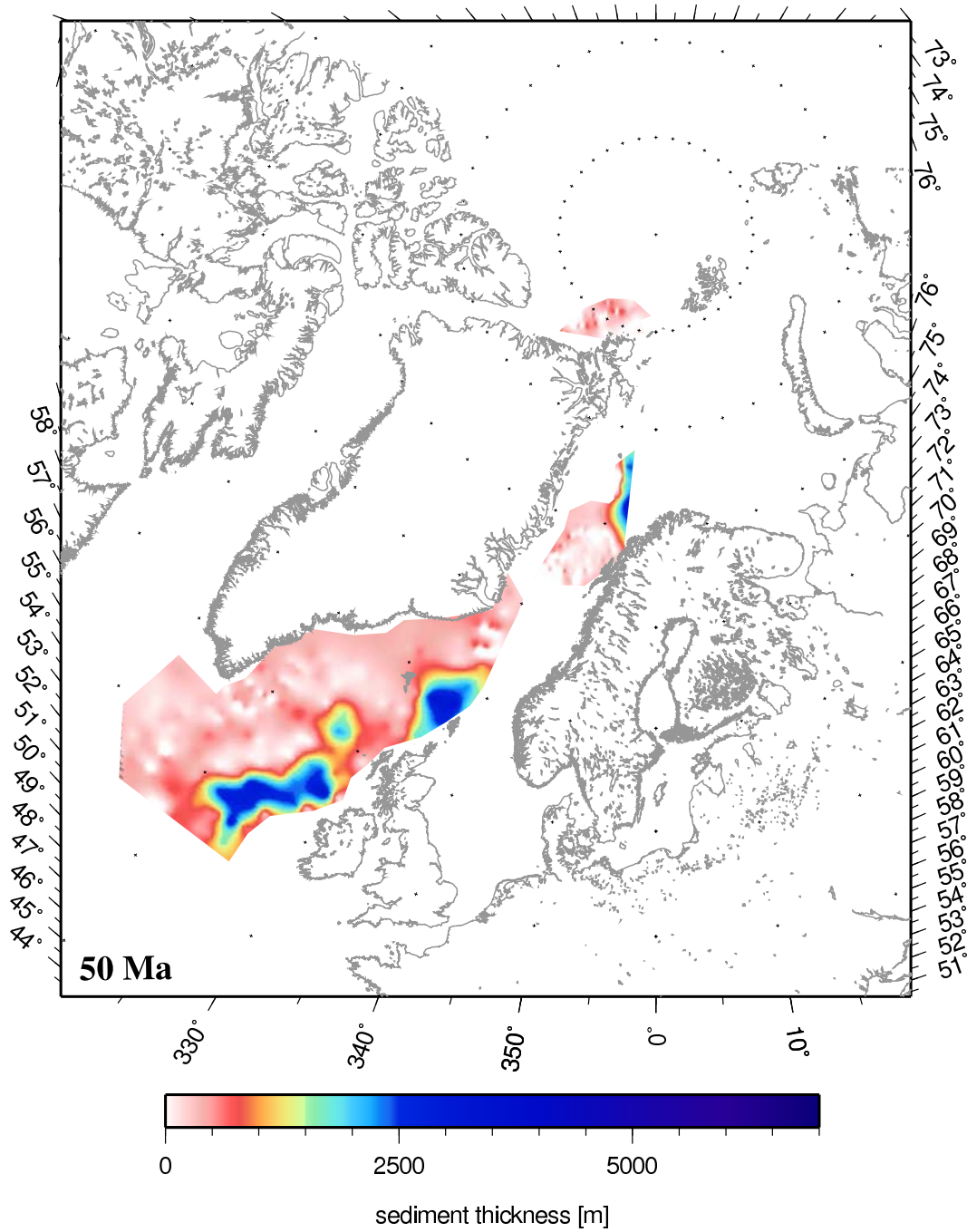


Figure A.39: Palaeo-sediment thickness reconstruction for 50 Ma

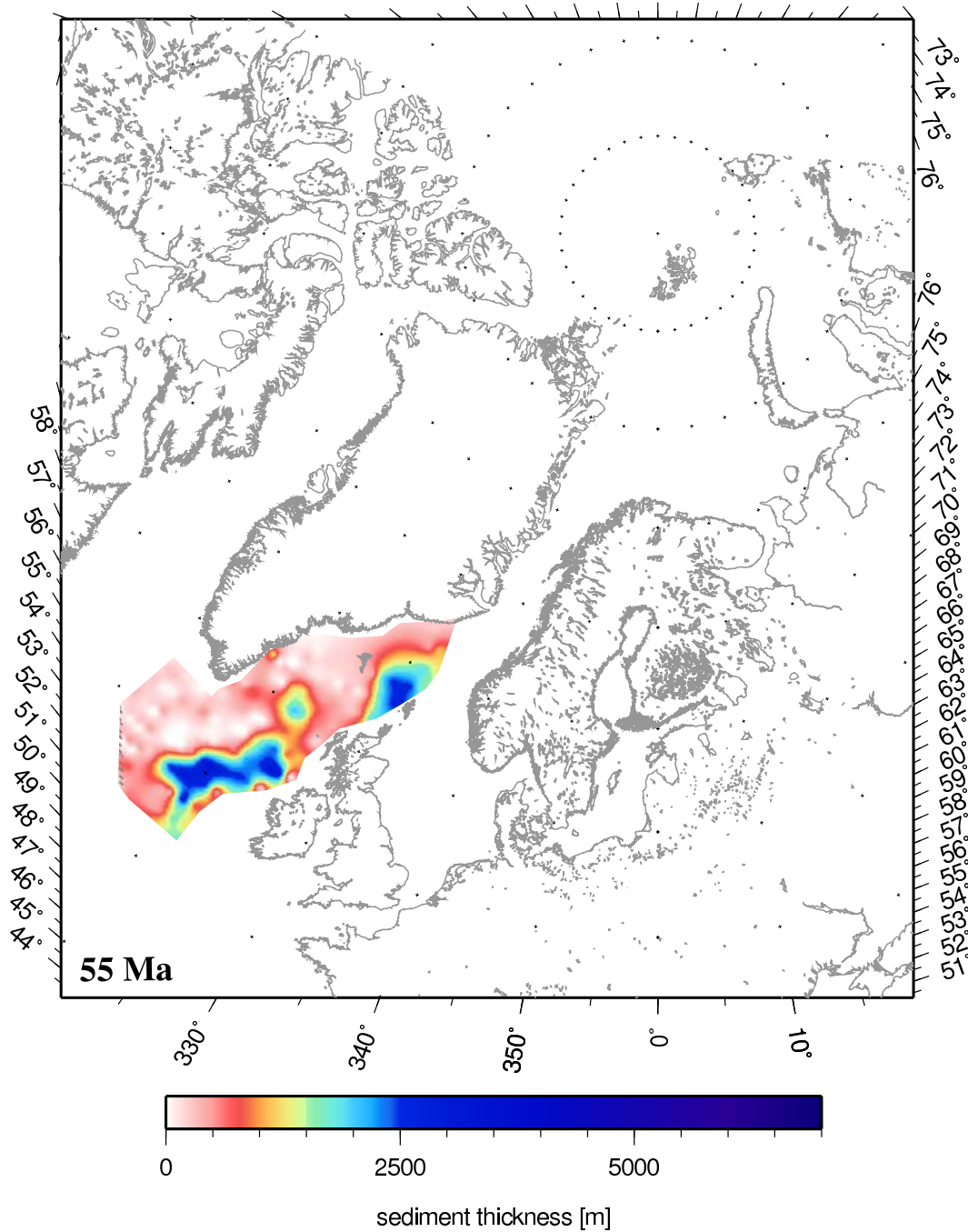


Figure A.40: Palaeo-sediment thickness reconstruction for 55 Ma

A.0.4 World wide palaeobathymetry for oceanographic modelling

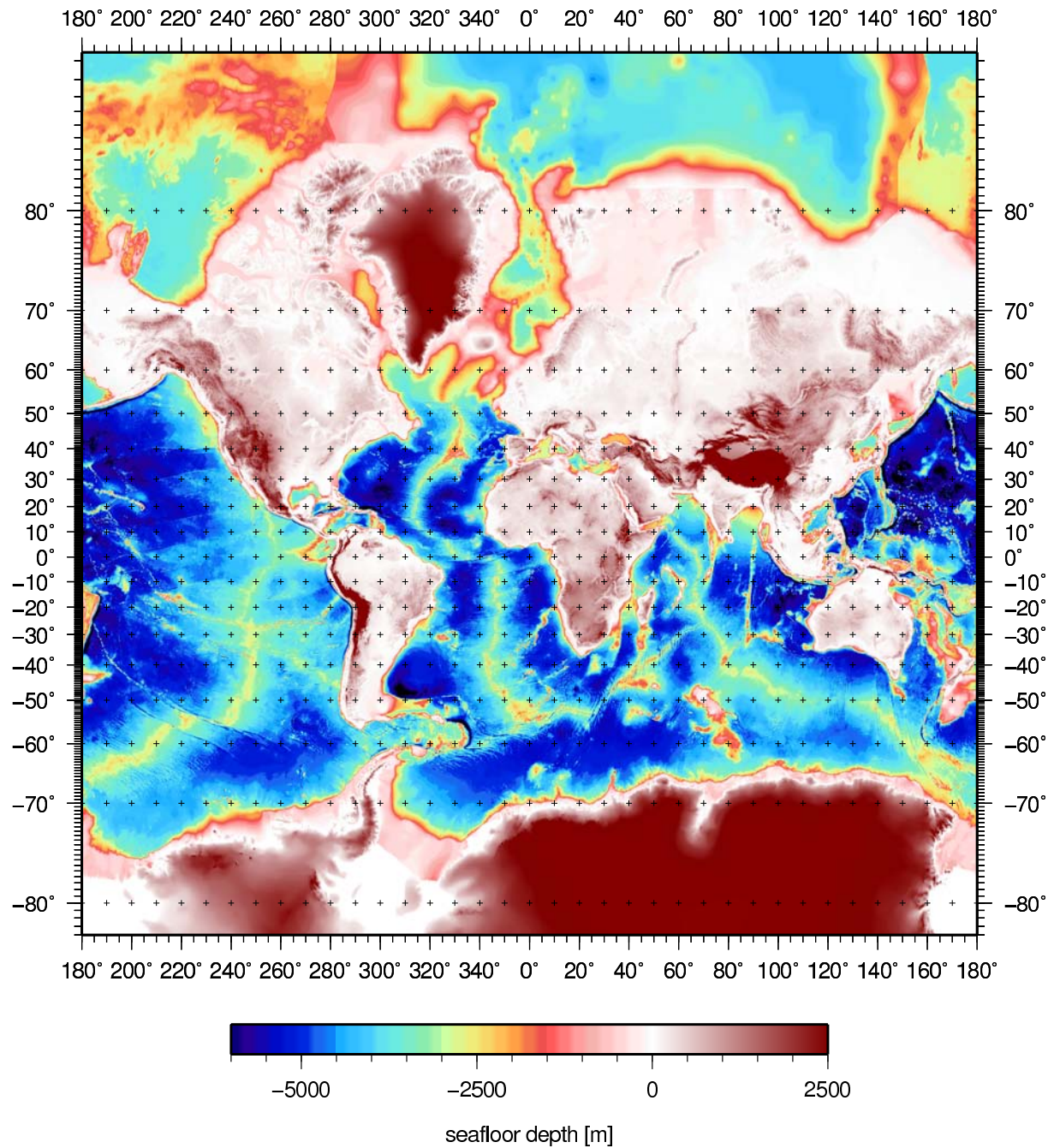


Figure A.41: Palaeobathymetry data of the North Atlantic and the Arctic ocean (this study) combined with the world wide palaeobathymetry data for 0 Ma (Müller et al., 2008)

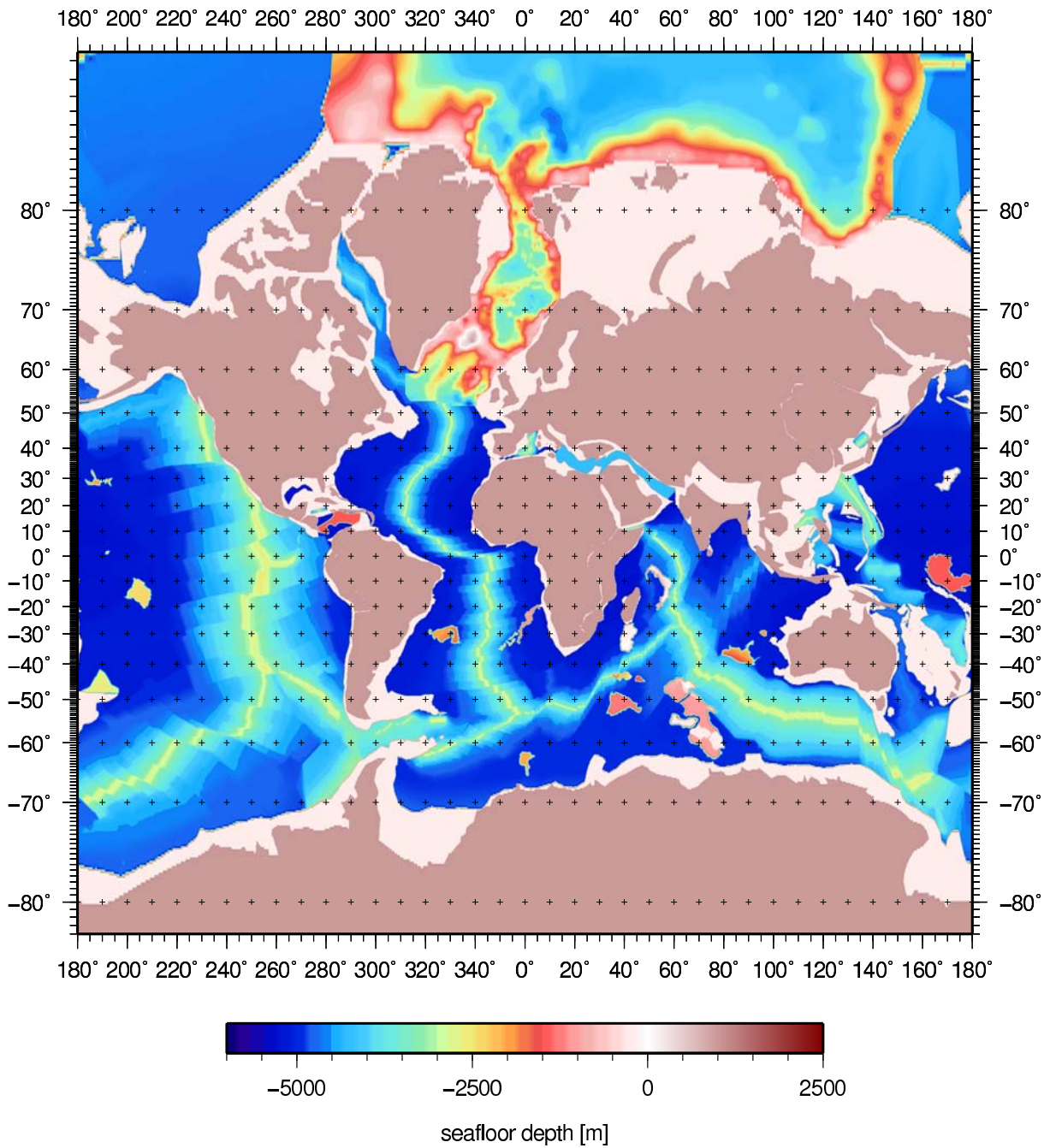


Figure A.42: Palaeobathymetry data of the North Atlantic and the Arctic ocean (this study) combined with the world wide palaeobathymetry data for 15 Ma (Müller et al., 2008)

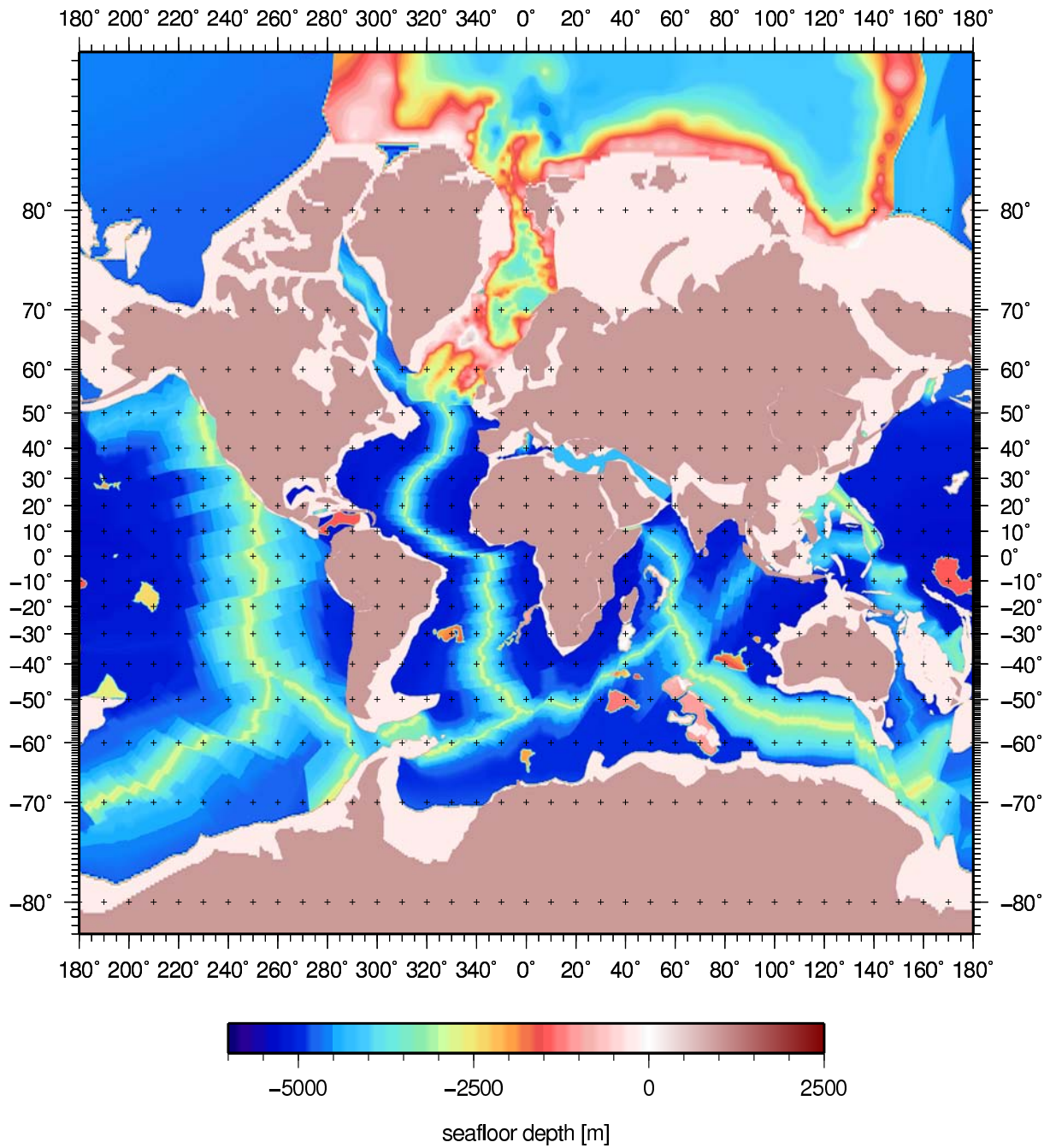


Figure A.43: Palaeobathymetry data of the North Atlantic and the Arctic ocean (this study) combined with the world wide palaeobathymetry data for 20 Ma (Müller et al., 2008)

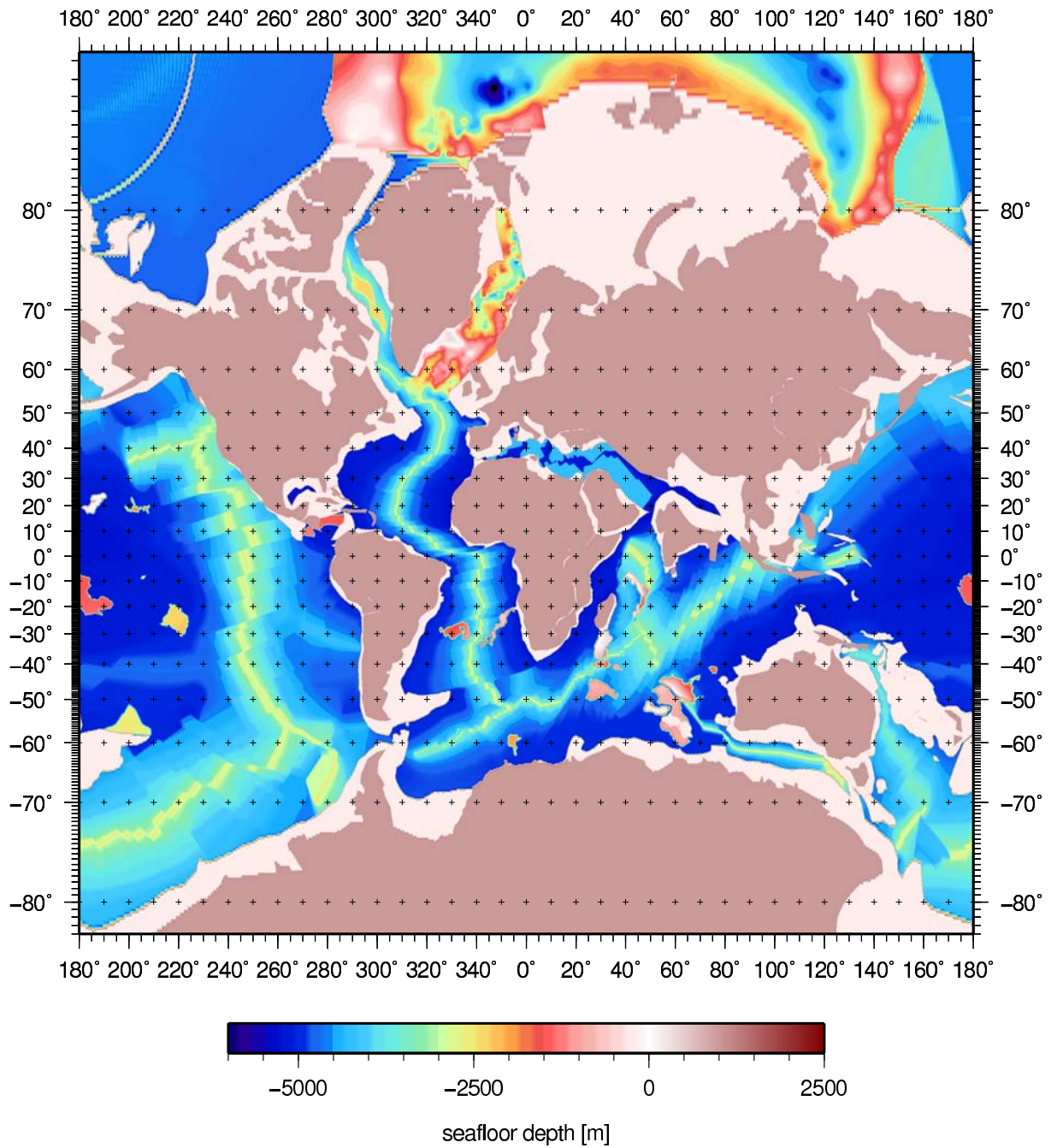


Figure A.44: Palaeobathymetry data of the North Atlantic and the Arctic ocean (this study) combined with the world wide palaeobathymetry data for 45 Ma (Müller et al., 2008)

A.0.5 Modelled crustal thickness

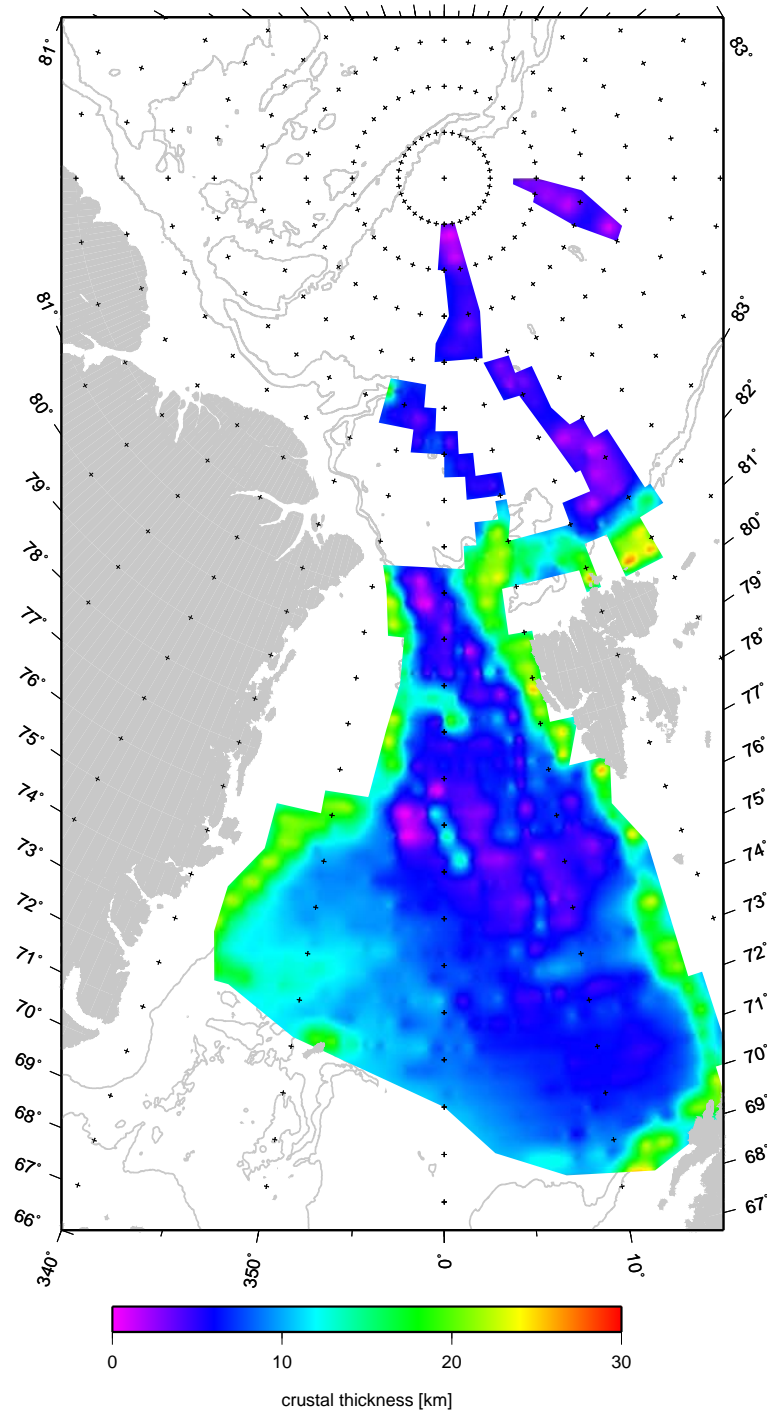


Figure A.45: Calculations of “BalPal v. 0.9” (Wold, 1995): modelled crustal thickness for a present day northern North Atlantic and Arctic Ocean

Appendix B

Additional tables

B.0.6 Sampled angles of rotation

poles of rotation: Eurasia - North America			
longitude[°]	latitude[°]	angle[°]	age[Ma]
132.98	66.44	+1	5 Myr in future
132.98	66.44	0	0
132.98	66.44	-1.00396	5
132.98	66.44	-2.13498	10
132.98	66.44	-3.31365	15
132.98	66.44	-3.54571	16
132.98	66.44	-3.84414	17
132.98	66.44	-4.18029	18
132.59	68.91	-4.5091	19
132.59	68.91	-4.81694	20
132.59	68.91	-6.17944	25
132.59	68.91	-7.4294	30
131.53	68.22	-8.37145	35
131.53	68.22	-10.1308	40
131.53	68.22	-11.8336	45
138.44	65.38	-13.3925	50
144.26	63.07	-15.8	55

poles of rotation: Greenland - North America			
longitude[°]	latitude[°]	angle[°]	age[Ma]
-84.00	62.80	-0.391321	35
-84.00	62.80	-1.40406	40
-84.00	62.80	-2.40	45
-134.35	39.29	-1.14877	50
-134.35	39.29	-1.47921	55

Table B.1: Sampled poles of rotation and rotation angles and for age intervals of 5 Myr or 1 Myr respectively

B.0.7 Input data “BalPal v. 0.9”

Grid cell for “BalPal v.0.9”		
CELL_CENTER	=	4.75 76.25
CELL_SIZE_LON	=	0.5
CELL_SIZE_LAT	=	0.5
DEPTH_UNITS	=	METERS
ELEVATION	=	0
WATER_DEPTH	=	-2854.78, SW
CRUST_TYPE	=	OC
CRUST_AGE	=	10.365
TECT_PLATE	=	GRN
TOTAL_SED_THICK	=	784
TOP_AGE	=	0.0
LAYER	=	1
LITHOLOGY	=	SJ
STRAT_AGE_BASE	=	-175, 3
LAYER	=	2
LITHOLOGY	=	SJ
STRAT_AGE_BASE	=	-311, 5
LAYER	=	3
LITHOLOGY	=	ST
BOT_AGE	=	-784, 10.3

Table B.2: One of 1515 grid cells for a run of the software packet “BalPal v. 0.9” between the Jan Mayen Fracture Zone and the Lomonosov Ridge. This example grid cell with a size of $0.5^\circ \times 0.5^\circ$ has its center at 4.75°E and 76.25°N .

Additional tables

(1) Isostatic parameters				
compensation depth	100 km			
reference thickness of oceanic crust	6.5 km			
reference age of oceanic crust	200 Ma			
density sea water	1027 kg/m ³			
density oceanic crust	2900 kg/m ³			
density continental crust	2850 kg/m ³			
maximal density of asthenosphere	3310 kg/m ³			
(2) Sediment compaction parameters				
lithology	shale	silt	sandstone	limestone
equation type	exponential	parabolic	exponential	power-law
term A	0.7070	0.7110	0.4900	0.7540
term B	0.6330	0.3170	0.2700	0.1575
term C		0.0020		
unit of depth	km	km	km	km
upper limit	0.000	0.001	0.000	0.001
lower limit	10.4	2.3	23.0	6.0
(3) Thermal subsidence parameter				
thermal function type	square-root	exponential		
coefficient A	2500	5651		
coefficient B	350	2473		
coefficient C		0.0278		
younger limit	0.000 Ma	57.116 Ma		
older limit	57.116 Ma	200.000 Ma		

Table B.3: Parameters for the program packet “BalPal v. 0.9” for (1) the Airy type isostasy, (2) the calculation of sediment decompaction and (3) the subsidence calculation

Declaration

I declare, that I have written this PhD thesis independently and that this PhD thesis has not been submitted at another University for the conferral of a Degree.

Bremerhaven, 17th December 2008

Acknowledgements

Thank you very much

- to Dr. Wilfried Jokat, who supervised this PhD-project at the Alfred Wegender Institute and supported me for all three manuscripts
- to Prof. Dr. Vikram Unnithan, my Jacobs University Bremen supervisor, for all his support
- to Prof. Dr. Joachim Vogt and Dr. Carmen Gaina, who are further members of my PhD-committee
- to Dr. Klaus Grosfeld and Dr. Martin Butzin for running the palaeo-ocean circulation model and for being co-authors of the third manuscript
- to Dr. Wolfram Geissler and Dr. Matthias König for their support on the introduction text and their helpful discussions
- to Daniela Berger for a great time in room D-3200 and for many serious and funny discussions
- to Julia Schinkel and Hartmut Martens for the entertaining year in room D-3140
- to the whole AWI geophysics group: Mechita, Estella, Karsten, Max, Catalina, Norbert, Jan, Vera, Gabi, Carsten, Alfons, Bettina, Volker, Carsten, Philip, Nicole, Jürgen, Monika, Florian, Christine, Ansa and all the rest of them
- to Ansa Lindeque, Hans Mürkens, Aysel Sorensen, Dr. Graeme Eagles and Birgit Fockner for many English corrections
- to Matthias Lankhorst for checking my new oceanographic knowledge
- to the handball team of the LTS, the tennis team of the TC Rot-Weiss Bremerhaven and the AWI/Skiclub Innebandy group for uncountable sportive and funny evenings, weekends, games and parties...
- to my parents, my brother and the rest of the family for supporting me in whatever I do and wherever I am
- to Jens Köhler for spending his holidays in Bremerhaven and mostly for being a “Zweinzeltgänger 😊”!

Thanks a lot! 😊

Curriculum Vitae

Birte-Marie Ehlers

Date of birth: 27.11.1977
Place of birth: Bremerhaven, Germany
Nationality: German

EMPLOYMENTS

01/2009 **Turbine Load Calculation Engineer**
Suzlon Energy GmbH, Research & Development

08/2005–10/2008 **PhD student**
Alfred Wegener Institute for Polar and Marine Research, Bremerhaven,
department Marine Geophysics

08/2003–08/2005 **Research assistant**
member of the overwintering team at Neumayer Station (Antarctica) as
a geophysicist, overwintering for 15 month, Alfred Wegener Institute
for Polar and Marine Research, Bremerhaven

RESEARCH EXPEDITIONS

09/2007 **Research assistant**
expedition to the North Atlantic and Svalbard with the MS Horizont II,
Alfred Wegener Institute for Polar and Marine Research, Bremerhaven

02/2007–04/2007 **Research assistant**

04/2006–06/2006 expedition to Prydz Bay, East-Antarctica (2007) and to the South
Atlantic (2006) with the RV Polarstern, Alfred Wegener Institute for
Polar and Marine Research, Bremerhaven

04/1999–11/2002 **Student research assistant**
numerous archaeometric projects in Germany, Turkey, Greece, Italy and
Iran with different geophysical measurements, Christian-Albrechts-
University Kiel

12/2001–01/2002 **Student research assistant**

02/2001–04/2001 expedition to the Weddell Sea, Antarctica (2002) and the Bellinghausen
Sea, Antarctica (2001), Alfred Wegener Institute for Polar and Marine
Research Bremerhaven

06/1998–08/1998 **Student research assistant**
land expedition to the 79°-glacier in North East Greenland, Alfred
Wegener Institute for Polar and Marine Research, Bremerhaven

EDUCATION

- since 08/2005 **PhD candidate**
Jacobs University Bremen and Alfred Wegener Institute for Polar and Marine Research, Bremerhaven
- 07/2002–07/2003 **Diploma**
Christian-Albrecht-University Kiel, thesis title: D-GPS gesteuerte geomagnetische Kartierung in der archäologischen Prospektion
- 10/1997–07/2002 **Undergraduate student of geophysics**
Christian-Albrecht-University Kiel
- 1984–1997 **School qualification**
Gymnasium Wesermünde, Bremerhaven, Abitur (general qualification for university entrance)

SCIENTIFIC PUBLICATIONS AND PRESENTATIONS

Scientific publications

- 06/2007 Ehlers, B.-M. and Jokat, W. (GJI,accepted)
Subsidence and crustal roughness of ultra-slow spreading ridges in the northern North Atlantic and the Arctic Ocean
- 10/2008 Ehlers, B.-M. and Jokat, W. (GJI,submitted)
Palaeobathymetric study of the North Atlantic and the Eurasia Basin
- 12/2008 Ehlers, B.-M., Butzin, M., Grosfeld, K. and Jokat, W. (GPC, submitted)
A palaeoceanographic study of the northern North Atlantic and the Arctic Ocean

Conference presentations (talks and posters)

- 04/2008 A palaeobathymetric study of the northern North Atlantic
EGU General Assembly, Vienna, Austria
- 12/2007 Constraints on a palaeobathymetric model of the northern North Atlantic
AGU Fall Meeting, San Francisco, USA
(outstanding student award for poster presentation)
- 09/2007 Constraints on the geodynamic evolution of the northern North Atlantic
International Conference on Arctic Margins (ICAM), Tromsø, Norway